Preprints.org

Article

Not peer-reviewed version

Dilatant Dark Fluid: Toward a Unified Quantum-Hydrodynamic Origin of Lorentz Invariance, Gravity, and Cosmological Phenomenology

Marco Fedi *

Posted Date: 7 September 2026

doi: 10.20944/preprints202608.2283.v2

Keywords: dilatant dark fluid; material spacetime; quantum gravity; superfluid dark matter; shear-thickening fluids; quantum hydrodynamics; Lorentz invariance; general relativity; Painlevé–Gullstrand coordinates; galactic dynamics; large-scale structure

Preprints.org is a free multidisciplinary platform providing preprint service that is dedicated to making early versions of research outputs permanently available and citable. Preprints posted at Preprints.org appear in Web of Science, Crossref, Google Scholar, Scilit, Europe PMC, OpenAlex.

Copyright: This open access article is published under a Creative Commons CC BY 4.0 license, which permit the free download, distribution, and reuse, provided that the author and preprint are cited in any reuse.

Preprints.org (www.preprints.org) | NOT PEER-REVIEWED | Posted: 7 September 2026 doi:10.20944/preprints202608.2283.v2

Disclaimer/Publisher's Note: The statements, opinions, and data contained in all publications are solely those of the individual author(s) and contributor(s) and not of MDPI and/or the editor(s). MDPI and/or the editor(s) disclaim responsibility for any injury to people or property resulting from any ideas, methods, instructions, or products referred to in the content.

Article

Dilatant Dark Fluid: Toward a Unified Quantum-Hydrodynamic Origin of Lorentz Invariance, Gravity, and Cosmological Phenomenology

Marco Fedi

Ministero dell'Istruzione e del Merito, Rome, Italy; marco.fedi@istruzione.it

Abstract

This work introduces the dilatant dark fluid (DDF), a pervasive cosmic cold dark medium comprising two coupled ultralight bosonic sectors: a superfluid ϕ and a heavier dispersed phase φ undergoing stress-induced shear jamming, distinguishing the framework from earlier superfluid-vacuum models. The DDF's velocity-dependent dilatant response drives the local φ sector toward a saturated jammed state that supports the propagation at c of coupled transverse phonons identified with photons, while remaining asymptotically inaccessible to massive bodies. This constitutive response generates a *jamming factor* identical to the Lorentz factor, recovering Lorentz-form kinetic energy, clock rate, and length relations, alongside interferometric and resonator nulls. By governing both matter dynamics and operational measurement standards, the DDF provides a quantum-hydrodynamic material realization of geometric relativistic spacetime. The superfluid sector supports quantized vortices interpreted as particles; their circulation encodes spin and generates Bernoulli pressure gradients seeded near the core by the associated quantum potential, which upon many-vortex coarse-graining yield macroscopic gravitational acceleration. Painlevé–Gullstrand river coordinates geometrically encode this material dynamics in general-relativistic exterior solutions, recovering classical weak- and strong-field benchmarks, including leading Kerr–Lense–Thirring behavior. At galactic scales, an isothermal regime of ϕ yields nearly flat rotation profiles, thereby providing a quantum-hydrodynamic route to MOND-like phenomenology. Cosmologically, expansion is treated as a coarse-grained deformation of the DDF, with primordial vortex–antivortex annihilation as a possible trigger for the hot epoch and inflation-like expansion, while the cosmic web is associated with vortex-filament networks in doped superfluids. Together, these results define a unified dark-medium framework; the Appendices present a direct gravitational discriminator from general relativity, an astrophysical probe of the proposed superfluid interpretation of the cosmic web, and laboratory tests of the DDF constitutive rheology.

Keywords: dilatant dark fluid; material spacetime; quantum gravity; superfluid dark matter; shear-thickening fluids; quantum hydrodynamics; Lorentz invariance; general relativity; Painlevé–Gullstrand coordinates; galactic dynamics; large-scale structure

1. Introduction

The dilatant dark fluid (DDF) is proposed as a cold dark substrate comprising two ultralight bosonic sectors governed by quantum hydrodynamics. Its continuous component, ϕ, is a coherent superfluid phase coupled to a comparatively heavier, noncondensed dispersed phase φ that undergoes progressive shear thickening under increasing stress, culminating in transient local shear jamming [1–3]. This second component is the principal distinction from earlier superfluid astrophysical approaches [4,5] and superfluid-vacuum models [6–13]: the superfluid phase provides coherent flow, quantized vorticity, and pressure dynamics, whereas the dispersed phase provides the stress-dependent inertial and transverse response that a single superfluid component does not supply. The framework therefore starts from one coupled material system whose two components play different but mutually constraining physical roles.

© 2026 by the author(s). Distributed under a Creative Commons CC BY license.

Preprints.org (www.preprints.org) | NOT PEER-REVIEWED | Posted: 7 September 2026 doi:10.20944/preprints202608.2283.v2

The motion of a massive body through the φ background induces a quantum-hydrodynamic dilatant response that dictates matter dynamics, clock rates, and length standards, thereby physically generating the effects conventionally described as relativistic kinematics. Rather than merely occupying a pre-existing geometric spacetime like an ordinary medium, the DDF's own dynamics determine the operational spatiotemporal relations measured by matter—constituting, in this quantum-hydrodynamic sense, a *material spacetime*. The progressive shear-thickening response is governed by a *jamming factor* algebraically identical to the Lorentz factor, revealing the standard relativistic factor not as an empirical fit, but as the exact mathematical law describing the jamming of the DDF. Consequently, worldline action recovers Lorentz-form energy–momentum, simultaneity, and null interferometric results [14–21]. The DDF avoids observable ether-wind effects: its leading local kinematic relations retain Lorentz form via dilatancy-induced length contraction and time dilation, recovering standard null results for local Lorentz-invariance tests. Crucially, this speed limit applies only to motion of massive bodies *through* the substrate, not to the collective flow *of* the DDF itself; the strong-field ϕ-superflow can therefore advect the φ-quanta at $v_\varphi = v_\phi \geq c$, producing an acoustic trapping horizon where its inward component reaches c. The same φ substrate also carries coupled transverse phonons, which locally self-induce the saturated stiff state through which they propagate at the characteristic speed c; these excitations are identified as on-shell photons. In the coherent ϕ sector, fundamental massive particles emerge as persistent toroidal superfluid vortices, including advected φ-quanta, whose mass reflects the complete dressed vortex dynamics, not merely the bare sum of circulating quanta. The ratio toroidal to poloidal circulation is identified with particle spin and generates local ϕ-pressure deficits, producing a Bernoulli force on immersed matter that the DDF identifies macroscopically as gravity: $\mathbf{g}_\phi = -\boldsymbol{\nabla} P_\phi / \varrho_{\phi,0}$. For idealized spherical sources, this yields the Newtonian inverse-square law. Macroscopic gravity is then modeled using Painlevé–Gullstrand (PG) river coordinates as a DDF superflow [22–24], reframing metric and Einstein-tensor expressions as encodings of fluid observables rather than fundamental geometrical substances.

Crucially, while energy stored in persistent vortices sources the gravitational ϕ-pressure sink, energy transferred to free photons escapes this circulation. Thus, the framework uniquely predicts that free radiation is gravitationally source-null—a direct, falsifiable discriminator.

Macroscopic LVK-class signals arise when strong-field binaries directly stress the dispersed phase, launching collective shear waves governed by the saturated φ-stiffness. Within the DDF approach, this naturally accounts for the observed multi-messenger coincidence [25–30], while keeping these waves distinct from coherent photon ensembles.

This ontology redefines quantum gravity. Because microscopic sources already possess quantized circulation within a number-conserving $\phi + \varphi$ Hamiltonian, the DDF avoids quantizing a fundamental metric or introducing spin-2 gravitons. The goal is instead to derive dressed-vortex dynamics, macroscopic expectation values, and the microscopic source and correlation structure directly from this Hamiltonian. Consequently, standard quantum gravity programs serve as comparison classes, not foundational templates [31–35].

At galactic scales, the superfluid enters a different coarse-grained regime. In low-acceleration outskirts, the ϕ background relaxes toward a weakly compressible isothermal barotropic response, yielding constant asymptotic orbital speeds. Rather than phenomenologically inserting MOND, this isothermal closure provides a quantum-hydrodynamic mechanism for its emergence [36–38]. Its viability must be judged against standard galactic observables [39,40]. On a cosmological scale, the vortex-filament web observed in doped superfluids [41] offers a material basis for the filamentary large-scale structure [42], while cosmological expansion models the coarse-grained deformation of the DDF substrate. Though less quantitatively mature than the local relativistic sector, these extensions supply critical cross-sector constraints.

Ultimately, this framework seeks to establish whether relativistic kinematics, gravitation, radiation, dark matter, strong-field signals, large-scale structure and cosmological observables in general emerge as collective regimes of a single two-component dark quantum fluid. This approach avoids

© 2026 by the author(s). Distributed under a Creative Commons CC BY license.

Preprints.org (www.preprints.org) | NOT PEER-REVIEWED | Posted: 7 September 2026 doi:10.20944/preprints202608.2283.v2

ad hoc phenomenological patching; instead, a universal saturated φ-stiffness governs the inertial, photon, and LVK limits, while a common ϕ-vortex ontology dictates particle mass, gravitation, galactic dynamics and large-scale structure. Because the framework's sectors are strictly interdependent, this article's broad scope follows from the need to establish cross-sector consistency, rather than from an encyclopedic survey of topics. By presenting a unified formulation—even while acknowledging the differing degrees of theoretical maturity across sectors—this work rigorously tests whether a cohesive quantum-hydrodynamic ontology can withstand simultaneous constraints across all physical scales.

The paper is organized as follows. Section 2 defines the DDF constitution, coupling, and stress-dependent rheology [2,4,12,43–49], including the historical rigidity–transparency problem of material carriers [50–53]. Sections 3 through 7 develop the vortex, transverse-excitation, conservative-Hamiltonian, jamming, and Lorentz-form sectors; Sec. 8 applies the resulting material relations to precision Lorentz-invariance tests. Sections 9 through 11 develop the pressure-gradient origin of gravity and its PG/GR benchmark representation. Section 12 examines weak-field precision benchmarks, Sec. 13 treats the galactic isothermal extension, and Sec. 14 addresses compact objects and LVK-class transients. Section 15 formulates the DDF-specific quantum-completion program. Sections 16 and 17 extend the framework to cosmic filaments and the cosmological background. The work concludes in Sec. 18; the appendices summarize compatibility with established precision tests and present prospective source-level, cosmic filament, and laboratory constitutive tests.

2. Two Coupled Cold Dark Sectors

At the microscopic level, the DDF consists exclusively of two coupled cold bosonic backgrounds: a coherent superfluid continuous phase ϕ and a comparatively heavier, noncondensed dispersed phase φ. The latter exhibits stress-induced shear thickening and can form, under sufficiently strong shear or impulse, a transient, locally load-bearing shear-jammed contact network. Because the resulting dilatant response governs not only the inertial behavior of matter but also the rates of physical clocks, these two coupled backgrounds jointly constitute the *material cosmic spacetime* of the framework. The quanta of the two sectors are postulated to be the smallest material entities in nature, with finite microscopic extension and no subcomponents. The ϕ-branch provides coherent flow, quantized vorticity, Bernoulli pressure gradients, and the gravitational sector; the φ-branch provides stress-induced dilatancy, transverse radiation, and the speed-dependent dilatant response. This bicomponent constitution distinguishes the DDF from earlier superfluid-vacuum and superfluid-dark-matter approaches [4,6–8,10–13,46,54].

The two fields are physical medium degrees of freedom, not auxiliary scalars added to a retained metric theory [55–59]. In the DDF ontology, spacetime is not an empty or independently existing geometric arena: its local temporal and spatial relations are the effective chronometric and kinematic structure of the two-component material substrate. Metric expressions are used later as geometric encodings of those DDF observables, not as a second coexisting background. A Standard-Model embedding and a precision cosmological background model remain separate developments. The two-sector hypothesis is guided by the cosmological evidence for a dominant effectively cold dark component [60,61], condensed-matter universality [62,63], and the established shear-thickening and shear-jamming behavior of dense suspensions [2,49,64,65]. Ultralight bosons with large phase-space occupancy provide a consistent long-wavelength superfluid description; axion-like models supply an existence proof for technically natural spin–0 sectors without fixing the DDF microphysics [66–70].

Field content and medium ontology.

The continuous branch is represented by the condensate order parameter $\phi(\mathbf{x},t) = \langle\hat{\phi}(\mathbf{x},t)\rangle$, whereas the quiescent dispersed branch has no macroscopic condensate order parameter:

$$\begin{aligned} n_\phi &= |\phi|^2, \qquad \varrho_\phi = m_\phi n_\phi, \\ \langle\hat{\varphi}(\mathbf{x},t)\rangle &= 0, \qquad n_\varphi \equiv n_{\text{dispersed}}, \qquad \varrho_\varphi = m_\varphi n_\varphi. \end{aligned} \tag{1}$$

© 2026 by the author(s). Distributed under a Creative Commons CC BY license.

Preprints.org (www.preprints.org) | NOT PEER-REVIEWED | Posted: 7 September 2026 doi:10.20944/preprints202608.2283.v2

Thus n_ϕ and n_φ are number densities, while ϱ_ϕ and ϱ_φ are inertial mass densities. The microscopic operator $\hat{\varphi}$ annihilates dispersed φ-quanta; the same symbol φ is also used as a subscript, when unambiguous, for coarse-grained density, displacement, strain, configurational, or transverse-excitation variables. Under sufficient shear or impulse, the dispersed quanta form a transient, locally ordered contact network. This saturated jammed state is mechanically stiff but is neither the quiescent cosmic state nor a permanent condensate.

Both sectors are chargeless and colorless. Although their masses dictate basic fluid properties, individual ϕ and φ dark quanta do not source gravity. A homogeneous, quiescent $\phi + \varphi$ sea is therefore gravitationally inactive. Instead, active gravity is a strictly collective phenomenon, arising from persistent, vortex-supported Bernoulli pressure gradients (i.e., enthalpy deficits) in ϕ (Sec. 9). While all dark quanta are passively accelerated by gravity, they only generate a gravitational field when participating in this coherent vortex circulation.

Photons are identified below with transverse φ excitations, while fundamental massive particles are the persistent quantized-vortex configurations—composed of circulating ϕ-quanta and advected φ-quanta—that source gravity. Unlike the proposal of Sinha, Sivaram, and Sudarshan [6], particle–antiparticle pairs are therefore vortex–antivortex excitations of the superfluid rather than constituents from which the superfluid itself is formed.

The theory requires that the coherent ϕ phase remain compatible with dilatancy of the dispersed branch. Its low-dissipation redistribution through narrowing interstitial regions may additionally facilitate contact-network rearrangement, as examined in Appendix B.4; such enhancement is a possible secondary effect, not a prerequisite of the framework. Laboratory doped superfluids provide a qualitative analog [41,71–73], although the DDF assumes a mechanically active dispersed loading. Their disturbed filamentary structures also motivate the large-scale comparison developed in Sec. 16.

Coherent ϕ branch.

The ϕ-sector is a neutral ultralight spin–0 background with benchmark mass $m_\phi \sim 10^{-19}\,\mathrm{eV}/c^2$. The familiar fuzzy-dark-matter scale $m \sim 10^{-22}\,\mathrm{eV}/c^2$ is a phenomenological benchmark chosen to place the de Broglie wavelength $\lambda_{\mathrm{dB}} = h/(mv)$ near galactic scales for $v \sim 10^{-3}c$, not a unique axion prediction [66,68,74,75]. More generally, $m_{\mathrm{ALP}} \sim \Lambda^2/f_a$ is model dependent, so axion-like sectors readily admit larger but still ultralight masses [68–70,76]. The quoted DDF value is therefore a working EFT benchmark used in the later vortex-core, stiffness, clustering, and filament estimates[1] [77], not a uniquely derived constant.

The term "superfluid" refers to persistent macroscopic coherence of the neutral ϕ branch, not to cooling the baryonic Universe below an ordinary laboratory critical temperature. Electromagnetic thermality, including T_{CMB} and the temperatures of baryonic plasmas, is carried by ordinary matter and the radiative transverse φ sector and does not directly disorder the ϕ order parameter. At long wavelengths, coherence is represented by

$$\begin{aligned} \phi(\mathbf{x},t) &= \sqrt{n_\phi(\mathbf{x},t)}\, e^{iS_\phi(\mathbf{x},t)}, \\ \mathbf{v}_{\phi,\mathrm{mic}} &= \frac{\hbar}{m_\phi}\boldsymbol{\nabla} S_\phi - \mathbf{A}_v. \end{aligned} \tag{2}$$

Here $\mathbf{v}_{\phi,\mathrm{mic}}$ denotes the smooth microscopic condensate velocity after the singular phase-winding contribution has been separated by $\mathbf{A}_v$. The full microscopic circulation field entering the Bernoulli pressure deficit is $\mathbf{v}_{\mathrm{B}} = \mathbf{v}_{\phi,\mathrm{mic}} + \mathbf{A}_v$. When many vortex cores are unresolved on a coarse-graining scale ℓ, the physical macroscopic superflow used in the gravitational and propagation sectors is

$$\mathbf{v}_\phi(\mathbf{x},t) \equiv \big\langle \mathbf{v}_{\mathrm{B}}(\mathbf{x},t) \big\rangle_\ell. \tag{3}$$

[1] Short-distance physics is collected into low-energy parameters such as $g_{\phi\phi}$, m_ϕ, and $n_{\phi,0}$.

© 2026 by the author(s). Distributed under a Creative Commons CC BY license.

Preprints.org (www.preprints.org) | NOT PEER-REVIEWED | Posted: 7 September 2026 doi:10.20944/preprints202608.2283.v2

Thus $\mathbf{v}_\phi$ contains the collective contribution of the underlying quantized-vortex population and need not be curl-free even though the smooth microscopic field is locally a phase gradient away from resolved cores. Condensate dominance requires

$$N_{0,\phi} \equiv \int d^3x\, |\langle \hat{\phi}(\mathbf{x}, t)\rangle|^2 \gg N_\phi^{\rm incoh}. \tag{4}$$

Energy transfer into incoherent ϕ excitations must therefore remain subdominant; the corresponding cosmological coherence history is left to the material-background extension. Persistent localized vortices constitute the massive-particle sector of Sec. 3, while on cosmological scales, extended loops and bundles provide the vortex-filament ontology used in Sec. 16.

With the physical normalization $n_\phi = |\phi|^2$, the long-wavelength Gross–Pitaevskii Lagrangian is

$$\begin{aligned} \mathcal{L}_\phi = {} & \frac{i\hbar}{2}(\phi^* \partial_t \phi - \phi\, \partial_t \phi^*) \\ & - \frac{\hbar^2}{2m_\phi}\left|\left(\boldsymbol{\nabla} - i\frac{m_\phi}{\hbar}\mathbf{A}_v\right)\phi\right|^2 \\ & - \frac{g_{\phi\phi}}{2}|\phi|^4. \end{aligned} \tag{5}$$

Here $g_{\phi\phi}$ has units of energy times volume and $\mathbf{A}_v$ localizes quantized circulation [78–80]. This is a directly physical Gross–Pitaevskii normalization; no natural-unit normalization of an underlying relativistic scalar is required. Its number-conserving many-body completion follows from

$$\hat{\phi}(\mathbf{x}) = \int \frac{d^3k}{(2\pi)^{3/2}} e^{i\mathbf{k}\cdot\mathbf{x}} \hat{a}_\mathbf{k}, \qquad [\hat{a}_\mathbf{k}, \hat{a}^\dagger_{\mathbf{k}'}] = \delta^{(3)}(\mathbf{k} - \mathbf{k}'), \tag{6}$$

with $D_i \equiv \partial_i - i(m_\phi/\hbar)A_{v,i}$:

$$\begin{aligned} \hat{H}_\phi &= \int d^3x \left[\frac{\hbar^2}{2m_\phi}(D_i\hat{\phi})^\dagger (D_i\hat{\phi}) + \frac{g_{\phi\phi}}{2}\hat{\phi}^\dagger\hat{\phi}^\dagger\hat{\phi}\hat{\phi}\right], \\ \hat{N}_\phi &= \int d^3x\, \hat{\phi}^\dagger\hat{\phi}, \qquad [\hat{H}_\phi, \hat{N}_\phi] = 0. \end{aligned} \tag{7}$$

The equal-time algebra is $[\hat{\phi}(\mathbf{x}), \hat{\phi}^\dagger(\mathbf{y})] = \delta^{(3)}(\mathbf{x} - \mathbf{y})$, with the remaining like-field commutators vanishing.

Hydrodynamic matching gives

$$\begin{aligned} P_\phi(n_\phi) &= \frac{g_{\phi\phi}}{2}n_\phi^2, & \mu_\phi(n_\phi) &= g_{\phi\phi}n_\phi, \\ c_\phi^2 &= \frac{1}{m_\phi}\frac{\partial P_\phi}{\partial n_\phi} = \frac{g_{\phi\phi}n_{\phi,0}}{m_\phi}, \\ \xi &= \frac{\hbar}{\sqrt{2m_\phi g_{\phi\phi}n_{\phi,0}}}. \end{aligned} \tag{8}$$

Thus, for $\varrho_{\phi,0} = m_\phi n_{\phi,0}$,

$$\begin{aligned} g_{\phi\phi} &= \frac{m_\phi c_\phi^2}{n_{\phi,0}} = \frac{\hbar^2}{2m_\phi\xi^2 n_{\phi,0}}, \\ g_{\phi\phi} &= \frac{4\pi\hbar^2 a_s}{m_\phi} \qquad (s\text{-wave parameterization}). \end{aligned} \tag{9}$$

© 2026 by the author(s). Distributed under a Creative Commons CC BY license.

Preprints.org (www.preprints.org) | NOT PEER-REVIEWED | Posted: 7 September 2026 doi:10.20944/preprints202608.2283.v2

The last equality is a physical s-wave scattering parameterization. The Heisenberg equation is

$$i\hbar\,\partial_t\hat{\phi} = \left[-\frac{\hbar^2}{2m_\phi}\left(\boldsymbol{\nabla} - i\frac{m_\phi}{\hbar}\mathbf{A}_v\right)^2 + g_{\phi\phi}\hat{\phi}^\dagger\hat{\phi}\right]\hat{\phi}. \tag{10}$$

Its coherent-state expectation value recovers the Gross–Pitaevskii equation obtained from Eq. (5); working with $\hat{H}_\phi - \mu_\phi\hat{N}_\phi$ fixes the bulk density. For a time-independent phase redefinition, the simultaneous transformations $\phi \to e^{i\alpha_g}\phi$ and $\mathbf{A}_v \to \mathbf{A}_v + (\hbar/m_\phi)\boldsymbol{\nabla}\alpha_g$ leave the spatial kinetic term invariant and encode quantized circulation.

Dispersed φ branch.

The φ-sector is a noncondensed, mechanically interacting dispersed phase with working mass benchmark $m_\varphi \sim 10^{-16}\,\mathrm{eV}/c^2 \sim 10^3 m_\phi$. The hierarchy $m_\varphi/m_\phi \sim 10^3$ is not a microscopic prediction; it is chosen so that a low dispersed number fraction can provide a mechanically relevant mass loading while the background remains ϕ-dominated. For number fractions $x \sim 10^{-6}$–10^{-4}, the corresponding mass loading $f_M \simeq (m_\varphi/m_\phi)x$ spans $\sim 10^{-3}$–10^{-1}. This interval brackets the few-percent morphology-supporting regime quantified in Eqs. (460) and (461); it is not a derived cosmological abundance. Conventional weakly interacting dark-matter candidates are not normally endowed with the finite-size contact structure required for this shear-jamming response. The φ-quanta are advected by the coherent flow $\mathbf{v}_\phi$; departures from passive entrainment are measured by $\mathbf{v}_\varphi - \mathbf{v}_\phi$. Transient incoherent ϕ-excitations are allowed but are not modeled as a persistent normal component of the quiescent background.

Finite-size non-overlap, direct contact, and constrained rearrangement make the dispersed branch capable of reversible hydrocluster and contact-network formation under shear, without introducing an additional gauge interaction. For a massive body assigned a relative three-speed v in a local material comparison, the shear-thickened body–DDF response contributes a reversible, velocity-dependent energy, shown later to reproduce the Lorentz-form kinetic-energy increment. The additional work required to overcome the speed-dependent dilatant response of the φ sector is identified in the DDF with the relativistic kinetic energy of a body moving through the substrate. For a massive body moving through the DDF, the shear-thickened φ configuration forms part of the complete body–DDF inertial state rather than an external resistance acting on it. The work required to establish this speed-dependent dressing, whose energy remains stored at the corresponding speed, is identified with the Lorentz-form kinetic energy $K_{\mathcal{D}} = mc^2[\gamma_\varphi(v) - 1]$; being conservative and reversible, this loading does not constitute an additional drag channel or produce secular orbital-energy loss (Sec. 7).

The characteristic transverse speed of the maximally jammed state is [2,81]

$$\boxed{c = \sqrt{\frac{G_\varphi^{\max}}{\varrho_\varphi^{\max}}} = \frac{1}{\sqrt{\varrho_\varphi^{\max} j_\varphi^{\min}}}}, \tag{11}$$

where $G_\varphi^{\max}$ is the maximum shear modulus of φ, characterizing its maximally jammed state, and $j_\varphi^{\min} = 1/G_\varphi^{\max}$ is the corresponding minimum shear compliance. The density $\varrho_\varphi^{\max}$ is an inertial mass density, not a number density. Transient shear jamming therefore gives the dispersed phase the solid-like rigidity required to support transverse disturbances with limiting speed c. When such a disturbance is excited microscopically—for example by an electronic transition transferring energy to the surrounding φ sector—its quantized transverse excitation is a coupled φ-phonon, identified in the DDF with a photon. The observed speed of light is consequently identified with the propagation speed c of this saturated transverse branch.

The dispersed-carrier advection and its approach to saturation are represented by the convective derivative

$$D_t\varphi \equiv \partial_t\varphi + \mathbf{v}_\varphi \cdot \boldsymbol{\nabla}\varphi \tag{12}$$

© 2026 by the author(s). Distributed under a Creative Commons CC BY license.

Preprints.org (www.preprints.org) | NOT PEER-REVIEWED | Posted: 7 September 2026 doi:10.20944/preprints202608.2283.v2

and the shear-dependent transverse speed [2,49,64,65]

$$
\begin{aligned}
c_T(\dot\gamma) &\equiv \Big[\varrho_{\varphi,\mathrm{eff}}(\dot\gamma) j_{\varphi,\mathrm{eff}}(\dot\gamma)\Big]^{-1/2}, \\
\dot\gamma &\equiv \sqrt{2\,\mathbf{S}:\mathbf{S}}, \qquad \mathbf{S} = \frac{1}{2}\Big[\boldsymbol{\nabla}\mathbf{w} + (\boldsymbol{\nabla}\mathbf{w})^{\mathsf{T}}\Big].
\end{aligned}
\tag{13}
$$

Here $\mathbf{w}$ is the local relative-deformation field of the coupled body–DDF configuration. In a selected local material frame, a simple scale estimate is $\dot\gamma \sim v/\ell$, where v is the relative three-speed used in that comparison. In the stiff branch, $\varrho_{\varphi,\mathrm{eff}} \to \varrho_\varphi^{\max}$, $j_{\varphi,\mathrm{eff}} \to j_\varphi^{\min}$, and $c_T \to c$. In gravitational applications the dispersed branch may be passively advected, $\mathbf{v}_\varphi \simeq \mathbf{v}_\phi$, away from boundary layers; this source-generated flow is separate from the local three-speed used in the Lorentz-sector jamming factor. Scalar perturbations $\delta\varphi$ describe density and configurational response in the chosen local material frame, whereas the gapless transverse photon variable is the displacement potential $\mathbf{A}$ introduced in Sec. 4.

A number-conserving microscopic description is

$$
\begin{aligned}
\hat\varphi(\mathbf{x}) &= \int \frac{d^3k}{(2\pi)^{3/2}} e^{i\mathbf{k}\cdot\mathbf{x}} \hat b_{\mathbf{k}}, \\
[\hat b_{\mathbf{k}}, \hat b_{\mathbf{k}'}^\dagger] &= \delta^{(3)}(\mathbf{k}-\mathbf{k}'), \\
\hat N_\varphi &= \int d^3x\, \hat\varphi^\dagger \hat\varphi, \qquad \langle\hat\varphi(\mathbf{x})\rangle = 0.
\end{aligned}
\tag{14}
$$

Its Hamiltonian and coupling to the ϕ-density are

$$
\begin{aligned}
\hat H_\varphi &= \int d^3x \left[\frac{\hbar^2}{2m_\varphi}\boldsymbol{\nabla}\hat\varphi^\dagger\cdot\boldsymbol{\nabla}\hat\varphi + \mathcal{U}_\varphi[\hat n_\varphi, \hat{\mathcal{Q}}_\varphi]\right], \\
\hat H_{\mathrm{int}} &= g_{\mathrm{int}} \int d^3x\, (\hat\phi^\dagger\hat\phi)(\hat\varphi^\dagger\hat\varphi),
\end{aligned}
\tag{15}
$$

where $\hat n_\varphi = \hat\varphi^\dagger\hat\varphi$ and $\hat{\mathcal{Q}}_\varphi$ collects contact-connectivity, configurational, and ordering variables. The functional $\mathcal{U}_\varphi$ encodes direct material non-overlap, contact, and constrained many-body rearrangement. Both particle numbers are conserved:

$$
[\hat H_\varphi + \hat H_{\mathrm{int}}, \hat N_\varphi] = [\hat H_\varphi + \hat H_{\mathrm{int}}, \hat N_\phi] = 0.
$$

A local estimate may use $P_\varphi(n_\varphi) = g_{\varphi\varphi} n_\varphi^2/2$, without identifying $g_{\varphi\varphi}$ with $g_{\phi\phi}$.

The corresponding collective constitutive field has the Born–Infeld-type square-root Lagrangian [50]

$$
\begin{aligned}
\mathcal{L}_\varphi = &-\Lambda_\varphi^4\left[\sqrt{1-\frac{(D_t\varphi)^2 - c_T^2(\dot\gamma)|\boldsymbol{\nabla}\varphi|^2}{\Lambda_\varphi^4}} - 1\right] \\
&- \frac{1}{2}\Omega_{\varphi,0}^2\varphi^2 - V_{\mathrm{jam}}(\varphi),
\end{aligned}
\tag{16}
$$

with

$$
\Omega_{\varphi,0} \equiv \frac{m_\varphi c^2}{\hbar}. \tag{17}
$$

The field normalization gives energy-density units to $(D_t\varphi)^2$, $c_T^2|\boldsymbol{\nabla}\varphi|^2$, and $\Omega_{\varphi,0}^2\varphi^2$; Λ_φ^4 sets the nonlinear saturation scale and V_{jam} encodes the local packing or configurational background. The square-root term is an EFT constitutive closure, not a spacetime postulate: it reduces to a convected massive-wave response at small gradients and approaches a finite-speed stiff branch under strong shear or impulse.

Defining

$$
X_\varphi \equiv (D_t\varphi)^2 - c_T^2(\dot\gamma)|\boldsymbol{\nabla}\varphi|^2,
$$

© 2026 by the author(s). Distributed under a Creative Commons CC BY license.

Preprints.org (www.preprints.org) | NOT PEER-REVIEWED | Posted: 7 September 2026 doi:10.20944/preprints202608.2283.v2

the derivative expansion is

$$\mathcal{L}_\varphi = \frac{1}{2}X_\varphi - \frac{1}{2}\Omega_{\varphi,0}^2\varphi^2 + \frac{X_\varphi^2}{8\Lambda_\varphi^4} - V_{\rm jam}(\varphi) + \cdots . \tag{18}$$

For positive X_φ, the quartic term increases the canonical momentum and Hamiltonian cost of further impulse-dominated excitation. The quasi-static increase of the incremental shear modulus is encoded jointly by the stress dependence of c_T, equivalently $G_\varphi(\sigma)$, the configurational functional, and $V_{\rm jam}$. The scalar gap governs microscopic density and configurational excitations, whereas the observable photon is the gapless transverse collective mode of the locally saturated contact state.

Motion of microscopic matter produces localized shear-thickened and shear-stiffened sheaths, while sufficiently strong emission and absorption impulses can access a transient locally jammed state. The latter regime is relevant, for example, to accelerated charges in synchrotron emission, with

$$c_T[\dot\gamma(v)] = \left(\varrho_{\varphi,\rm eff}\dot\jmath_{\varphi,\rm eff}\right)^{-1/2} \longrightarrow c \qquad (v \to c).$$

This response anticipates the jamming factor $\gamma_\varphi(v)$ of Sec. 6. The saturation-fixed luminal branch has real frequency and conserved energy flux: its local contact configuration loads and unloads reversibly as the phase pattern propagates, while submaximal transverse, longitudinal, and configurational disturbances remain separate internal modes. The zero-hysteresis, polarization, and on-shell stability conditions are developed in Sec. 4.

Historical and constitutive motivation.

Maxwell's attempt to give electromagnetic propagation a mechanical foundation exposed the rigidity–transparency problem: a carrier capable of supporting very rapid transverse disturbances appeared incompatible with the absence of detectable drag on celestial bodies [82,83]. The incompatibility with known materials contributed historically to the abandonment of explicit mechanical-ether models. Modern electrodynamics instead encodes $c = 1/\sqrt{\epsilon_0\mu_0}$ directly in the field equations. Quantum field theory, however, treats the vacuum as a nontrivial ground state with measurable response properties, exemplified by Casimir, Unruh, and Heisenberg–Euler phenomena [84–88], while a cosmological constant is represented as a uniform vacuum-energy density. These results do not establish a material ether or preferred frame, but they leave room for medium-based effective descriptions [51,52,89,90].

The DDF recasts the historical tension as a constitutive question. Dilatant media may remain fluid-like below a threshold and form transient load-bearing contact structures above it [91],

$$\eta_{\rm app}(\dot\gamma) \nearrow, \qquad G_{\rm eff}(\sigma) \nearrow \quad \text{for} \quad \dot\gamma \gtrsim \dot\gamma_c \text{ or } \sigma \gtrsim \sigma_c. \tag{19}$$

Reynolds identified granular dilatancy in 1885 [92]; suspension evidence and industrial applications followed [93,94]. The Ostwald–Waele model admits shear-thickening behavior for $n > 1$ [95,96], and later order–disorder, microhydrodynamic, frictional-contact, and jamming descriptions supplied mechanism-based accounts [49,65,97–99]. This rheology provides the proof of principle that weak-stress transparency and strong-stress rigidity are not intrinsically incompatible.

In the DDF, the φ carrier remains fluid-like under weak macroscopic shear and becomes locally stiff only on the saturated branch, thereby avoiding dissipative drag while supporting propagating transverse φ-phonon modes. The resulting conservative inertial response and its consequences for material standards, clock rates, and optical propagation are developed in Secs. 7 and 8. The Maxwell/QED equations remain the long-wavelength description, while their propagation properties are assigned to the constitutive response of the dark medium.

Although the microscopic constituents are scalar, the jammed many-body state possesses vector displacement modes. Its coarse-grained stiffness tensor admits two degenerate transverse eigenmodes in the isotropic saturated limit [100,101]; residual anisotropy would split their speeds and is con-

© 2026 by the author(s). Distributed under a Creative Commons CC BY license.

Preprints.org (www.preprints.org) | NOT PEER-REVIEWED | Posted: 7 September 2026 doi:10.20944/preprints202608.2283.v2

strained by birefringence measurements [87,88]. Longitudinal density modes may also exist in the φ sector but remain phenomenologically dark because they do not couple to standard electromagnetic instrumentation.

3. Quantized ϕ-Sector Vortices

Quantized vortices are intrinsic topological excitations of a superfluid [44,102–104] and can arise spontaneously in the ϕ sector during the formation and evolution of the coherent phase [4,5,13]. Vortex lines can terminate on boundaries or extend through the system; localized finite-energy configurations in an effectively boundary-free region are naturally represented by closed vortex rings [79,102,105–107], i.e. vortex tori characterized by a healing length ξ [45,108,109].

Microscopic circulation and quantization.

Using the superfluid order parameter introduced in Sec. 2,

$$\phi = \sqrt{n_\phi}\, e^{iS_\phi},$$

the full microscopic circulation field entering the Bernoulli pressure deficit is

$$\mathbf{v}_\mathrm{B} \equiv \frac{\hbar}{m_\phi}\boldsymbol{\nabla} S_\phi. \tag{20}$$

Around a quantized vortex core,

$$\oint \mathbf{v}_\mathrm{B}\cdot d\boldsymbol{\ell} = \kappa_\phi n, \qquad \kappa_\phi \equiv \frac{h}{m_\phi}, \qquad n\in\mathbb{Z}. \tag{21}$$

For calculations in which the phase-winding contribution is separated from the smooth condensate flow, decompose $S_\phi = S_{\phi,\mathrm{reg}} + S_{\phi,\mathrm{v}}$ and introduce the vortex connection

$$\mathbf{A}_v \equiv \frac{\hbar}{m_\phi}\boldsymbol{\nabla} S_{\phi,\mathrm{v}}. \tag{22}$$

The smooth microscopic condensate velocity appearing in the covariant Gross–Pitaevskii derivative is

$$\mathbf{v}_{\phi,\mathrm{mic}} \equiv \frac{\hbar}{m_\phi}\boldsymbol{\nabla} S_\phi - \mathbf{A}_v = \frac{\hbar}{m_\phi}\boldsymbol{\nabla} S_{\phi,\mathrm{reg}}. \tag{23}$$

Thus $\mathbf{A}_v$ isolates the quantized phase-winding contribution of the vortex core without removing the physical circulation. The full microscopic circulation field is

$$\mathbf{v}_\mathrm{B} = \mathbf{v}_{\phi,\mathrm{mic}} + \mathbf{A}_v = \frac{\hbar}{m_\phi}\boldsymbol{\nabla} S_\phi, \tag{24}$$

and it is $\mathbf{v}_\mathrm{B}$ that supplies the vortex kinetic energy and Bernoulli pressure deficit. The notation $\mathbf{v}_{\phi,\mathrm{mic}}$ therefore labels the resolved smooth microscopic contribution, whereas $\mathbf{v}_\phi = \langle \mathbf{v}_\mathrm{B}\rangle_\ell$ denotes the physical coarse-grained superflow when the action of many vortex-particles is unresolved.

Helmholtz constraint and ring geometry.

Vorticity in an inviscid superfluid is frozen into tube cores of radius $a \sim \xi$. Helmholtz's theorem then requires each tube to end on a boundary or to close [79,102] (Figure 1); in a boundary-free cosmic medium the generic configuration is a closed loop—a *vortex ring* [45,108,109] with major radius $R \gg a$

© 2026 by the author(s). Distributed under a Creative Commons CC BY license.

Preprints.org (www.preprints.org) | NOT PEER-REVIEWED | Posted: 7 September 2026 doi:10.20944/preprints202608.2283.v2

[110]. Introduce angles θ (toroidal revolution) and χ (poloidal rotation). A minimal internal phase that encodes the two windings is

$$S_\phi(\theta,\chi,t) = n_\theta\,\theta + n_\chi\,\chi - \frac{\mathcal{E}_{\rm v}t}{\hbar}, \qquad n_\theta, n_\chi \in \mathbb{Z}, \tag{25}$$

where $\mathcal{E}_{\rm v}$ denotes the stationary phase-energy parameter of the vortex configuration. Together with Eq. (23), this fixes the local smooth microscopic flow on the torus.

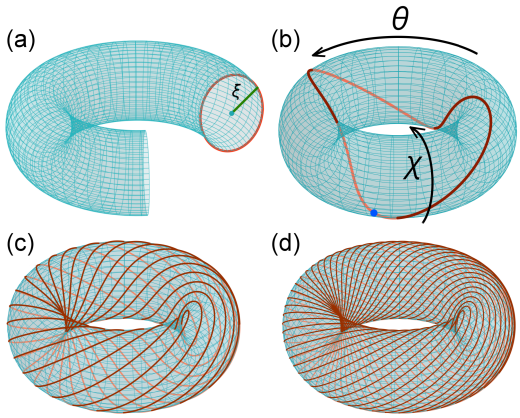


Figure 1. Schematic representation of a vortex quasiparticle arising from the emergent collective dynamics of DDF quanta. (a) A vortex tube with healing length ξ; (b) closure of the tube into a loop, forming a torus (vortex ring), where a poloidal angle χ and a toroidal angle θ are defined, and a Möbius-like trajectory of ϕ-quanta and advected φ-quanta, with spin-$\frac{1}{2}$ assignment for one toroidal revolution accompanied by two poloidal turns, so that closure occurs only after a 4π transport; (c) example showing 12 such trajectories; (d) an example of 24 such trajectories, illustrating the proposed candidate particle-like vortex construction. The figure is schematic and does not establish a quark or lepton identification.

In the thin-ring approximation the metric scale factors are $h_\theta \simeq R$ and $h_\chi \simeq a$, giving the velocity projections

$$\begin{aligned} \mathbf{v}_{\phi,\rm mic}\cdot\hat{\boldsymbol{\theta}} &\simeq \frac{\hbar}{m_\phi}\,\frac{n_\theta}{R} - A_{v,\theta}, \\ \mathbf{v}_{\phi,\rm mic}\cdot\hat{\boldsymbol{\chi}} &\simeq \frac{\hbar}{m_\phi}\,\frac{n_\chi}{a} - A_{v,\chi}. \end{aligned} \tag{26}$$

A geometric winding ratio, proposed as a spin label, is defined by

$$s_{\rm v} \equiv \frac{\Delta\theta}{\Delta\chi} = \frac{n_\theta}{n_\chi}. \tag{27}$$

For the proposed fermionic assignment $s_{\rm v} = \frac{1}{2}$ $(n_\chi : n_\theta = 2:1)$, one toroidal revolution is accompanied by two poloidal turns. The scalar phase remains single-valued modulo 2π. The additional statement that a material frame attached to the tube is Möbius-like and closes only after 4π is a framed-tube ansatz; it is not implied by the scalar phase alone and must ultimately be derived from a microscopic particle model. Within that ansatz, the transport law is

$$\begin{aligned} (\theta,\chi) \to (\theta+2\pi,\chi+4\pi): &\quad \text{frame} \mapsto -\text{frame}, \\ (\theta,\chi) \to (\theta+4\pi,\chi+8\pi): &\quad \text{frame} \mapsto \quad \text{frame}. \end{aligned} \tag{28}$$

Within this framed-tube construction, spin is represented by the internal kinematics of the vortex configuration, as anticipated in related mechanical models [111,112]. A convenient core profile consistent with the healing length is

$$\begin{aligned} \phi(\mathbf{x},t) &= \sqrt{n_{\phi,0}}\, f(r_\perp/\xi)\, e^{iS_\phi(\theta,\chi,t)}, \\ f(0) &= 0, \qquad f(\infty) = 1. \end{aligned} \tag{29}$$

© 2026 by the author(s). Distributed under a Creative Commons CC BY license.

Preprints.org (www.preprints.org) | NOT PEER-REVIEWED | Posted: 7 September 2026 doi:10.20944/preprints202608.2283.v2

Here $r_\perp$ is the distance to the ring centerline (e.g. $f(u) \approx \tanh[u/\sqrt{2}]$). This construction implements Helmholtz closure, quantized circulation on a toroidal core of size $a \sim \xi$, and the geometric spin label s_v as the ratio of toroidal to poloidal windings.

The orientation label is specified by the sign of s_v together with the signed circulation winding $\mathrm{sgn}(n\kappa_\phi) = \mathrm{sgn}(n)$, since $\kappa_\phi = h/m_\phi > 0$. For $s_v = \frac{1}{2}$, the framed-tube ansatz supplies the proposed spinor-like 4π closure.

These quantized vortices are identified in the DDF ontology with the fundamental massive particles of the Standard Model [4,13,113]. This identification is made at the level of the DDF ontology: spin is associated with stable quantized-vortex circulation and internal winding, with its value determined by the toroidal-to-poloidal winding ratio, while inertial mass arises from the local organization and dynamical dressing of the vortex by φ-quanta. The spin-$\frac{1}{2}$ construction discussed above is therefore one particular winding assignment rather than a restriction of the vortex ontology to fermions. A complete microscopic embedding into the Standard Model—including the detailed mapping of vortex configurations to the observed particle species, spin values, quantum numbers, gauge charges, flavor structure, chirality, and Higgs-sector phenomenology—is not attempted in the present paper and is left for dedicated follow-up work.

The conceptual possibility considered here is a departure from the standard description of massive particles as effectively point-like excitations of quantum fields: they are instead modeled as dynamical quantized-vortex excitations of a material dark field ϕ, within an effective field theory framework. In the conventional picture, particles such as electrons and quarks are treated as elementary quanta with no resolved internal structure. In the present picture, by contrast, they are modeled as emergent vortex configurations of the underlying dark superfluid, so that properties such as mass and spin are associated with the geometry and internal dynamics of the vortex rather than assumed to be structureless and fundamental.

The finite invariant rest mass m of the complete dressed vortex is a dynamical property of the vortex–DDF configuration rather than a bare sum of the masses of its entrained φ-quanta. In particular, these quanta contribute through both their inertial content and the kinetic energy associated with their circulation within the vortex, together with the ϕ-core dynamics and polarization of the surrounding φ population. In this sense, the phenomenological mass of a fundamental vortex-particle has primarily a hydrodynamic kinetic origin in the internal vortex dynamics. Its slow-motion branch then admits

$$E(v) = E_0 + \tfrac{1}{2}mv^2 + \mathcal{O}(v^4). \tag{30}$$

The rest-energy identification $E_0 = mc^2$ is calibrated below against the annihilation channel into transverse φ-phonons (see Sec. 4.3). The same invariant mass parameter is used in the later DDF momentum and worldline relations, whereas active gravity remains tied to the persistent vortex-supported pressure deficit in ϕ.

Multi-vortex bound states.

Bernoulli pressure deficits around vortex cores provide an attractive channel for composite, non-annihilating configurations [114–116]. In the proposed particle interpretation, three-vortex bound states such as $\uparrow\downarrow\uparrow$ or $\downarrow\uparrow\downarrow$ provide schematic candidates for baryons, while suitably stabilized two-vortex configurations may represent meson-like states. The arrows denote the proposed vortex-spin orientations. The same hydrodynamic picture suggests a possible physical basis for Pauli exclusion: for strongly overlapping identical fermionic vortex-particles, opposite spin orientations produce complementary circulation and Bernoulli-pressure fields whose superposition is hydrodynamically cooperative, providing a possible dynamical origin for the energetic preference of the antisymmetric spin state. The antisymmetric configuration may therefore represent the dynamically favored arrangement when two otherwise identical fermionic vortex-particles occupy the same spatial state. A complete derivation of fermionic exchange antisymmetry, color structure, and QCD confinement remains part of the microscopic quantum-number realization.

© 2026 by the author(s). Distributed under a Creative Commons CC BY license.

Preprints.org (www.preprints.org) | NOT PEER-REVIEWED | Posted: 7 September 2026 doi:10.20944/preprints202608.2283.v2

Bernoulli pressure.

As for quantized vortices in general, a pressure gradient develops around the core, drawing the fluid inward via the *Bernoulli effect* [102,106,109]. This behavior is intrinsic to superfluids rather than an additional DDF assumption. The present section develops the microscopic vortex structure, its local Bernoulli pressure deficit, and its φ-sector inertial dressing. Section 9 then coarse-grains these vortex-supported fields and examines their identification with the macroscopic gravitational acceleration.

In the incompressible far field $n_\phi \simeq n_{\phi,0}$; near cores the GP quantum pressure sets the healing length ξ, as introduced in Eq. (8), and a convenient stationary profile is

$$n_\phi(r_\perp) \simeq n_{\phi,0}\, \tanh^2\!\Big(\frac{r_\perp}{\sqrt{2}\,\xi}\Big), \tag{31}$$

with $r_\perp$ the distance to the filament centerline. Outside the core ($r_\perp \gtrsim$ a few ξ), the density may be taken uniform and the classical Bernoulli relations apply with $\varrho_{\phi,0} = m_\phi n_{\phi,0}$.

In a finite-core representation, for a ring or a set of rings a convenient smeared-core form is

$$\boldsymbol{\nabla} \times \mathbf{A}_v(\mathbf{r}) = \kappa_\phi \sum_j n_j \int ds\; \delta_\xi\big(\mathbf{r} - \mathbf{R}_j(s)\big)\, \hat{\mathbf{t}}_j(s), \tag{32}$$

where n_j is the integer circulation winding of the j-th vortex, $\mathbf{R}_j(s)$ is its centerline with tangent $\hat{\mathbf{t}}_j$, and δ_ξ is a normalized mollifier of width ξ that fixes the tube radius $a \sim \xi$.

Local φ organization and inertial loading.

The φ sector is described by the effective dynamics introduced in Sec. 2, together with the density–density coupling $g_{\rm int}$ to the ϕ sector. The dispersed quanta already pervade the DDF; a vortex does not draw them from a remote reservoir through an additional long-range force. In the immediate vortex neighborhood, the nearby φ carrier is passively advected and locally reorganized by the full physical circulation field. Away from boundary layers one may therefore take

$$\mathbf{v}_\varphi \simeq \mathbf{v}_{\rm B}. \tag{33}$$

From the steady ϕ-phase equation and the barotropic GP equation of state $P_\phi(n_\phi) = \frac{g_{\phi\phi}}{2} n_\phi^2$, the streamline invariant is

$$\begin{aligned} h_\phi(n_\phi) + \frac{v_{\rm B}^2}{2} + Q_\phi &= h_{\phi,\infty}, \\ h_\phi(n_\phi) \equiv \int^{n_\phi} \frac{dP_\phi}{m_\phi n} &= \frac{g_{\phi\phi} n_\phi}{m_\phi}, \end{aligned} \tag{34}$$

where

$$Q_\phi \equiv -\frac{\hbar^2}{2m_\phi^2} \frac{\nabla^2\sqrt{n_\phi}}{\sqrt{n_\phi}}. \tag{35}$$

Equivalently, the local specific-enthalpy deficit is

$$\Delta h_\phi \equiv h_\phi - h_{\phi,\infty} = -\left(\frac{v_{\rm B}^2}{2} + Q_\phi\right). \tag{36}$$

In the nearly incompressible regime, $\Delta h_\phi \simeq \Delta P_\phi / \varrho_{\phi,0}$, so that

$$\Delta P_\phi(\mathbf{x}) \simeq -\varrho_{\phi,0}\left(\frac{v_{\rm B}^2}{2} + Q_\phi\right). \tag{37}$$

© 2026 by the author(s). Distributed under a Creative Commons CC BY license.

Preprints.org (www.preprints.org) | NOT PEER-REVIEWED | Posted: 7 September 2026 doi:10.20944/preprints202608.2283.v2

The quantum-potential contribution Q_ϕ is important in the near-core region, where it contributes to the microscopic enthalpy and pressure deficit associated with the quantized vortex. It becomes negligible for $r_\perp \gtrsim$ a few ξ, where the circulation-induced classical Bernoulli contribution dominates and, in the nearly incompressible regime,

$$\Delta P_\phi \simeq -\tfrac{1}{2}\,\varrho_{\phi,0}\,v_{\mathrm{B}}^2 \tag{38}$$

applies.

The pressure and velocity fields modify the local environment of the ubiquitous dispersed branch. In addition, the interaction energy $g_{\mathrm{int}} n_\phi n_\varphi$ makes the depleted core a locally preferred configuration for nearby φ-quanta when $g_{\mathrm{int}} > 0$. Passive advection, contact rearrangement, and this short-range energetic preference can therefore organize and entrain the surrounding φ population within the vortex structure. This local loading renormalizes the composite inertial and kinetic coefficients; it is not gravitational capture from distance and does not turn φ mass into an active Bernoulli source. The circulation quantum remains topologically fixed, $\kappa_\phi = h/m_\phi$.

The reframing of gravity as a classical Bernoulli force originating from the coarse-graining of vortex-supported pressure gradients, with the local pressure deficit triggered in the near-core region by the quantum-potential contribution and sustained outward by the quantized circulation field, is further developed in Sec. 9.

Structural comparison with loop quantum gravity.

Loop quantum gravity (LQG) quantizes geometry through SU(2) holonomies and spin-network states [32,117–121]. The DDF vortex construction uses loops in a fundamentally different sense: the closed curves are material centerlines of quantized ϕ-vortex tubes, characterized by $\kappa_\phi = h/m_\phi$, the winding pair (n_θ, n_χ), and the internal label $s_{\mathrm{v}} = n_\theta/n_\chi$. The circulation integral is a U(1) holonomy of the superfluid order-parameter phase, and framed vortex tubes may carry linking or self-linking data, but these structures describe material particle candidates rather than quantum geometry. The analogy is therefore strictly structural: loops, holonomies, and discrete labels occur in both constructions, whereas their ontologies and gravitational mechanisms differ. The broader distinction between DDF quantum completion and metric or loop-geometric quantization is developed in Sec. 15.

4. A Coupled Transverse-Phonon Candidate for the Photon Sector

Einstein famously wrote to Michele Besso in 1951: *"All these fifty years of conscious pondering have not brought me any closer to answering the question, 'What are light quanta?'"* [122].

In the DDF framework, a photon is a coupled transverse phonon of the dispersed φ sector. Its wave aspect is an extended, phase-coherent transverse normal mode; its particle aspect is the discrete occupation quantum carrying $E_\gamma = \hbar\omega_\gamma$, momentum, and helicity. The φ-quanta participating at any location execute reversible oscillatory displacements about their local positions. The phase and energy–momentum pattern of the collective mode propagates through the medium.

The microscopic contact between the massive-particle and photon sectors is provided by a rapid time-dependent reconfiguration of a vortex defect. For an atomic electronic transition, the electron is represented by the toroidal quantized-vortex configuration introduced in Sec. 3. Its abrupt change of bound state changes the local vortex current and the torque exerted on the surrounding dispersed φ carrier, thereby imposing a localized shear impulse. This impulse locally drives the φ contact network into its saturated jammed state, thereby generating the shear rigidity required for the disturbance to project onto its two coupled transverse polarization components and excite a propagating eigenmode [123–125]. The resulting coupled phonon is transverse precisely because this impulse-induced stiffness allows the φ sector to sustain shear displacement, whereas its unsaturated fluid-like state does not support the same transverse restoring response. In this sense the vortex does not eject a pre-existing corpuscle: it acoustically triggers a new collective excitation of the DDF. The usual language of photon emission remains operationally valid, but its DDF microphysical meaning is the conservative creation of a transverse φ-phonon by a localized vortex–carrier impulse.

© 2026 by the author(s). Distributed under a Creative Commons CC BY license.

Preprints.org (www.preprints.org) | NOT PEER-REVIEWED | Posted: 7 September 2026 doi:10.20944/preprints202608.2283.v2

The same construction provides a cautious material link between particle spin and photon helicity. In the DDF ontology, the electron's intrinsic angular momentum is associated with quantized circulation and the framed internal winding of its vortex configuration. A transition of that spinning defect can therefore act as a localized rotational source for the surrounding carrier and transfer angular momentum, as well as energy and linear momentum, into the outgoing transverse mode. The photon does not, however, inherit the numerical spin of the electron: the electron vortex is assigned a spin-$\frac{1}{2}$ state, whereas the freely propagating radiation branch is an independent gapless spin–1 transverse sector with helicities $\lambda = \pm 1$. The DDF claim is instead that vortex circulation supplies the microscopic angular-momentum reservoir and chiral impulse from which a helical transverse excitation can be launched. Its allowed helicity and polarization remain fixed by the transverse eigenmode structure, the quantum transition amplitudes and selection rules, and conservation of the total angular momentum of the complete atom–field system, including orbital and recoil contributions.

The excitation is conservative. If the complete initial and final material states, including atomic recoil, have energies E_i and E_f and momenta $\mathbf{P}_i$ and $\mathbf{P}_f$, then

$$E_\gamma = E_i - E_f = \hbar\omega_\gamma, \qquad \mathbf{p}_\gamma = \mathbf{P}_i - \mathbf{P}_f = \hbar\mathbf{k}. \tag{39}$$

For an isolated transition, angular momentum is conserved schematically as

$$\begin{aligned} \mathbf{J}_i^{\mathrm{mat}} &= \mathbf{J}_f^{\mathrm{mat}} + \mathbf{J}_\gamma, \\ \mathbf{J}_\gamma &= \mathbf{L}_\gamma + \mathbf{S}_\gamma, \quad \mathbf{S}_\gamma\cdot\widehat{\mathbf{k}} = \lambda\hbar, \qquad \lambda = \pm 1. \end{aligned} \tag{40}$$

where the initial and final material angular momenta include the relevant internal, orbital, center-of-mass, and recoil contributions. The decomposition of $\mathbf{J}_\gamma$ allows for a structured wave packet with orbital angular momentum, while its spin projection along the propagation direction is the photon helicity. Absorption is the reverse process: an incident transverse mode transfers its energy, momentum, and angular momentum to the atomic vortex system, understood in the DDF ontology as a composite configuration of mutually interacting constituent vortices. Throughout its propagation up to the absorption event, the shear stress carried by the mode organizes the local dispersed φ-quanta into the saturated contact state that sustains the luminal transverse response. This state persists over the coherence region and lifetime of the wave packet: contacts load at the advancing part of the phase pattern and unload at the trailing part.

The limiting speed is the transverse-wave speed of the saturated state already defined in Eq. (11),

$$c^2 = \frac{G_\varphi^{\max}}{\varrho_\varphi^{\max}} = \frac{1}{\varrho_\varphi^{\max} j_\varphi^{\min}}. \tag{41}$$

The working mass benchmark $m_\varphi \sim 10^{-16}\,\mathrm{eV}/c^2$ is a microscopic input to the dispersed contact-network sector and to the number- and mass-loading estimates of Sec. 16; it does not determine the luminal speed. The conservative normal-mode structure of the saturated branch determines the propagation law.

Constitutive basis of the second postulate.

Within the DDF framework, the invariant local speed of light is not introduced as an independent kinematic postulate. It is the characteristic eigen-speed of the transiently saturated, maximally shear-supporting φ-state. The propagating photon mode locally induces and maintains this wave-supported contact state and travels through it as a transverse normal mode at the constitutive speed c. The motion of the emitter can alter the emitted frequency, direction, recoil and momentum balance, but it does not alter the local eigen-speed of the saturated branch.

The same branch is approached differently by massive matter. For every finite relative three-speed $v < c$, a massive vortex configuration remains dressed by a nonsaturated, progressively shear-

© 2026 by the author(s). Distributed under a Creative Commons CC BY license.

Preprints.org (www.preprints.org) | NOT PEER-REVIEWED | Posted: 7 September 2026 doi:10.20944/preprints202608.2283.v2

thickened, shear-stiffened, and compressed φ response. As shown in Sec. 6, its longitudinal pile-up is governed by $\gamma_\varphi(v) = [1 - v^2/c^2]^{-1/2}$, which diverges as $v \to c$. The saturated state therefore constitutes a material asymptote that cannot be attained or crossed by a massive body through finite work. It is not, however, a propagation barrier for transverse φ-phonons: it is precisely the saturation-fixed eigenbranch on which they propagate. Together with the material-frame transformations developed in Sec. 7, this constitutive distinction provides the DDF realization of the second postulate of special relativity: light propagates locally at the same limiting speed c, independently of the motion of its source, while massive bodies can approach but cannot reach that speed. This limit arises physically because, as their velocity approaches c, massive bodies stress the DDF so severely that they drive it into a maximally jammed state, facing a transient, local, and impenetrable wall of jammed cold dark matter particles.

Conservative contact microphysics and local saturated response.

The finite extension of the dispersed quanta defines an admissible configuration domain

$$\mathcal{A}_\varphi = \big\{\{\mathbf{r}_i\} : |\mathbf{r}_i - \mathbf{r}_j| \geq d_{\varphi,ij}, \quad i \neq j\big\}, \tag{42}$$

where $d_{\varphi,ij}$ is the contact distance determined by their microscopic sizes, shapes, and relative orientations. A representative microscopic Hamiltonian is

$$H_\varphi = \sum_i \frac{\mathbf{p}_i^2}{2m_\varphi} + U_{\rm jam}^{\rm cell}(\{\mathbf{r}_i\}; \boldsymbol{\lambda}_{\rm jam}) + H_{\phi\varphi}, \qquad \{\mathbf{r}_i\} \in \mathcal{A}_\varphi, \tag{43}$$

where $U_{\rm jam}^{\rm cell}$ is the intrinsic collective configurational energy associated with collective strain, direct contact, connectivity, and ordering, and $H_{\phi\varphi}$ describes the constitutive coupling and advection of the dispersed carrier by the continuous ϕ background. At continuum level the same physics is encoded by the stress-dependent shear modulus $G_\varphi(\sigma, \lambda_\varphi)$, the effective compliance $j_{\varphi,\rm eff}(\sigma, \lambda_\varphi)$, and the local jamming potential.

A wave-supported HCP-like contact arrangement can provide a representative microscopic closure for the saturated branch. Oblique contacts couple the two orthogonal transverse displacements, so the local response has two polarization components belonging to one shear mode. In the isotropic or orientationally averaged limit,

$$c_{\perp,1} = \sqrt{\frac{G_{\perp,1}^{\max}}{\varrho_\varphi^{\max}}}, \qquad c_{\perp,2} = \sqrt{\frac{G_{\perp,2}^{\max}}{\varrho_\varphi^{\max}}}, \tag{44}$$

with

$$G_{\perp,1}^{\max} \simeq G_{\perp,2}^{\max} \equiv G_\varphi^{\max}, \qquad c_{\perp,1} \simeq c_{\perp,2} \simeq c. \tag{45}$$

Saturation-fixed conservative luminal eigenbranch.

The photon is the quantum of a transverse eigenmode supported by the saturated contact response of the local φ medium. At the advancing part of the mode, elastic work is stored in the contact strain; at the trailing part, the same local contact response unloads and returns the stored energy to the transverse mode. The saturated branch is defined by a reversible loading cycle with fixed elastic contact topology,

$$\oint \sigma_{ij}\, d\epsilon_{ij} = 0. \tag{46}$$

Here *saturation-fixed* means that the propagation properties of this branch are determined by the limiting saturated constitutive state of the φ medium, rather than by an independently imposed protection mechanism.

The underlying φ-sector contact interaction is taken to be conservative and Hermitian. At the microscopic level, this permits elastic redistribution of energy and momentum among the dispersed

© 2026 by the author(s). Distributed under a Creative Commons CC BY license.

Preprints.org (www.preprints.org) | NOT PEER-REVIEWED | Posted: 7 September 2026 doi:10.20944/preprints202608.2283.v2

quanta, but two-body elasticity alone would not guarantee preservation of a coherent forward mode. The lossless ideal limit instead refers to the complete saturation-fixed transverse eigenbranch: transversality, the symmetry and fixed topology of the saturated contact response, and energy–momentum and polarization selection suppress on-shell conversion into longitudinal, configurational, and relaxational channels. Thus $\mathrm{Im}\,\Sigma_R(\omega_\gamma, k) = 0$ is a property of the collective photon pole rather than of classical rigid-body collisions between individual φ-quanta.

A reduced propagator may be written as

$$G_R^{-1}(\omega, k) = \omega^2 - c^2k^2 - \Sigma_R(\omega, k). \tag{47}$$

After the real part of the self-energy has been absorbed into the saturated inertia and stiffness, the pole is $\omega_\gamma = ck$, and the saturation-fixed luminal eigenbranch satisfies

$$\mathrm{Im}\,\Sigma_R(\omega_\gamma, k) = 0, \qquad \omega_\gamma^2 = c^2k^2. \tag{48}$$

Transversality, the symmetry of the saturated contact state, and energy–momentum and polarization selection isolate the luminal branch from resonant longitudinal and configurational decay channels in the leading effective theory.

In the ideal long-wavelength, on-shell constitutive limit, the saturation-fixed maximally stiff transverse φ eigenbranch is lossless. Finite correlation-length effects, imperfect mode isolation, or nonideal coupling to internal channels may generate a small linewidth, whose integrated cosmological effect is constrained separately below. Subluminal transverse, longitudinal, and configurational φ-modes may undergo dissipative relaxation, while the continuous ϕ sector carries distinct superfluid sound, vortex, and Bernoulli responses. The contact Hamiltonian in Eq. (43) provides the microscopic setting for evaluating the topology, stability, and selection rules of the elastic branch.

Polarization and leading-order propagation.

The correspondence "photon $\leftrightarrow$ transverse φ phonon" is defined at the level of the physical free-radiation sector. The maximally stiff branch carries two transverse helicities, and the transverse constraint selects the observable propagation sector. The Maxwell-form representation below is the effective transverse-gauge description of this radiation mode.

For the saturation-fixed observable transverse branch, the effective theory imposes the exact on-shell relation

$$\boxed{\omega_\gamma = ck, \qquad v_{g,\gamma} = \frac{d\omega_\gamma}{dk} = c.} \tag{49}$$

This exactness is a defining constitutive property of the photon sector within the domain of the effective DDF description. Every local inertial material observer measures the same limiting speed c; relative motion changes the transformed frequency and wavevector but preserves $\omega_\gamma/k = c$ and does not create additional photon jamming. Finite-correlation-length, longitudinal, configurational, and off-shell excitations may possess their own submaximal or dispersive spectra, but they are not identified with the saturation-fixed on-shell photon branch.

4.1. Two-helicity Transverse Modes and a Spin-1 Embedding

In the jammed regime of the dispersed jamming fraction φ, the electromagnetic sector propagates at the speed defined in Eq. (11) and involves strictly transverse displacements

$$\nabla\cdot\mathbf{A} = 0, \qquad \mathbf{u}_1 = -\partial_t\mathbf{A} \perp \mathbf{k}, \tag{50}$$

where $\mathbf{A}(\mathbf{x}, t)$ is the transverse displacement potential, leaving two polarizations as in a massless spin–1 field. This spin–1 classification follows from the vector character and the two-dimensional transverse mode space of the propagating eigenmode; it is not inferred by equating the photon's spin with the

© 2026 by the author(s). Distributed under a Creative Commons CC BY license.

Preprints.org (www.preprints.org) | NOT PEER-REVIEWED | Posted: 7 September 2026 doi:10.20944/preprints202608.2283.v2

spin-$\frac{1}{2}$ of the electron vortex that triggers it. The vortex supplies a localized rotating source and the corresponding angular-momentum transfer, whereas the normal-mode representation determines how that angular momentum is carried by the free radiation field. The three-component construction below is a representation embedding of the transverse mode: the physical on-shell one-particle subspace contains only the two helicities ψ_R and ψ_L, while ψ_Z is a constrained longitudinal component used to display the parent vector representation. The spin operators are the standard SO(3) generators in the spin-1 representation acting on $\vec{\Psi} = (\psi_R, \psi_Z, \psi_L)^T$:

$$\hat{\mathcal{S}}_z = \begin{pmatrix} 1 & 0 & 0 \\ 0 & 0 & 0 \\ 0 & 0 & -1 \end{pmatrix}, \quad \hat{\mathcal{S}}_x = \frac{1}{\sqrt{2}} \begin{pmatrix} 0 & 1 & 0 \\ 1 & 0 & 1 \\ 0 & 1 & 0 \end{pmatrix}, \\ \hat{\mathcal{S}}_y = \frac{1}{i\sqrt{2}} \begin{pmatrix} 0 & 1 & 0 \\ -1 & 0 & 1 \\ 0 & -1 & 0 \end{pmatrix}, \tag{51}$$

with helicity operator

$$\hat{\Lambda} = \hat{\mathbf{k}} \cdot \hat{\boldsymbol{\mathcal{S}}} \in \{+1, 0, -1\}, \tag{52}$$

where incompressibility projects out the longitudinal $m_s = 0$ mode, leaving only the transverse $m_s = \pm 1$ states ($\psi_{R/L}$) [126]. An effective Hamiltonian,

$$\hat{H}_{\text{eff}}(k_x) = \hbar v_g k_x \hat{\mathcal{S}}_z + \Delta \hat{\mathcal{S}}_x + E_0(k_x)\hat{I}, \qquad v_g \simeq c, \tag{53}$$

captures dispersion with weak virtual mixing through ψ_Z, though on shell only helicity eigenmodes propagate. The spin and helicity densities from the acoustic fields are

$$\mathbf{s} = \frac{\varrho_\varphi^{\max}}{2\omega} \Im(\mathbf{u}_1^* \times \mathbf{u}_1), \\ \mathcal{H}_{\text{hel}} = \frac{1}{2} \Re(\mathbf{A}^* \cdot \nabla \times \mathbf{A}), \tag{54}$$

nonzero only for circular or elliptical polarization. For a circularly polarized eigenmode,

$$\frac{\int s_\parallel \, dV}{\int (\mathcal{E}_{\text{tot}}/\omega) \, dV} = \pm 1. \tag{55}$$

Quantization, $E = \hbar\omega$, then gives integrated spin $\pm\hbar$ per transverse phonon. The photon branch therefore has spin one and two physical helicities, while the $m_s = 0$ component remains a nonpropagating constraint.

4.2. Source-free Maxwell-form Equations

Here electromagnetic radiation is represented by a coupled transverse φ-eigenmode with two helicity polarizations and two kinematically linked shear fields, $\mathbf{u}_1$ and $\mathbf{u}_2$ [83,127–129]. The shear stress of the mode organizes the local dispersed fraction into the transient saturated state that supports propagation at the limiting speed c of Eq. (11), $c = (\varrho_\varphi^{\max} J_\varphi^{\min})^{-1/2}$. Considering also Eq. (50), define

$$\mathbf{u}_1 \equiv -\partial_t \mathbf{A}, \qquad \mathbf{u}_2 \equiv \nabla \times \mathbf{A}, \tag{56}$$

and adopt the correspondence $\mathbf{E} \mathrel{\widehat{=}} \mathbf{u}_1$, $\mathbf{B} \mathrel{\widehat{=}} \mathbf{u}_2$, in the sense that $\mathbf{u}_1$ and $\mathbf{u}_2$ enter the field equations in the same way as the electric and magnetic fields do in Maxwell theory. Here $\mathbf{u}_1$ represents the local transverse velocity, while $\mathbf{u}_2$ represents the rotational (vorticity-like) shear field associated with the same mode.

© 2026 by the author(s). Distributed under a Creative Commons CC BY license.

Preprints.org (www.preprints.org) | NOT PEER-REVIEWED | Posted: 7 September 2026 doi:10.20944/preprints202608.2283.v2

In a local inertial material frame, the quadratic Lagrangian density is

$$\mathcal{L}_{\text{phonon}} = \frac{1}{2}\,\varrho_{\varphi}^{\max}\,(\partial_t \mathbf{A})^2 - \frac{1}{2}\,j_{\varphi}^{\min\,-1}\,(\nabla \times \mathbf{A})^2. \tag{57}$$

It encodes linear momentum balance for the saturated φ contact response in the incompressible limit $\nabla\cdot\mathbf{A} = 0$.

The corresponding field equations and transversality conditions follow directly. The Euler–Lagrange equations derived from Eq. (57) yield

$$\varrho_{\varphi}^{\max}\,\partial_t^2 \mathbf{A} + \frac{1}{j_{\varphi}^{\min}}\nabla \times (\nabla \times \mathbf{A}) = 0. \tag{58}$$

With $\mathbf{u}_1, \mathbf{u}_2$ from Eq. (56) and the identity $\nabla \times (\nabla \times \mathbf{A}) = \nabla(\nabla\cdot\mathbf{A}) - \nabla^2\mathbf{A}$, the incompressibility constraint $\nabla\cdot\mathbf{A} = 0$ gives the Maxwell pair

$$\nabla\cdot\mathbf{u}_1 = 0, \qquad \nabla\cdot\mathbf{u}_2 = 0, \tag{59}$$

$$\nabla \times \mathbf{u}_1 = -\partial_t \mathbf{u}_2 \quad \text{(Faraday)}, \tag{60}$$

$$\nabla \times \mathbf{u}_2 = \varrho_{\varphi}^{\max} j_{\varphi}^{\min}\,\partial_t \mathbf{u}_1 = \tfrac{1}{c^2}\,\partial_t \mathbf{u}_1 \quad \text{(Ampère–Maxwell)}. \tag{61}$$

Equations (59) enforce strict transversality,

$$\mathbf{k}\cdot\mathbf{u}_1 = 0, \qquad \mathbf{k}\cdot\mathbf{u}_2 = 0, \tag{62}$$

for every Fourier component.

The construction to this point establishes the source-free propagation equations for the on-shell transverse photon mode. In particular, $\mathbf{u}_1$ and $\mathbf{u}_2$ are reserved here for the two kinematically linked, divergence-free fields of that propagating branch. Static or quasistatic electromagnetic binding is an off-shell sector and is not obtained by simply allowing $\nabla\cdot\mathbf{u}_1 \neq 0$. The charged source construction below therefore introduces a distinct bound φ-configuration field for the longitudinal/static response. Charged sources, matter–mode forces, and scattering processes belong to the coupled vortex–φ interaction sector developed separately; the equations below concern the energy, flux, and momentum carried by freely propagating radiation.

For energy density, flux, and momentum, the acoustic expressions reproduce the electromagnetic form under the constitutive map $\epsilon_0 \leftrightarrow \varrho_{\varphi}^{\max}$, $\mu_0 \leftrightarrow j_{\varphi}^{\min}$:

$$\mathcal{E}_{\text{tot}} = \frac{1}{2}\,\varrho_{\varphi}^{\max}\,\mathbf{u}_1^2 + \frac{1}{2 j_{\varphi}^{\min}}\,\mathbf{u}_2^2, \tag{63}$$

and the Poynting theorem follows from Eqs. (60)–(61),

$$\begin{gathered} \partial_t \mathcal{E}_{\text{tot}} + \nabla\cdot\mathbf{S}_{\text{ac}} = 0, \\ \mathbf{S}_{\text{ac}} = \frac{1}{j_{\varphi}^{\min}}\,\mathbf{u}_1 \times \mathbf{u}_2, \quad \mathbf{g}_{\text{ac}} = \varrho_{\varphi}^{\max}\,\mathbf{u}_1 \times \mathbf{u}_2 = \mathbf{S}_{\text{ac}}/c^2. \end{gathered} \tag{64}$$

Equations (60)–(61) imply the wave equations

$$\partial_t^2 \mathbf{u}_{1,2} - c^2\nabla^2\mathbf{u}_{1,2} = 0, \qquad \nabla\cdot\mathbf{u}_{1,2} = 0. \tag{65}$$

For plane waves $\mathbf{u}_{1,2}(\mathbf{x}, t) = \Re\{\mathbf{u}_{1,2}^{(0)}\, e^{i(\mathbf{k}\cdot\mathbf{x} - \omega t)}\}$, Eq. (65) gives the leading transverse dispersion within the quadratic closure

$$\omega^2 = c^2 k^2, \qquad \mathbf{k}\cdot\mathbf{u}_{1,2}^{(0)} = 0. \tag{66}$$

© 2026 by the author(s). Distributed under a Creative Commons CC BY license.

Preprints.org (www.preprints.org) | NOT PEER-REVIEWED | Posted: 7 September 2026 doi:10.20944/preprints202608.2283.v2

For the saturation-fixed observable photon branch, the on-shell relation

$$\boxed{\omega^2 = c^2 k^2} \tag{67}$$

is taken to be exact. Possible higher-gradient, longitudinal, configurational, or off-shell excitations belong to distinct microscopic sectors and do not modify the luminal transverse photon pole considered here.

Consider now the polarization structure and let $\hat{\mathbf{k}} = \mathbf{k}/k$. Choose any orthonormal transverse basis $\{\mathbf{e}_1(\hat{\mathbf{k}}), \mathbf{e}_2(\hat{\mathbf{k}})\}$ with $\mathbf{e}_i \cdot \hat{\mathbf{k}} = 0$ and $\mathbf{e}_1 \times \mathbf{e}_2 = \hat{\mathbf{k}}$. From Eqs. (60)–(61), the fields satisfy

$$\mathbf{u}_2^{(0)} = \frac{1}{\omega}\,\mathbf{k} \times \mathbf{u}_1^{(0)} = \frac{k}{\omega}\,\hat{\mathbf{k}} \times \mathbf{u}_1^{(0)} = \frac{1}{c}\,\hat{\mathbf{k}} \times \mathbf{u}_1^{(0)} \quad (\omega = ck), \tag{68}$$

so the two circularly polarized eigenmodes are $\mathbf{u}_{1,\pm}^{(0)} = u_0\,(\mathbf{e}_1 \pm i\,\mathbf{e}_2)/\sqrt{2}$ with helicities ± 1; $\mathbf{u}_2^{(0)}$ is then fixed by Eq. (68).

At finite compressibility, a submaximal internal state of the dispersed sector may also admit a longitudinal response with constitutive speed

$$c_L^2(\sigma) = \frac{K_\varphi + \frac{4}{3}G_\varphi(\sigma)}{\varrho_\varphi(\sigma)}, \qquad K_\varphi + \frac{4}{3}G_\varphi(\sigma) \le \varrho_\varphi(\sigma)c^2, \tag{69}$$

with K_φ the corresponding effective bulk modulus. The inequality is the DDF causal closure for any propagating internal branch; it is not obtained by inserting the transverse modulus of the maximally saturated state into a longitudinal formula. In the saturation-fixed radiation sector, longitudinal compression is removed by the transverse constraint $\nabla \cdot \mathbf{A} = 0$, so the photon pole is not accompanied by an independent longitudinal signal channel.

Projecting Eq. (58) with $\mathbb{P}_T = \mathbb{I} - \hat{\mathbf{k}}\hat{\mathbf{k}}$ leaves the transverse eigenmodes invariant. A small longitudinal contamination caused by finite compressibility is suppressed by the shear-to-bulk stiffness ratio,

$$\frac{\|\nabla \cdot \mathbf{u}_1\|}{\|\nabla \times \mathbf{u}_1\|} \sim \frac{G_\varphi}{K_\varphi + \frac{4}{3}G_\varphi} \ll 1. \tag{70}$$

The constitutive radiation solution is restricted to the transverse subspace of the saturated branch; any finite-compressibility leakage into internal modes is parametrically suppressed.

The maximally jammed φ transverse dynamics is strongly hyperbolic on the divergence-free transverse subspace. Its principal symbol,

$$\mathcal{P}(\omega, \mathbf{k}) = \varrho_\varphi^{\max}\omega^2\mathbf{I} - \left(j_\varphi^{\min}\right)^{-1}|\mathbf{k}|^2\mathbf{I}, \tag{71}$$

has real eigenvalues and a complete transverse eigenbasis, with characteristic speed $c = (\varrho_\varphi^{\max} j_\varphi^{\min})^{-1/2}$. The luminal branch uses the conservative operator above. Viscous or configurational terms belong to the submaximal internal φ branches. The ϕ-sector acoustics, with $c_\phi^2 = dP_\phi/d\varrho_\phi > 0$, forms a separate hyperbolic superfluid channel. Observable electromagnetic propagation is assigned to the maximally stiff transverse φ branch; the Bernoulli gravitational field is carried by ϕ and sourced by persistent quantized-vortex configurations and their bound loading.

4.2.1. Lossless Shear–Phonon Electrodynamics with Advection

Let

$$\begin{aligned} &D_t = \partial_t + \mathbf{v}_\varphi \cdot \boldsymbol{\nabla}, \\ &\mathbf{v}_\varphi \simeq \mathbf{v}_\phi \quad \text{under passive entrainment} \end{aligned} \tag{72}$$

© 2026 by the author(s). Distributed under a Creative Commons CC BY license.

Preprints.org (www.preprints.org) | NOT PEER-REVIEWED | Posted: 7 September 2026 doi:10.20944/preprints202608.2283.v2

denote the derivative along the locally advected dispersed carrier. The saturation-fixed luminal mode obeys

$$D_t^2\mathbf{u} - c^2\nabla^2\mathbf{u} = 0, \qquad \boldsymbol{\nabla}\cdot\mathbf{u} = 0. \tag{73}$$

For a locally uniform background,

$$\left(\omega - \mathbf{k}\cdot\mathbf{v}_\varphi\right)^2 = c^2k^2, \tag{74}$$

so the frequency measured in the local rest frame of the advecting φ flow is real and the transverse energy remains on the same eigenbranch.

For locally uniform, divergence-free advection, the acoustic flux $\mathbf{S}_{\rm ac}$ defined in Eq. (64) gives the local energy balance

$$\partial_t\mathcal{E}_{\rm tot} + \boldsymbol{\nabla}\cdot\left(\mathcal{E}_{\rm tot}\mathbf{v}_\varphi + \mathbf{S}_{\rm ac}\right) = 0. \tag{75}$$

In the local rest frame of the advecting flow this reduces to the Poynting law already obtained from the Maxwell-form equations. The wave-supported contact state stores and releases elastic energy reversibly as the transverse phase pattern passes. Subluminal internal φ-modes may possess viscous or configurational relaxation terms; the maximally stiff branch obeys the conservative equations above.

Birefringence.

Although in the homogeneous jammed φ carrier the two transverse polarization modes developed above are degenerate and the DDF is intrinsically non-birefringent, an apparent polarization rotation as an *environmental* effect can be mediated by the superfluid ϕ via vortex alignment in strong fields [130]. In the DDF picture, antimatter corresponds to antivortices, and the framework permits a fluctuating population of vortex–antivortex pairs in the dark superfluid doped with φ quanta. These transient configurations provide the DDF material realization of quantum-vacuum fluctuations commonly represented as virtual particle–antiparticle pairs, thereby replacing the usual heuristic picture of particles continually appearing and disappearing from an otherwise structureless vacuum with fluctuations of an underlying physical medium. If a strong external field (with the effective-field correspondence introduced above) biases their orientation, the resulting anisotropy can make the DDF respond as an effective birefringent medium, with polarization-dependent corrections to transverse φ-phonon propagation [86–88].

In this language, the Heisenberg–Euler effective Lagrangian that renders Maxwell's equations nonlinear finds a direct hydrodynamic analog in the φ sector. Using the identifications $\mathbf{E} \leftrightarrow \mathbf{u}_1$ and $\mathbf{B} \leftrightarrow \mathbf{u}_2$ introduced above, the quartic invariants of the Heisenberg–Euler theory correspond to weakly nonlinear corrections to the phonon Lagrangian density (57), of schematic form

$$\delta\mathcal{L}_{\rm HE} \propto \left(\mathbf{u}_1^2 - c^2\mathbf{u}_2^2\right)^2 + \left(\mathbf{u}_1\cdot\mathbf{u}_2\right)^2, \tag{76}$$

arising from the strain- and orientation-dependence of the jammed φ moduli in the presence of aligned vortices. Vacuum birefringence is thus reinterpreted in the DDF framework as a polarization-dependent modification of the transverse shear response of the φ medium in strong fields, induced by vortex and antivortex alignment in the underlying ϕ superfluid.

4.3. Constitutive Rest-Energy Calibration and Mass–Energy Conversion

Equation (11) fixes the squared characteristic speed of transverse excitations specifically in the maximally jammed φ branch. Here $G_\varphi^{\max}$ is the saturated shear modulus of the locally jammed carrier, $j_\varphi^{\min} = 1/G_\varphi^{\max}$ is its minimum shear compliance, and $\varrho_\varphi^{\max}$ is the corresponding inertial mass density.

In the DDF framework, the saturated shear modulus is not used here as the small-strain elastic energy density $u_{\rm el} = \frac{1}{2}G\gamma^2$. Rather, because $G_\varphi^{\max}$ characterizes the maximally stiff state capable of supporting the limiting transverse response, it defines the maximum transverse acoustic energy-density scale of the locally solidified φ branch. The DDF constitutive identification is therefore

$$\rho_{E,\varphi}^{\max} \equiv G_\varphi^{\max}, \tag{77}$$

© 2026 by the author(s). Distributed under a Creative Commons CC BY license.

Preprints.org (www.preprints.org) | NOT PEER-REVIEWED | Posted: 7 September 2026 doi:10.20944/preprints202608.2283.v2

where $\rho_{E,\varphi}^{\max}$ denotes the maximum energy-density scale available to the coupled transverse φ-phonon channel in the saturated state. This identification is not imported from special relativity: it is the constitutive statement that the maximum shear stiffness of the jammed carrier sets the maximum transverse acoustic energy density that the same carrier can support and release through its propagating phonon branch.

Combining Eq. (77) with Eq. (11) gives

$$c^2 = \frac{\rho_{E,\varphi}^{\max}}{\varrho_{\varphi}^{\max}}. \tag{78}$$

For a reference volume V of maximally jammed φ-medium, define

$$E_{\varphi,\mathrm{sat}}(V) \equiv \rho_{E,\varphi}^{\max} V, \qquad M_{\varphi,\mathrm{sat}}(V) \equiv \varrho_{\varphi}^{\max} V. \tag{79}$$

Here $E_{\varphi,\mathrm{sat}}(V)$ has a specific physical meaning: it is the maximum transverse acoustic energy associated with that saturated carrier volume, i.e. the energy that can be carried away as coupled transverse φ-phonons under complete excitation or conversion of the saturated response. Hence

$$c^2 = \frac{E_{\varphi,\mathrm{sat}}(V)/V}{M_{\varphi,\mathrm{sat}}(V)/V} = \frac{E_{\varphi,\mathrm{sat}}(V)}{M_{\varphi,\mathrm{sat}}(V)}, \tag{80}$$

and therefore

$$E_{\varphi,\mathrm{sat}}(V) = M_{\varphi,\mathrm{sat}}(V) c^2. \tag{81}$$

At this stage the equation has a precise carrier-level meaning. Since the starting wave-speed relation contains the maximum shear modulus and minimum shear compliance, Eq. (81) refers specifically to the maximally jammed φ state: the inertial mass contained in a reference volume fixes the maximum transverse-phonon energy associated with the saturated acoustic response of that same volume. Equivalently,

$$E_{\varphi,\mathrm{sat}}(V) = c^2 \int_V \varrho_{\varphi}^{\max}\, dV = M_{\varphi,\mathrm{sat}}(V) c^2. \tag{82}$$

This is an energy-per-inertial-carrier-mass calibration, not a photon rest-mass relation: the emitted transverse φ-phonon remains a massless excitation of the carrier.

The same carrier-level relation also clarifies the DDF interpretation of the photon. Here the reference volume V is the small local portion of the φ carrier impulsively driven into its saturated jammed state by the energy-level transition of the electron vortex. The resulting localized perturbation excites a propagating transverse eigenmode of the φ sector, whose quantization is identified with the photon. Thus Eq. (81) characterizes the local generation of the photon at the emission event, not the spatial region subsequently traversed by the propagating mode.

The passage from the carrier mass $M_{\varphi,\mathrm{sat}}(V)$ to the invariant mass m of a massive particle or macroscopic body follows from the DDF particle ontology rather than from a formal replacement of symbols. As detailed in Sec. 3, a fundamental massive particle is modeled as a quantized toroidal vortex of the ϕ-superfluid dynamically dressed by φ-quanta, while composite matter consists of interacting bound systems of such vortex states. The entrained φ-quanta participate in the vortex circulation and therefore contribute not merely through their bare mass content but, crucially, through their organized kinetic energy and inertial loading. The phenomenological invariant mass of matter is thus a property of the complete vortex–DDF dynamical state, with an important hydrodynamic kinetic contribution from the circulating dark degrees of freedom.

This common φ content provides the physical bridge to the carrier-level calibration above. If a critical mechanical event destroys the organized vortex circulation—most directly, vortex–antivortex annihilation, corresponding in the DDF ontology to matter–antimatter annihilation—the circulating and polarized φ configuration can be converted into free transverse excitations of the same carrier. The mechanical event acts as the trigger for this conversion; the energy already stored in the complete

© 2026 by the author(s). Distributed under a Creative Commons CC BY license.

Preprints.org (www.preprints.org) | NOT PEER-REVIEWED | Posted: 7 September 2026 doi:10.20944/preprints202608.2283.v2

dressed vortex configuration is transferred into outgoing channels, including coupled transverse φ-phonons, which in the corresponding annihilation-energy range are observed as gamma photons.

The DDF interpretation of rest energy is therefore that the invariant mass m of a massive vortex-built state measures the maximum acoustic energy that can be liberated through complete conversion of its organized DDF dynamics into the free transverse φ-phonon channel. Energy conservation across such a complete conversion calibrates

$$\boxed{E = mc^2.} \tag{83}$$

Thus the DDF recovers $E = mc^2$ through two physically linked constitutive steps. First, the maximally jammed φ carrier obeys $E_{\varphi,\mathrm{sat}} = M_{\varphi,\mathrm{sat}}c^2$, where the energy is the maximum transverse acoustic energy associated with the saturated carrier state. Second, because the same φ-quanta participate dynamically in the circulation and inertial loading of massive ϕ-vortex states, a complete mechanical destruction of that organized state can convert its rest-energy reservoir into free transverse φ-phonons. The passage from $M_{\varphi,\mathrm{sat}}$ to the general massive-body parameter m is therefore supplied by this common carrier and conversion mechanism, rather than by analogy alone. Thus $E = mc^2$ emerges directly from the DDF relation for the limiting transverse-phonon speed c, once the saturated shear modulus is recognized, through Eq. (77), as the corresponding transverse acoustic energy-density scale. The rest-energy relation is therefore recovered from the constitutive dynamics of the φ sector rather than introduced as an external relativistic input [131].

Annihilation and radiation channel.

In this hydrodynamic context, annihilation is modeled as the destruction of a vortex–antivortex pair [132,133] carrying opposite topological charges when the two cores are brought into close proximity. Reconnection and cascade dynamics convert the kinetic energy stored in the circulating ϕ and entrained φ components of the vortex configuration into excitations of the corresponding DDF sectors [134–137]. No conversion of the bare rest masses of the underlying DDF quanta is implied: the released energy is the dynamical energy stored in their organized vortex circulation. Only transverse excitations of the observable φ branch are identified with photons.

In this process Kelvin waves provide an intermediate channel for transferring energy out of the destroyed ϕ-vortex configuration and into phononic excitations of the DDF [138–140]. For the ϕ-sector, the cascade may be summarized schematically by

$$\begin{aligned} \omega(k) &\approx \frac{\kappa_\phi}{2\pi}\, k^2 \ln\!\left(\frac{1}{k\xi}\right), \\ \mathcal{E}_{\mathrm{KW}}(k) &\propto \epsilon^{2/3}\kappa_\phi^{-1}k^{-5/3}, \\ \epsilon &\sim P_{\mathrm{phonon}}, \\ E_{\mathrm{phonon}} &= \hbar c_\phi k_{\mathrm{phonon}}, \end{aligned} \tag{84}$$

where ϵ is the Kelvin-wave cascade flux transferred to phonons. Because the φ-quanta participating in the dressed particle also circulate with and are dynamically organized by the vortex, destruction of the vortex configuration releases their kinetic loading as well. The resulting impulse locally excites the φ sector, driving the relevant carrier into the stiff transverse response and converting part of the released energy into free coupled transverse φ-phonons. Energy, momentum, and angular momentum are redistributed among recoil, internal excitations, and the allowed transverse eigenmodes in accordance with the corresponding quantum selection rules. The outgoing observable transverse modes are the photons of the annihilation process. A possible primordial extension of this annihilation channel, in which oppositely circulation-biased DDF domains leave a residual net topological charge after extensive vortex–antivortex annihilation, is considered in Sec. 17 as a possible topological origin of the observed baryon asymmetry.

The relation $E = mc^2$ is understood here at the observable φ-sector level. In the DDF ontology, the invariant mass m corresponds to the kinetic energy stored in the entrained φ-quanta circulating with

© 2026 by the author(s). Distributed under a Creative Commons CC BY license.

Preprints.org (www.preprints.org) | NOT PEER-REVIEWED | Posted: 7 September 2026 doi:10.20944/preprints202608.2283.v2

the vortex. Upon complete vortex–antivortex annihilation, this organized kinetic energy is converted into free transverse φ-phonons, identified with the observable gamma-photon channel:

$$\boxed{E_{\rm rest} \equiv E_{\varphi}^{\rm vort} = E_{\gamma}^{\rm out} = mc^2.} \tag{85}$$

The underlying hydrodynamic conversion of vortex energy into acoustic excitations is not peculiar to the DDF construction: vortex–antivortex annihilation accompanied by direct phonon emission has been observed in laboratory quantum superfluids [137], while quantized-vortex reconnections and the ensuing Kelvin-wave emission have been directly observed in superfluid ^{4}He [138,141]. The subsequent transfer of vortex energy into phonon radiation provides a standard dissipation channel for superfluid ^{4}He [136,142,143].

Within the DDF matter–antimatter annihilation picture, the continuous ϕ superfluid provides the dark hydrodynamic scaffolding of the vortex itself, which advects and organizes the φ-quanta. Vortex–antivortex annihilation necessarily perturbs the ϕ background as well, but no presently observable energy-conversion channel is associated with this response. The corresponding ϕ-sector dynamics therefore remain outside the operational relation $E = mc^2$.

5. Conservative Hamiltonian Framework: Saturated Transverse Spectrum and the Low-Speed Dressed-Vortex Branch

The microscopic ingredients introduced above can be assembled into a single number-conserving Hamiltonian,

$$\boxed{\hat{H}_{\rm DDF}(\mathbf{R}) = \hat{H}_{\phi}\Big[\hat{\phi}, \hat{\phi}^{\dagger}; \mathbf{A}_v(\mathbf{x} - \mathbf{R})\Big] + \hat{H}_{\varphi} + \hat{H}_{\rm int},} \tag{86}$$

where $\mathbf{R}$ is the collective position of the vortex configuration, $\hat{H}_{\phi}$ is given by Eq. (7), and $\hat{H}_{\varphi} + \hat{H}_{\rm int}$ is given by Eq. (15). The dependence on $\mathbf{R}$ enters through the vortex connection $\mathbf{A}_v(\mathbf{x} - \mathbf{R})$ and through the self-consistent depleted ϕ-density profile sampled by the dispersed φ-quanta. Equation (86) contains no dissipative force: inertial dressing, contact stiffening, and transverse propagation arise from conservative rearrangement of the coupled many-body state.

Saturated contact spectrum.

Within a local cell containing N_{φ} dispersed quanta, a first-quantized representation of the configurational energy is

$$\begin{aligned} U_{\rm cell} &= U_{\rm jam}^{\rm cell}(\{\mathbf{r}_i\}; \boldsymbol{\lambda}_{\rm jam}) + g_{\rm int} \sum_i n_{\phi}(\mathbf{r}_i; \mathbf{R}), \\ &\{\mathbf{r}_i\} \in \mathcal{A}_{\varphi}. \end{aligned} \tag{87}$$

where $n_{\phi}(\mathbf{x}; \mathbf{R})$ is the vortex-supported condensate density. A mechanically stable saturated contact configuration $\{\mathbf{r}_i^{(0)}\}$ is a stationary point,

$$\left.\frac{\partial U_{\rm cell}}{\partial r_i^{\alpha}}\right|_{\{\mathbf{r}_j^{(0)}\}} = 0. \tag{88}$$

Writing $\mathbf{r}_i = \mathbf{r}_i^{(0)} + \mathbf{q}_i$, the quadratic Hamiltonian for small contact displacements is

$$H_{\varphi}^{(2)} = \sum_i \frac{\pi_i^2}{2m_{\varphi}} + \frac{1}{2} \sum_{i,j} q_i^{\alpha} \mathsf{D}_{ij}^{\alpha\beta} q_j^{\beta}, \tag{89}$$

with microscopic Hessian

$$\boxed{\mathsf{D}_{ij}^{\alpha\beta} \equiv \left.\frac{\partial^2 U_{\rm cell}}{\partial r_i^{\alpha} \partial r_j^{\beta}}\right|_{\{\mathbf{r}_{\ell}^{(0)}\}}.} \tag{90}$$

© 2026 by the author(s). Distributed under a Creative Commons CC BY license.

Preprints.org (www.preprints.org) | NOT PEER-REVIEWED | Posted: 7 September 2026 doi:10.20944/preprints202608.2283.v2

The normal modes obey

$$\sum_{j,\beta} \mathsf{D}_{ij}^{\alpha\beta} e_{j\beta}^{(\lambda)} = m_\varphi \omega_\lambda^2 e_{i\alpha}^{(\lambda)}. \tag{91}$$

After coarse-graining over a locally isotropic or orientationally averaged saturated contact network, let

$$\mathbf{P}_T = \mathbf{I} - \widehat{\mathbf{k}}\widehat{\mathbf{k}} \tag{92}$$

be the transverse projector. The long-wavelength projection of the frequency matrix obtained from Eq. (90) has the form

$$\mathbf{P}_T \mathbf{\Omega}^2(\mathbf{k}) \mathbf{P}_T = \frac{G_\varphi^{\max}}{\varrho_\varphi^{\max}} k^2 \mathbf{P}_T + \mathcal{O}\Big(k^4 a_\varphi^2\Big), \tag{93}$$

where a_φ is the microscopic contact or correlation scale. Since $\mathbf{P}_T$ has rank two, the saturated Hamiltonian possesses two transverse eigenvectors $\mathbf{e}_\lambda \cdot \mathbf{k} = 0$, with $\lambda = 1, 2$, and

$$\boxed{\omega_{T,\lambda}^2(k) = \frac{G_\varphi^{\max}}{\varrho_\varphi^{\max}} k^2 + \mathcal{O}\Big(k^4 a_\varphi^2\Big) = c^2 k^2 + \mathcal{O}\Big(k^4 a_\varphi^2\Big).} \tag{94}$$

Thus the conservative contact Hessian yields the two leading transverse modes and their common saturated speed $c^2 = G_\varphi^{\max}/\varrho_\varphi^{\max}$. The stronger statement that the observable photon pole obeys the exact on-shell relation $\omega_\gamma = ck$ with $\operatorname{Im}\Sigma_R(\omega_\gamma, k) = 0$ remains the saturation-fixed on-shell selection condition stated in Eqs. (48) and (67). Internal longitudinal and configurational modes remain distinct microscopic sectors and are not obtained by inserting the transverse modulus of the saturated state into a longitudinal elastic formula.

Collective-coordinate dressed-vortex branch.

Let $|\Psi_0(\mathbf{R})\rangle$ denote a stationary localized state of Eq. (86) containing a quantized ϕ-vortex centered at $\mathbf{R}$, together with its self-consistent bound, entrained, and polarized φ cloud. A uniformly translating dressed vortex is defined by extremizing the energy at fixed total momentum:

$$\delta_\Psi \Big[\langle \Psi_v | \hat{H}_{\mathrm{DDF}} | \Psi_v \rangle - \mathbf{v} \cdot \langle \Psi_v | \hat{\mathbf{P}}_{\mathrm{tot}} | \Psi_v \rangle - \mu_\phi N_\phi - \mu_\varphi N_\varphi \Big] = 0. \tag{95}$$

The corresponding traveling-state representation is

$$\begin{aligned} \phi_v(\mathbf{x}, t) &= e^{-i\mu_\phi t/\hbar} \Phi_v(\mathbf{x} - \mathbf{R}_0 - \mathbf{v}t), \\ n_{\varphi,v}(\mathbf{x}, t) &= \mathcal{N}_{\varphi,v}(\mathbf{x} - \mathbf{R}_0 - \mathbf{v}t). \end{aligned} \tag{96}$$

Both profiles are determined by the same constrained stationary problem. The moving matter constituent is therefore not a bare vortex translated through an unchanged dispersed phase, but a self-consistent vortex plus its velocity-dependent φ dressing.

Define

$$E_v \equiv \langle \Psi_v | \hat{H}_{\mathrm{DDF}} | \Psi_v \rangle, \qquad P_a(v) \equiv \langle \Psi_v | \hat{P}_{\mathrm{tot},a} | \Psi_v \rangle. \tag{97}$$

At low speed, the stationary branch defines the dressed inertial tensor by

$$P_a(v) = M_{ab}^{\mathrm{dress}} v_b + \mathcal{O}(v^3), \qquad M_{ab}^{\mathrm{dress}} \equiv \left. \frac{\partial P_a}{\partial v_b} \right|_{\mathbf{v}=\mathbf{0}}, \tag{98}$$

and therefore

$$E_v = E_0 + \frac{1}{2} M_{ab}^{\mathrm{dress}} v_a v_b + \mathcal{O}(v^4). \tag{99}$$

For an isotropic dressing cloud, $M_{ab}^{\mathrm{dress}} = M_{\mathrm{dress}} \delta_{ab}$. This mass contains the ϕ-core contribution, the bound or entrained φ population, and the polarization energy of the surrounding contact network.

© 2026 by the author(s). Distributed under a Creative Commons CC BY license.

Preprints.org (www.preprints.org) | NOT PEER-REVIEWED | Posted: 7 September 2026 doi:10.20944/preprints202608.2283.v2

Equations (98) and (99) therefore give a microscopic collective-coordinate definition of the inertial parameter used in the local kinematic sector.

Continuum transverse limiting operator of the saturated state.

On the divergence-free transverse subspace, the long-wavelength quadratic Hamiltonian associated with Eq. (89) can be written as

$$H_T^{\mathrm{sat}} = \frac{1}{2}\int d^3x \left[\frac{\mathbf{\Pi}_T^2}{\varrho_\varphi^{\max}} + G_\varphi^{\max}\partial_i u_{T,j}\,\partial_i u_{T,j}\right] - \int d^3x\, \mathbf{J}_T(\mathbf{x}-\mathbf{R})\cdot\mathbf{u}_T, \qquad \boldsymbol{\nabla}\cdot\mathbf{u}_T = 0, \tag{100}$$

where $\mathbf{J}_T$ is the transverse source produced by the dressed vortex. Hamilton's equations give

$$\varrho_\varphi^{\max}\partial_t^2\mathbf{u}_T - G_\varphi^{\max}\nabla^2\mathbf{u}_T = \mathbf{J}_T(\mathbf{x}-\mathbf{R}), \tag{101}$$

or equivalently

$$\frac{1}{c^2}\partial_t^2\mathbf{u}_T - \nabla^2\mathbf{u}_T = \frac{\mathbf{J}_T(\mathbf{x}-\mathbf{R})}{G_\varphi^{\max}}. \tag{102}$$

The transverse limiting operator used in the next section is therefore the Hamilton equation obtained by expanding the same conservative contact network about its mechanically stable saturated state. For uniform translation, $\mathbf{R}(t) = \mathbf{R}_0 + \mathbf{v}t$, the source depends on $\mathbf{x} - \mathbf{v}t$. This operator fixes the limiting speed c and the asymptotic endpoint of the massive-body response; it does not imply that the finite-speed sheath surrounding a massive body is already maximally saturated. The progressively shear-thickened and shear-stiffened source-attached profile developed in Sec. 6 supplies the finite-speed continuation.

Result and microscopic organization of the reduction.

The construction unifies the leading saturated transverse spectrum, the low-speed dressed-vortex branch, and the transverse continuum operator within one conservative many-body problem. It thereby places the photon carrier, the inertially dressed matter defect, and the limiting shear response in one dynamical setting rather than treating them as unrelated assumptions. A specified contact geometry $d_{\varphi,ij}$ and constitutive cell functional $U_{\mathrm{jam}}^{\mathrm{cell}}$ permit numerical evaluation of the Hessian, dressed mass, and finite-speed energy branch.

The same Hamiltonian defines a natural microscopic action,

$$S_{\mathrm{micro}} = \int dt\, \big\langle \Psi(t)\big| i\hbar\partial_t - \hat{H}_{\mathrm{DDF}}\big|\Psi(t)\big\rangle, \tag{103}$$

with the common parameter set

$$\Theta_{\mathrm{DDF}} = \{m_\phi,\, g_{\phi\phi},\, n_{\phi,0},\, m_\varphi,\, d_\varphi,\, \boldsymbol{\lambda}_{\mathrm{jam}},\, g_{\mathrm{int}}\}. \tag{104}$$

Here d_φ denotes a representative microscopic contact scale and $\boldsymbol{\lambda}_{\mathrm{jam}}$ the parameters entering the intrinsic configurational jamming functional. This parameter set organizes the healing length, circulation scale, inertial dressing, saturated elastic response, Bernoulli coupling, and vortex-network properties used across the manuscript. Its explicit microscopic evaluation is the quantitative continuation of the effective framework developed here.

6. Lorentz Factor from DDF Jamming Dynamics

This section derives the Lorentz factor from the limiting-branch constitutive response of the dispersed φ phase, showing that its standard form arises in the DDF as the speed-dependent jamming factor of the dilatant medium. The physical starting point is the distinction between transverse φ-

© 2026 by the author(s). Distributed under a Creative Commons CC BY license.

Preprints.org (www.preprints.org) | NOT PEER-REVIEWED | Posted: 7 September 2026 doi:10.20944/preprints202608.2283.v2

phonons, which propagate naturally through the jammed carrier at the limiting speed c, and massive bodies, which remain restricted to $v < c$ by the impenetrable stiff limit of the φ sector. Transverse φ-phonons propagate on the locally saturated branch, whereas a massive body at every finite relative three-speed $v < c$ remains accompanied by a nonsaturated, progressively shear-thickened, shear-stiffened, and longitudinally compressed φ sheath. The saturated state therefore provides both the photon propagation branch and the material endpoint that a massive configuration can approach but cannot attain through finite work, corresponding to the asymptote of the jamming factor at $v = c$.

Throughout this section, v is the local three-speed of the massive source relative to the material observer whose coordinates $(t, \mathbf{x})$ describe the traveling sheath. It is not an absolute speed through the DDF. The invariant norm c of the corresponding material four-velocity is defined in Eq. (159); here c first enters as the characteristic speed of the saturated transverse φ branch.

Saturated branch and the massive-body domain.

For an effective shear rate $\dot{\gamma}$, the transverse propagation speed of the dispersed phase is

$$c_T(\dot{\gamma}) = \left[\varrho_{\varphi,\mathrm{eff}}(\dot{\gamma}) j_{\varphi,\mathrm{eff}}(\dot{\gamma})\right]^{-1/2}, \tag{105}$$

where $\varrho_{\varphi,\mathrm{eff}}$ is the effective inertial density and $j_{\varphi,\mathrm{eff}}$ the effective shear compliance. Increasing stress drives the dispersed phase toward the limiting values

$$\varrho_{\varphi,\mathrm{eff}} \longrightarrow \varrho_\varphi^{\max}, \qquad j_{\varphi,\mathrm{eff}} \longrightarrow j_\varphi^{\min}, \tag{106}$$

which define the saturated-branch speed of Eq. 11, i.e., $c \equiv \left(\varrho_\varphi^{\max} j_\varphi^{\min}\right)^{-1/2}$. Here $\varrho_\varphi^{\max}$ is the maximal constitutive packing/energization of the transiently shear-jammed state, and $j_\varphi^{\min}$ is its minimum shear compliance. Within the DDF construction, the saturated state represents the maximal quantum packing attainable by the dispersed φ phase, with no remaining configurational free volume. Packing alone does not determine the absolute mass density of the saturated φ phase, because that value depends on the microscopic properties of the φ quanta. The DDF ontology nevertheless provides a natural lower benchmark: even the densest known material configurations, such as neutron-star matter, consist of fundamental particles represented as quantized ϕ-vortices, whose cores are strongly density depleted, vanishing ideally on the vortex centerline. Such matter therefore retains an intrinsically non-space-filling microscopic structure. By contrast, the saturated φ state corresponds to a fully compacted contact network of dispersed quanta, with no analogous vortex-core depletion. Its mass density is therefore expected to exceed that attainable by neutron-star matter, which provides the relevant empirical reference scale for the constitutive bound. Taking $10^{18}\,\mathrm{kg\,m^{-3}}$ as a characteristic upper-end density for neutron-star interiors [144,145], the adopted DDF benchmark is

$$\boxed{\varrho_\varphi^{\max} > 10^{18}\,\mathrm{kg\,m^{-3}}.} \tag{107}$$

The actual saturated density may be substantially higher. Together with Eq. (11), this gives

$$\boxed{j_\varphi^{\min} = \frac{1}{\varrho_\varphi^{\max} c^2} < \frac{1}{10^{18} c^2} \simeq 1.1 \times 10^{-35}\,\mathrm{Pa^{-1}}.} \tag{108}$$

The saturated state is accessed differently by radiation and massive matter. A massive vortex configuration remains on the nonsaturated branch for every finite $v < c$. Its sheath becomes progressively denser, stiffer, and more strongly compressed as v increases, approaching the limiting values in Eq. (106) only as $v \to c$. Accordingly, c is a real-domain boundary for the relative motion of a massive localized configuration *through* the dispersed carrier, rather than merely a speed at which a constitutive coefficient happens to diverge: the saturated state is the propagation branch of transverse phonons but an impenetrable material asymptote for massive configurations. The speed v entering $\gamma_\varphi(v)$ is

© 2026 by the author(s). Distributed under a Creative Commons CC BY license.

Preprints.org (www.preprints.org) | NOT PEER-REVIEWED | Posted: 7 September 2026 doi:10.20944/preprints202608.2283.v2

therefore a body–carrier relative speed and must not be identified with the coarse-grained background superflow $\mathbf{v}_\phi$ used later in the gravitational sector.

This endpoint condition alone fixes the limiting speed but does not determine the complete speed dependence of the massive-body response. The exact form is obtained from the limiting-branch operator and the profile closure stated below.

Limiting-branch profile closure.

The locally saturated φ state defines the isotropic second-order transverse operator

$$\frac{1}{c^2}\partial_t^2\mathbf{u} - \nabla^2\mathbf{u} = \mathbf{s}_v(\mathbf{x}, t), \tag{109}$$

where $\mathbf{u}$ is the transverse displacement field and $\mathbf{s}_v$ is the compact source associated with the moving massive body. Equation (109) is used as the normalized limiting-branch operator anchoring the finite-speed family; it does not assert that the actual sheath surrounding a massive body is already saturated for $v < c$. Its second-order principal part is the same saturated transverse wave structure obtained independently in the photon/contact-network sector; it is not selected by fitting a desired relativistic factor.

The finite-speed sheath is assumed to undergo a speed-dependent deformation primarily along the direction of motion. Its dependence on the spatial coordinates perpendicular to the velocity is retained from the reference profile, while its longitudinal extent is allowed to change through an unknown positive scale factor $\Lambda_\parallel(v)$, normalized by $\Lambda_\parallel(0) = 1$. No specific velocity dependence is assumed at this stage.

Let

$$x_\parallel = \widehat{\mathbf{v}} \cdot \mathbf{x}, \qquad \mathbf{x}_\perp = \mathbf{x} - x_\parallel \widehat{\mathbf{v}}, \tag{110}$$

where $\mathbf{x}_\perp$ denotes only the spatial coordinates perpendicular to the direction of motion and is unrelated to the transverse polarization of the φ-phonon branch. Define

$$\zeta \equiv \Lambda_\parallel(v)(x_\parallel - vt). \tag{111}$$

The uniformly translating sheath is then written as

$$\mathbf{u}_v(\mathbf{x}, t) = \mathbf{u}_0(\mathbf{x}_\perp, \zeta), \tag{112}$$

where $\mathbf{u}_0$ is the source-attached reference profile. The source is represented analogously by $\mathbf{s}_0(\mathbf{x}_\perp, \zeta)$.

Thus $\Lambda_\parallel(v)$ describes only the speed-dependent longitudinal compression of the sheath and is to be determined from the DDF constitutive dynamics. No Lorentz transformation, proper-time law, or relativistic energy relation is assumed in this ansatz.

The derivatives of Eq. (112) are

$$\begin{aligned} \partial_t^2\mathbf{u}_v &= \Lambda_\parallel^2(v)v^2\partial_\zeta^2\mathbf{u}_0, \\ \partial_\parallel^2\mathbf{u}_v &= \Lambda_\parallel^2(v)\partial_\zeta^2\mathbf{u}_0, \\ \nabla_\perp^2\mathbf{u}_v &= \nabla_\perp^2\mathbf{u}_0. \end{aligned} \tag{113}$$

Substitution into Eq. (109) gives

$$-\Lambda_\parallel^2(v)\left(1 - \frac{v^2}{c^2}\right)\partial_\zeta^2\mathbf{u}_0 - \nabla_\perp^2\mathbf{u}_0 = \mathbf{s}_0(\mathbf{x}_\perp, \zeta). \tag{114}$$

The normalized reference configuration satisfies

$$-\partial_\zeta^2\mathbf{u}_0 - \nabla_\perp^2\mathbf{u}_0 = \mathbf{s}_0(\mathbf{x}_\perp, \zeta). \tag{115}$$

© 2026 by the author(s). Distributed under a Creative Commons CC BY license.

Preprints.org (www.preprints.org) | NOT PEER-REVIEWED | Posted: 7 September 2026 doi:10.20944/preprints202608.2283.v2

The defining profile closure requires the translating configuration, when expressed in its source-attached material coordinate ζ, to obey the same normalized profile equation as the reference configuration. Comparison of Eqs. (114) and (115) therefore yields

$$\boxed{\Lambda_{\parallel}^2(v)\left(1-\frac{v^2}{c^2}\right)=1.} \tag{116}$$

The factor $1-v^2/c^2$ is generated by the difference between the quadratic time and longitudinal derivatives of the saturated-branch operator. Hence the power $(v/c)^2$, rather than a higher even power, follows from the second-order material operator itself. Because the matching equation is quadratic in the longitudinal rescaling, its positive solution contains the square root. Neither the exponent nor the square root is inserted as a fit to the Lorentz factor. Imposing $\Lambda_{\parallel}(0)=1$ gives uniquely

$$\Lambda_{\parallel}(v)=\frac{1}{\sqrt{1-v^2/c^2}}. \tag{117}$$

The DDF jamming factor is therefore identified as

$$\boxed{\gamma_{\varphi}(v)\equiv\Lambda_{\parallel}(v)=\frac{1}{\sqrt{1-(v/c)^2}}.} \tag{118}$$

This result is real only for $|v|<c$, diverges as $|v|\to c^-$, and has no real massive-body continuation to $|v|>c$ within the stated constitutive closure. The saturated branch thus fixes the material endpoint, while the second-order limiting operator and the source-attached profile law fix the exact Lorentz form of the approach to that endpoint. Within these stated operator and source-profile closures, the Lorentz form is therefore obtained as the DDF jamming factor without separately assuming a Lorentz transformation or relativistic energy law. Within the DDF constitutive description of the saturated φ branch, requiring the uniformly translating sheath to satisfy the same normalized source-attached profile equation as the reference configuration fixes $\Lambda_{\parallel}^2(v)(1-v^2/c^2)=1$, whose positive solution is the Lorentz factor. Its functional form is therefore obtained algebraically from the constitutive equation, not assumed or fitted in advance.

The term "jamming factor" denotes the longitudinal pile-up accompanying the approach to the saturated shear-jammed branch. It is not an apparent-viscosity ratio or a conventional rheological order parameter. For $v\ll c$,

$$\gamma_{\varphi}(v)-1=\frac{v^2}{2c^2}+\mathcal{O}\left(\frac{v^4}{c^4}\right), \tag{119}$$

so the DDF dressing becomes negligible and the Newtonian regime is recovered. As $v\to c$, the pile-up diverges and the massive sheath approaches the maximally stiff state without reaching it, whereas transverse φ-phonons propagate on that state at c. The speed dependence is shown in Figure 2.

The profile calculation determines the longitudinal pile-up factor independently of any prior clock-rate law. Its chronometric identification with the ratio between material-frame time and worldline proper time is developed in Sec. 7, where the response of physical clocks and the resulting material-spacetime interval are introduced.

Reversible inertial energy of the compressed sheath.

To connect the derived pile-up factor with inertial dynamics, the DDF adopts a conservative momentum closure that acts additively on the quantized-vortex constituents of massive matter rather than as an area-dependent drag on the macroscopic body

$$\mathbf{p}_{\mathcal{D}}(v)=m\gamma_{\varphi}(v)\mathbf{v}, \tag{120}$$

© 2026 by the author(s). Distributed under a Creative Commons CC BY license.

Preprints.org (www.preprints.org) | NOT PEER-REVIEWED | Posted: 7 September 2026 doi:10.20944/preprints202608.2283.v2

where m is the total invariant rest mass of the constituent vortex configuration. Here and below, the subscript $\mathcal{D}$ denotes quantities expressed in the DDF material reframing of the corresponding relativistic relations. This is the momentum of the complete body–DDF dressed state, not the sum of a classical momentum and an additional drag contribution.

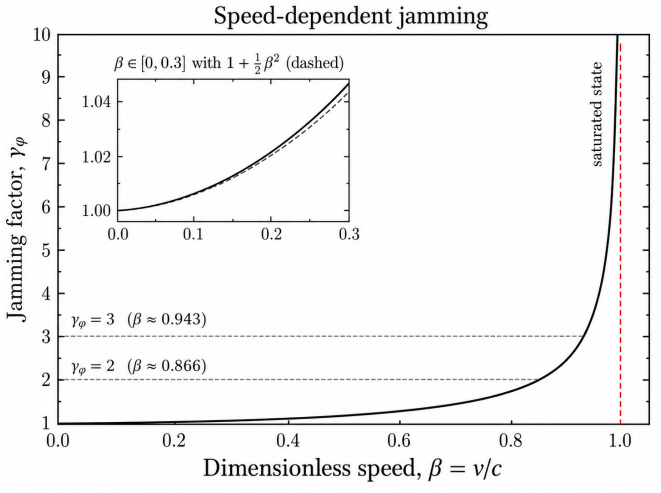


Figure 2. DDF jamming factor and its Lorentz-form speed dependence. The saturated state supports transverse-phonon propagation at c, while remaining asymptotically inaccessible to massive bodies.

For rectilinear acceleration, the reversible work–energy relation gives

$$dK_{\mathcal{D}} = \mathbf{v} \cdot d\mathbf{p}_{\mathcal{D}}. \tag{121}$$

Using

$$\frac{d}{dv}\left[\gamma_\varphi(v)v\right] = \gamma_\varphi^3(v), \tag{122}$$

the kinetic energy acquired from rest is

$$\begin{aligned} K_{\mathcal{D}}(v) &= \int_0^v u\,\frac{d}{du}\left[m\gamma_\varphi(u)u\right]du \\ &= m\int_0^v u\gamma_\varphi^3(u)\,du \\ &= mc^2\left[\gamma_\varphi(v) - 1\right]. \end{aligned} \tag{123}$$

Hence

$$\boxed{K_{\mathcal{D}}(v) = mc^2\left[\gamma_\varphi(v) - 1\right].} \tag{124}$$

This is the DDF analog of relativistic kinetic energy. It is the reversible work stored in the progressively shear-thickened, shear-stiffened, and compressed body–DDF configuration. It is not an independent dissipative power or a force proportional to the frontal area of the body.

Using the branch-calibrated zero-speed dressing energy $E_{\varphi,0} = mc^2$, Eq. (124) is equivalently

$$E_\varphi(v) = E_{\varphi,0} + K_{\mathcal{D}}(v) = \gamma_\varphi(v)E_{\varphi,0}. \tag{125}$$

The low-speed expansion is

$$K_{\mathcal{D}}(v) = \frac{1}{2}mv^2 + \frac{3}{8}m\frac{v^4}{c^2} + \mathcal{O}\left(\frac{v^6}{c^4}\right), \tag{126}$$

so the Newtonian kinetic term is recovered at leading order. The divergence of $K_{\mathcal{D}}$ as $v \to c$ is the energetic counterpart of the real-domain boundary found in the profile calculation: an unbounded amount of work would be required to force a massive configuration into the saturated φ branch.

© 2026 by the author(s). Distributed under a Creative Commons CC BY license.

Preprints.org (www.preprints.org) | NOT PEER-REVIEWED | Posted: 7 September 2026 doi:10.20944/preprints202608.2283.v2

Universality and branch normalization.

The leading factor $\gamma_\varphi(v)$ is composition-independent because it is fixed by the universal limiting operator and the common saturated values $\varrho_\varphi^{\max}$ and $j_\varphi^{\min}$, rather than by ordinary chemical composition. Finite-size, internal-structure, and higher-gradient effects may modify subleading details of the nonsaturated sheath, but all massive vortex-supported constituents share the same leading longitudinal pile-up law. Because the leading DDF response couples to the microscopic vortex-supported constituents of matter rather than to the macroscopic frontal area, the energy is additive over inertial mass contributions

$$\begin{aligned} K_{\mathcal{D}}^{(N)} &\simeq \sum_{i=1}^{N} m_i c^2 \left[\gamma_\varphi(v) - 1\right] \\ &= mc^2\left[\gamma_\varphi(v) - 1\right], \qquad m \simeq \sum_{i=1}^{N} m_i, \end{aligned} \tag{127}$$

where the constituent sum applies when binding corrections are negligible; more generally, m denotes the total invariant rest mass, including the bound-field and binding contributions discussed in Sec. 9.1. Here the common v is the center-of-mass three-speed of the rigid composite relative to the chosen local material observer. No macroscopic-area drag law is added. This microscopic additivity explains why the inertial and kinetic-energy responses scale with total rest mass rather than with the macroscopic size, shape, or frontal section of a composite body.

The application of this universal response to material lengths and clock rates is developed in Sec. 7.

The normalization $E_{\varphi,0} = mc^2$ used above is supplied independently by the saturated-branch mass–energy construction of Sec. 4.3; it is not inferred from Eq. (118). In that construction, the limiting transverse-phonon speed is fixed by the ratio of the maximum transverse kinetic/shear energy density of the jammed φ branch to its maximum inertial mass density. A massive particle, modeled as a ϕ-vortex state dressed by trapped φ-circulatory energy, carries the same branch-calibrated energy per unit trapped inertial mass through the constitutive identification

$$\rho_{E,\varphi}^{\max} \equiv G_\varphi^{\max}. \tag{128}$$

Accordingly, the jamming-factor derivation and the rest-energy normalization are distinct constitutive steps. Their kinematic and chronometric implications are developed separately in Sec. 7.

7. Lorentz-Form Kinematics of Material DDF Spacetime

The Lorentz-factor energy, momentum, clock, and length-contraction laws [131,146,147] are developed here in a local inertial material chart $(t, \mathbf{x})$. Throughout this section, v is the relative three-speed measured in the chart in which the corresponding clock, rod, momentum, or energy comparison is stated. The factor $\gamma_\varphi(v)$ is the longitudinal pile-up law obtained from the limiting-branch profile closure in Sec. 6; it is not rederived below. Its observer dependence, and that of the associated momentum and kinetic energy, represents the temporal and spatial decomposition of one covariant body–DDF state.

A massive vortex defect, or any macroscopic mass obtained by coarse-graining such defects, exhibits at nonzero relative speed the *excess inertia* governed by the DDF jamming factor, namely greater resistance to acceleration than in classical mechanics. Using the jamming factor derived in Sec. 6, the frame-dependent effective inertia is

$$\boxed{m_{\mathcal{D}}^{\mathrm{eff}}(v) \equiv m\gamma_\varphi(v).} \tag{129}$$

This quantity is not a new invariant rest mass, nor does it by itself provide a scalar acceleration law for arbitrary force directions. It is the frame-dependent coefficient multiplying $\mathbf{v}$ in the momentum of the

© 2026 by the author(s). Distributed under a Creative Commons CC BY license.

Preprints.org (www.preprints.org) | NOT PEER-REVIEWED | Posted: 7 September 2026 doi:10.20944/preprints202608.2283.v2

speed-dependent dressed state; the complete acceleration response follows from the derivative in the DDF-inclusive momentum balance

$$\mathbf{F}_{\text{ext}} = \frac{d}{dt}\big[m\gamma_\varphi(v)\mathbf{v}\big] \equiv \mathbf{F}_{\mathcal{D}}, \tag{130}$$

where $\mathbf{F}_{\mathcal{D}}$ denotes the complete DDF-inclusive balance, not an additional force superposed on the observed relativistic dynamics. For a given forcing of the particle–DDF system, the acceleration is smaller than the classical value because the reversible dilatant response increases the effective inertia. When $v \ll c$, $\gamma_\varphi \simeq 1$, and the standard Newtonian relation is recovered.

Substituting Eq. (129) into the momentum definition gives Eq. (120), which is mathematically identical to relativistic momentum, while its DDF interpretation is the momentum of the complete massive vortex–dressing state. Consistently with the reversible energy amplification obtained in Eq. (124), the corresponding total energy is

$$\boxed{E_{\mathcal{D}}^{\text{tot}} \equiv m\gamma_\varphi(v)c^2.} \tag{131}$$

Subtracting the branch-calibrated rest energy of Eq. (83) gives

$$E_{\mathcal{D}}^{\text{tot}} - mc^2 = mc^2\big[\gamma_\varphi(v) - 1\big], \tag{132}$$

and therefore Eq. (124), which is the Lorentz-form kinetic energy, but in the DDF reading it is the reversible work required against the progressive dilatant stiffening of the DDF to establish the speed-dependent inertial state of the moving body. The accounting is conservative: the microscopic energy paths associated with progressive shear thickening, reversible sheath loading, and subthreshold rearrangement of the φ background are not added as an independent macroscopic drag power. Their leading contribution is already encoded in the same γ_φ-dependent state energy. Because γ_φ diverges as $v \to c$, finite supplied work cannot accelerate a massive body to the saturated transverse-wave speed within the limiting-branch closure.

Material action, proper time, and clock-rate dilation.

The clock-rate law need not be introduced as an independent copy of its special-relativistic form. Its speed dependence follows from the same inertial state already characterized by the DDF momentum and energy laws. In particular, Eqs. (120) and (131) were obtained without assuming a proper-time relation:

$$\mathbf{p}_{\mathcal{D}} = m\gamma_\varphi(v)\mathbf{v}, \qquad E_{\mathcal{D}}^{\text{tot}} = m\gamma_\varphi(v)c^2. \tag{133}$$

For an autonomous isotropic body–DDF state, canonical consistency relates the material Lagrangian to these quantities through the Legendre relation

$$E_{\mathcal{D}}^{\text{tot}} = \mathbf{p}_{\mathcal{D}} \cdot \mathbf{v} - \mathcal{L}_{\mathcal{D}}. \tag{134}$$

The branch-calibrated total energy fixes the otherwise velocity-independent normalization, giving

$$\begin{aligned} \mathcal{L}_{\mathcal{D}} &= \mathbf{p}_{\mathcal{D}} \cdot \mathbf{v} - E_{\mathcal{D}}^{\text{tot}} \\ &= m\gamma_\varphi(v)v^2 - m\gamma_\varphi(v)c^2 \\ &= -\frac{mc^2}{\gamma_\varphi(v)} \\ &= -mc^2\sqrt{1 - \frac{v^2}{c^2}}. \end{aligned} \tag{135}$$

Indeed,

$$\frac{\partial \mathcal{L}_{\mathcal{D}}}{\partial \mathbf{v}} = m\gamma_\varphi(v)\mathbf{v} = \mathbf{p}_{\mathcal{D}}. \tag{136}$$

© 2026 by the author(s). Distributed under a Creative Commons CC BY license.

Preprints.org (www.preprints.org) | NOT PEER-REVIEWED | Posted: 7 September 2026 doi:10.20944/preprints202608.2283.v2

No clock-rate law, material interval, or Lorentz transformation has been used in obtaining Eq. (135); its speed dependence follows from the independently derived jamming factor and the conservative DDF momentum–energy closure.

The corresponding action along the material trajectory $\mathbf{x}(t)$ through the DDF is

$$\begin{aligned} S_{\mathcal{D}} &= \int \mathcal{L}_{\mathcal{D}}\, dt \\ &= -mc^2 \int \frac{dt}{\gamma_\varphi(v)} \\ &= -mc^2 \int \sqrt{1-\frac{v^2}{c^2}}\, dt. \end{aligned} \tag{137}$$

The DDF chronometric closure enters only at this point. Physical clocks are themselves bound systems of massive DDF-coupled constituents, and their internal periodic processes, transition phases, and signal exchanges are postulated to accumulate according to the same universal action-defined trajectory parameter. The positive coefficient of $-mc^2$ in Eq. (137) is therefore identified with the proper material time measured by an ideal clock:

$$dS_{\mathcal{D}} \equiv -mc^2 d\tau_{\mathcal{D}}. \tag{138}$$

Comparison with Eq. (137) then gives

$$\boxed{d\tau_{\mathcal{D}} = \frac{dt}{\gamma_\varphi(v)} = dt\sqrt{1-\frac{v^2}{c^2}}.} \tag{139}$$

Equivalently,

$$\boxed{\gamma_\varphi(v) = \frac{dt}{d\tau_{\mathcal{D}}} = \frac{1}{\sqrt{1-v^2/c^2}}.} \tag{140}$$

The profile calculation of Sec. 6 therefore determines the jamming factor, the momentum–energy closure determines the corresponding material action, and the chronometric closure identifies the action-defined worldline parameter with the elapsed time of physical clocks. This identification has a direct material basis: a clock is itself a physical system moving through the DDF and is therefore subject to the same speed-dependent φ-sector action that governs the inertial response of matter. The functional form of the clock-rate law is consequently inherited from the derived DDF inertial response rather than introduced independently.

Since $d\mathbf{x}^2 = v^2 dt^2$, Eq. (139) gives

$$\boxed{c^2 d\tau_{\mathcal{D}}^2 = c^2 dt^2 - d\mathbf{x}^2.} \tag{141}$$

The material interval is thus a consequence of the action-derived clock-rate law. It has not been assumed in order to obtain either $\gamma_\varphi(v)$ or $d\tau_{\mathcal{D}}$.

The DDF is therefore not interpreted merely as matter distributed through a pre-existing spatial arena. Its coupled $\phi + \varphi$ dynamics governs the inertial and spatial behavior of material systems, while physical clocks, being material systems themselves, undergo the same universal DDF action in their temporal evolution. In this precise operational sense, the DDF supplies both the spatial and chronometric structure of a *material spacetime*. Accordingly, the trajectory of a material system through the DDF defines its material worldline, parametrized by $\tau_{\mathcal{D}}$.

For uniform relative motion, integration of Eq. (139) gives

$$\boxed{\Delta t = \gamma_\varphi(v)\Delta\tau_{\mathcal{D}} = \frac{\Delta\tau_{\mathcal{D}}}{\sqrt{1-v^2/c^2}}.} \tag{142}$$

© 2026 by the author(s). Distributed under a Creative Commons CC BY license.

Preprints.org (www.preprints.org) | NOT PEER-REVIEWED | Posted: 7 September 2026 doi:10.20944/preprints202608.2283.v2

For nonuniform motion, proper time is accumulated locally along the worldline:

$$\boxed{\Delta\tau_{\mathcal{D}} = \int_{t_1}^{t_2} \frac{dt}{\gamma_\varphi[v(t)]} = \int_{t_1}^{t_2} \sqrt{1 - \frac{v^2(t)}{c^2}}\, dt.} \tag{143}$$

This proper time is unique for a specified worldline and supplies the parameter used to define the DDF four-velocity in Eq. (159). The resulting identity

$$\left(U^0_{\mathcal{D}}\right)^2 - \left|\mathbf{U}^{\mathrm{sp}}_{\mathcal{D}}\right|^2 = c^2$$

is therefore a consequence of the action-derived proper-time law, not an assumption used to obtain it.

For standard collinear charts in uniform relative motion, linear preservation of the same interval yields the local Lorentz transformation,

$$x' = \gamma_\varphi(v)(x - vt), \qquad t' = \gamma_\varphi(v)\left(t - \frac{vx}{c^2}\right). \tag{144}$$

Longitudinal material contraction.

The spatial consequence of the material transformation follows by applying its longitudinal part to the two endpoints of a moving rod. Let the rod be at rest in the primed material chart, with fixed endpoint coordinates

$$x'_A = 0, \qquad x'_B = L_0, \tag{145}$$

so that L_0 is its proper length. An observer in the unprimed chart measures the moving rod by recording the positions of its two endpoints *simultaneously in that chart*. For the corresponding pair of endpoint events,

$$\Delta t = 0, \qquad L_{\mathcal{D}} \equiv \Delta x = x_B - x_A. \tag{146}$$

Taking the difference of the spatial transformation in Eq. (144) gives

$$\Delta x' = \gamma_\varphi(v)(\Delta x - v\Delta t). \tag{147}$$

Because the endpoints have fixed primed coordinates, $\Delta x' = x'_B - x'_A = L_0$, while the simultaneity condition $\Delta t = 0$ reduces Eq. (147) to

$$L_0 = \gamma_\varphi(v) L_{\mathcal{D}}. \tag{148}$$

Hence the longitudinal length measured in the chart relative to which the rod moves is

$$\boxed{L_{\mathcal{D}} = \frac{L_0}{\gamma_\varphi(v)} = L_0\sqrt{1 - \frac{v^2}{c^2}}.} \tag{149}$$

Equivalently,

$$L_{\mathcal{D}} \equiv L_0 \gamma_\varphi^{-1}(v). \tag{150}$$

The two endpoint events used in this measurement are not simultaneous in the rod's rest chart. Indeed, the temporal part of Eq. (144) gives

$$\Delta t' = -\gamma_\varphi(v)\frac{vL_{\mathcal{D}}}{c^2}, \tag{151}$$

which identifies the change of simultaneity required to compare the spatial extensions assigned by the two material charts. The result is therefore not obtained from a separate force law or from the clock-rate equation alone; it is the spatial projection of the same material interval whose temporal projection yields time dilation.

© 2026 by the author(s). Distributed under a Creative Commons CC BY license.

Preprints.org (www.preprints.org) | NOT PEER-REVIEWED | Posted: 7 September 2026 doi:10.20944/preprints202608.2283.v2

The inverse scaling is also consistent with the source-attached profile coordinate derived in Sec. 6, $\zeta = \gamma_\varphi(v)(x_\parallel - vt)$: at fixed material-frame time, a fixed longitudinal profile interval satisfies $\Delta x_\parallel = \Delta\zeta/\gamma_\varphi(v)$. The profile calculation therefore supplies the microscopic longitudinal rescaling of the DDF dressing; because the same universal dressing acts on the constituents of material bodies, the corresponding composite length inherits the same $\gamma_\varphi^{-1}(v)$ scaling.

Within the DDF interpretation, length contraction has a direct material origin. As a body moves through the local DDF, the progressive stiffening and longitudinal pile-up of the surrounding φ carrier produce a reversible compression of the DDF-coupled material configuration along the direction of motion. The equilibrium longitudinal scale therefore follows the same factor derived for the source-attached sheath, $L_\mathcal{D} = L_0/\gamma_\varphi(v)$. This contraction persists only while the relative motion is maintained and disappears when the body returns to rest with respect to the local DDF; it is neither a permanent deformation nor the result of dissipative frontal drag. Reciprocal operational length measurements between material charts follow from the corresponding inverse transformations.

Material basis of the first postulate.

The first postulate of special relativity states that the laws of physics have the same form in all inertial frames. In the DDF framework, this equivalence is not imposed independently of the substrate dynamics. The same universal constitutive response governs the spatial standards, clock rates, momenta, energies, and transverse radiation used by every local inertial observer. Its spatial and temporal effects are correlated through the single factor $\gamma_\varphi(v)$ and the invariant material interval in Eq. (141). Consequently, the changes of material lengths and clock pace are accompanied by the corresponding transformations of momentum and energy. For electromagnetic propagation, the same material-frame relations generate the usual Doppler shifts and aberration of the propagation direction, while the locally measured propagation speed remains the universal value c, fixed by the transverse φ-phonon branch. These are not separate corrections that could be compared to reveal one preferred chart, but mutually consistent manifestations of the same DDF-governed dynamics.

The interval in Eq. (141), the massive-particle dispersion relation in Eq. (162), and the local Maxwell-form equations discussed in Sec. 8.1 therefore retain their form under transformations between inertial material charts. In any sufficiently local region where source-generated gravitational gradients and other environmental inhomogeneities can be neglected, no nongravitational experiment constructed from DDF-governed matter and radiation can distinguish one uniformly moving inertial material frame from another. The relativity principle is thus realized in the DDF through the material Lorentz covariance of its complete spatial and chronometric response.

For atmospheric muons, the atmosphere and detector define one local material frame, in which the muon speed is measured as u. Let $\tau_{\mathcal{D},0}$ denote the muon's mean lifetime measured by an ideal clock comoving with the muon; it is therefore its intrinsic proper lifetime, not the proper time accumulated during a particular flight. The survival law is

$$P = \exp\left(-\frac{\Delta\tau_\mathcal{D}}{\tau_{\mathcal{D},0}}\right), \tag{152}$$

where the DDF proper time accumulated between production and detection is

$$\Delta\tau_\mathcal{D} = \frac{\Delta t}{\gamma_\varphi(u)} = \frac{L}{u\gamma_\varphi(u)}. \tag{153}$$

Consequently,

$$\boxed{P = \exp\left[-\frac{L}{u\gamma_\varphi(u)\tau_{\mathcal{D},0}}\right].} \tag{154}$$

© 2026 by the author(s). Distributed under a Creative Commons CC BY license.

Preprints.org (www.preprints.org) | NOT PEER-REVIEWED | Posted: 7 September 2026 doi:10.20944/preprints202608.2283.v2

The enhancement of the laboratory decay length therefore follows from the reduced DDF proper time accumulated along the muon worldline, while $\tau_{\mathcal{D},0}$ remains the invariant mean lifetime of the decay process.

Local material frames, relative velocity, and light propagation.

The local Lorentz sector is formulated relationally. If two local inertial material observers have relative collinear speed V, and one measures a body speed u, the other measures

$$u' = \frac{u - V}{1 - uV/c^2}. \tag{155}$$

The same transformation preserves Eq. (141) and the four-velocity norm. Consequently, the speed entering γ_φ is always the speed measured in the local frame in which the clock, rod, or momentum comparison is stated.

A photon is a transverse excitation of the saturated φ branch. In every local inertial material frame its measured speed is

$$\left| \frac{d\mathbf{x}_\gamma}{dt} \right| = c. \tag{156}$$

The emitter's motion through the DDF may change the frequency, direction, and momentum balance of the emitted mode, but not the local limiting speed. The two-way and one-way local values are therefore both c when measured with consistently synchronized material standards.

Doppler relations in material DDF spacetime.

For collinear relative motion at measured speed u, the longitudinal Doppler relations are

$$\nu_{\text{app}} = \nu_0 \sqrt{\frac{1 + u/c}{1 - u/c}}, \qquad \nu_{\text{rec}} = \nu_0 \sqrt{\frac{1 - u/c}{1 + u/c}}, \tag{157}$$

and hence

$$\frac{\nu_{\text{app}} + \nu_{\text{rec}}}{2} = \nu_0 \gamma_\varphi(u). \tag{158}$$

The DDF interpretation assigns the clock-rate factor to the dilatant material response, while the measured formulas retain their standard Lorentz form.

DDF four-velocity and the invariant four-speed.

Because the DDF chronometric closure identifies $\tau_{\mathcal{D}}$ with the elapsed time of physical clocks, the four-velocity can now be defined directly within the material-spacetime description, without introducing an independent relativistic proper-time postulate. For a material worldline $x^\mu = (ct, \mathbf{x})$, define

$$\boxed{U^\mu_{\mathcal{D}} \equiv \frac{dx^\mu}{d\tau_{\mathcal{D}}} = \gamma_\varphi(v)(c, \mathbf{v}).} \tag{159}$$

It is a material-spacetime four-vector and satisfies

$$\boxed{\left(U^0_{\mathcal{D}}\right)^2 - \left|\mathbf{U}^{\text{sp}}_{\mathcal{D}}\right|^2 = c^2.} \tag{160}$$

The fixed value c is the invariant four-speed of every massive body. It must not be confused with either the observer-relative three-speed v or the proper spatial velocity $\gamma_\varphi(v)\mathbf{v}$, neither of which has a universal fixed magnitude. Temporal and spatial components compensate so that the norm remains c for every observer.

The four-momentum is

$$P^\mu_{\mathcal{D}} = mU^\mu_{\mathcal{D}} = \left(E^{\text{tot}}_{\mathcal{D}}/c, \mathbf{p}_{\mathcal{D}}\right), \tag{161}$$

© 2026 by the author(s). Distributed under a Creative Commons CC BY license.

Preprints.org (www.preprints.org) | NOT PEER-REVIEWED | Posted: 7 September 2026 doi:10.20944/preprints202608.2283.v2

with the invariant dispersion relation

$$\boxed{\frac{(E_{\mathcal{D}}^{\mathrm{tot}})^2}{c^2} - |\mathbf{p}_{\mathcal{D}}|^2 = m^2c^2.} \tag{162}$$

Together with $E_\gamma = p_\gamma c$, this places matter and light under the same material-spacetime speed scale c: transverse φ-phonons propagate at c, whereas massive bodies remain restricted to $v < c$ and can approach this value only asymptotically, consistently with their distinct DDF microphysics.

Particle scattering and a conserved DDF collision functional.

Scattering is interpreted as a finite, causal interaction of vortex defects, their shear-thickened and shear-stiffened φ sheaths, the coherent ϕ sector, and any transverse radiation. Far from the collision region, the sheath energy is included in the dressed particle energies of Eq. (161). During close approach, the separate sheaths overlap and that decomposition is replaced by a conserved functional for the complete coupled interaction region.

For a spatial domain Ω, let $\mathscr{E}_\Omega(t)$ and $\mathscr{P}_\Omega(t)$ denote, respectively, the total energy and total momentum of the coupled DDF state contained in that domain. They include both the localized contributions of massive vortex cores and the distributed energy and momentum carried by the ϕ and φ sectors, their interaction, and transverse φ-phonon radiation. Explicitly,

$$\mathscr{E}_\Omega(t) = \sum_{a\in\Omega} E_a^{\mathrm{core}} + \int_\Omega (\mathcal{E}_\phi + \mathcal{E}_\varphi + \mathcal{E}_{\mathrm{int}} + \mathcal{E}_\gamma)\, d^3x, \tag{163}$$

and

$$\mathscr{P}_\Omega(t) = \sum_{a\in\Omega} \mathbf{p}_a^{\mathrm{core}} + \int_\Omega (\mathbf{\Pi}_\phi + \mathbf{\Pi}_\varphi + \mathbf{\Pi}_{\mathrm{int}} + \mathbf{\Pi}_\gamma)\, d^3x. \tag{164}$$

Their local conservative balance laws are postulated as

$$\frac{d\mathscr{E}_\Omega}{dt} = -\oint_{\partial\Omega} \mathbf{S}_{\mathrm{tot}} \cdot d\mathbf{A}, \qquad \frac{d\mathscr{P}_\Omega}{dt} = -\oint_{\partial\Omega} \mathbf{T}_{\mathrm{tot}} \cdot d\mathbf{A}. \tag{165}$$

For a domain containing the complete interaction and all outgoing fluxes,

$$\mathscr{E}_{\mathrm{in}} = \mathscr{E}_{\mathrm{out}}, \qquad \mathscr{P}_{\mathrm{in}} = \mathscr{P}_{\mathrm{out}}. \tag{166}$$

These total-energy and total-momentum functionals define the conservative collision description; their microscopic densities and fluxes must ultimately be derived from the coupled DDF Hamiltonian. Within that description, accelerator work stored in translating vortex–sheath configurations remains part of the conserved coupled state when the configurations overlap. It can be redistributed into outgoing massive defects, reconstructed sheaths, and emitted transverse phonons. The sheath contribution is counted either in the asymptotic dressed particle energy or explicitly in the interaction-region integral, but not in both.

For an asymptotic process $1 + 2 \to 3 + 4$, the local measured conservation laws reduce to

$$\begin{aligned} \mathbf{p}_{\mathcal{D},1} + \mathbf{p}_{\mathcal{D},2} &= \mathbf{p}_{\mathcal{D},3} + \mathbf{p}_{\mathcal{D},4}, \\ E_{\mathcal{D},1}^{\mathrm{tot}} + E_{\mathcal{D},2}^{\mathrm{tot}} &= E_{\mathcal{D},3}^{\mathrm{tot}} + E_{\mathcal{D},4}^{\mathrm{tot}}. \end{aligned} \tag{167}$$

Introduce the algebraic pair

$$P_{\mathcal{D},i} \equiv \left(E_{\mathcal{D},i}^{\mathrm{tot}}/c, \mathbf{p}_{\mathcal{D},i}\right), \tag{168}$$

© 2026 by the author(s). Distributed under a Creative Commons CC BY license.

Preprints.org (www.preprints.org) | NOT PEER-REVIEWED | Posted: 7 September 2026 doi:10.20944/preprints202608.2283.v2

and define

$$s \equiv \frac{(E_1 + E_2)^2}{c^2} - |\mathbf{p}_1 + \mathbf{p}_2|^2, \tag{169}$$

$$t \equiv \frac{(E_1 - E_3)^2}{c^2} - |\mathbf{p}_1 - \mathbf{p}_3|^2, \tag{170}$$

$$u \equiv \frac{(E_1 - E_4)^2}{c^2} - |\mathbf{p}_1 - \mathbf{p}_4|^2, \tag{171}$$

where all energies and momenta are the local DDF-dressed quantities. The exact dispersion and conservation laws give

$$s + t + u = \sum_{i=1}^{4} m_i^2 c^2, \tag{172}$$

as in the standard algebraic scattering bookkeeping [148].

Charge motion and Lorentz force in the DDF framework.

Within one material platform, charge motion retains the operational form

$$q(\mathbf{E} + \mathbf{u} \times \mathbf{B}) = \frac{d}{dt_A}\left[m\gamma_\varphi(u)\mathbf{u}\right], \tag{173}$$

where $\mathbf{u}$ is the center-of-vortex velocity relative to the platform. The increasing accelerator work as $u \to c$ is the kinetic and inertial loading of the massive vortex–DDF configuration. It does not modify the already saturated photon branch. Synchrotron radiation transfers part of this material kinetic energy into transverse phonons that subsequently propagate at the invariant local material-spacetime speed c.

Relativistic fluid dynamics as an effective description.

The DDF framework does not treat relativistic fluid dynamics as the dynamics of an empty geometric arena. The fundamental fields are the coupled (ϕ, φ) material-spacetime variables, with finite characteristic speeds and a saturation-fixed photon branch fixed at c. Standard relativistic hydrodynamics may therefore be used as the effective Lorentz-covariant description whenever the DDF energy, momentum, proper-time, and constitutive relations reduce to their established relativistic forms. Source-generated superflows and inhomogeneities enter separately through the gravitational and astrophysical field equations [149–151].

8. Interferometric Null Results from the DDF Material-Spacetime Response

The same DDF constitutive response that generates the jamming factor also governs material lengths, clock rates, and transverse propagation. Let λ_{opt} denote the optical wavelength. Thus $\gamma_\varphi(v)$ is not an isolated inertial correction: it enters the complete Lorentz-form response of rods, clocks, and photon-carrying φ modes.

Consider an inertial material chart in which a Michelson interferometer with equal proper arm lengths L has relative speed v along one arm. The longitudinal arm has length $L/\gamma_\varphi(v)$, by Eq. (150),

© 2026 by the author(s). Distributed under a Creative Commons CC BY license.

Preprints.org (www.preprints.org) | NOT PEER-REVIEWED | Posted: 7 September 2026 doi:10.20944/preprints202608.2283.v2

whereas the transverse arm retains length L. The round-trip times before and after a 90° rotation are then

$$\begin{aligned} t_1 &= \frac{L/\gamma_\varphi}{c-v} + \frac{L/\gamma_\varphi}{c+v} = \frac{2L}{c}\,\gamma_\varphi, \quad t_2 = \frac{2L}{\sqrt{c^2-v^2}} = \frac{2L}{c}\,\gamma_\varphi \\ t_1' &= \frac{2L}{\sqrt{c^2-v^2}} = \frac{2L}{c}\,\gamma_\varphi, \quad t_2' = \frac{L/\gamma_\varphi}{c-v} + \frac{L/\gamma_\varphi}{c+v} = \frac{2L}{c}\,\gamma_\varphi \\ \Delta t &= t_1 - t_2 = 0, \quad \Delta t' = t_1' - t_2' = 0, \end{aligned} \tag{174}$$

$$\boxed{\Delta(\Delta t) = \Delta t' - \Delta t = 0, \quad N_{\rm fr} = \frac{c\,\Delta(\Delta t)}{\lambda_{\rm opt}} = 0}$$

Here $c-v$ and $c+v$ are the closing rates between the photon and the moving mirrors; the photon speed in the inertial material chart remains c.

This gives the Michelson–Morley null result [14] directly from the DDF-derived longitudinal contraction.

The corresponding apparatus proper times also agree. Using $d\tau_{\mathcal{D}} = dt/\gamma_\varphi(v)$,

$$\Delta\tau_{\mathcal{D},1} = \frac{t_1}{\gamma_\varphi} = \frac{2L}{c}, \qquad \Delta\tau_{\mathcal{D},2} = \frac{t_2}{\gamma_\varphi} = \frac{2L}{c}. \tag{175}$$

Length contraction and clock-rate dilation are therefore the spatial and temporal manifestations of the same DDF material transformation, rather than independent compensating hypotheses.

The same cancellation applies to the unequal-arm Michelson–Pease–Pearson configuration [15]. For proper arm lengths L_1 and L_2, the round-trip times before and after rotation are

$$\begin{aligned} t_1 &= \frac{L_1/\gamma_\varphi}{c-v} + \frac{L_1/\gamma_\varphi}{c+v} = \frac{2L_1}{c}\,\gamma_\varphi, \quad t_2 = \frac{2L_2}{c}\,\gamma_\varphi \\ t_1' &= \frac{2L_1}{c}\,\gamma_\varphi, \quad t_2' = \frac{L_2/\gamma_\varphi}{c-v} + \frac{L_2/\gamma_\varphi}{c+v} = \frac{2L_2}{c}\,\gamma_\varphi \end{aligned} \tag{176}$$

Hence

$$\begin{aligned} \Delta t &= t_1 - t_2 = \frac{2\gamma_\varphi}{c}(L_1 - L_2), \\ \Delta t' &= t_1' - t_2' = \frac{2\gamma_\varphi}{c}(L_1 - L_2), \end{aligned} \tag{177}$$

$$\boxed{\Delta(\Delta t) = \Delta t' - \Delta t = 0, \qquad N_{\rm fr} = \frac{c\,\Delta(\Delta t)}{\lambda_{\rm opt}} = 0}$$

The unequal arm lengths produce a fixed phase offset, but no change under rotation.

Kennedy–Thorndike, modern resonator, and closed-loop nulls follow from the same universal transformation of lengths, clock rates, frequencies, and transverse propagation [16,18–21,152,153]. Within the DDF closure developed here, these experiments therefore reproduce the same operational predictions as special relativity and do not by themselves discriminate the material DDF description from the geometric SR description. Appendix A examines additional established tests within the DDF framework.

8.1. Maxwell-Form Dynamics in Local DDF Material Frames

The interferometric null is consistent with the Maxwell-form equations (59)–(61) derived from the transverse Lagrangian in Eq. (57). For a plane mode, the Euler–Lagrange equation gives

$$\boxed{\omega^2 = c^2k^2, \qquad c^2 = \left(\varrho_\varphi^{\max} j_\varphi^{\min}\right)^{-1}.} \tag{178}$$

© 2026 by the author(s). Distributed under a Creative Commons CC BY license.

Preprints.org (www.preprints.org) | NOT PEER-REVIEWED | Posted: 7 September 2026 doi:10.20944/preprints202608.2283.v2

For two inertial material charts in relative motion along x, invariance of the wave phase gives

$$\begin{aligned} \omega' &= \gamma_\varphi(v)(\omega - vk_x), \\ k'_x &= \gamma_\varphi(v)\Big(k_x - \frac{v\omega}{c^2}\Big), \\ k'_y &= k_y, \qquad k'_z = k_z. \end{aligned} \tag{179}$$

It follows that

$$\frac{\omega'^2}{c^2} - |\mathbf{k}'|^2 = \frac{\omega^2}{c^2} - |\mathbf{k}|^2. \tag{180}$$

Therefore,

$$\boxed{k_\mu k^\mu = 0, \qquad \omega'^2 = c^2|\mathbf{k}'|^2,} \tag{181}$$

and the source-free transverse equations retain the same Maxwell form in every local inertial material frame.

Their covariance and the interferometric null are thus two consequences of the same DDF material-spacetime structure: the common factor $\gamma_\varphi(v)$ governs longitudinal material standards and clock rates, while the saturated transverse branch fixes the invariant characteristic speed c.

A source-generated, inhomogeneous ϕ superflow introduces the distinct moving-medium relation

$$\big(\omega - \mathbf{k}\cdot\mathbf{v}_\phi\big)^2 = c^2k^2, \tag{182}$$

as given and defined in Eq. (201). This physical advection bends or traps photon-carrying φ modes in the gravitational sector, but does not alter the local Maxwell-form propagation law. It must not be confused with the relative inertial-frame speed v entering $\gamma_\varphi(v)$.

9. Bernoulli-Force Framework for the Gravitational Sector

Building on Sec. 3, the DDF identifies gravity with the coarse-grained Bernoulli force associated with the specific-enthalpy gradient generated by persistent quantized-vortex configurations of the coherent ϕ medium. Individual quanta of the homogeneous $\phi + \varphi$ sea carry inertia but are not assigned particle-by-particle active gravitational charge. Active sourcing begins with a persistent vortex-supported pressure deficit and superflow; entrained φ content contributes only through that collective configuration.

The isolated-vortex near field and the observable many-vortex closure must be distinguished. A single quantized vortex remains an active gravitational source, with its local Bernoulli-pressure field producing the isolated-core $r_\perp^{-3}$ acceleration scaling. For ordinary composite sources, however, the experimentally accessible gravitational field is the coarse-grained result of the superposed and collectively organized fields of many constituent vortices, yielding the macroscopic r^{-2} closure. This material ontology realizes the chronometric and spatial structure physically, rather than treating spacetime geometry as an independently fundamental substance, and differs accordingly from analog-gravity, entropic, and emergent-geometry programs [8,154–162].

In laboratory studies involving superfluid helium doped with fine metal particles, it has been observed that these particles are attracted to quantum vortices due to the Bernoulli pressure produced by them [41,71,102,106,109,163–165]. This laboratory vortex decoration and Bernoulli trapping mechanism are illustrated in Figure 3.

© 2026 by the author(s). Distributed under a Creative Commons CC BY license.

Preprints.org (www.preprints.org) | NOT PEER-REVIEWED | Posted: 7 September 2026 doi:10.20944/preprints202608.2283.v2

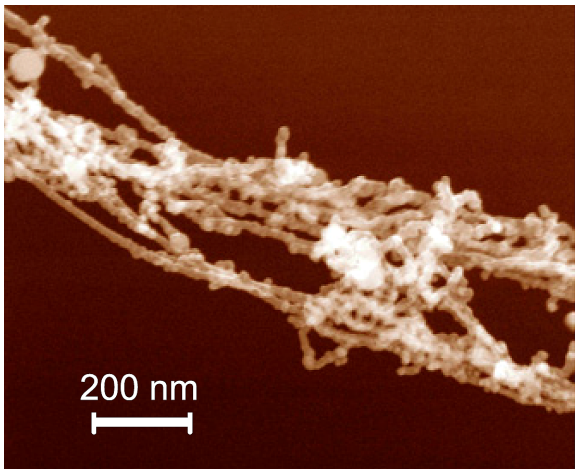


Figure 3. Scanning electron microscopy (SEM) image of entangled gold nanowire networks produced via laser ablation in superfluid helium (He II) at 1.5 K (Credit: Moroshkin et al. [41]). The formation of these high-aspect-ratio macroscopic filaments is attributed to the coalescence of metallic nanofragments along the cores of quantized vortices. The nanowire ropes observed here trace the structure of quantized vortex bundles. The nanoparticles are drawn toward and trapped on the one-dimensional vortex lines by a radial pressure gradient generated by the circulatory motion of the superfluid around the core—a manifestation of the Bernoulli effect. The displayed microstructures were harvested from the pressure cell after cryostat warming and stabilized on a glass substrate via a 1.5 nm carbon film for ex situ imaging.

The present section specializes that Bernoulli picture to the vortex-ring configurations identified in Sec. 3 as toroidal quantized vortices representing fundamental massive particles in the doped ϕ superfluid. Outside the core the density is taken as uniform ($\varrho_\phi \simeq \varrho_{\phi,0}$), and the quantum-pressure term is neglected for $r_\perp \gtrsim$ a few ξ. Gravity is thus modeled as an emergent, non-fundamental classical Bernoulli force with a quantum origin in the vortex structure of matter. In the DDF material-spacetime description, gravitational effects arise from source-generated pressure gradients in the ϕ medium, equivalently expressed as specific-enthalpy gradients. These material gradients produce the gravitational trajectories and clock-rate variations represented geometrically by spacetime curvature in GR.

Using Eqs. (20) and (21), the local flow around a locally straight tube segment takes the standard near-core form

$$\mathbf{v}_{\rm self}(r_\perp) \approx \frac{n\kappa_\phi}{2\pi r_\perp}\,\hat{\boldsymbol{\theta}}, \qquad r_\perp \gtrsim \xi, \tag{183}$$

where $\hat{\boldsymbol{\theta}}$ is the azimuthal unit vector about the local tube axis.

Microscopic near field of an isolated vortex.

For a single isolated ring in otherwise quiescent fluid, the classical limit of Eq. (37) gives

$$\begin{aligned}\Delta P_\phi^{\rm iso}(r_\perp) &\equiv P_\phi(r_\perp) - P_{\phi,\infty} \\ &\simeq -\frac{1}{2}\varrho_{\phi,0}|\mathbf{v}_{\rm self}|^2 = -\frac{\varrho_{\phi,0} n^2\kappa_\phi^2}{8\pi^2}\frac{1}{r_\perp^2}.\end{aligned} \tag{184}$$

Therefore,

$$|\boldsymbol{\nabla} P_\phi| \sim \frac{\varrho_{\phi,0} n^2\kappa_\phi^2}{4\pi^2}\frac{1}{r_\perp^3}. \tag{185}$$

Thus the *microscopic* near-field prediction for an isolated elementary vortex is

$$\Delta P_\phi^{\rm iso} \sim r_\perp^{-2}, \qquad |\boldsymbol{\nabla} P_\phi| \sim r_\perp^{-3}. \tag{186}$$

© 2026 by the author(s). Distributed under a Creative Commons CC BY license.

Preprints.org (www.preprints.org) | NOT PEER-REVIEWED | Posted: 7 September 2026 doi:10.20944/preprints202608.2283.v2

In the present theory this isolated-vortex law is not identified with the directly observed Newtonian field; no experiment has ever measured the gravitational field of a single fundamental fermion in a regime capable of distinguishing a $1/r^3$ microscopic near field from a $1/r^2$ macroscopic one.

Observable gravity is the coarse-grained many-vortex field.

The physically relevant gravitational sources are not isolated elementary vortices in quiescent fluid, but *multi-vortex bound systems* and, at larger scales, enormous aggregates of such systems (Figure 4). This is already true at the microscopic baryonic level: even a single proton is a multi-vortex object in the DDF framework. Therefore every gravitational field that is feasibly measurable is, in the theory, a *many-vortex field*.

In a many-vortex environment, neighboring vortices induce at a chosen local vortex segment a background velocity $\mathbf{U}_{\rm ext}$ with tangential projection

$$U_\theta \equiv \hat{\boldsymbol{\theta}} \cdot \mathbf{U}_{\rm ext}. \tag{187}$$

Bernoulli for $\mathbf{v} = \mathbf{v}_{\rm self} + \mathbf{U}_{\rm ext}$ then gives, after subtracting the background constant,

$$\begin{aligned} \Delta P_\phi^{\rm mv}(r_\perp) &\equiv P_\phi(r_\perp) - P_{\phi,\infty} \\ &= -\varrho_{\phi,0}\, \mathbf{U}_{\rm ext}\cdot\mathbf{v}_{\rm self} - \frac{1}{2}\varrho_{\phi,0}|\mathbf{v}_{\rm self}|^2 \\ &= -\varrho_{\phi,0} U_\theta \frac{n\kappa_\phi}{2\pi r_\perp} - \frac{\varrho_{\phi,0} n^2\kappa_\phi^2}{8\pi^2}\frac{1}{r_\perp^2}. \end{aligned} \tag{188}$$

Whenever the induced tangential flow dominates the local isolated-ring swirl and varies slowly across the local radial interval,

$$|U_\theta| \gg v_{\rm self}(r_\perp), \qquad |r_\perp\, \partial_{r_\perp} \ln |U_\theta|| \ll 1, \tag{189}$$

the cross term controls the local pressure profile and one obtains

$$\frac{dP_\phi}{dr_\perp} \simeq \varrho_{\phi,0}\, \frac{n\kappa_\phi}{2\pi}\, \frac{U_\theta}{r_\perp^2}. \tag{190}$$

Hence the associated Bernoulli acceleration is

$$\mathbf{a}_\phi^{\rm LO}(r_\perp) = -\frac{1}{\varrho_{\phi,0}}\boldsymbol{\nabla} P_\phi \simeq -\hat{\mathbf{r}}_\perp\, \frac{n\kappa_\phi}{2\pi}\, \frac{U_\theta}{r_\perp^2}. \tag{191}$$

Microscopic vs. macroscopic scaling.

The theory therefore distinguishes two regimes:

$$\begin{aligned} &\text{Single vortex-particle (e.g. quark/lepton):} \\ &\quad \Delta P_\phi^{\rm iso} \sim r_\perp^{-2}, \qquad |\nabla P_\phi| \sim r_\perp^{-3}, \\ &\text{Coarse-grained many-vortex source:} \\ &\quad \Delta P_\phi \sim r^{-1}, \qquad |\nabla P_\phi| \sim r^{-2}. \end{aligned} \tag{192}$$

The first is a microscopic near-field statement. The second is the proposed coarse-grained far-field closure for the idealized spherical source class used throughout the benchmark construction. Non-spherical bodies are represented, at this level, by the corresponding higher multipoles and boundary data rather than by changing the underlying Bernoulli law.

© 2026 by the author(s). Distributed under a Creative Commons CC BY license.

Preprints.org (www.preprints.org) | NOT PEER-REVIEWED | Posted: 7 September 2026 doi:10.20944/preprints202608.2283.v2

Macroscopic Bernoulli force and gravitational acceleration.

Once the many-vortex pressure field has been coarse-grained into the macroscopic profile $P_\phi(r)$, the operational weak-equivalence-principle closure requires the effective displaced volume of a test body to be proportional to its inertial mass. Writing $V_p^{\rm eff} = m/\varrho_{\phi,0}$ implements this universal ratio in the nearly incompressible exterior.

The resulting Bernoulli force is, in the DDF framework, identified directly with the gravitational force:

$$\boxed{\begin{aligned}\mathbf{F}_g(r) \equiv \mathbf{F}_B(r) &= -\,V_p^{\rm eff}\,\boldsymbol{\nabla} P_\phi(r) \\ &= -\,m\,\frac{\boldsymbol{\nabla} P_\phi(r)}{\varrho_{\phi,0}} = -\,m\,\boldsymbol{\nabla}\Phi_\phi(r) = m\,\mathbf{g}_\phi(r).\end{aligned}} \tag{193}$$

Thus gravity and the macroscopic Bernoulli force are not distinct phenomena in the DDF, but two descriptions of the same emergent force: gravitational in phenomenological language and hydrodynamic in its underlying DDF mechanism. Dividing Eq. (193) by the inertial mass gives the universal acceleration field

$$\boxed{\mathbf{g}_\phi(r) = -\,\frac{\boldsymbol{\nabla} P_\phi(r)}{\varrho_{\phi,0}} \equiv -\,\boldsymbol{\nabla}\Phi_\phi(r).} \tag{194}$$

This is the operational gravitational law of the DDF in the weak-field/macroscopic exterior limit: measurable gravity is the pressure-gradient acceleration generated by the coarse-grained many-vortex state of baryonic matter.

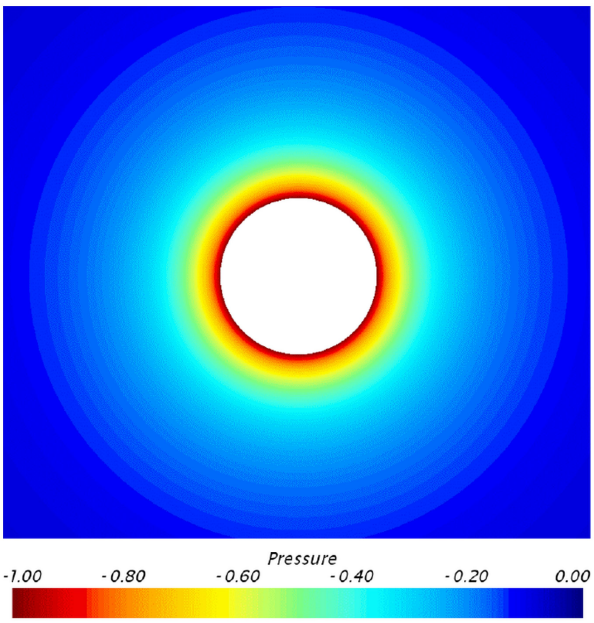


Figure 4. Schematic computational visualization (CFD simulation) of the coarse-grained gravitational field of a celestial body as a pressure-gradient field in the dark superfluid ϕ, producing a $1/r^2$ inward acceleration in the macroscopic regime. The color scale is normalized from the minimum to maximum plotted pressure and represents relative pressure contrast only, not an absolute pressure calibration.

Potential–enthalpy identification and emergent coupling.

For the superfluid component, the nearly incompressible macroscopic exterior satisfies

$$\boldsymbol{\nabla} h_\phi = \frac{1}{\varrho_{\phi,0}}\,\boldsymbol{\nabla} P_\phi, \tag{195}$$

© 2026 by the author(s). Distributed under a Creative Commons CC BY license.

Preprints.org (www.preprints.org) | NOT PEER-REVIEWED | Posted: 7 September 2026 doi:10.20944/preprints202608.2283.v2

where $\varrho_{\phi,0} = m_\phi n_{\phi,0}$ is the background mass density of the superfluid sector. Let the pressure perturbation relative to infinity be

$$\Delta P_\phi(r) \equiv P_\phi(r) - P_{\phi,\infty}. \tag{196}$$

For an attractive Bernoulli well, $\Delta P_\phi(r) < 0$. The DDF gravitational potential is identified with the corresponding specific-enthalpy perturbation,

$$\boxed{\begin{aligned} \Phi_\phi(r) &\equiv \frac{\Delta P_\phi(r)}{\varrho_{\phi,0}} = h_\phi(r) - h_{\phi,\infty}, \\ \Phi_\phi(\infty) &= 0, \qquad \Phi_\phi(r) < 0. \end{aligned}} \tag{197}$$

Its gradient therefore generates the gravitational acceleration already defined in Eq. (194); no additional gravitational interaction is introduced.

In the weak-field spherical exterior, the DDF potential may equivalently be written in the conventional Newtonian form

$$\Phi_\phi(r) = -\frac{G_\phi M}{r}. \tag{198}$$

Hence

$$\boxed{G_\phi = -\frac{r}{M}\frac{\Delta P_\phi(r)}{\varrho_{\phi,0}} = -\frac{r\,\Phi_\phi(r)}{M} = \text{const.}} \tag{199}$$

Equation (199) is a Newtonian-form rewriting of the DDF pressure–density relation. The quantity G_ϕ is not a fundamental coupling of the theory, but a conversion parameter expressing the coarse-grained Bernoulli enthalpy field in terms of the conventional macroscopic variables M and r. In the DDF interpretation, the Newtonian constant G thus plays the role of a conversion factor between the underlying quantum-hydrodynamic description in terms of P_ϕ and ϱ_ϕ and its classical macroscopic mass–distance representation.

Interpretation.

The DDF claim is therefore a symmetry-reduced collective-vortex closure. For an idealized spherical source, the Newtonian $1/r^2$ acceleration is assigned to the collectively organized Bernoulli field of its constituent vortices after the appropriate coarse-graining, whereas the $1/r^3$ behavior derived above refers specifically to the microscopic near field of an isolated single vortex.

The use of spherical symmetry is a benchmark idealization, analogous to selecting a definite symmetry class in standard gravitational solutions; the present work does not attempt shape-resolved numerical gravity for arbitrary bodies. Composition independence is likewise formulated at the coarse-grained level: atoms and molecules remain bound systems of the same vortex-supported massive constituents, while their binding and internal dynamical energies modify the total Bernoulli sink strength. Departures from spherical symmetry enter source multipoles and boundary data rather than replacing the foundational pressure-gradient law.

9.1. Active Gravitational Sourcing, Bound Dynamics, and Free Radiation

In Bernoulli gravity the *active* gravitational source is not "energy in general" as a geometric axiom, but the persistent DDF configuration that produces an enthalpy/pressure profile in the coherent superfluid ϕ. Recalling Eqs. (194) and (197), the gravitational field is the Bernoulli pressure gradient in the nearly incompressible regime, or more generally

$$\mathbf{g}_\phi = -\boldsymbol{\nabla} h_\phi \tag{200}$$

when barotropic density variations must be retained. Active sourcing is therefore associated with persistent vortex-supported configurations of the ϕ sector and with the bound dynamics that form part of their stationary hydrodynamic structure. These include internal orbital, electromagnetic, and strong-

© 2026 by the author(s). Distributed under a Creative Commons CC BY license.

Preprints.org (www.preprints.org) | NOT PEER-REVIEWED | Posted: 7 September 2026 doi:10.20944/preprints202608.2283.v2

binding contributions insofar as they modify the circulation and Bernoulli-pressure configuration of the composite source. The inertial mass of an isolated ϕ- or φ-quantum is not by itself a Bernoulli source. Freely propagating on-shell radiation is likewise distinct: it transports energy through the φ sector without independently establishing a persistent ϕ-sector pressure sink.

Free photons: advected propagation of the constitutive c-speed branch.

Photons are modeled as transverse phonons of φ, propagating locally at the constitutive speed c of the transverse φ-phonon branch while being advected by the physical coarse-grained ϕ superflow (Sec. 12.2). At resolved microscopic scales, this carrier motion is built from the full circulation field $\mathbf{v}_B$; after averaging over the many-vortex state it is represented by the same macroscopic field $\mathbf{v}_\phi$ defined in Eq. (3). In the eikonal limit, transverse modes in the moving medium obey

$$\left(\omega - \mathbf{k}\cdot\mathbf{v}_\phi\right)^2 = c^2k^2, \tag{201}$$

where c remains the local propagation speed of the transverse φ-phonon branch relative to the carrier, while $\mathbf{v}_\phi$ produces the source-dependent advective contribution to ray propagation.

The forward eikonal branch defines the ray Hamiltonian

$$\omega_\gamma(\mathbf{r},\mathbf{k},t) = \mathbf{k}\cdot\mathbf{v}_\phi(\mathbf{r},t) + c|\mathbf{k}|, \tag{202}$$

so that the frequency measured in the local rest frame of the carrier satisfies

$$\omega_\gamma - \mathbf{k}\cdot\mathbf{v}_\phi = c|\mathbf{k}|,$$

and the intrinsic photon propagation speed therefore remains c. The ray equations

$$\dot{\mathbf{r}} = \frac{\partial\omega_\gamma}{\partial\mathbf{k}}, \qquad \dot{\mathbf{k}} = -\frac{\partial\omega_\gamma}{\partial\mathbf{r}} \tag{203}$$

then describe how the background ϕ superflow advects and redirects this local c-speed propagation, providing the material propagation law used below for gravitational bending, propagation delay, and horizon characteristics.

Bound systems, internal energy, and radiative transitions.

Eötvös-, Eöt-Wash-, MICROSCOPE-, and atom-interferometric tests constrain composition dependence of the ratio $m_{\rm pass}/m_{\rm inert}$ to very high precision [166–172], while Kreuzer-type experiments and Earth–Moon/Lunar Laser Ranging constrain differences between the active and passive gravitational masses of ordinary composite matter [173–176]. The DDF description must therefore reproduce this observed universality for complete bound systems. In the present framework this does not require every microscopic energy contribution to act as an independent Bernoulli source. Rather, bound internal energy contributes to gravity through the persistent vortex-supported hydrodynamic configuration in which that energy is embodied.

This applies in particular to electromagnetic and other binding energies. Processes represented in the Standard Model by virtual photons, gluons, and other binding degrees of freedom are interpreted in the DDF as particular localized or exchanged configurations of the underlying ϕ and φ quanta that organize the dynamics of the constituent vortices. Their detailed microscopic embedding into the Standard Model is left for future work. The essential point here is that such off-shell and binding processes belong to the internal dynamics of the bound vortex system rather than to the freely propagating transverse φ-phonon branch. They can therefore contribute to the stationary circulation and pressure-deficit structure that determines the active Bernoulli source.

An electronic transition provides the simplest example. In the DDF microscopic picture, the electron is a toroidal quantized vortex whose quantized bound-state dynamics within the nuclear vortex configuration form part of the persistent dynamics of the atom. A higher-energy electronic state

© 2026 by the author(s). Distributed under a Creative Commons CC BY license.

Preprints.org (www.preprints.org) | NOT PEER-REVIEWED | Posted: 7 September 2026 doi:10.20944/preprints202608.2283.v2

corresponds to a more energetic bound vortex configuration, while radiative de-excitation transfers the difference in that internal energy to the surrounding φ population, exciting the transverse phonon identified with the on-shell photon. Let $E_{\rm vb}$ denote the relevant dynamical energy of the vortex-supported bound system and $E_\gamma^{\rm on}$ the energy carried by the emitted photon. Neglecting recoil and other channels for notational simplicity, local energy conservation gives

$$\boxed{\Delta E_{\rm vb} + \Delta E_\gamma^{\rm on} = 0.} \tag{204}$$

Because the orbital and binding dynamics themselves contribute to the persistent Bernoulli source configuration, the transition to a lower-energy bound state also corresponds to a slightly weaker active source. At the effective source-bookkeeping level used here,

$$\boxed{\Delta M_{\rm act} \simeq \frac{\Delta E_{\rm vb}}{c^2}, \qquad \Delta M_{\rm act}|_{\gamma,\rm free} = 0.} \tag{205}$$

The first relation refers to the change of the complete bound vortex configuration, not to a change in the intrinsic rest mass of the electron vortex itself. During emission the electron remains the same fundamental vortex constituent but enters a lower-energy orbital configuration, thereby reducing the bound system's contribution to the Bernoulli sink. The emitted on-shell photon carries away the corresponding energy as a free transverse φ-phonon without acquiring an independent persistent ϕ-sector pressure sink.

Absorption reverses the process. An incident transverse φ-phonon transfers energy to an allowed internal vortex-supported degree of freedom, raising the system to a more energetic bound configuration and correspondingly increasing its active Bernoulli source strength. Total material energy is therefore conserved throughout emission and absorption, while the active gravitational contribution follows whether that energy is incorporated into persistent bound vortex dynamics or transported away as free on-shell radiation.

Strong binding and the mass defect.

The same principle applies to strongly bound composite systems. Let $E_{\rm bind}^{(\rm str)} > 0$ denote the magnitude of the strong binding energy [131,177,178]. In the DDF description, the isolated-constituent rest energies already include the intrinsic internal kinetic energy of the corresponding vortex-supported particles; for a bound state one may therefore write

$$M_{\rm tot}c^2 = \sum_a E_a^{(\rm rest)} + E_{\rm field} - |E_{\rm bind}|, \tag{206}$$

where $\sum_a E_a^{(\rm rest)}$ is the sum of the isolated constituent rest energies, $E_{\rm field}$ denotes additional field energy stored in the bound configuration, and $-|E_{\rm bind}|$ is the binding contribution. The negative sign expresses the ordinary mass defect: the bound state has lower total energy than the corresponding isolated constituents.

The DDF hypothesis assigns the strong-binding channel to shared inter-vortex dynamics of the ϕ superflow and the associated organization of the φ sector, rather than to an additional energy independently localized inside each vortex core [179,180]. Strong binding is therefore part of the persistent hydrodynamic configuration of the composite source itself. At the effective active-source level, the corresponding relation may be written

$$M_{\rm active} \simeq \sum_i m_i^{(\rm rest)} + \frac{E_{\rm field}}{c^2} - \frac{|E_{\rm bind}|}{c^2}, \tag{207}$$

with the composite object required to reproduce $m_{\rm act} \simeq m_{\rm pass} \simeq m_{\rm inert}$ within the established experimental bounds. This expression is not an independent postulate that arbitrary energy automatically

© 2026 by the author(s). Distributed under a Creative Commons CC BY license.

Preprints.org (www.preprints.org) | NOT PEER-REVIEWED | Posted: 7 September 2026 doi:10.20944/preprints202608.2283.v2

gravitates. Rather, it summarizes how positive internal field energy and negative binding energy modify the persistent vortex-supported configuration and hence its Bernoulli sink strength.

The resulting distinction is therefore between energy incorporated into the persistent hydrodynamics of a bound material source and energy transported as free on-shell radiation. Bound electromagnetic, orbital, and strong-interaction energies contribute to active gravity because they form part of the coupled vortex dynamics that establishes the source pressure field. A freely propagating photon, by contrast, is gravitationally deflected because its transverse φ-phonon propagation is advected by an existing ϕ-sector superflow, but its transported energy does not independently generate a persistent Bernoulli pressure sink. Emission and absorption move energy between these two dynamical regimes while preserving total material energy. This difference in the active gravitational role of freely propagating on-shell radiation is the specific DDF departure from the GR source description.

10. Painlev é–Gullstrand Representation of the DDF Superflow

Painlevé–Gullstrand (PG) coordinates provide the natural geometric encoding of the macroscopic material flow generated by the DDF Bernoulli dynamics. The physical gravitational variables are the coarse-grained superflow $\mathbf{v}_\phi$, pressure/enthalpy field P_ϕ or Φ_ϕ, and the many-vortex source and correlation stresses. No independent gravitational metric is introduced into the DDF ontology. Instead, wherever a GR solution admits a PG-type representation, its river velocity is identified with the corresponding macroscopic DDF superflow,

$$\boxed{\mathbf{v}_{\rm PG}(\mathbf{x},t) \overset{\rm DDF}{\longleftrightarrow} \mathbf{v}_\phi(\mathbf{x},t).} \tag{208}$$

The GR line element is therefore used as the geometric representation of a material flow whose microscopic origin lies in the coherent ϕ phase and its quantized-vortex population.

10.1. Coarse-grained Current Bridge and PG Flow Variables

The identification in Eq. (208) concerns the macroscopic superflow obtained after coarse-graining the full microscopic circulation $\mathbf{v}_{\rm B}$. Exact ϕ-number conservation applies to the density-weighted current rather than to the factorized product of mean density and mean velocity. Writing

$$n_\phi = \bar{n}_\phi + \delta n_\phi, \qquad \mathbf{v}_{\rm B} = \mathbf{v}_\phi + \delta\mathbf{v}_{\rm B}, \tag{209}$$

with $\langle \delta n_\phi \rangle_\ell = 0$ and $\langle \delta \mathbf{v}_{\rm B} \rangle_\ell = 0$, coarse-graining the microscopic current gives

$$\boxed{\bar{\mathbf{j}}_\phi = \langle n_\phi \mathbf{v}_{\rm B} \rangle_\ell = \bar{n}_\phi \mathbf{v}_\phi + \mathbf{J}_\phi^{\rm corr},} \tag{210}$$

where

$$\mathbf{J}_\phi^{\rm corr} \equiv \langle \delta n_\phi \, \delta \mathbf{v}_{\rm B} \rangle_\ell \tag{211}$$

is the unresolved density–velocity correlation current of the many-vortex state. The corresponding conservation law is

$$\boxed{\partial_t \bar{n}_\phi + \boldsymbol{\nabla}\cdot\left(\bar{n}_\phi \mathbf{v}_\phi + \mathbf{J}_\phi^{\rm corr}\right) = 0.} \tag{212}$$

The operator form of Eqs. (210)–(212) is given in Sec. 15. Thus a nonzero mean superflow does not require a secular accumulation or depletion of the condensate: the conserved particle current also contains the correlated counterflow generated by the unresolved vortex configuration.

For a stationary spherically symmetric exterior, Eq. (212) gives

$$4\pi r^2 \left[\bar{n}_\phi(r) v_{\phi,r}(r) + J_{\phi,r}^{\rm corr}(r)\right] = \mathcal{F}_\phi = \text{const.} \tag{213}$$

© 2026 by the author(s). Distributed under a Creative Commons CC BY license.

Preprints.org (www.preprints.org) | NOT PEER-REVIEWED | Posted: 7 September 2026 doi:10.20944/preprints202608.2283.v2

For a nonaccreting stationary configuration, $\mathcal{F}_\phi = 0$, so

$$J^{\rm corr}_{\phi,r}(r) = -\bar{n}_\phi(r) v_{\phi,r}(r). \tag{214}$$

This is a conservation constraint on the coarse-grained many-vortex state, not an added source or sink. Microscopically it is supplied by the same unresolved density, phase, vortex-position, and ϕ–φ correlations that enter the coarse-grained momentum stress below.

On the GR side, a configuration in PG coordinates is encoded by the river velocity through

$$ds^2_{\rm GR} = -\Big(c^2 - |\mathbf{v}_{\rm PG}|^2\Big)dt^2 - 2\,\mathbf{v}_{\rm PG}\cdot d\mathbf{x}\,dt + d\mathbf{x}^2. \tag{215}$$

This is a 3+1 split with unit lapse and Euclidean spatial slices; on the GR side the shift is $\boldsymbol{\beta} = -\mathbf{v}_{\rm PG}/c$ [181,182]. The strong flat-slice PG form is exact for Schwarzschild; Kerr requires the corresponding generalized PG/Doran/Natário representation. These are geometric representations on the GR side, while Eq. (208) assigns their river variables a material realization in the DDF cold dark sector.

With the extrinsic-curvature sign convention used here, the symmetric gradient of the flow is represented geometrically by the PG extrinsic curvature,

$$K_{ij} = \frac{1}{2c}\Big(\partial_i v_{\phi,j} + \partial_j v_{\phi,i}\Big), \tag{216}$$

under the DDF–PG identification. This equality is a representation of the material velocity gradient; K_{ij} is not introduced as an independent DDF degree of freedom.

At the superfluid level the Bernoulli gravitational acceleration remains

$$\mathbf{g}_\phi = -\boldsymbol{\nabla}\Phi_\phi, \tag{217}$$

while the mean superflow obeys the momentum balance

$$\boxed{\partial_t \mathbf{v}_\phi + (\mathbf{v}_\phi\cdot\boldsymbol{\nabla})\mathbf{v}_\phi = \mathbf{g}_\phi - \frac{1}{\varrho_{\phi,0}}\boldsymbol{\nabla}\cdot\boldsymbol{\Pi}^{\rm corr}_\phi.} \tag{218}$$

Here $\boldsymbol{\Pi}^{\rm corr}_\phi$ denotes the coarse-grained vortex, finite-core, density–phase, and intercomponent correlation stress. In the leading stationary spherical exterior closure used below, its divergence is subleading, so the Bernoulli first integral follows. In rotating configurations the same stress supplies the nonpotential balance associated with the coarse-grained vorticity of the vortex ensemble. The quantum operator origin of this term is developed in Sec. 15.

10.2. Bernoulli Potential and the Newtonian/Poisson Limit

The DDF gravitational field is the Bernoulli/enthalpy gradient of the same material flow represented geometrically by the PG river. For a stationary irrotational exterior the Euler identity integrates to

$$\Phi_\phi = -\frac{|\mathbf{v}_\phi|^2}{2}, \tag{219}$$

with the normalization $\Phi_\phi(\infty) = 0$ and $\mathbf{v}_\phi(\infty) = 0$ [22,23]. The PG river potential therefore represents the physical DDF enthalpy potential,

$$\begin{aligned}\Phi_{\rm PG} &\equiv -\frac{|\mathbf{v}_{\rm PG}|^2}{2} \overset{\rm DDF}{\longleftrightarrow} \Phi_\phi \\ &= \frac{\Delta P_\phi}{\varrho_{\phi,0}} = -\frac{|\mathbf{v}_\phi|^2}{2}, \\ &\qquad \text{(nearly incompressible exterior).}\end{aligned} \tag{220}$$

© 2026 by the author(s). Distributed under a Creative Commons CC BY license.

Preprints.org (www.preprints.org) | NOT PEER-REVIEWED | Posted: 7 September 2026 doi:10.20944/preprints202608.2283.v2

This is the Bernoulli first integral of the stationary irrotational coarse-grained material flow. Its compatibility with exact ϕ-number conservation is supplied by the full current law, Eq. (212), rather than by the factorized condition $\boldsymbol{\nabla}\cdot(\bar{n}_\phi \mathbf{v}_\phi) = 0$ alone. The direction of $\mathbf{v}_\phi$ is fixed by the physical boundary conditions; for the Schwarzschild sector it is the inward radial branch.

Taking a divergence yields the Poisson form of the Bernoulli field,

$$\boldsymbol{\nabla}\cdot \mathbf{g}_\phi = -\boldsymbol{\nabla}^2\Phi_\phi \overset{\text{NR}}{=} -4\pi G_\phi\, \rho_M, \tag{221}$$

where ρ_M is the coarse-grained source mass density and G_ϕ is the *macroscopic conversion constant* introduced above (Eq. 199) only when one chooses to express the Bernoulli potential Φ_ϕ in the customary (M, r) bookkeeping.

Exterior normalization (spherical NR limit).

In a stationary, spherically symmetric weak-field exterior one may parameterize the observed $1/r$ normalization as

$$\Phi_\phi(r) \simeq -\frac{G_\phi M}{r}, \qquad G_\phi \equiv \lim_{r\to\infty} \frac{-\Phi_\phi(r)\, r}{M}. \tag{222}$$

In the native Bernoulli description, however, the potential is $\Phi_\phi = \Delta P_\phi / \varrho_{\phi,0}$ and no separate universal constant is required; G_ϕ enters only as an external normalization used to compare the $(P_\phi, \varrho_{\phi,0})$ description with the conventional (M, r) parameterization.

GR comparison normalization.

In GR,

$$G_{\mu\nu} = \frac{8\pi G}{c^4}\, T_{\mu\nu}. \tag{223}$$

The coefficient is normalized so that the weak-field, slow-motion limit gives $\nabla^2\Phi = 4\pi G\rho_M$ when $T_{00} \simeq \rho_M c^2$. For the DDF benchmark map the corresponding coefficient is used directly as

$$\frac{8\pi G_\phi}{c^4} = 8\pi G_\phi \left(\varrho_\varphi^{\max} j_\varphi^{\min}\right)^2, \tag{224}$$

where $c^2 = (\varrho_\varphi^{\max} j_\varphi^{\min})^{-1}$. This is only a conversion into conventional GR comparison units; it does not introduce a new DDF coupling or a geometric field equation.

10.3. GR Stress–Energy Bookkeeping for DDF Source Loads

On the GR comparison side, a 3+1 split decomposes $T_{\mu\nu}$ into energy density, momentum density, and spatial stress relative to a chosen congruence with unit normal n^μ and projector $\gamma_{\mu\nu} = g_{\mu\nu} + n_\mu n_\nu$ [181,182]. These are not DDF geometric variables; the split is retained only to organize the corresponding material source loads. The GR decomposition is

$$\begin{aligned} T_{\mu\nu} &= \rho\, n_\mu n_\nu + 2n_{(\mu} S_{\nu)} + S_{\mu\nu}, \\ \rho &\equiv T_{\alpha\beta} n^\alpha n^\beta, \\ S_\mu &\equiv -\gamma_{\mu\alpha} T^{\alpha\beta} n_\beta, \\ S_{\mu\nu} &\equiv \gamma_{\mu\alpha}\gamma_{\nu\beta} T^{\alpha\beta}. \end{aligned} \tag{225}$$

Here $S_\mu n^\mu = 0$ and $S_{\mu\nu} n^\nu = 0$. Writing the spatial stress as

$$S_{ij} = p_{\text{eff}}\, \gamma_{ij} + \pi_{ij}, \qquad \pi^i{}_i = 0, \tag{226}$$

where p_{eff} is the isotropic (pressure-like) load and π_{ij} is the traceless shear stress.

Active versus propagating sectors in the DDF source map. The physical DDF distinction is between configurations that sustain a persistent Bernoulli pressure deficit and excitations that only propagate

© 2026 by the author(s). Distributed under a Creative Commons CC BY license.

Preprints.org (www.preprints.org) | NOT PEER-REVIEWED | Posted: 7 September 2026 doi:10.20944/preprints202608.2283.v2

through the medium. In the GR comparison equation this distinction is represented by an effective active coarse-grained tensor,

$$T_{\mu\nu}^{(\mathrm{eff})} \equiv T_{\mu\nu}^{(\mathrm{def/bound})} = T_{\mu\nu}^{(\mathrm{def})} + T_{\mu\nu}^{(\mathrm{bound})}, \tag{227}$$

built from quantized-vortex content and bound (off-shell) field energy that produces a persistent Bernoulli pressure deficit in ϕ. Free quanta of the quiescent $\phi + \varphi$ medium and propagating on-shell transverse φ modes are treated as *passive* inertial or transport content. They undergo and transmit the medium response but are not counted as independent long-range sources of ∇P_ϕ. The source selection is therefore

$$\begin{aligned} T_{\mu\nu}^{(\mathrm{eff})} &= T_{\mu\nu}^{(\mathrm{def})} + T_{\mu\nu}^{(\mathrm{bound/conf})}, \\ T_{\mu\nu}^{(\mathrm{eff})}\Big|_{\text{free }\phi,\,\text{free }\varphi,\,\gamma} &= 0. \end{aligned} \tag{228}$$

where $T_{\mu\nu}^{(\mathrm{bound/conf})}$ denotes stationary field or configurational stresses only insofar as they sustain the vortex-supported ϕ pressure deficit. This is the precise sense in which DDF departs from GR on radiation gravitation while retaining the kinematic influence of the physical coarse-grained superflow on photon propagation (Sec. 9.1).

GR comparison congruence and the DDF source frame.

In the GR river representation, the natural comparison congruence is comoving with the coordinate shift. Under Eq. (208) this congruence is paired with the local material rest frame of the coarse-grained ϕ superflow. The vector n^μ remains a GR-side object, whereas $\mathbf{v}_\phi$ is the physical DDF velocity field. The split in Eqs. (225)–(226) then organizes the representation of (i) persistent quantized-vortex and bound-field configurations that sustain the Bernoulli deficit and (ii) inertial or transport content of the surrounding φ branch. Entrained φ mass is not an independent active source charge.

T_{00} / ρ: GR representation of the DDF active load.

The physical DDF source is the coarse-grained sink strength of persistent quantized-vortex populations and bound internal configurations insofar as they modify the sustained ϕ pressure deficit. The parameter ρ_M is the nonrelativistic calibration of this vortex-supported active mass, not a sum of the inertial masses of advected φ quanta. In the GR comparison bookkeeping it is represented as

$$\rho_{\mathrm{eff}} \equiv T_{\alpha\beta}^{(\mathrm{eff})} n^\alpha n^\beta \simeq \varepsilon_{\mathrm{def/bound}} \equiv \rho_M c^2. \tag{229}$$

Propagating on-shell φ phonons contribute to *passive* energy transport and redshift along rays, but are not included in ρ_{eff} because they do not generate a Bernoulli deficit in ϕ. In the weak-field, stationary limit this is precisely the quantity that enters the Bernoulli/Poisson closure (Sec. 10.2), i.e. it fixes the large-scale pressure deficit in ϕ through $\nabla\cdot\mathbf{g}_\phi \propto -\rho_M$ with $\mathbf{g}_\phi = -(1/\varrho_{\phi,0})\nabla P_\phi$.

T_{0i} / S_i: GR representation of DDF source momentum.

On the comparison side, the mixed components encode the momentum density or energy flux of active sources relative to the mapped river frame. The physical DDF quantity is the ordinary transport of quantized-vortex and bound-field energy relative to the ϕ-carrier. For slowly moving sources one has, in the customary $c = 1$ normalization of the 3+1 source split, schematically

$$S_i \sim \rho_M u_i \qquad (|u| \ll c), \tag{230}$$

where $\mathbf{u}$ is the source drift relative to the local DDF material frame. Restoring SI units introduces the corresponding power of c according to the chosen time-coordinate convention; the multipole relation below is unaffected. Crucially, S_i is a source momentum-density variable, not the physical superflow $\mathbf{v}_\phi$ or the conserved particle current $\bar{\mathbf{j}}_\phi$. In the GR representation it sources the shift sector; in DDF

© 2026 by the author(s). Distributed under a Creative Commons CC BY license.

Preprints.org (www.preprints.org) | NOT PEER-REVIEWED | Posted: 7 September 2026 doi:10.20944/preprints202608.2283.v2

the corresponding physical source momentum fixes the boundary data and correlation stresses that determine the rotational component of $\mathbf{v}_\phi$. The far-field swirl developed below is therefore a physical coarse-grained vortex flow whose PG/Kerr form is its geometric encoding. In particular, S_i refers to transport of the *active* defect/bound energy density; it is not the flux of propagating photon energy (which belongs to $T^{(\gamma)}_{\mu\nu}$ and is excluded from $T^{(\mathrm{eff})}_{\mu\nu}$ by Eq. (228)). At the level of multipoles, the total angular momentum

$$\mathbf{J} \propto \int d^3x\, \mathbf{r} \times \mathbf{S} \tag{231}$$

controls the leading far-field dipolar swirl, consistent with the hydrodynamic rotating-source solution developed in Sec. 11.2.

T_{ij} / S_{ij}: GR representation of material loading.

The GR-side spatial stress S_{ij} is used to represent how the physical DDF source distribution loads the surrounding medium. The corresponding DDF quantities are the actual isotropic and anisotropic material stresses, for which the split (226) provides convenient comparison notation:

(a) The isotropic part p_{eff} is the coarse-grained *source load* on the surrounding medium. The corresponding *response* of the ϕ background is the Bernoulli pressure field P_ϕ (and its enthalpy perturbation $\Phi_\phi = \Delta P_\phi/\varrho_{\phi,0}$), which directly determines the gravitational acceleration and enters the Euler equation for the physical coarse-grained superflow $\mathbf{v}_\phi$. In the Schwarzschild sector, the same superflow obeys $\Delta P_\phi/\varrho_{\phi,0} = -|\mathbf{v}_\phi|^2/2$ (Sec. 10.2); the gravitational potential itself remains literally a pressure/enthalpy in ϕ.

(b) The traceless part π_{ij} represents anisotropic stresses: (i) ordinary material shear within the source and, more distinctively in DDF, (ii) the shear transmitted to the dispersed dilatant phase φ in the near-field sheath. This provides the natural bridge to the jamming-based phenomenology of Sec. 6. In this gravitational near-field application, however, the local rheological loading is characterized by the shear-rate invariant rather than by the observer-relative Lorentz-sector factor. Define

$$\dot\gamma_{\mathrm{loc}} \equiv \left(2\,\sigma^{(\mathrm{shear})}_{ij}\sigma^{ij}_{(\mathrm{shear})}\right)^{1/2}. \tag{232}$$

The effective anisotropic response may then be parameterized as

$$\begin{aligned}\pi_{ij} &\sim 2\,\eta_{\mathrm{eff}}(\dot\gamma_{\mathrm{loc}})\,\sigma^{(\mathrm{shear})}_{ij}\\ &\equiv 2\,\mu_{\mathrm{eff}}(\dot\gamma_{\mathrm{loc}})\,u^{(\mathrm{shear})}_{ij},\end{aligned} \tag{233}$$

where the constitutive growth of η_{eff} or μ_{eff} encodes progressive shear thickening and approach to local shear jamming. Source-centered ϕ superflows remain physical in this sector, but they do not define or calibrate the observer-relative factor $\gamma_\varphi(v)$ used in local Lorentz kinematics.

Role of the split in the comparison map.

The set $\{\rho, S_i, S_{ij}\}$ organizes three GR-side comparison roles: ρ represents the monopolar active load, S_i the rotational multipoles, and S_{ij} the isotropic and anisotropic source stresses. DDF contains instead the corresponding physical quantized-vortex density, source momentum transport, and material stress fields. These jointly determine the physical pressure/enthalpy field, the conserved coarse-grained current, and the boundary-value problem for $\mathbf{v}_\phi$; the gravitational interaction is the resulting material acceleration and Bernoulli field $\mathbf{g}_\phi = -\boldsymbol{\nabla}\Phi_\phi$. The PG variables then provide the geometric representation of this same macroscopic solution.

GR tensors as comparison encodings of DDF flow observables.

The following objects belong exclusively to the GR comparison description. The DDF theory contains only the mapped material quantities stated on the right:

© 2026 by the author(s). Distributed under a Creative Commons CC BY license.

Preprints.org (www.preprints.org) | NOT PEER-REVIEWED | Posted: 7 September 2026 doi:10.20944/preprints202608.2283.v2

(i) *GR metric* $g_{\mu\nu}^{(\mathrm{GR})}$. In PG coordinates the GR shift is parameterized by $\mathbf{v}_{\mathrm{PG}}$. Under Eq. (208), its river profile is identified with the physical coarse-grained DDF superflow $\mathbf{v}_\phi$; no independent gravitational metric field is thereby introduced.

(ii) *GR connection* $\Gamma^\lambda{}_{\mu\nu}$. Its first-derivative combinations represent derivatives of the macroscopic $\mathbf{v}_\phi$ field; they should not be confused with the resolved smooth microscopic field $\mathbf{v}_{\phi,\mathrm{mic}}$ of a single vortex patch.

(iii) *GR curvature* $R_{\mu\nu}$. Its weak-field second-derivative content is compared with the divergence of the physical Bernoulli acceleration, which in DDF is obtained directly from P_ϕ and Φ_ϕ:

$$R_{00} \propto \boldsymbol{\nabla}\cdot\mathbf{g}_\phi = -\boldsymbol{\nabla}^2\Phi_\phi, \tag{234}$$

consistent with Eq. (221).

10.4. GR Comparison Equation in PG Variables

For term-by-term comparison with GR observables, the mapped variables may be inserted into the standard field equation in PG form,

$$\boxed{\begin{gathered} G_{\mu\nu}\Big[g_{\alpha\beta}^{(\mathrm{GR,PG})}(\mathbf{v}_{\mathrm{PG}})\Big] = \frac{8\pi G_\phi}{c^4}T_{\mu\nu}^{(\mathrm{eff})}, \\ \mathbf{v}_{\mathrm{PG}} \overset{\mathrm{map}}{\longleftrightarrow} \mathbf{v}_\phi. \end{gathered}} \tag{235}$$

This is the GR representation of the DDF material solution, not an independent DDF field equation or an additional metric degree of freedom. The physical fields follow from the Hamiltonian, the coarse-grained current law, Euler–Bernoulli dynamics, and the constitutive source/stress closure; the PG form encodes the resulting $\mathbf{v}_\phi$ and Φ_ϕ in geometric variables. Likewise, $T_{\mu\nu}^{(\mathrm{eff})}$ is comparison bookkeeping restricted to persistent quantized-vortex sources and bound configurational stresses that sustain the ϕ-sector pressure deficit. Free background quanta, entrained φ mass considered independently, and on-shell transverse radiation are not inserted as separate active sources.

The mapped Bianchi condition requires consistency with conservation, but the physical conservation law remains the local Hamiltonian exchange among ϕ, φ, quantized-vortex configurations, and bound fields. The normalization G_ϕ is the weak-field exterior coupling fixed by Eq. (199); it does not replace the intrinsic closure

$$\begin{aligned} \partial_t\mathbf{v}_\phi + (\mathbf{v}_\phi\cdot\boldsymbol{\nabla})\mathbf{v}_\phi &= \mathbf{g}_\phi - \frac{1}{\varrho_{\phi,0}}\boldsymbol{\nabla}\cdot\boldsymbol{\Pi}_\phi^{\mathrm{corr}}, \\ \mathbf{g}_\phi &= -\boldsymbol{\nabla}\left(\frac{\Delta P_\phi}{\varrho_{\phi,0}}\right). \end{aligned} \tag{236}$$

In the weak-field limit the mapped 00 component reproduces $\nabla^2\Phi_\phi = 4\pi G_\phi\rho_M$, while the mixed components organize the source-current/swirl comparison. The physical equations remain Eq. (236), the correlated continuity law (212), and the source constitutive relations. In the stationary spherical weak-field sector the leading correlation-stress divergence is absorbed into the coarse-grained closure, whereas in rotating configurations it supplies the non-potential vortex balance described in Sec. 11.2.

Where DDF genuinely departs from GR.

The PG correspondence does not retain a geometric theory alongside DDF. Its principal empirical separation surfaces are:

(i) *Active sourcing.* Only persistent quantized-vortex configurations and bound stresses that sustain the Bernoulli deficit are active sources. Free background quanta, independently counted entrained φ mass, and freely propagating on-shell transverse modes are not.

© 2026 by the author(s). Distributed under a Creative Commons CC BY license.

Preprints.org (www.preprints.org) | NOT PEER-REVIEWED | Posted: 7 September 2026 doi:10.20944/preprints202608.2283.v2

(ii) *Material propagation.* Observable radiation is the saturated transverse φ branch, propagating locally at its constitutive speed c while being advected by the physical carrier field $\mathbf{v}_\phi$. Other transverse, longitudinal, or configurational modes remain dark internal channels with their own constitutive speeds and stability conditions.

(iii) *Material cosmology.* The scale factor used in Sec. 17 denotes coarse-grained deformation of a pre-existing substrate rather than a physical FLRW geometry; its microscopic dynamics remain to be derived.

These distinctions locate the principal falsifiable differences in the active source rule, strong-field signal propagation, and the cosmological background.

Particle motion and horizon condition.

The Bernoulli gravitational acceleration acting on a test body is

$$\mathbf{g}_\phi = -\boldsymbol{\nabla}\Phi_\phi, \qquad \frac{d^2\mathbf{r}_p(t)}{dt^2} = \mathbf{g}_\phi\big(\mathbf{r}_p(t), t\big), \tag{237}$$

which in the nearly incompressible exterior is $\mathbf{g}_\phi = -(1/\varrho_{\phi,0})\boldsymbol{\nabla}P_\phi$. The same many-vortex state determines the material river through

$$\partial_t\mathbf{v}_\phi + (\mathbf{v}_\phi\cdot\boldsymbol{\nabla})\mathbf{v}_\phi = \mathbf{g}_\phi - \frac{1}{\varrho_{\phi,0}}\boldsymbol{\nabla}\cdot\boldsymbol{\Pi}_\phi^{\mathrm{corr}}, \tag{238}$$

together with the correlated continuity law Eq. (212). The correlation stress is an internal coarse-grained support term for the material flow; it does not replace the Bernoulli definition of the gravitational force.

A moving-medium trapping horizon for the saturation-fixed transverse photon branch occurs where the inward component of the physical superflow reaches the local branch speed [53,183,184]. In the spherical sector,

$$|\mathbf{v}_\phi(r_H)| = c \tag{239}$$

is simultaneously the DDF material characteristic condition and the PG river condition represented geometrically in the Schwarzschild benchmark.

Universality of free fall (operational WEP).

Because the Bernoulli force enters as $\mathbf{F}_B = m\,\mathbf{g}_\phi$ with

$$\mathbf{g}_\phi \;\equiv\; -\frac{\boldsymbol{\nabla}P_\phi}{\varrho_{\phi,0}}\,, \tag{240}$$

the test-body acceleration is composition independent at leading order, reproducing the operational weak equivalence principle in the same sense probed by Eötvös- and MICROSCOPE-type experiments [167,169].

11. DDF Bernoulli/PG Representations of Standard Gravitational Benchmarks

11.1. Schwarzschild Benchmark: Spherical DDF Exterior and PG River Representation

The Schwarzschild exterior is the spherical benchmark in which the PG river has a direct material realization as the coarse-grained ϕ superflow generated by the source's persistent quantized-vortex population. Under $\mathbf{v}_{\mathrm{PG}} \overset{\mathrm{DDF}}{\longleftrightarrow} \mathbf{v}_\phi$, the GR line element geometrically encodes the same velocity profile obtained from the DDF Bernoulli field:

$$\begin{aligned} ds^2_{\mathrm{GR,map}} &= -\Big(c^2 - v_\phi^2(r)\Big)dt^2 - 2\,v_\phi(r)\,dr\,dt \\ &\quad + dr^2 + r^2 d\Omega^2 \\ &= -c^2dt^2 + \big(dr - v_\phi(r)\,dt\big)^2 + r^2 d\Omega^2. \end{aligned} \tag{241}$$

© 2026 by the author(s). Distributed under a Creative Commons CC BY license.

Preprints.org (www.preprints.org) | NOT PEER-REVIEWED | Posted: 7 September 2026 doi:10.20944/preprints202608.2283.v2

with $\mathbf{v}_\phi(r) = v_\phi(r)\,\mathbf{e}_r$.

Source-free exterior in PG variables ("vacuum" in the GR correspondence).

In the exterior region (outside the compact support of the *coarse-grained quantized-vortex sources*), one sets $T^{(\mathrm{eff})}_{\mu\nu} \simeq 0$ in the PG-form correspondence equation of Sec. 10.4,

$$G_{\mu\nu}\Big[g^{(\mathrm{PG})}_{\alpha\beta}(\mathbf{v}_\phi)\Big] = 0. \tag{242}$$

Here $T^{(\mathrm{eff})}_{\mu\nu} \simeq 0$ means *source-free with respect to the active tensor* defined in the river split of Sec. 10.3: the split fields built from $T^{(\mathrm{eff})}_{\mu\nu}$ vanish outside the compact body,

$$\rho_{\mathrm{eff}} \simeq 0, \qquad (S_{\mathrm{eff}})_i \simeq 0, \qquad (S_{\mathrm{eff}})_{ij} \simeq 0,$$

where ρ_{eff} denotes the effective active energy density in the GR split, not the background ϕ-sector density ϱ_ϕ. The material fields P_ϕ, Φ_ϕ, and $\mathbf{v}_\phi$ remain nontrivial in this active-source-free exterior and are sustained by boundary data and the many-vortex state. Their number-current consistency is governed by Eq. (212). Propagating on-shell transverse φ modes remain passive test excitations: they do not enter $T^{(\mathrm{eff})}_{\mu\nu}$ and propagate through the same physical $\mathbf{v}_\phi$ background.

The exterior solution is therefore fixed by the conserved monopole charge carried by the compact quantized-vortex population. Using the river energy density $\rho_{\mathrm{eff}} \equiv T^{(\mathrm{eff})}_{\mu\nu} n^\mu n^\nu$ (Sec. 10.3), one may define the corresponding inertial/gravitating mass bookkeeping variable as

$$\begin{aligned} M &\equiv \int d^3x\, \rho_M(\mathbf{x}) = \frac{1}{c^2}\int d^3x\, \rho_{\mathrm{eff}}(\mathbf{x}), \\ \rho_M &\equiv \frac{\rho_{\mathrm{eff}}}{c^2}. \end{aligned} \tag{243}$$

Thus, M is the integrated quantized-vortex energy content expressed in mass units via the calibration $E_\varphi(0) = mc^2$ (Sec. 4.3).

Gauss-law form in the spherical exterior.

For a stationary spherically symmetric exterior, the same coarse-grained field may be written in Newton–Gauss form as

$$\oint_{S_r} \mathbf{g}_\phi \cdot d\mathbf{S} = -4\pi G_\phi M, \tag{244}$$

so that

$$\mathbf{g}_\phi(r) = -\frac{G_\phi M}{r^2}\mathbf{e}_r, \qquad -\frac{1}{\varrho_{\phi,0}}\frac{dP_\phi}{dr} = -\frac{G_\phi M}{r^2}. \tag{245}$$

This is the spherical-flux form of Bernoulli gravity in the ϕ medium.

Bernoulli potential and physical river profile.

For the stationary spherical flow, Eq. (218) reduces at leading order to the irrotational Bernoulli relation

$$\Phi_\phi(r) = -\frac{v_\phi^2(r)}{2}. \tag{246}$$

Using the macroscopic exterior normalization

$$\Phi_\phi(r) = -\frac{G_\phi M}{r} \tag{247}$$

© 2026 by the author(s). Distributed under a Creative Commons CC BY license.

Preprints.org (www.preprints.org) | NOT PEER-REVIEWED | Posted: 7 September 2026 doi:10.20944/preprints202608.2283.v2

gives

$$\begin{aligned}\mathbf{v}_\phi(r) &= -\sqrt{\frac{2G_\phi M}{r}}\,\mathbf{e}_r,\\ \mathbf{g}_\phi(r) &= -\frac{G_\phi M}{r^2}\,\mathbf{e}_r.\end{aligned} \tag{248}$$

The first line is a physical coarse-grained superflow, not the current of an isolated vortex. Exact number conservation is satisfied by

$$4\pi r^2\left[\bar{n}_\phi v_{\phi,r} + J^{\mathrm{corr}}_{\phi,r}\right] = \mathcal{F}_\phi, \tag{249}$$

as already derived in Eq. (213). For the nonaccreting exterior, the correlated many-vortex countercurrent balances the mean inward contribution according to Eq. (214).

Identification with the Schwarzschild PG river.

The Schwarzschild vacuum solution has

$$v_{\mathrm{PG}}(r) = -\sqrt{\frac{2GM}{r}}. \tag{250}$$

Equation (248) has exactly the same functional profile with $G \to G_\phi$. Within the DDF ontology this is not merely a numerical analogy: the PG river is the geometric representation of the coarse-grained material ϕ superflow. The combination v^2/c^2 entering the PG coefficients is therefore the geometric encoding of the physical Bernoulli enthalpy perturbation $\Phi_\phi = \Delta P_\phi/\varrho_{\phi,0}$.

11.2. Rotating Sources: Kerr/Lense–Thirring Benchmark from the Coarse-Grained Vortex Flow

For a rotating source the macroscopic ϕ flow inherits vorticity from the unresolved quantized-vortex population. A microscopic flow is locally a phase gradient away from vortex cores, but coarse-graining the full circulation gives

$$\boldsymbol{\omega}_\phi \equiv \boldsymbol{\nabla}\times\mathbf{v}_\phi = \kappa_\phi \overline{\sum_j n_j \int ds\; \delta_\xi\big(\mathbf{r}-\mathbf{R}_j(s)\big)\hat{\mathbf{t}}_j(s)}^{\,\ell}, \tag{251}$$

where the overbar denotes averaging on scales larger than the individual vortex cores. Hence a nonzero smooth macroscopic vorticity is compatible with quantized microscopic circulation.

Stationary axisymmetric material flow.

Decompose the physical coarse-grained superflow into the spherical monopole part and the leading angular-momentum contribution,

$$\mathbf{v}_\phi(\mathbf{r}) \;=\; v_{\phi,\mathrm{in}}(r)\,\mathbf{e}_r \;+\; \mathbf{v}_{\phi,\mathrm{swirl}}(\mathbf{r}), \qquad \boldsymbol{\nabla}\cdot\mathbf{v}_{\phi,\mathrm{swirl}} = 0. \tag{252}$$

In the corresponding generalized PG/Doran/Natário representation write $\mathbf{v}_{\mathrm{PG}} = v_{\mathrm{PG,in}}\mathbf{e}_r + v_{\mathrm{PG},\blacksquare}\mathbf{e}_\psi$. The GR-side line element is

$$\begin{aligned}ds^2_{\mathrm{GR}} = &-\Big(c^2 - v^2_{\mathrm{PG,in}}(r) - v^2_{\mathrm{PG},\blacksquare}(r,\theta)\Big)dt^2\\ &- 2v_{\mathrm{PG,in}}(r)\,dr\,dt\\ &- 2r\sin\theta\, v_{\mathrm{PG},\blacksquare}(r,\theta)\,d\psi\,dt\\ &+ dr^2 + r^2 d\theta^2 + r^2\sin^2\theta\, d\psi^2.\end{aligned} \tag{253}$$

The DDF identification is $v_{\mathrm{PG,in}} \leftrightarrow v_{\phi,\mathrm{in}}$ and $v_{\mathrm{PG},\blacksquare} \leftrightarrow v_{\phi,\psi}$. The metric expression is the GR encoding; the underlying DDF variables are the material velocity, enthalpy, conserved current, and vortex/correlation stresses.

© 2026 by the author(s). Distributed under a Creative Commons CC BY license.

Preprints.org (www.preprints.org) | NOT PEER-REVIEWED | Posted: 7 September 2026 doi:10.20944/preprints202608.2283.v2

The inward term follows from the spherical Bernoulli solution,

$$v_{\phi,\mathrm{in}}(r) \;=\; -\sqrt{\frac{2\,G_\phi M}{r}} \qquad (r \gg r_s), \tag{254}$$

with M the integrated quantized-vortex energy content expressed in mass units (Eq. (243)). Its stationary number-current balance is supplied by Eq. (213).

Angular-momentum flow and the role of $T_{0i}^{(\mathrm{eff})}$ / S_i^{eff}.

On the GR representation side, the ADM shift sector is associated with source momentum density. The corresponding bookkeeping quantity is

$$(S^{\mathrm{eff}})_\mu \;\equiv\; -\gamma_{\mu\alpha}\, T^{(\mathrm{eff})\,\alpha\beta}\, n_\beta, \qquad (S^{\mathrm{eff}})_\mu n^\mu = 0, \tag{255}$$

whose spatial components reduce in the weak-field bookkeeping to momentum density. In DDF, $T_{\mu\nu}^{(\mathrm{eff})}$ represents the persistent quantized-vortex sources and bound configurational stresses; propagating on-shell transverse φ modes remain passive test excitations.

Although the exterior is source-free in this active sense, the rotating state is selected by the conserved angular-momentum multipole of the interior vortex current,

$$\mathbf{J} \;\propto\; \int d^3x\; \mathbf{r} \times \mathbf{S}^{\mathrm{eff}}(\mathbf{x}). \tag{256}$$

The leading stationary axisymmetric coarse-grained vortex flow has the dipolar rotlet structure

$$\begin{aligned} \mathbf{v}_{\phi,\mathrm{swirl}}(\mathbf{r}) &= \Gamma_{\mathrm{rot}}\, \frac{\mathbf{J}\times\mathbf{r}}{r^3} \;+\; \mathcal{O}(r^{-4}), \\ \Gamma_{\mathrm{rot}} &= \frac{2\,G_\phi}{c^2}. \end{aligned} \tag{257}$$

Choosing the polar axis along $\mathbf{J} = J\mathbf{e}_z$ gives

$$v_{\phi,\psi}(r,\theta) = \frac{2G_\phi}{c^2}\,\frac{J}{r^2}\,\sin\theta + \mathcal{O}(r^{-3}). \tag{258}$$

The PG representation then has

$$\begin{aligned} [dt\,d\psi]^{\mathrm{GR,map}}_{\mathrm{coeff}} &= -\,2r\sin\theta\, v_{\phi,\psi} \\ &= -\,\frac{4G_\phi J}{c^2 r}\,\sin^2\theta + \mathcal{O}(r^{-2}), \end{aligned} \tag{259}$$

and hence

$$g_{t\psi}^{\mathrm{GR,map}} = -\,r\sin\theta\, v_{\phi,\psi} = -\,\frac{2G_\phi J}{c^2 r}\,\sin^2\theta + \mathcal{O}(r^{-2}). \tag{260}$$

Thus the physical coarse-grained DDF flow has the leading Lense–Thirring coefficient when expressed in the conventional $(G_\phi, \mathbf{J})$ source units. The associated angular drift is

$$\Omega_{\mathrm{drag}}(r,\theta) \equiv \frac{\mathbf{v}_{\phi,\mathrm{swirl}}\cdot\mathbf{e}_\psi}{r\sin\theta} = \frac{2G_\phi}{c^2}\,\frac{|\mathbf{J}|}{r^3} + \mathcal{O}(r^{-4}), \tag{261}$$

and its curl is

$$\boldsymbol{\omega}_\phi = \boldsymbol{\nabla}\times\mathbf{v}_{\phi,\mathrm{swirl}} = \frac{2G_\phi}{c^2}\,\frac{3\hat{\mathbf{r}}(\hat{\mathbf{r}}\cdot\mathbf{J}) - \mathbf{J}}{r^3} + \mathcal{O}(r^{-4}), \tag{262}$$

which is the Kerr/Lense–Thirring far-field pattern expressed as a material coarse-grained vorticity of the ϕ superflow [185–188].

© 2026 by the author(s). Distributed under a Creative Commons CC BY license.

Preprints.org (www.preprints.org) | NOT PEER-REVIEWED | Posted: 7 September 2026 doi:10.20944/preprints202608.2283.v2

Coarse-grained Euler balance.

The Bernoulli force remains $\mathbf{g}_\phi = -\boldsymbol{\nabla}\Phi_\phi$, while the rotating material flow obeys

$$\partial_t \mathbf{v}_\phi + (\mathbf{v}_\phi \cdot \boldsymbol{\nabla})\mathbf{v}_\phi = \mathbf{g}_\phi - \frac{1}{\varrho_{\phi,0}} \boldsymbol{\nabla} \cdot \boldsymbol{\Pi}_\phi^{\mathrm{corr}}. \tag{263}$$

Using

$$(\mathbf{v}_\phi \cdot \boldsymbol{\nabla})\mathbf{v}_\phi = \boldsymbol{\nabla}\left(\frac{v_\phi^2}{2}\right) - \mathbf{v}_\phi \times (\boldsymbol{\nabla} \times \mathbf{v}_\phi), \tag{264}$$

shows how the rotating many-vortex state differs from a purely irrotational single-phase flow. The Bernoulli enthalpy supplies the gravitational force, while the divergence of the coarse-grained vortex/correlation stress supplies the internal non-potential balance required for the rotating material river. No violation of microscopic quantization is involved: the smooth macroscopic vorticity is the average of the singular quantized circulation carried by the underlying vortex-particles.

Component form of the Bernoulli field.

For later use, the potential contribution is

$$-\boldsymbol{\nabla}\Phi_\phi = -\frac{\partial \Phi_\phi}{\partial r}\mathbf{e}_r - \frac{1}{r}\frac{\partial \Phi_\phi}{\partial \theta}\mathbf{e}_\theta - \frac{1}{r\sin\theta}\frac{\partial \Phi_\phi}{\partial \psi}\mathbf{e}_\psi. \tag{265}$$

For a nonrotating spherical exterior the correlation-stress divergence has no leading transverse component and this reduces to the ordinary Bernoulli field. For rotating sources, Φ_ϕ and $\boldsymbol{\Pi}_\phi^{\mathrm{corr}}$ are jointly fixed by the same coarse-grained vortex boundary-value problem.

Remark on density variations.

Where the ϕ medium may not be treated as strictly incompressible, the pressure–gradient law is written in its general barotropic form

$$\begin{aligned} \mathbf{g}_\phi &= -\frac{1}{\varrho_\phi}\boldsymbol{\nabla} P_\phi \equiv -\boldsymbol{\nabla}\Phi_\phi, \\ \Phi_\phi(P) &\equiv h_\phi(P) - h_\phi(P_{\phi,\infty}) = \int_{P_{\phi,\infty}}^{P} \frac{dP'}{\varrho_\phi(P')}. \end{aligned} \tag{266}$$

For $\varrho_\phi \simeq \varrho_{\phi,0}$, this reduces to $\Phi_\phi = \Delta P_\phi / \varrho_{\phi,0}$. This refinement is used in the isothermal outer-regime applications (Sec. 13).

Interpretation.

The enthalpy-derived monopole flow together with the dipolar vortex/source-current swirl fixed by $\mathbf{J}$ reproduces the leading Kerr/Lense–Thirring coefficient in its PG representation. The physical DDF acceleration follows from the coupled Bernoulli and correlation-stress balance, while the full particle-number current is conserved through Eq. (212). Thus the rotating PG river and the coarse-grained material ϕ flow are two descriptions of the same macroscopic solution.

11.3. Charged Sources: DDF Exterior and Reissner–Nordstr Öm Benchmark

A charged DDF source combines its persistent quantized-vortex monopole content with a long-lived bound transverse-shear configuration of φ. The bound field contributes to $T_{\mu\nu}^{(\mathrm{eff})}$, whereas freely propagating on-shell photons do not. This is the material counterpart of the GR electrovac benchmark [189–193].

© 2026 by the author(s). Distributed under a Creative Commons CC BY license.

Preprints.org (www.preprints.org) | NOT PEER-REVIEWED | Posted: 7 September 2026 doi:10.20944/preprints202608.2283.v2

DDF charge variable and its units (and DDF Coulomb law).

The source-free Maxwell-form construction of Sec. 4.2 reserves $\mathbf{u}_1$ and $\mathbf{u}_2$ for the two linked, divergence-free fields of the on-shell transverse photon. A static electric field belongs instead to the bound, off-shell sector. Introduce therefore a distinct velocity-like bound field $\mathbf{u}_\mathrm{b}$, representing the organized/grouped φ configuration associated with a stationary charge. In the electrostatic sector it is longitudinal,

$$\mathbf{u}_\mathrm{b} = -\boldsymbol{\nabla}\Phi_\varphi, \qquad \boldsymbol{\nabla}\times\mathbf{u}_\mathrm{b} = 0, \tag{267}$$

and it is not required to satisfy the on-shell photon dispersion $\omega = ck$. For a stable charged vortex configuration, the DDF-native charge parameter is defined by its Gauss flux,

$$\begin{aligned} Q_\varphi &\equiv \oint_{S^2} \varrho_\varphi^{\max}\, \mathbf{u}_\mathrm{b}\cdot d\mathbf{A} \\ &= \int d^3x\, \rho_\mathrm{ch}, \\ \boldsymbol{\nabla}\cdot\mathbf{u}_\mathrm{b} &= \frac{\rho_\mathrm{ch}}{\varrho_\varphi^{\max}}. \end{aligned} \tag{268}$$

Because $\varrho_\varphi^{\max}$ has units $\mathrm{kg\,m^{-3}}$, one has

$$[Q_\varphi] = [\varrho_\varphi^{\max} u_\mathrm{b} r^2] = \mathrm{kg\,s^{-1}},$$

i.e. Q_φ is a *mass-flow-rate-like* flux quantity in the native hydrodynamic variables. This is not a unit inconsistency: the DDF field used for static electric sourcing has velocity-like units, while laboratory SI charge is obtained through the operational map below. The usual Coulomb prefactor is correspondingly replaced by the DDF constitutive scale $\varrho_\varphi^{\max}$. For a stationary isolated charge, spherical symmetry implies

$$\begin{aligned} \mathbf{u}_\mathrm{b}(r) &= \frac{Q_\varphi}{4\pi\varrho_\varphi^{\max}}\frac{\mathbf{e}_r}{r^2} \\ \Phi_\varphi(r) &= \frac{Q_\varphi}{4\pi\varrho_\varphi^{\max}}\frac{1}{r} \\ \mathbf{u}_\mathrm{b} &= -\boldsymbol{\nabla}\Phi_\varphi, \end{aligned} \tag{269}$$

so that the analog of the Coulomb force between two static charges is

$$\begin{aligned} \mathbf{F}_{2\leftarrow 1} &= -Q_{\varphi,2}\boldsymbol{\nabla}\Phi_\varphi \\ &= \left(\frac{Q_{\varphi,1}Q_{\varphi,2}}{4\pi\varrho_\varphi^{\max} r^2}\right)\mathbf{e}_r. \end{aligned} \tag{270}$$

To compare with laboratory electrodynamics, one may introduce an *operational* conversion by matching the electrostatic and DDF bound-field energy densities,

$$\begin{aligned} \frac{1}{2}\epsilon_0 E^2 &\equiv \frac{1}{2}\varrho_\varphi^{\max} u_\mathrm{b}^2 \\ \Longrightarrow\ \mathbf{E} &= \sqrt{\frac{\varrho_\varphi^{\max}}{\epsilon_0}}\,\mathbf{u}_\mathrm{b} \\ Q &= \sqrt{\frac{\epsilon_0}{\varrho_\varphi^{\max}}}\,Q_\varphi \end{aligned} \tag{271}$$

where Q is the SI charge, measured in coulombs. In this sense Q_φ is the DDF-native charge parameter and Q its SI-reduced value. This dictionary also clarifies the usual GR/QED statement that electrostatics

© 2026 by the author(s). Distributed under a Creative Commons CC BY license.

Preprints.org (www.preprints.org) | NOT PEER-REVIEWED | Posted: 7 September 2026 doi:10.20944/preprints202608.2283.v2

gravitates: a static Coulomb field corresponds to *off-shell* (bound) field energy, which contributes to inertial and active gravitational bookkeeping (Sec. 9.1). By contrast, propagating on-shell photons are treated as passive φ phonons: they propagate through the physical Bernoulli/carrier background but do not enter $T_{\mu\nu}^{(\mathrm{eff})}$.

Electrostatic exterior field and bound energy density.

For a stationary isolated charge, $\mathbf{u}_2 = \mathbf{0}$. Substituting Eq. (269) into Eq. (63) gives the bound-field energy density

$$\mathcal{E}_{\mathrm{bound}}(r) = \frac{1}{2}\,\varrho_\varphi^{\max} u_{\mathrm{b}}^2 = \frac{Q_\varphi^2}{32\pi^2 \varrho_\varphi^{\max}}\,\frac{1}{r^4}, \tag{272}$$

with the corresponding anisotropic stress generating the familiar Q^2/r^2 correction to the RN lapse/river potential (equivalently a Q^2/r^3 correction to the radial acceleration), as in the GR electrovac benchmark.

RN comparison sector in PG/river form.

On the GR comparison side, the PG line element keeps the river form

$$\begin{aligned} ds^2_{\mathrm{GR,map}} = & -\Big(c^2 - v_\phi^2(r)\Big)dt^2 - 2\,v_\phi(r)\,dr\,dt \\ & + dr^2 + r^2 d\Omega^2. \end{aligned} \tag{273}$$

where the mapped river profile is modified by the electrovac bound stress [194]. The corresponding GR RN lapse function is

$$f_{\mathrm{RN}}(r) = 1 - \frac{2G_\phi M}{c^2 r} + \frac{G_\phi}{c^4}\,\frac{Q_\varphi^2}{4\pi \varrho_\varphi^{\max} r^2}, \tag{274}$$

Using the GR PG identity together with the benchmark map then gives the RN material-flow profile

$$\begin{aligned} v_\phi^2(r) &= \frac{2G_\phi M}{r} - \frac{G_\phi}{c^2}\frac{Q_\varphi^2}{4\pi \varrho_\varphi^{\max} r^2} \\ &= \frac{G_\phi}{r}\left(2M - \frac{Q_\varphi^2}{4\pi}\, j_\varphi^{\min}\frac{1}{r}\right) \end{aligned} \tag{275}$$

where the last equality uses $c^2 = (\varrho_\varphi^{\max} j_\varphi^{\min})^{-1}$. The Q_φ^2/r^2 term has the same sign and radial scaling as in GR: it increases $f(r)$ and therefore reduces the inward superflow speed $|v_\phi|$ relative to the neutral Schwarzschild sector. "Vacuum RN" in this DDF sense means: no exterior defect matter, but a nonzero exterior $T_{\mu\nu}^{(\mathrm{bound})}$ supplied by the stationary, nonradiative φ-sector stress configuration associated with the charged source.

11.4. Charged Rotating Sources: DDF Exterior and Kerr–Newman Benchmark

A rotating charged source is characterized by its active mass M, angular momentum $\mathbf{J}$, and DDF charge Q_φ. Its exterior combines the bound-field modification of the radial Bernoulli/material river flow with the angular-momentum component of the same coarse-grained ϕ superflow; on-shell photons remain passive probes.

River decomposition: RN-modified monopole plus Kerr-like swirl.

In the PG/river dictionary, the physical superflow is decomposed as

$$\mathbf{v}_\phi(\mathbf{r}) = v_{\phi,\mathrm{in}}(r)\,\mathbf{e}_r + \mathbf{v}_{\phi,\mathrm{swirl}}(\mathbf{r}), \qquad \boldsymbol{\nabla}\cdot\mathbf{v}_{\phi,\mathrm{swirl}} = 0, \tag{276}$$

© 2026 by the author(s). Distributed under a Creative Commons CC BY license.

Preprints.org (www.preprints.org) | NOT PEER-REVIEWED | Posted: 7 September 2026 doi:10.20944/preprints202608.2283.v2

where the inward monopole component is set by the charged RN comparison sector,

$$v_{\phi,\mathrm{in}}(r) = -\sqrt{\frac{2G_\phi M}{r} - \frac{G_\phi}{c^2}\frac{Q_\varphi^2}{4\pi\varrho_\varphi^{\max} r^2}}\,, \tag{277}$$

and the leading far-field swirl is fixed by the conserved angular momentum multipole of the active sources, as in the Kerr correspondence (Sec. 11.2),

$$\mathbf{v}_{\phi,\mathrm{swirl}}(\mathbf{r}) = \frac{2G_\phi}{c^2}\frac{\mathbf{J}\times\mathbf{r}}{r^3} + \mathcal{O}(r^{-4}). \tag{278}$$

As in the Kerr sector, $\mathbf{v}_{\phi,\mathrm{swirl}}$ is the exterior angular-momentum component of the physical coarse-grained superflow fixed by $(M,\mathbf{J})$. Charge modifies the radial component through the bound-field contribution but does not alter the leading r^{-3} frame-dragging multipole fixed by $\mathbf{J}$. The complete flow remains subject to the correlated continuity and momentum equations.[2]

Kerr–Newman comparison parameters and candidate DDF trapping data.

On the GR comparison side, the axisymmetric PG/river line element has the form (253). Its mapped radial and azimuthal profiles are compared with $v_{\phi,\mathrm{in}}(r)$ from Eq. (277) and the physical swirl from Eq. (278). In the standard Kerr–Newman parameterization [185,195], one introduces $a \equiv |\mathbf{J}|/(Mc)$ and the usual KN combination

$$\Delta(r) = r^2 - \frac{2G_\phi M}{c^2}\,r + a^2 + \frac{G_\phi}{c^4}\frac{Q_\varphi^2}{4\pi\varrho_\varphi^{\max}}, \tag{279}$$

so the GR PG/DDF horizon radii satisfy $\Delta(r_\pm) = 0$,

$$r_\pm = \frac{G_\phi M}{c^2} \pm \sqrt{\left(\frac{G_\phi M}{c^2}\right)^2 - a^2 - \frac{G_\phi}{c^4}\frac{Q_\varphi^2}{4\pi\varrho_\varphi^{\max}}}\,, \tag{280}$$

as the Kerr–Newman comparison values, with the DDF constitutive replacement $\epsilon_0 \leftrightarrow \varrho_\varphi^{\max}$ (Sec. 4) for the bound-field term. These radii are not independently existing geometric horizons in DDF. The physical trapping surface is reached where the inward coarse-grained superflow attains the saturated transverse speed c, so that outward-propagating φ-phonons can no longer escape. When the DDF strong-field solution reproduces the Kerr–Newman benchmark, this material surface is represented by the corresponding PG/DDF radius.

11.5. DDF Compact-Object Equilibrium and the TOV Benchmark

The exterior correspondences above are complemented by a spherical interior benchmark for a body whose matter is a distributed population of microscopic persistent quantized-vortex configurations and bound energies. The TOV class is used only to compare this active material load with relativistic stellar equilibrium [196,197].

Active interior tensor and spherical reduction.

Assume a static, spherically symmetric coarse-grained interior with

$$T^{(\mathrm{eff})\mu}{}_\nu = \mathrm{diag}\Big(-\varepsilon_{\mathrm{eff}}(r),\, p_r^{\mathrm{eff}}(r),\, p_t^{\mathrm{eff}}(r),\, p_t^{\mathrm{eff}}(r)\Big), \tag{281}$$

[2] A spinning charged body also carries bound electromagnetic angular momentum (magnetostatic sector). In the DDF bookkeeping this contribution is included in $\mathbf{J}$ via the active momentum density $(S^{\mathrm{eff}})_i$ (Sec. 10.3). Any additional Q_φ-dependent corrections to the far-field swirl appear at higher multipole order beyond (278).

© 2026 by the author(s). Distributed under a Creative Commons CC BY license.

Preprints.org (www.preprints.org) | NOT PEER-REVIEWED | Posted: 7 September 2026 doi:10.20944/preprints202608.2283.v2

where $\varepsilon_{\rm eff}$ is the active defect/bound energy density, and $p_r^{\rm eff}$, $p_t^{\rm eff}$ are the radial and tangential active stresses (allowing anisotropy, consistent with the split $p_{\rm eff}, \pi_{ij}$ in Sec. 10.3). Propagating on-shell radiation is not included in (281); it affects signal propagation but not the equilibrium sourcing.

Define the interior mass function (active energy content in mass units)

$$m(r) \equiv \frac{1}{c^2}\int_0^r 4\pi r'^2\,\varepsilon_{\rm eff}(r')\,dr' \qquad \Rightarrow \qquad m(R) = M, \tag{282}$$

where R is the body radius and M matches the exterior monopole parameter of Eq. (243).

TOV-class equilibrium as a benchmark map.

For comparison with the standard relativistic stellar-equilibrium formulas, the mapped DDF active profiles may be inserted into the GR-side equation (235). This gives the TOV structure with $G \to G_\phi$ and with $T^{(\rm eff)}_{\mu\nu}$ understood solely as the comparison representation of the active quantized-vortex and bound-field loads. In particular, for an isotropic effective stress ($p_r^{\rm eff} = p_t^{\rm eff} \equiv p_{\rm eff}$) one obtains

$$\frac{dp_{\rm eff}}{dr} = -\frac{G_\phi}{r^2}\,\frac{\left(\varepsilon_{\rm eff}+p_{\rm eff}\right)\left(m(r)c^2+4\pi r^3 p_{\rm eff}\right)}{c^4\left(1-\dfrac{2G_\phi m(r)}{c^2 r}\right)}. \tag{283}$$

More generally, for anisotropic active stresses one has the usual anisotropic correction term [198],

$$\begin{aligned}\frac{dp_r^{\rm eff}}{dr} = &-\frac{G_\phi}{r^2}\,\frac{\left(\varepsilon_{\rm eff}+p_r^{\rm eff}\right)\left(m(r)c^2+4\pi r^3 p_r^{\rm eff}\right)}{c^4\left(1-\dfrac{2G_\phi m(r)}{c^2 r}\right)}\\ &+\frac{2}{r}\left(p_t^{\rm eff}-p_r^{\rm eff}\right)\end{aligned} \tag{284}$$

Equations (283)–(284) are not DDF field equations. They state the GR benchmark that a DDF compact-object solution must reproduce observationally. The physical DDF interior is determined instead by force balance among the distributed quantized-vortex load, bound-field energy, material stresses, and the stationary ϕ pressure/enthalpy response.

Boundary conditions and matching to the exterior PG shift.

Given an effective equation of state/constitutive closure for the defect medium, $p_{\rm eff} = p_{\rm eff}(\varepsilon_{\rm eff})$ (or its anisotropic generalization), the interior problem is posed by

$$m(0) = 0, \qquad p_r^{\rm eff}(0) = p_c, \qquad \varepsilon_{\rm eff}(0) = \varepsilon_c,$$

and the surface radius R is defined by $p_r^{\rm eff}(R) = 0$. The physical DDF matching conditions impose $m(R) = M$ together with continuity of the relevant pressure, enthalpy, and flow variables. Under the GR comparison map, these conditions correspond to the usual continuity of the PG benchmark data. The exterior DDF flow is fixed by M (and by $Q_\varphi, \mathbf{J}$ if present), while the interior solution determines how that monopole content arises from a distributed quantized-vortex population.

Newtonian limit and the vortex-density interpretation.

In the weak-field limit $2G_\phi m(r)/(c^2 r) \ll 1$ and $p_{\rm eff} \ll \varepsilon_{\rm eff}$, Eq. (283) reduces to hydrostatic balance with the Bernoulli/Poisson closure,

$$\begin{aligned}\frac{dp_{\rm eff}}{dr} &\simeq -\rho_M(r)\frac{G_\phi m(r)}{r^2},\\ m(r) &= 4\pi\int_0^r \rho_M(r')\,r'^2\,dr'\end{aligned} \tag{285}$$

© 2026 by the author(s). Distributed under a Creative Commons CC BY license.

Preprints.org (www.preprints.org) | NOT PEER-REVIEWED | Posted: 7 September 2026 doi:10.20944/preprints202608.2283.v2

where $\rho_M \equiv \varepsilon_{\rm eff}/c^2$ is the coarse-grained quantized-vortex mass density. This makes explicit that the "interior solution" in DDF is naturally formulated in terms of an *interior vortex-density profile* rather than an abstract geometric fluid.

11.6. DDF Weak-Field Observables and the PPN Comparison

The PPN/1PN formalism is used only to organize precision weak-field observables [199–202]. The DDF question is whether its Bernoulli potential, material clocks and rods, and transverse-mode propagation reproduce the measured coefficients.

PG weak-field expansion and identification of the Newtonian potential.

For a stationary irrotational field, the GR-side PG material-flow representation reads

$$ds^2_{\rm GR,map} = -(c^2 - v_\phi^2)\, dt^2 - 2\,\mathbf{v}_\phi \cdot d\mathbf{x}\, dt + d\mathbf{x}^2. \tag{286}$$

In the weak field $v_\phi^2/c^2 \ll 1$ one has

$$g_{tt} = -c^2\left(1 - \frac{v_\phi^2}{c^2}\right), \qquad g_{ti} = -v_{\phi,i}, \qquad g_{ij} = \delta_{ij}. \tag{287}$$

Using the DDF–PG identity $\Phi_\phi = -v_\phi^2/2$ yields

$$g_{tt} \simeq -c^2\left(1 + \frac{2\Phi_\phi}{c^2}\right), \qquad \Phi_\phi(r) \simeq -\frac{G_\phi M}{r}, \tag{288}$$

so the geometric PG variables encode the standard Newtonian coefficient of the DDF Bernoulli field. The physical DDF result remains the force law $\mathbf{g}_\phi = -\boldsymbol{\nabla}\Phi_\phi$.

1PN structure and predictive interface.

To confront high-precision tests (Shapiro delay, perihelion advance, light deflection, LLR, etc.), one expands the GR-side comparison variables to order c^{-4} and compares them with the canonical PPN form. The physical DDF question is whether the next-order corrections generated by the Bernoulli/Euler dynamics and the source constitutive laws, when expressed through the PG representation, yield the required PPN coefficients. Equation (235) organizes the corresponding GR-side bookkeeping for a given source $T^{(\rm eff)}_{\mu\nu}$; it does not generate the DDF corrections. At leading order, the Bernoulli exterior $\Phi_\phi = -G_\phi M/r$ and the associated material-flow profile $v^2_{\phi,\rm in} = 2G_\phi M/r$ already fix the $1/r$ coefficients. When these enthalpy-derived material profiles are written in PG variables, the corresponding Schwarzschild-sector coefficients therefore take their standard GR values, while any deviations would arise only from additional constitutive input (e.g. anisotropic stresses in $T^{(\rm eff)}_{\mu\nu}$ or nontrivial barotropy of ϕ).

Lorentz-violating PPN parameters and operational status.

Local inertial observables are organized by the material four-velocity and the Lorentz-form constitutive interval, so uniform relative motion produces no leading preferred-frame PPN term. The PPN interface tests source-dependent DDF physics: barotropy, anisotropic stresses, flow boundary conditions, and source-structure effects entering $T^{(\rm eff)}_{\mu\nu}$ and the Bernoulli constitutive law. Any nonzero Lorentz-violating PPN coefficient must arise from such additional inhomogeneous material dynamics and is constrained in the usual way.

11.7. Two-body and Many-Body Regime: Weak-Field Superposition in the Active Sector

In the weak-field multi-body regime, the autonomous DDF equations reduce to the linear Bernoulli–Poisson sector. Conventional post-Newtonian notation is used below only to display the scalar and source-current superposition of the active sector.

© 2026 by the author(s). Distributed under a Creative Commons CC BY license.

Preprints.org (www.preprints.org) | NOT PEER-REVIEWED | Posted: 7 September 2026 doi:10.20944/preprints202608.2283.v2

Scalar (monopole) sector.

In the stationary weak-field limit the 00 component reduces to the Bernoulli/Poisson form

$$\nabla^2\Phi_\phi = 4\pi G_\phi \rho_M, \qquad \rho_M \equiv \rho_{\rm eff}/c^2,$$

so for a collection of well-separated compact sources one has the superposed solution

$$\Phi_\phi(\mathbf{x}) \simeq -G_\phi \sum_A \frac{M_A}{|\mathbf{x}-\mathbf{x}_A|} \qquad (|\Phi_\phi|/c^2 \ll 1). \tag{289}$$

The corresponding leading acceleration is $\mathbf{g}_\phi = -\nabla\Phi_\phi$, providing the Newtonian N-body correspondence in the operational variables.

Vector (shift / swirl) sector from active momentum density.

At the same order, the mixed components encode the sourcing of the shift sector by the active momentum density $S_i^{\rm eff}$ (Sec. 10.3). Introducing the standard vector potential associated with the source currents,

$$\mathbf{W}(\mathbf{x}) \;\equiv\; G_\phi \int d^3x' \, \frac{\mathbf{S}^{\rm eff}(\mathbf{x}')}{|\mathbf{x}-\mathbf{x}'|}, \tag{290}$$

the far-field of a slowly rotating body reduces to the dipolar rotlet/swirl found in Sec. 11.2. For a moving two-body system, the same DDF source-current structure is represented in the GR comparison variables by the standard gravitomagnetic corrections (Lense–Thirring / de Sitter precession) at 1PN order [186,203].

Operational meaning and exclusion of on-shell radiation.

In Eqs. (289)–(290) the sources are those in $T_{\mu\nu}^{(\rm eff)}$, i.e. quantized-vortex content and bound (off-shell) field energy. Propagating on-shell φ phonons (photons) are excluded from active sourcing, so they do not enter the right-hand side of the linearized multi-body equations. They nevertheless propagate on the resulting background via the physical coarse-grained superflow $\mathbf{v}_\phi$ and the associated eikonal bending (Sec. 12.2) and redshift (Sec. 12.3).

12. Weak-Field Benchmark Tests in the DDF Framework

12.1. Perihelion Precession in DDF

The additional $1/r^3$ effective-potential term that enters the weak-field Schwarzschild treatment of perihelion precession [202,204] can be assigned a physical origin within the DDF framework. It is not introduced as an external post-Newtonian correction and is not interpreted as a drag or dissipative force. Rather, it is read as the leading conservative coupling between the Solar Bernoulli enthalpy well and the DDF-dressed inertial state of the orbiting body. In this sector the jamming response increases the inertial bookkeeping of orbital motion according to the same γ_φ-dependent kinetic-energy law derived above, while the orbital dynamics remains conservative.

In the macroscopic exterior region the DDF gravitational potential is the specific enthalpy perturbation

$$\Phi_\phi(r) = \frac{\Delta P_\phi(r)}{\varrho_{\phi,0}} = -\frac{\mu_{\rm B}}{r}, \qquad \mu_{\rm B} \equiv G_\phi M_\odot, \tag{291}$$

so that $\mathbf{g}_\phi = -\boldsymbol{\nabla}\Phi_\phi$. For a bound orbit with specific angular momentum $j_{\rm orb}$, the tangential speed in the Sun-centered orbital frame is

$$v_t = r\dot\theta = \frac{j_{\rm orb}}{r}. \tag{292}$$

© 2026 by the author(s). Distributed under a Creative Commons CC BY license.

Preprints.org (www.preprints.org) | NOT PEER-REVIEWED | Posted: 7 September 2026 doi:10.20944/preprints202608.2283.v2

The corresponding first-post-Newtonian DDF inertial fraction is

$$\delta_{\mathrm{J,t}} \equiv 2(\gamma_{\varphi,t} - 1) = \frac{v_t^2}{c^2} + \mathcal{O}\left(\frac{v_t^4}{c^4}\right),$$
$$\gamma_{\varphi,t} = \left(1 - \frac{v_t^2}{c^2}\right)^{-1/2}. \tag{293}$$

Here the factor 2 is the conversion between the leading jamming excess $\gamma_{\varphi,t} - 1 \simeq v_t^2/(2c^2)$ and the dimensionless post-Newtonian inertial fraction v_t^2/c^2. Because $\delta_{\mathrm{J,t}}$ is even in v_t, the associated radial correction has the same sign on both halves of the orbit and therefore belongs to the conservative central dynamics.

As in the standard GR treatment of perihelion precession, the radial dynamics is written at fixed specific angular momentum j_{orb}. At the present effective level, the minimal local scalar coupling between the Bernoulli well and the tangential jamming fraction is adopted as the constitutive closure

$$\delta\Phi_{\mathcal{D}}^{(1\mathrm{PN})}(r) = \delta_{\mathrm{J,t}}\,\Phi_\phi(r) + \mathcal{O}(c^{-4}). \tag{294}$$

This closure reproduces the leading post-Newtonian radial term; a complete DDF derivation must obtain it from the coupled two-sector action rather than treat it as an independently adjustable orbital correction. Using Eqs. (291)–(293), one obtains

$$\delta\Phi_{\mathcal{D}}^{(1\mathrm{PN})}(r) = -\frac{\mu_{\mathrm{B}}}{r}\frac{j_{\mathrm{orb}}^2}{c^2 r^2} = -\frac{\mu_{\mathrm{B}} j_{\mathrm{orb}}^2}{c^2 r^3} + \mathcal{O}(c^{-4}). \tag{295}$$

Thus, after adopting Eq. (294), the $1/r^3$ effective-potential term is obtained from the product of the $1/r$ Solar Bernoulli enthalpy well and the $1/r^2$ tangential inertial fraction. The radial form is therefore fixed algebraically by the closure, not predicted independently of it.

The associated radial acceleration is

$$\delta\mathbf{g}_{\mathcal{D}}^{(1\mathrm{PN})} = -\boldsymbol{\nabla}\delta\Phi_{\mathcal{D}}^{(1\mathrm{PN})} = -\frac{3\mu_{\mathrm{B}} j_{\mathrm{orb}}^2}{c^2 r^4}\,\hat{\mathbf{r}} + \mathcal{O}(c^{-4}). \tag{296}$$

The numerical coefficient 3 is fixed by the radial derivative of the closure-generated r^{-3} enthalpy term. The acceleration is radius-dependent, but its sign is fixed:

$$\delta g_{\mathcal{D},r}^{(1\mathrm{PN})} < 0 \qquad \text{for all } r \text{ in the exterior bound region.} \tag{297}$$

Hence this term is continuously present and always sunward. It is not an alternating radial projection of ordinary viscous drag and it does not remove orbital energy. It is the conservative radial representation of the DDF-dressed inertial correction in the Solar Bernoulli well.

With $u = 1/r$, the central-force Binet equation reads [81]

$$\frac{d^2u}{d\theta^2} + u = -\frac{g_r(r)}{j_{\mathrm{orb}}^2 u^2}. \tag{298}$$

For

$$g_r(r) = -\frac{\mu_{\mathrm{B}}}{r^2} - \frac{3\mu_{\mathrm{B}} j_{\mathrm{orb}}^2}{c^2 r^4}, \tag{299}$$

Eq. (298) becomes

$$\frac{d^2u}{d\theta^2} + u = \frac{\mu_{\mathrm{B}}}{j_{\mathrm{orb}}^2} + \frac{3\mu_{\mathrm{B}}}{c^2}u^2. \tag{300}$$

© 2026 by the author(s). Distributed under a Creative Commons CC BY license.

Preprints.org (www.preprints.org) | NOT PEER-REVIEWED | Posted: 7 September 2026 doi:10.20944/preprints202608.2283.v2

Let

$$p_{\rm orb} \equiv \frac{j_{\rm orb}^2}{\mu_{\rm B}} = a(1-e^2), \qquad u_0(\theta) = \frac{1}{p_{\rm orb}}(1+e\cos\theta) \tag{301}$$

be the unperturbed Keplerian solution. The term proportional to u^2 is treated to first order in $\mu_{\rm B}/(c^2 p_{\rm orb})$. The secular part of the solution is obtained by writing

$$u(\theta) = \frac{1}{p_{\rm orb}}[1+e\cos((1-\kappa)\theta)] + \mathcal{O}(c^{-2})_{\rm nonres}, \tag{302}$$

where $\mathcal{O}(c^{-2})_{\rm nonres}$ denotes bounded constant and higher-harmonic corrections that renormalize the orbital elements but do not determine the apsidal drift.

Substituting Eq. (302) into the left-hand side of Eq. (300) and expanding to first order in κ gives the resonant contribution

$$\frac{d^2u}{d\theta^2} + u = \frac{1}{p_{\rm orb}} + \frac{2\kappa e}{p_{\rm orb}}\cos((1-\kappa)\theta) + \mathcal{O}(\kappa^2). \tag{303}$$

On the right-hand side of Eq. (300), the resonant part is

$$\frac{\mu_{\rm B}}{j_{\rm orb}^2} + \frac{3\mu_{\rm B}}{c^2}u^2 = \frac{1}{p_{\rm orb}} + \frac{6\mu_{\rm B}e}{c^2 p_{\rm orb}^2}\cos((1-\kappa)\theta) + \mathcal{O}_{\rm nonres}(c^{-2}). \tag{304}$$

Equating the resonant coefficients yields

$$\frac{2\kappa e}{p_{\rm orb}} = \frac{6\mu_{\rm B}e}{c^2 p_{\rm orb}^2}, \qquad \Rightarrow \qquad \kappa = \frac{3\mu_{\rm B}}{c^2 p_{\rm orb}}. \tag{305}$$

Thus the precession parameter is determined by the resonant part of the DDF-corrected Binet equation, not by an assumed orbital form.

The apsidal advance per revolution is [202,204]

$$\boxed{\Delta\varpi_{\mathcal{D}} = 2\pi\kappa = \frac{6\pi\mu_{\rm B}}{c^2 p_{\rm orb}} = \frac{6\pi G_\phi M_\odot}{c^2 a(1-e^2)}}. \tag{306}$$

In this form the GR $1/r^3$ perihelion term is reinterpreted as a first-post-Newtonian consequence of the stated conservative DDF/PG closure. The Solar Bernoulli pressure well supplies the background $1/r$ enthalpy deficit, while the tangential DDF-dressed inertial fraction supplies the $j_{\rm orb}^2/(c^2r^2)$ factor. Their product yields the conservative $1/r^3$ effective-potential correction and, through its radial gradient, the corresponding sunward r^{-4} acceleration. No dissipative drag, area-dependent resistance, or secular loss of orbital energy is introduced in this conservative DDF reconstruction.

12.1.1. Orbital Stability in the DDF Inertial Sector

The existence of a DDF jamming response does not imply an ordinary viscous decay of planetary orbits [81,205]. In this formulation, the jamming factor is not a one-sided drag law and does not introduce an anti-velocity force acting on planets. It is instead the DDF-origin of the relativistic inertial dressing already encoded in Eq. (124),

$$K_{\mathcal{D}} = mc^2[\gamma_\varphi(v) - 1].$$

Thus the velocity-dependent energy assigned to relative motion in material DDF spacetime is not an additional dissipative loss channel. It is the same γ_φ-dependent kinetic-energy bookkeeping that, in the operational description, reproduces the standard relativistic inertial response.

© 2026 by the author(s). Distributed under a Creative Commons CC BY license.

Preprints.org (www.preprints.org) | NOT PEER-REVIEWED | Posted: 7 September 2026 doi:10.20944/preprints202608.2283.v2

For bound Solar-system motion, the DDF correction is therefore absorbed into the conservative orbital dynamics. A planet has, in this reading, a speed-dependent DDF-dressed inertia, but this does not imply secular slowdown. The central Bernoulli/PG field supplies the conservative force required to bend the trajectory, just as the central gravitational field in the standard post-Newtonian treatment supplies the force required for relativistic orbital motion. For nearly circular motion, the force is predominantly transverse to the velocity and changes the direction of the momentum rather than removing kinetic energy. For eccentric motion, kinetic and potential terms are exchanged along the orbit within the same conserved orbital-energy budget.

In the weak-field limit the leading non-Newtonian correction is encoded by the conservative effective-potential term

$$\delta\Phi_{\mathcal{D}}^{(1\mathrm{PN})}(r) = -\frac{\mu_{\mathrm{B}} j_{\mathrm{orb}}^2}{c^2 r^3},$$

which is the DDF/PG representation of the usual Schwarzschild $1/r^3$ post-Newtonian contribution. This term modifies the apsidal dynamics and produces the perihelion advance derived above, but it does not remove orbital energy.

This is why the dilatant character of the DDF does not destabilize planetary orbits. Planetary systems simply evolve with the DDF-dressed relativistic inertial law, in the same operational sense in which GR describes stable post-Newtonian orbits. No additional drag acceleration or secular DDF-induced orbital decay is predicted in the bound-orbit sector.

12.2. Gravitational Lensing as Wave Bending in Pressure Gradients

Light is a transverse φ mode propagating at c relative to its locally saturated carrier, while the physical coarse-grained ϕ superflow enters the moving-medium eikonal relation. In the weak spherical exterior the same material river represented by the Schwarzschild PG shift is $\mathbf{v}_\phi = v_{\phi,\mathrm{in}}(r)\hat{\mathbf{r}}$, with $v_{\phi,\mathrm{in}} < 0$, generated by the Bernoulli potential of the persistent many-vortex source,

$$\begin{aligned} \boldsymbol{\nabla}\Phi_\phi &= \frac{1}{\varrho_\phi}\boldsymbol{\nabla}P_\phi, \\ \Phi_\phi &\simeq \frac{\Delta P_\phi}{\varrho_{\phi,0}} \qquad \text{(nearly incompressible limit)}. \end{aligned}$$

No galaxy- or cluster-centered φ-mass halo is introduced: the ubiquitous dispersed phase supplies the photon carrier but is not an independent active source. The corresponding ray characteristics are

$$(\omega - \mathbf{v}_\phi\cdot\mathbf{k})^2 = c^2k^2, \tag{307}$$

with directional index

$$n_{\mathrm{eff}} = \frac{c}{c - w_\parallel} = \frac{1}{1 - w_\parallel/c}, \qquad w_\parallel \equiv \mathbf{v}_\phi\cdot\hat{\mathbf{k}}. \tag{308}$$

Equation (307) is a benchmark propagation closure. A literal material-advection derivation requires the physical superflow to realize the same local characteristic field; that transport condition is not inferred from the PG map itself. For $|w_\parallel|/c \ll 1$,

$$n_{\mathrm{eff}} = 1 + \frac{w_\parallel}{c} + \frac{w_\parallel^2}{c^2} + \mathcal{O}\left(\frac{w_\parallel^3}{c^3}\right). \tag{309}$$

Along an approximately z-directed ray with transverse impact vector $\mathbf{b}$, $b \equiv |\mathbf{b}|$,

$$w_\parallel = v_{\phi,\mathrm{in}}(r)\frac{z}{r}, \qquad r^2 = b^2 + z^2, \tag{310}$$

© 2026 by the author(s). Distributed under a Creative Commons CC BY license.

Preprints.org (www.preprints.org) | NOT PEER-REVIEWED | Posted: 7 September 2026 doi:10.20944/preprints202608.2283.v2

so the odd term cancels on a symmetric in–out path. Using

$$\frac{1}{2}v_{\phi,\mathrm{in}}^2 + \Phi_\phi = 0, \tag{311}$$

the leading even perturbation is

$$\delta n_{\mathrm{even}} = \frac{w_\parallel^2}{c^2} = \frac{v_{\phi,\mathrm{in}}^2}{c^2}\frac{z^2}{r^2} = -\frac{2\Phi_\phi}{c^2}\frac{z^2}{r^2}. \tag{312}$$

With the standard thin-lens convention $\boldsymbol{\beta} = \boldsymbol{\theta} - (D_{ds}/D_s)\hat{\boldsymbol{\alpha}}$, the DDF deflection is

$$\hat{\boldsymbol{\alpha}} = -\int_{-\infty}^{+\infty} \boldsymbol{\nabla}_\perp \delta n_{\mathrm{even}}\, dz. \tag{313}$$

For $\Phi_\phi = -G_\phi M/r$,

$$\delta n_{\mathrm{even}} = \frac{2G_\phi M z^2}{c^2(b^2+z^2)^{3/2}},$$
$$\boldsymbol{\nabla}_\perp \delta n_{\mathrm{even}} = -\frac{6G_\phi M z^2}{c^2(b^2+z^2)^{5/2}}\,\mathbf{b},$$

and $\int_{-\infty}^{+\infty} z^2(b^2+z^2)^{-5/2}dz = 2/(3b^2)$, giving

$$\hat{\boldsymbol{\alpha}} = \frac{4G_\phi M}{c^2 b^2}\mathbf{b}, \qquad |\hat{\boldsymbol{\alpha}}| = \frac{4G_\phi M}{c^2 b}. \tag{314}$$

Equivalently,

$$|\hat{\boldsymbol{\alpha}}| = -\frac{4\Phi_\phi(b)}{c^2} = \frac{4}{c^2}\frac{|\Delta P_\phi(b)|}{\varrho_{\phi,0}}$$
$$= \boxed{4\,\varrho_\varphi^{\max} f_\varphi^{\min}\frac{|\Delta P_\phi(b)|}{\varrho_{\phi,0}}}. \tag{315}$$

Writing $v_e^2 = 2|\Phi_\phi|$,

$$\boxed{|\hat{\boldsymbol{\alpha}}| \simeq 2\Big(\frac{v_e}{c}\Big)^2 = \frac{4G_\phi M}{c^2 b}}. \tag{316}$$

Thus the standard weak-field coefficient is recovered from the material superflow and its PG representation without introducing an independent physical curvature field. The same coarse-grained velocity enters the photon ray Hamiltonian, while exact number conservation is maintained by the correlated current bridge.

12.2.1. Strong Lensing in the DDF

Strong-lensing phenomenology can arise from cumulative weak-field bending by an extended or asymmetric Bernoulli sink: the ray map may develop critical curves and caustics even when $|\Phi_\phi|/c^2 \ll 1$ [206–208]. The general potential is the specific-enthalpy difference

$$\Phi_\phi(\mathbf{r},t) = h_\phi[P_\phi(\mathbf{r},t)] - h_\phi(P_{\phi,\infty}), \qquad \mathbf{g}_\phi = -\boldsymbol{\nabla}\Phi_\phi,$$

with $\Phi_\phi \simeq \Delta P_\phi/\varrho_{\phi,0}$ in the nearly incompressible limit. The Bernoulli force is $\mathbf{g}_\phi = -\boldsymbol{\nabla}\Phi_\phi$, while the coarse-grained material flow obeys

$$(\mathbf{v}_\phi\cdot\boldsymbol{\nabla})\mathbf{v}_\phi = \mathbf{g}_\phi - \frac{1}{\varrho_{\phi,0}}\boldsymbol{\nabla}\cdot\boldsymbol{\Pi}_\phi^{\mathrm{corr}}, \tag{317}$$

© 2026 by the author(s). Distributed under a Creative Commons CC BY license.

Preprints.org (www.preprints.org) | NOT PEER-REVIEWED | Posted: 7 September 2026 doi:10.20944/preprints202608.2283.v2

together with the correlated continuity law Eq. (212). The PG representation encodes this same macroscopic flow. The moving-medium ray Hamiltonian and wave-vector equation are

$$H(\mathbf{r},\mathbf{k}) = c|\mathbf{k}| + \mathbf{v}_\phi(\mathbf{r})\cdot\mathbf{k} = \omega, \tag{318}$$

$$\frac{d\mathbf{k}}{dt} = -\frac{\partial H}{\partial \mathbf{r}} = -\boldsymbol{\nabla}(\mathbf{v}_\phi\cdot\mathbf{k}). \tag{319}$$

The source-to-image map has intensity

$$I(\mathbf{r}_D) \propto |\det \mathcal{J}|^{-1}, \qquad \mathcal{J}_{ij} = \frac{\partial(\mathbf{r}_D)_i}{\partial b_j},$$

so $\det \mathcal{J} = 0$ defines critical focusing and caustics [209–213]. Spherical symmetry yields a circular critical image for exact alignment; perturbations produce arcs, while rotation and anisotropic pressure profiles may generate multifocal maps. In vortical geometries the Bernoulli relation is applied along streamlines and the full directional index must be retained.

The thin-lens geometry is

$$\boldsymbol{\beta} = \boldsymbol{\theta} - \frac{D_{ds}}{D_s}\hat{\boldsymbol{\alpha}}(\boldsymbol{\theta}). \tag{320}$$

For propagation direction $\hat{\mathbf{s}}$,

$$n_{\rm eff}(\mathbf{r}) = \frac{c}{c - \mathbf{v}_\phi(\mathbf{r})\cdot\hat{\mathbf{s}}}, \tag{321}$$

$$n_{\rm eff} = 1 + \frac{\mathbf{v}_\phi\cdot\hat{\mathbf{s}}}{c} + \left(\frac{\mathbf{v}_\phi\cdot\hat{\mathbf{s}}}{c}\right)^2 + \mathcal{O}\left(\frac{|\mathbf{v}_\phi|^3}{c^3}\right). \tag{322}$$

In the symmetric thin-lens sector the odd term cancels, giving

$$\delta n \simeq \left(\frac{v_{\phi,z}}{c}\right)^2, \qquad v_{\phi,z} \equiv \mathbf{v}_\phi\cdot\hat{\mathbf{z}}, \tag{323}$$

$$\hat{\boldsymbol{\alpha}}(\mathbf{b}) = -\int_{-\infty}^{+\infty} \boldsymbol{\nabla}_\perp \delta n\, dz, \qquad \boldsymbol{\nabla}_\perp = \frac{1}{D_d}\boldsymbol{\nabla}_{\boldsymbol{\theta}}. \tag{324}$$

For the PG-matched symmetric benchmark one may instead adopt the scalar closure

$$\delta n_{\rm PG}(\mathbf{r}) \equiv -\frac{2\Phi_\phi(\mathbf{r})}{c^2}, \tag{325}$$

which yields

$$\begin{aligned}\hat{\boldsymbol{\alpha}}_{\rm PG}(\mathbf{b}) &= \frac{2}{c^2}\int_{-\infty}^{+\infty} \boldsymbol{\nabla}_\perp \Phi_\phi\, dz \\ &= \frac{2}{D_d c^2}\boldsymbol{\nabla}_{\boldsymbol{\theta}} \int_{-\infty}^{+\infty} \Phi_\phi(D_d\boldsymbol{\theta}, z)\, dz.\end{aligned} \tag{326}$$

This scalar closure is not interchangeable with the directional index for general asymmetric or vortical physical flows and should be read as the GR-coefficient benchmark rather than as a derived microscopic advection law. Defining

$$\Psi_{\rm ac}(\boldsymbol{\theta}) \equiv \frac{2D_{ds}}{D_d D_s c^2}\int_{-\infty}^{+\infty} \Phi_\phi(D_d\boldsymbol{\theta}, z)\, dz, \tag{327}$$

one obtains the master equation

$$\boxed{\boldsymbol{\beta} = \boldsymbol{\theta} - \boldsymbol{\nabla}_{\boldsymbol{\theta}}\Psi_{\rm ac}(\boldsymbol{\theta})}. \tag{328}$$

Its roots give image positions; multiple roots generate multiple images, and $\boldsymbol{\beta} = 0$ gives the ring condition. The lens strength is governed by the projected specific-enthalpy potential $\Phi_\phi = \int_{P_{\phi,\infty}}^{P} dP'/\varrho_\phi(P')$, together with the full directional flow projection outside the symmetric reduction.

© 2026 by the author(s). Distributed under a Creative Commons CC BY license.

Preprints.org (www.preprints.org) | NOT PEER-REVIEWED | Posted: 7 September 2026 doi:10.20944/preprints202608.2283.v2

Cluster mergers provide a direct strong-lensing application of this DDF mechanism. Lensing is governed by the dynamically evolved $(\Phi_\phi, \mathbf{v}_\phi)$ fields rather than by an independently transported active-mass halo or by the instantaneous gas-density distribution alone. During a merger, the collisional intracluster gas and the galaxy-associated persistent vortex systems undergo different dynamical evolution, while both contribute to the time-dependent ϕ-sector pressure and superflow fields and their wakes. The resulting projected specific-enthalpy field therefore need not remain centered on the shocked gas, allowing lensing maxima and gas-density maxima to become spatially separated. Coupled time-dependent DDF evolution and ray tracing are required to determine the magnitude, location, and detailed morphology of these offsets for a given merger, rather than to establish their qualitative possibility.

12.3. Gravitational Redshift from the Bernoulli Potential

In the DDF kinematics, proper-time rates are reduced by $\gamma_\varphi^{-1}(v) = \sqrt{1-(v/c)^2}$ (see Eq. (142)). The gravitational clock law [214] is obtained by using the Bernoulli potential defined in Eq. (197).

$$\Phi_\phi(r) = \frac{\Delta P_\phi(r)}{\varrho_{\phi,0}}, \qquad \Phi_\phi(\infty) = 0, \qquad \Phi_\phi(r) < 0. \tag{329}$$

The associated escape-speed parameter is

$$v_e^2(r) = 2\,[\,\Phi_\phi(\infty) - \Phi_\phi(r)\,] = -2\Phi_\phi(r). \tag{330}$$

The DDF gravitational clock law is defined directly by inserting this positive escape-speed parameter into the same proper-time factor,

$$\frac{d\tau_{\mathcal{D}}(r)}{dt_\infty} = \gamma_\varphi^{-1}(v_e(r)) = \sqrt{1-\frac{v_e^2(r)}{c^2}}. \tag{331}$$

Here $v_e(r)$ is the positive Bernoulli-potential parameter entering the DDF time-dilation factor.

Comparing an emitter at r_e and an observer at r_o gives

$$\begin{aligned} 1+z = \frac{f_e}{f_o} &= \frac{\gamma_\varphi(v_e(r_e))}{\gamma_\varphi(v_e(r_o))} \\ &= \sqrt{\frac{1-\dfrac{v_e^2(r_o)}{c^2}}{1-\dfrac{v_e^2(r_e)}{c^2}}}\,. \end{aligned} \tag{332}$$

For a distant observer $r_o \to \infty$, $v_e(r_o) = 0$, and hence

$$1+z = \frac{1}{\sqrt{1+\dfrac{2\Phi_\phi(r_e)}{c^2}}} = \frac{1}{\sqrt{1-\dfrac{2[\Phi_\phi(\infty)-\Phi_\phi(r_e)]}{c^2}}}\,. \tag{333}$$

Because $\Phi_\phi(r_e) < 0$, the denominator is smaller than unity and the shift is a redshift.

Using the pressure-deficit definition of the potential gives

$$\boxed{\begin{aligned} 1+z &= \left[1+\frac{2\,\Delta P_\phi(r_e)}{\varrho_{\phi,0}c^2}\right]^{-1/2} \\ &= \left[1+2\,\Delta P_\phi(r_e)\frac{\varrho_\varphi^{\max}/\varrho_\varphi^{\min}}{\varrho_{\phi,0}}\right]^{-1/2}. \end{aligned}} \tag{334}$$

© 2026 by the author(s). Distributed under a Creative Commons CC BY license.

Preprints.org (www.preprints.org) | NOT PEER-REVIEWED | Posted: 7 September 2026 doi:10.20944/preprints202608.2283.v2

Here $\Delta P_\phi(r_e) < 0$. Substituting the exterior matching $\Phi_\phi(r) = -G_\phi M/r$ gives

$$1 + z = \frac{1}{\sqrt{1 - \dfrac{2G_\phi M}{r_e c^2}}}, \tag{335}$$

which reproduces the Schwarzschild-form gravitational-redshift relation in the spherical exterior. In the weak-field limit,

$$z \simeq \frac{\Phi_\phi(\infty) - \Phi_\phi(r_e)}{c^2} = -\frac{\Phi_\phi(r_e)}{c^2}. \tag{336}$$

12.3.1. GPS Clocks in the DDF Framework

In the DDF picture, the rate of a satellite clock [215,216] is determined by the platform-referenced kinematic response of the φ sector and by the Bernoulli potential of the superfluid ϕ sector generated by the Earth's microscopic quantized-vortex content. Let t_E denote the terrestrial timing-platform coordinate and let u be the satellite speed calibrated relative to that platform. The terrestrial timing standard supplies the comparison coordinate. At the effective factorized level used here, the local timing closure is

$$\frac{d\tau_{\mathcal{D}}(r,u)}{dt_E} = \gamma_\varphi^{-1}(u)\ \gamma_\varphi^{-1}(v_e(r)), \tag{337}$$

where $v_e(r)$ is the escape speed defined by the Bernoulli potential $\Phi_\phi(r)$ of the superfluid ϕ,

$$v_e^2(r) = 2\,[\Phi_\phi(\infty) - \Phi_\phi(r)]. \tag{338}$$

In the weak–field and low–speed regime relevant for GPS orbits, $\gamma_\varphi^{-1}(v) \simeq 1 - v^2/(2c^2)$, so that Eq. (337) becomes

$$\frac{d\tau_{\mathcal{D}}(r,u)}{dt_E} \simeq 1 - \frac{u^2}{2c^2} - \frac{v_e^2(r)}{2c^2} = 1 - \frac{u^2}{2c^2} - \frac{\Phi_\phi(\infty) - \Phi_\phi(r)}{c^2}. \tag{339}$$

For two clocks, one on a satellite at (r_S, u_S) and one on the ground at (r_G, u_G), Eq. (339) gives

$$\boxed{\left(\frac{\Delta\tau_S}{\Delta t_E} - \frac{\Delta\tau_G}{\Delta t_E}\right) \simeq \frac{\Phi_\phi(r_S) - \Phi_\phi(r_G)}{c^2} - \frac{u_S^2 - u_G^2}{2c^2}} \tag{340}$$

as the DDF analog of the post–Newtonian GR timing formula, reproducing the standard GPS corrections as the combined effect of the kinematic DDF response in φ and the Bernoulli potential of ϕ.

12.4. Shapiro Delay from Pressure-Gradient-Induced Path Prolongation

For Shapiro time delay [217,218], the relevant observable is the excess propagation time relative to the same path in the asymptotic DDF background. In geometric acoustics for the advected jammed medium, the eikonal relation

$$(\omega - \mathbf{k}\cdot\mathbf{v}_\phi)^2 = c^2 k^2$$

implies the effective moving-medium index

$$n_{\rm eff}(\mathbf{r}, \hat{\mathbf{s}}) = \frac{c}{c - \mathbf{v}_\phi(\mathbf{r})\cdot\hat{\mathbf{s}}} = 1 + \frac{\mathbf{v}_\phi\cdot\hat{\mathbf{s}}}{c} + \frac{(\mathbf{v}_\phi\cdot\hat{\mathbf{s}})^2}{c^2} + \cdots. \tag{341}$$

© 2026 by the author(s). Distributed under a Creative Commons CC BY license.

Preprints.org (www.preprints.org) | NOT PEER-REVIEWED | Posted: 7 September 2026 doi:10.20944/preprints202608.2283.v2

Along an in–out symmetric path through a stationary exterior field, the term linear in $\mathbf{v}_\phi \cdot \hat{\mathbf{s}}$ is odd and cancels at leading order. In the PG-matched scalar weak-field sector, the accumulated time delay is encoded by the DDF gravitational potential of Sec. 9:

$$\Phi_\phi \equiv \frac{\Delta P_\phi}{\varrho_{\phi,0}}, \qquad \mathbf{g}_\phi = -\boldsymbol{\nabla}\Phi_\phi = -\frac{1}{\varrho_{\phi,0}}\boldsymbol{\nabla} P_\phi. \tag{342}$$

Here $\boldsymbol{\nabla} P_\phi$ determines the local gravitational acceleration, whereas Φ_ϕ determines the accumulated optical time-of-flight effect. The additive constant of P_ϕ, and therefore of Φ_ϕ, is chosen so that

$$\Phi_\phi(\infty) = 0, \qquad \Phi_\phi(r) < 0 \tag{343}$$

inside an attractive Bernoulli pressure well.

The scalar PG index perturbation is

$$\delta n_{\mathrm{PG}}(r) \equiv -\frac{2\Phi_\phi(r)}{c^2} = -\frac{2}{c^2}\frac{\Delta P_\phi(r)}{\varrho_{\phi,0}}. \tag{344}$$

As in the lensing sector, this is an operational scalar closure of the PG correspondence rather than a pointwise identification with the projected quantity $(\mathbf{v}_\phi \cdot \hat{\mathbf{s}})^2/c^2$. A calculation must use either the full direction-dependent moving-medium index or the scalar PG closure consistently; adding both would double count the same matched weak-field optical effect.

The general weak-field path expression is

$$\begin{aligned} \Delta t^{\mathrm{DDF}}_{\mathrm{Shapiro}} &= \frac{1}{c}\int_{\mathrm{path}} \delta n_{\mathrm{PG}}\, ds \\ &= -\frac{2}{c^3}\int_{\mathrm{path}} \Phi_\phi\, ds = -\frac{2}{c^3}\int_{\mathrm{path}} \frac{\Delta P_\phi}{\varrho_{\phi,0}}\, ds. \end{aligned} \tag{345}$$

Equation (345) is the general weak-field DDF path integral. Its practical evaluation requires specification of the propagation path.

For Solar-system and weak-lensing applications, the leading Shapiro term may be evaluated along the unperturbed straight ray. With impact parameter b, $ds \simeq dz$, and $r = \sqrt{b^2 + z^2}$, this gives

$$\Delta t^{\mathrm{DDF}}_{\mathrm{Shapiro}} = -\frac{2}{c^3}\int_{z_A}^{z_B} \Phi_\phi\Big(\sqrt{b^2 + z^2}\Big)\, dz. \tag{346}$$

Equivalently, using $\Phi_\phi = \Delta P_\phi/\varrho_{\phi,0}$,

$$\Delta t^{\mathrm{DDF}}_{\mathrm{Shapiro}} = -\frac{2}{c^3}\int_{z_A}^{z_B} \frac{\Delta P_\phi\Big(\sqrt{b^2 + z^2}\Big)}{\varrho_{\phi,0}}\, dz. \tag{347}$$

Equations (346) and (347) are the same relation written in potential and pressure notation, respectively. They are not separate physical assumptions.

Finally, the saturated φ-branch relation

$$c^2 = \frac{1}{\varrho_\varphi^{\max} f_\varphi^{\min}}, \qquad \frac{1}{c^3} = \left(\varrho_\varphi^{\max} f_\varphi^{\min}\right)^{3/2} \tag{348}$$

© 2026 by the author(s). Distributed under a Creative Commons CC BY license.

Preprints.org (www.preprints.org) | NOT PEER-REVIEWED | Posted: 7 September 2026 doi:10.20944/preprints202608.2283.v2

turns the straight-ray result into the native DDF expression

$$\boxed{\begin{aligned}\Delta t^{\mathrm{DDF}}_{\mathrm{Shapiro}} &= -2\left(\varrho_\varphi^{\max} j_\varphi^{\min}\right)^{3/2} \int_{z_A}^{z_B} \Phi_\phi\left(\sqrt{b^2+z^2}\right) dz \\ &= -2\left(\varrho_\varphi^{\max} j_\varphi^{\min}\right)^{3/2} \int_{z_A}^{z_B} \frac{\Delta P_\phi\left(\sqrt{b^2+z^2}\right)}{\varrho_{\phi,0}} dz\end{aligned}}. \tag{349}$$

Since $\Phi_\phi < 0$ in an attractive Bernoulli well, the delay is positive. Equation (349) is the representative DDF result: the delay is expressed through the same gravitational potential and pressure-gradient notation used throughout the paper, together with the transverse sound speed supported by the saturated state of the φ branch.

For comparison with the usual Solar-system notation, the stationary, spherically symmetric exterior solution may be written as

$$\Phi_\phi(r) = \frac{\Delta P_\phi(r)}{\varrho_{\phi,0}} \simeq -\frac{G_\phi M}{r}, \tag{350}$$

where G_ϕ is the emergent macroscopic DDF conversion constant connecting the pressure-gradient field to the conventional (M, r) description in the weak-field exterior.

With Eq. (350), Eq. (346) becomes

$$\Delta t^{\mathrm{DDF}}_{\mathrm{Shapiro}} = \frac{2G_\phi M}{c^3} \int_{z_A}^{z_B} \frac{dz}{\sqrt{b^2+z^2}}. \tag{351}$$

Since

$$\int \frac{dz}{\sqrt{b^2+z^2}} = \ln\left(z + \sqrt{z^2+b^2}\right), \tag{352}$$

one obtains, for $r_A, r_B \gg b$,

$$\Delta t^{\mathrm{DDF}}_{\mathrm{Shapiro}} = \frac{2G_\phi M}{c^3} \ln\left(\frac{4r_A r_B}{b^2}\right). \tag{353}$$

Equation (353) is not a second DDF law. It is only the spherical exterior comparison form of Eq. (349), obtained after the DDF potential is normalized by $\Phi_\phi \simeq -G_\phi M/r$. The physical origin remains the Bernoulli pressure-gradient field in ϕ and the finite transverse propagation speed supported by the saturated state of the φ sector, rather than an independently fundamental curvature field.

13. Galactic Dynamics from Superfluid Isothermality and DDF-Mediated Lensing

Equation (130) describes the DDF reinterpretation of relativistic inertia through the jamming factor of the dispersed φ sector. It is not a MOND-like modification of galactic gravity and not a drag law. Galactic dynamics is instead governed by the Bernoulli acceleration established in the continuous ϕ superfluid,

$$\mathbf{g}_\phi = -\nabla h_\phi = -\frac{\nabla P_\phi}{\varrho_\phi}, \tag{354}$$

in the compressible outer regime, with the nearly incompressible form recovered by replacing ϱ_ϕ with $\varrho_{\phi,0}$.

The principal galactic Bernoulli well is established by the dense rotating central region, with the central black hole or black-hole system (reframed in the DDF approach as a black star or black-star system; see Sec. 14.1) providing its deepest sink. The rotating core, together with the remaining stellar and baryonic distribution of the galaxy, organizes a galaxy-scale pressure and superflow structure in the surrounding continuous ϕ medium. Stars in the disk and spiral arms therefore move within this material Bernoulli field, rather than following geodesic motion in a curved geometric spacetime as in

© 2026 by the author(s). Distributed under a Creative Commons CC BY license.

Preprints.org (www.preprints.org) | NOT PEER-REVIEWED | Posted: 7 September 2026 doi:10.20944/preprints202608.2283.v2

GR. The central core provides the dominant gravitational well, while the surrounding ϕ pressure field continuously mediates its dynamical influence throughout the galaxy.

An illustrative CFD realization of this mechanism is shown in Figure 5: a rotating binary central sink embedded in a continuous fluid medium generates an extended spiral pressure pattern, demonstrating the hydrodynamic route by which the central Bernoulli well can organize galaxy-scale structure.

Toward the outer galactic regions, where the Bernoulli acceleration decreases to the characteristic scale of order $10^{-10}\,\mathrm{m\,s^{-2}}$, the ϕ medium enters the approximately isothermal regime developed below. The resulting pressure–density behavior modifies the radial decline of the Bernoulli acceleration and provides the DDF mechanism for the approximately flat rotation-velocity profiles of spiral galaxies.

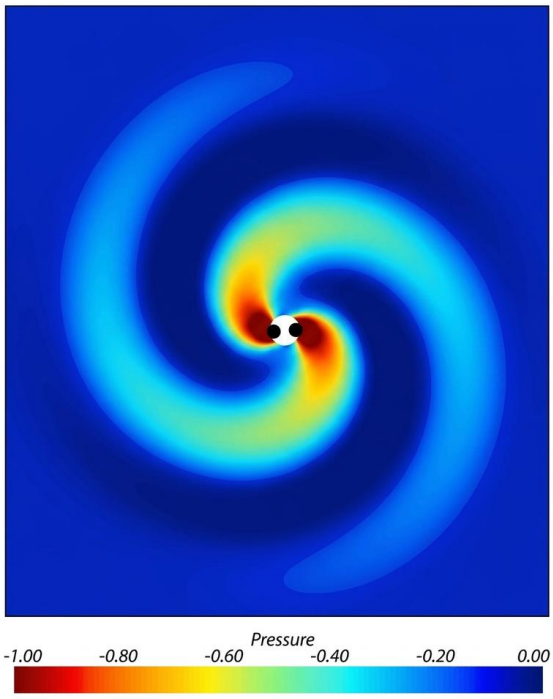


Figure 5. Schematic CFD visualization of a galaxy-like spiral pressure pattern generated hydrodynamically by a rotating binary central sink, representing a black-star pair in the DDF framework. The calculation illustrates how a rotating central sink embedded in a continuous fluid medium can organize an extended spiral structure. The color scale is normalized between the minimum and maximum plotted pressure and represents relative pressure contrast only, not an absolute pressure calibration.

No galaxy-centered φ-mass halo.

The two DDF sectors already pervade the galactic and intergalactic regions. The dispersed φ-quanta are therefore not a distant population that must be gravitationally captured to build a conventional dark-matter halo [219], and their constituent masses do not enter the Bernoulli field equation as an additional active galactic mass density. They remain essential to inertial dressing, dilatancy, and transverse-phonon transport, but not as a separate gravitating halo.

At galactic scales, the active source distribution is supplied by the ordinary material content of the galaxy and by its compact central objects, with the rotating core and especially its black-star component establishing the dominant central Bernoulli sink. The mass distribution, angular momentum, and boundary conditions of the complete galaxy determine the corresponding large-scale pressure and superflow fields of the pre-existing ϕ medium. A useful schematic source–response map is

$$\left\{\varrho_{\mathrm{def}}^{\mathrm{bar}}, \mathbf{J}_{\mathrm{gal}}, \mathcal{B}_{\mathcal{D}}\right\} \longrightarrow \left(\Phi_\phi, \mathbf{v}_\phi, P_\phi\right) \longrightarrow \{v_{\mathrm{circ}}, \hat{\boldsymbol{\alpha}}\}, \tag{355}$$

© 2026 by the author(s). Distributed under a Creative Commons CC BY license.

Preprints.org (www.preprints.org) | NOT PEER-REVIEWED | Posted: 7 September 2026 doi:10.20944/preprints202608.2283.v2

where $\mathcal{B}_{\mathcal{D}}$ denotes the constitutive and outer boundary data of the pre-existing DDF. The same physical DDF solution must therefore determine both the Bernoulli field governing stellar dynamics and the coarse-grained superflow governing photon propagation.

Regime separation: internal and outer regions.

Define the transition radius $r_{\rm iso}$ by

$$|\mathbf{g}_\phi(r_{\rm iso})| \simeq a_{\rm iso},$$

where $a_{\rm iso}$ denotes the empirically motivated order-of-magnitude acceleration scale characterizing the low-acceleration outskirts of disk galaxies, where mass discrepancies and approximately flat rotation profiles become prominent. The observed radial-acceleration phenomenology [39,40] places this scale at order

$$a_{\rm iso} \sim 10^{-10}\,\mathrm{m\,s^{-2}}.$$

The numerical order of magnitude is therefore an observational input, not a DDF prediction or fitted DDF constant. The DDF hypothesis is instead that the ϕ medium approaches its isothermal barotropic response in this empirically identified regime; no universal sharp transition or exact equality with MOND's a_0 is imposed. The two regimes may be represented as

$$\mathbf{g}_\phi(r) = \begin{cases} -\dfrac{\boldsymbol{\nabla} P_\phi(r)}{\varrho_{\phi,0}}, & r < r_{\rm iso} \quad \text{(NI)}, \\ -\dfrac{\boldsymbol{\nabla} P_\phi(r)}{\varrho_\phi(r)}, & r \geq r_{\rm iso} \quad \text{(ISO)}. \end{cases} \tag{356}$$

Here NI denotes the nearly incompressible internal regime, whereas ISO denotes the weakly compressible outer regime.

In the ISO regime define the specific enthalpy

$$h_\phi(P) \equiv \int_{P_{\phi,\infty}}^{P} \frac{dP'}{\varrho_\phi(P')}, \qquad \mathbf{g}_\phi = -\boldsymbol{\nabla} h_\phi. \tag{357}$$

For the isothermal barotrope

$$P_\phi = c_\phi^2 \varrho_\phi, \qquad c_\phi^2 = \left.\frac{\partial P_\phi}{\partial \varrho_\phi}\right|_{\rm iso} = \text{const.}, \tag{358}$$

one obtains

$$\mathbf{g}_\phi(r) = -c_\phi^2 \boldsymbol{\nabla} \ln \varrho_\phi(r), \qquad r \geq r_{\rm iso}. \tag{359}$$

This is a regime-specific coarse-grained closure and does not replace the microscopic Gross–Pitaevskii equation of state outside its domain of validity.

Flat outer rotation curves.

For circular motion in a spherically averaged outer configuration,

$$\begin{aligned} \frac{v^2}{r} &= |g_{\phi,r}| = -\frac{1}{\varrho_\phi}\frac{dP_\phi}{dr} \\ &= -c_\phi^2 \frac{d\ln \varrho_\phi}{dr}, \end{aligned} \tag{360}$$

and hence

$$\frac{d\ln \varrho_\phi}{d\ln r} = -\frac{v^2}{c_\phi^2}. \tag{361}$$

© 2026 by the author(s). Distributed under a Creative Commons CC BY license.

Preprints.org (www.preprints.org) | NOT PEER-REVIEWED | Posted: 7 September 2026 doi:10.20944/preprints202608.2283.v2

If the relaxed outer response approaches

$$\varrho_\phi(r) \propto r^{-q_\rho}, \qquad q_\rho > 0, \tag{362}$$

then

$$v_{\rm flat}^2 = q_\rho c_\phi^2 = \text{const.} \tag{363}$$

The familiar isothermal-sphere benchmark $q_\rho = 2$ gives

$$\varrho_\phi(r) \propto r^{-2}, \qquad v_{\rm flat}^2 = 2c_\phi^2. \tag{364}$$

The value of q_ρ is not fixed by the barotropic equation of state alone; it must emerge from the Bernoulli boundary-value problem generated by the baryonic quantized-vortex distribution, the galactic angular momentum, and the surrounding DDF state. No separately fitted φ-halo density profile is required within this closure.

The resulting outer-profile behavior, together with representative SPARC rotation-curve examples[3], is illustrated in Figure 6.

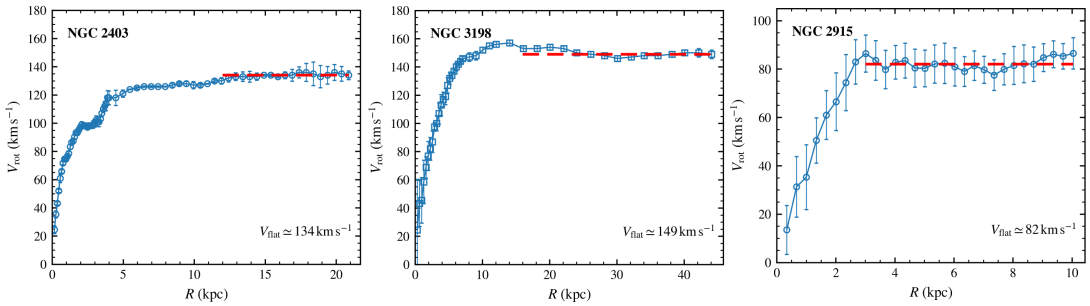


Figure 6. Rotation velocity $v(r)$ flattens when the DDF in the low-acceleration outer region enters the proposed isothermal ϕ-response regime (dashed red visual guides), producing an outer-disk plateau. The dashed guides indicate the observed outer plateau behavior and are not independently fitted DDF rotation curves. Examples for NGC 2403, NGC 3198, and NGC 2915 use data from the SPARC database [40].

DDF-mediated galactic lensing without additional lensing mass.

The same galactic configuration affects light because photons are transverse φ-phonons propagating through the DDF rather than through an empty exterior. For a rotating galaxy the physical coarse-grained superflow may be written schematically

$$\mathbf{v}_\phi = \mathbf{v}_{\phi,\rm in} + \mathbf{v}_{\phi,\rm rot}, \qquad \boldsymbol{\nabla} \times \mathbf{v}_{\phi,\rm rot} \neq 0, \tag{365}$$

where the rotational component can contain the coarse-grained contribution of quantized circulation and is therefore not reducible to the locally curl-free microscopic phase-gradient field $\mathbf{v}_{\phi,\rm mic}$ away from resolved vortex cores. The local eikonal relation is

$$\left(\omega - \mathbf{k}\cdot\mathbf{v}_\phi\right)^2 = c^2k^2, \qquad n_{\rm eff} = \frac{c}{c - \mathbf{v}_\phi \cdot \hat{\mathbf{s}}}, \tag{366}$$

with $\hat{\mathbf{s}}$ the ray direction. Spatial variation of the advection field changes the wave vector along the ray and bends the trajectory, analogously to the refraction of sound by a nonuniform wind.

In the symmetric weak-field PG-matched sector, the same result can be written through

$$\delta n_{\rm PG} = -\frac{2\Phi_\phi}{c^2}, \qquad \hat{\boldsymbol{\alpha}} = \frac{2}{c^2}\int \boldsymbol{\nabla}_\perp \Phi_\phi \, d\ell, \tag{367}$$

[3] For this analysis, galaxy rotation curve data from the SPARC database (Lelli et al., 2016 [40]) were utilized.

© 2026 by the author(s). Distributed under a Creative Commons CC BY license.

Preprints.org (www.preprints.org) | NOT PEER-REVIEWED | Posted: 7 September 2026 doi:10.20944/preprints202608.2283.v2

whereas the full direction-dependent index in Eq. (366) must be retained for a rotating or asymmetric flow. These are the same propagation mechanisms derived in Sec. 12.2.

The DDF itself is therefore the supplementary physical medium present between the stars. Its galactic rotation, inflow, and pressure structure can provide additional photon deflection relative to a baryons-in-empty- vacuum calculation without being reinterpreted as an additional active mass halo. Quantitative viability requires that the ϕ-flow derived from the same baryonic source and constitutive closure reproduce the observed weak- and strong-lensing maps. In observational terms, the object to be reconstructed is the DDF velocity/enthalpy field, not a φ-mass profile.

Relation to MOND's low-acceleration scale.

MOND introduces a modified dynamical relation below

$$a_0 \sim 1.2 \times 10^{-10}\,\mathrm{m\,s^{-2}}$$

[36–38].

The DDF construction does not introduce a MOND interpolation function and does not impose $a_{\mathrm{iso}} = a_0$. The commonality is the observed acceleration scale [39,40]: in galactic outskirts the inferred centripetal acceleration reaches the characteristic $10^{-10}\,\mathrm{m\,s^{-2}}$ regime. In the DDF interpretation, such ultra-low accelerations correspond to a weakly forced outer region of the continuous ϕ superfluid, where the diminishing source-induced perturbation allows the medium to approach local thermal equilibrium and an approximately isothermal state. The physical plausibility of thermalized and isothermal regimes in astrophysical superfluids is independently supported by finite-temperature superfluid-dark-matter studies [220,221]. The numerical value of a_{iso} is therefore not imposed as a microscopic superfluid transition threshold, but identifies the observed galactic regime in which the DDF isothermal closure becomes applicable. MOND modifies the force relation; DDF retains the Bernoulli gravity law, with the flat outer profile arising from the thermodynamic behavior of the weakly perturbed ϕ medium.

For the asymptotic response $\varrho_\phi \propto r^{-q_\rho}$, the equivalent forms are

$$v_{\mathrm{flat}}^2 = \frac{r}{\varrho_\phi}\left|\frac{dP_\phi}{dr}\right| = q_\rho \frac{P_\phi}{\varrho_\phi} = q_\rho c_\phi^2. \tag{368}$$

Thus the galactic fit constrains q_ρ, c_ϕ, and the flow boundary conditions, while lensing constrains the corresponding $(\Phi_\phi, \mathbf{v}_\phi)$ configuration.

Core regularity rather than a halo core–cusp problem.

Because the DDF model contains no galaxy-centered collisionless φ-mass halo, it does not predict an NFW-like φ cusp, and the standard halo core–cusp problem is therefore not transferred to that sector. The relevant central question is instead whether the baryonic source distribution and the nonlinear ϕ-pressure and superflow fields admit a regular, stable galactic solution. High-surface-brightness systems may remain in the nearly incompressible regime over most of their visible extent, whereas dwarf and low-surface-brightness galaxies may enter the approximately isothermal regime at smaller radii.

The DDF galactic closure is therefore jointly constrained by:

(i) the full radial rotation-curve profile, from the internal to the outer galactic region;
(ii) the baryonic radial-acceleration relation;
(iii) the baryonic Tully–Fisher relation, including its asymptotic normalization and scatter;
(iv) the weak- and strong-lensing maps generated by the same $(\Phi_\phi, \mathbf{v}_\phi)$ configuration;
(v) the transition between the nearly incompressible and approximately isothermal regimes, together with the regularity and stability of the central pressure–superflow configuration.

© 2026 by the author(s). Distributed under a Creative Commons CC BY license.

Preprints.org (www.preprints.org) | NOT PEER-REVIEWED | Posted: 7 September 2026 doi:10.20944/preprints202608.2283.v2

The compact galactic closure is therefore

$$\frac{d\ln \varrho_\phi}{d\ln r} = -q_\rho \quad \Longrightarrow \quad v_{\rm flat}^2 = q_\rho c_\phi^2, \tag{369}$$

together with the moving-medium ray equations of Sec. 12.2. Rotation curves and lensing are therefore two observables of the same DDF pressure–superflow configuration, not evidence for two independently added forces or for an additional φ-mass halo.

14. Strong-Field DDF Regimes and GR Benchmark Relations

14.1. Black Holes Reframed as Black Stars

In the DDF framework, the river-model/PG representation is the geometric encoding of the physical coarse-grained ϕ superflow. No autonomous GR metric or curvature field is postulated as an additional physical sector; the compact-object dynamics are governed by the substrate pressure, enthalpy, coarse-grained current, quantized-vortex stresses, and material velocity (Sec. 10).

Interior–exterior viewpoint (connection to the TOV-class interior). A "black star" [222,223] is not defined by an exterior profile alone: the strong-field configuration is a finite object with a nontrivial *interior* active source tensor $T_{\mu\nu}^{(\rm eff)} = T_{\mu\nu}^{(\rm def)} + T_{\mu\nu}^{(\rm bound)}$ supported by a distributed population of microscopic quantized vortices (Sec. 11.5). The interior equilibrium fixes the radial profile of the ϕ enthalpy $h_\phi(r)$ together with the corresponding physical river flow $\mathbf{v}_\phi(r)$. The full current satisfies Eq. (212), with the correlation term determined by the microscopic/coarse-grained boundary conditions of the many-vortex state. The exterior region is "source-free" only in the *active* sense ($T_{\mu\nu}^{(\rm eff)} \simeq 0$ outside the material radius R), so the exterior solution is selected by boundary data at $r = R$ (most importantly the conserved monopole $M = m(R)$) and by the constitutive behavior of the near-surface sheath. Propagating on-shell φ phonons (photons) remain passive probes throughout and do not enter $T_{\mu\nu}^{(\rm eff)}$ (Sec. 10.3 and Sec. 9.1).

For a non-rotating configuration the macroscopic field is the radial Bernoulli (pressure–gradient) acceleration already introduced in Sec. 9,

$$\mathbf{g}_\phi(r) \;=\; -\frac{1}{\varrho_\phi(r)}\,\boldsymbol{\nabla} P_\phi(r) \;\equiv\; -\,\boldsymbol{\nabla} h_\phi(r), \tag{370}$$

where h_ϕ is the ϕ-specific enthalpy,

$$h_\phi(P) \;\equiv\; \int_{P_{\phi,\infty}}^{P} \frac{dP'}{\varrho_\phi(P')}, \qquad h_\phi(P_{\phi,\infty}) = 0. \tag{371}$$

In the far exterior where $\varrho_\phi \simeq \varrho_{\phi,0}$ one may use $h_\phi \simeq \Delta P_\phi/\varrho_{\phi,0} \equiv \Phi_\phi$, but the strong-field region is generically *compressible*, so h_ϕ is the appropriate potential variable.

Bernoulli enthalpy and the river-speed correspondence.

The strong-field DDF quantities are the specific enthalpy $h_\phi(r)$ and the physical radial superflow. Their stationary Bernoulli relation is

$$\frac{v_\phi^2(r)}{2} + h_\phi(r) = 0, \qquad \mathbf{v}_\phi(r) = -\sqrt{-2h_\phi(r)}\,\mathbf{e}_r, \tag{372}$$

with $h_\phi(\infty) = v_\phi(\infty) = 0$. In the interior, $h_\phi(r)$ is not harmonic: its profile is fixed by the active loads and by matching at the material radius $r = R$, which selects the exterior comparison branch through the monopole $M = m(R)$. Equation (372) fixes the mean material river speed; its exact particle-number balance is supplied by the correlated current in Eq. (212), while the strong-field momentum balance includes the corresponding vortex/correlation stress.

© 2026 by the author(s). Distributed under a Creative Commons CC BY license.

Preprints.org (www.preprints.org) | NOT PEER-REVIEWED | Posted: 7 September 2026 doi:10.20944/preprints202608.2283.v2

Observable photon branch and advection by the superfluid.

The dispersed sector may support internal submaximal modes with constitutive speed

$$c_T^2(\mathbf{r}) = \frac{1}{\varrho_\varphi(\mathbf{r}) j_\varphi(\mathbf{r})} \leq c^2, \tag{373}$$

but the observable photon occupies the maximally stiff transverse branch defined in Sec. 4. Its local characteristic speed remains c. The dispersed carrier is advected by the physical ϕ-sector carrier field,

$$\partial_t \varrho_\varphi + \boldsymbol{\nabla} \cdot (\varrho_\varphi \mathbf{v}_\phi) \simeq 0, \tag{374}$$

where $\mathbf{v}_\phi$ is the physical coarse-grained superflow defined in Eq. (3). The local eikonal relation for the photon branch is

$$\left(\omega - \mathbf{k}\cdot\mathbf{v}_\phi\right)^2 = c^2 k^2. \tag{375}$$

Bulk superflow versus motion through the DDF.

The limiting speed c entering the jamming factor constrains the relative motion of a massive localized vortex-supported body *through* the surrounding φ carrier. It does not impose the same bound on the collective background velocity $\mathbf{v}_\phi$, which is a flow *of* the DDF itself. In the gravitational river regime the dispersed quanta are entrained and advected by this flow, $\mathbf{v}_\varphi \simeq \mathbf{v}_\phi$, so a locally comoving material element has

$$v_{\mathrm{rel}}^{\mathrm{jam}} \equiv \left|\mathbf{v}_{\mathrm{body}} - \mathbf{v}_\varphi\right| \simeq 0 \tag{376}$$

even when the magnitude of the coarse-grained river variable $|\mathbf{v}_\phi|$ reaches or exceeds c. This is the distinction between motion through the material carrier, which produces the massive-body jamming asymptote, and collective advection of the carrier itself. Accordingly, $|\mathbf{v}_\phi| > c$ in the strong-field river solution is not a superluminal continuation of the massive-particle branch governed by γ_φ.

Horizon condition.

If the physical superflow solution has a radial inward component, the outward group velocity is $v_g^{(\mathrm{out})} = -|\mathbf{v}_\phi| + c$. A material trapping surface would then occur at

$$\boxed{|\mathbf{v}_\phi(r_H)| = c} \tag{377}$$

and the trapped region satisfies

$$|\mathbf{v}_\phi(r)| \geq c. \tag{378}$$

Outside r_H, outward photon characteristics escape; inside, they are advected inward by the physical superflow. This is a material characteristic condition represented geometrically by the PG river profile. A constitutive failure of the saturated branch near a compact object would suppress or modify the observable photon channel; it is not represented here by assigning photons a variable sub-luminal speed.

Material surface versus trapping surface. Let $r = R$ denote the material radius of the compact object, defined by the interior equilibrium and matching conditions of Sec. 11.5. The trapping surface $r = r_H$ is defined by Eq. (377). In general R and r_H need not coincide: the interior source profile fixes the enthalpy and boundary data, while the physical transport solution determines whether and where an inward superflow reaches the characteristic speed c of the transverse photon branch. The exterior shadow is controlled by r_H, whereas material mass bookkeeping is controlled by R and $M = m(R)$.

Physical picture.

A candidate black star is a finite, strongly stratified configuration whose interior quantized-vortex content and bound loading sustain a strong Bernoulli enthalpy well. If the associated physical

© 2026 by the author(s). Distributed under a Creative Commons CC BY license.

Preprints.org (www.preprints.org) | NOT PEER-REVIEWED | Posted: 7 September 2026 doi:10.20944/preprints202608.2283.v2

superflow develops an inward component reaching c, the outward photon characteristic becomes stationary and is then swept inward. Because curvature is not a DDF variable, the compact-object core is described instead by a finite material interior. Its regularity follows from the proposed quantized-vortex and pressure profiles, not from reducing the local photon speed.

Acoustic Hawking–like emission (thermal channel).

An acoustic horizon at $r = r_H$ (Eq. 377) generically supports near-thermal phonon emission via near-horizon mode conversion, as in laboratory dumb-hole systems [224,225]. The associated "acoustic surface gravity" is

$$\kappa_{\rm ac} \;\equiv\; \partial_n\big(c - v_{\phi,n}\big)\big|_{r_H}, \qquad v_{\phi,n} \;\equiv\; \mathbf{v}_\phi\cdot\hat{\mathbf{n}}, \tag{379}$$

giving a Hawking-like temperature [226,227]

$$T_{\rm BS} \;=\; \frac{\hbar\,|\kappa_{\rm ac}|}{2\pi k_B}\,. \tag{380}$$

For a nonvortical stationary inflow satisfying the Bernoulli first integral, $\mathbf{g}_\phi = -\nabla h_\phi$ gives in spherical symmetry $\partial_r h_\phi = -v_\phi\,\partial_r v_\phi$ and hence $|\mathbf{g}_\phi| = |v_\phi\,\partial_r v_\phi|$. Under this transport realization, $\kappa_{\rm ac}$ is controlled by the gradient of the inward flow and can be related to the local enthalpy-gradient acceleration. The material-flow solution must also satisfy the DDF source and stress closure for this acoustic-emission step.

Treating the horizon as an emitting surface of area $A_H = 4\pi r_H^2$ yields the phenomenological luminosity

$$L_{\rm th} \;=\; \sigma_{{\rm SB},\varphi}\,A_H\,T_{\rm BS}^4, \tag{381}$$

where $\sigma_{{\rm SB},\varphi}$ is the Stefan–Boltzmann-like constant [228] for transverse phonons in the φ medium (model-dependent). Converting radiated power to an effective mass-loss rate uses the same rest-energy factor $c^2 = (\varrho_\varphi^{\max} j_\varphi^{\min})^{-1}$,

$$\dot{M}_{\rm th} \;=\; -\,\frac{L_{\rm th}}{c^2} \;=\; -\,\frac{\sigma_{{\rm SB},\varphi}\,A_H\,T_{\rm BS}^4}{c^2}\,. \tag{382}$$

Overload-induced decoherence (non-thermal channel).

Beyond the thermal leakage, continued accretion can drive the core vortex aggregate into a loss-of-coherence regime. A conservative criterion is the Landau condition [43] in the ϕ branch,

$$\mathrm{Ma}_\phi(r) \;\equiv\; \frac{v_\phi(r)}{c_\phi} \;\gtrsim\; 1, \tag{383}$$

with c_ϕ the longitudinal sound speed of ϕ defined by the hydrodynamic matching in Eq. (8). In this regime, reconnections and turbulent shedding convert coherent vortex structure into (i) transverse φ excitations and (ii) incoherent ϕ-branch excitations (tangle/turbulence [104,229] and low-frequency ϕ waves). A minimal parameterization for the associated non-thermal power is

$$L_{\rm OID} \;\simeq\; \eta_{\rm O}\,A_*\,\varrho_\phi(r_*)\,c_\phi^3\,\Big[\mathrm{Ma}_\phi^2(r_*) - 1\Big]_+, \tag{384}$$

where $A_* \sim 4\pi r_*^2$ is the area of an active shell, $\eta_{\rm O} \in (0,1)$ an effective efficiency for converting overload energy into emitted DDF excitations, and $[\cdot]_+$ the positive part. The corresponding mass-loss rate is

$$\dot{M}_{\rm OID} \;=\; -\,\frac{L_{\rm OID}}{c^2} \;=\; -\,\frac{\eta_{\rm O}\,A_*\,\varrho_\phi(r_*)\,c_\phi^3}{c^2}\,\Big[\mathrm{Ma}_\phi^2(r_*) - 1\Big]_+\,. \tag{385}$$

© 2026 by the author(s). Distributed under a Creative Commons CC BY license.

Preprints.org (www.preprints.org) | NOT PEER-REVIEWED | Posted: 7 September 2026 doi:10.20944/preprints202608.2283.v2

Energy partition and information accounting.

The non-thermal channel need not be dominantly radiative in photons: the released energy can be partitioned between a radiative component in φ and a non-radiative component in the ϕ branch. Introducing a radiative fraction $0 \le f_{\rm rad} \le 1$, one may write

$$\begin{aligned} L_\gamma &= f_{\rm rad}\, L_{\rm OID}, \\ L_\phi^{(\rm nr)} &= \left(1 - f_{\rm rad}\right) L_{\rm OID}. \end{aligned} \tag{386}$$

A Hamiltonian realization of the coupled (ϕ, φ) sectors permits the full microphysical evolution to remain unitary: coherent vortex microstates can be mapped, through reconnections and shear emission, into many-phonon states of φ together with long-wavelength ϕ excitations. The effective hydrodynamic model parameterizes the associated energy partition; a microscopic unitary map supplies the corresponding information accounting [230,231].

Model summary. In the DDF approach, the proposed strong-field alternative to a geometric black hole is a *black star*: a finite material object whose Bernoulli enthalpy well generates an inward ϕ-superflow. When $|\mathbf{v}_\phi(r_H)| = c$ (Eq. 377), outward photon propagation is trapped relative to the external material frame, although transverse φ-phonons continue to propagate locally at their constitutive speed c. The finite material interior thus replaces the classically singular black-hole interior of GR with a nonsingular material configuration.

14.2. LVK-class Transients as Macroscopic Transverse φ-Shear Waves

The Bernoulli inflow advects φ but does not itself provide the transverse shear associated with an LVK signal. The observable long-range channel is instead a macroscopic transverse disturbance of the saturated jammed φ branch; possible compressional ϕ modes lie outside the present scope. When binary or merger shear exceeds $\dot\gamma_\star$, the φ sector reaches its saturated shear response and the corresponding propagation speed is

$$c_g = \sqrt{\frac{G_\varphi^{\max}}{\varrho_\varphi^{\max}}} = \frac{1}{\sqrt{\varrho_\varphi^{\max} j_\varphi^{\min}}} = c. \tag{387}$$

Submaximal excitations do not enter the observable LVK channel. Thus photons and LVK-class disturbances propagate through the same saturated φ-sector speed branch at c, while remaining physically distinct excitations of that sector. This is consistent with GW170817/GRB 170817A and LVK dispersion bounds [25–30].

In a jammed patch, the transverse displacement field $\mathbf{u}(\mathbf{r}, t)$ satisfies the linear shear-wave equation with a quadrupolar mechanical source,

$$\varrho_\varphi^{\max}\, \partial_t^2 \mathbf{u} \;-\; \frac{1}{j_\varphi^{\min}}\, \nabla^2 \mathbf{u} \;=\; \boldsymbol{\nabla}\cdot\boldsymbol{\sigma}_{\rm src}(\mathbf{r}, t), \qquad \omega_{\rm src} \simeq 2\Omega, \tag{388}$$

where Ω is the orbital frequency and $\sigma_{\rm src}$ is the source shear-stress tensor encoding the rotating mass–quadrupole deformation imposed on the medium; its relevant radiative part is the transverse/deviatoric component, not an isotropic pressure perturbation.

Here $\mathbf{u}$ denotes the *solenoidal* (Helmholtz-transverse) displacement component, $\nabla\cdot\mathbf{u} = 0$, corresponding to shear-only transport in the jammed φ patch. Any compressional (longitudinal) component would correspond to bulk compression of the jammed network and is neglected in the LVK channel, both because it is not efficiently sourced by the quadrupolar tidal shear and because LVK data strongly disfavor additional scalar-like polarizations [25,30].

In the far field one obtains

$$u_{+,\times}(R, t) = \frac{\mathcal{A}_{+,\times}(\theta)}{R}\, \cos\Big[2\Omega\big(t - \tfrac{R}{c}\big) + \delta_{+,\times}\Big], \tag{389}$$

© 2026 by the author(s). Distributed under a Creative Commons CC BY license.

Preprints.org (www.preprints.org) | NOT PEER-REVIEWED | Posted: 7 September 2026 doi:10.20944/preprints202608.2283.v2

i.e. two radiative transverse polarizations with the familiar $(1/R,\, 2\Omega)$ structure, but carried by *macroscopic φ-shear* propagating at speed c in the stiff limit. Because both channels access the same saturated φ stiffness scale, the model enforces $c_{\rm GW} = c_\gamma = c$ in their respective propagating regimes. The observed multi-messenger coincidence is therefore a consistency requirement of that common constitutive scale, rather than an independent prediction of the source dynamics.

This assignment is not an additional material species inserted independently of the rest of the theory, but neither is the LVK disturbance identified with a classical electromagnetic wave. The two channels use the same dispersed φ material and the same saturated shear-stiffness scale in different ways. An on-shell photon is a microscopic *coupled* transverse phonon: its free Maxwell-form representation contains the two kinematically linked, reciprocally orthogonal transverse fields $\mathbf{u}_1$ and $\mathbf{u}_2$. The LVK channel is instead a directly driven macroscopic *simple-shear* displacement of the φ medium, represented here by the single solenoidal field $\mathbf{u}$. It is generated when the macroscopic binary stress acts on the dispersed phase as a whole and is not constructed as an ordered sum, coherent state, or coarse-graining of microscopic transverse φ-phonons. The common value c reflects the same limiting ratio of saturated shear stiffness to inertial density, not an identity of the two excitations.

The corresponding $1/R$ far-field amplitude and retarded phase structure are illustrated in Figure 7.

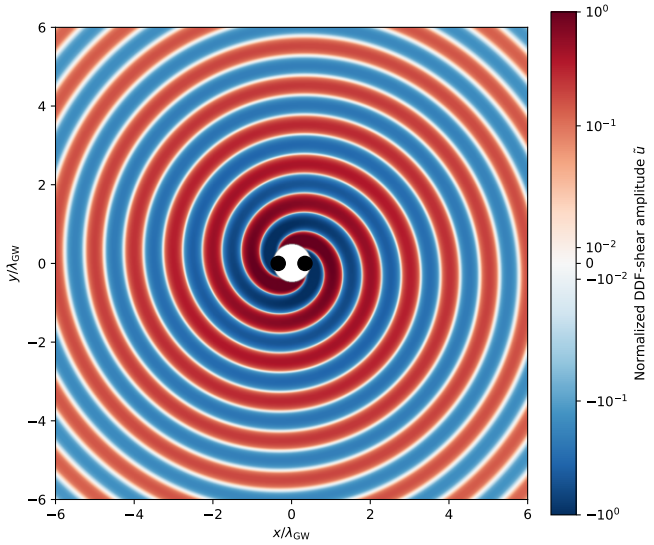


Figure 7. Normalized orbital-plane simulation of a macroscopic transverse φ-shear disturbance generated by a neutron-star or black-star binary. The plotted field is $\tilde{u}(R,\phi,t) \propto R^{-1}\cos(kR - \omega t + 2\phi + \delta)$, $k = \omega/c$, $\omega \simeq 2\Omega$. The combination of the retarded radial phase with the rotating quadrupolar $m = 2$ phase produces the spiral-like instantaneous pattern; for a fixed observer direction, the azimuthal term is absorbed into the polarization phase, recovering the far-field waveform used in the text. In the DDF interpretation, the binary dynamics locally drives the dispersed φ sector into its transient jammed state. This shear-supporting configuration is regenerated as the disturbance propagates, carrying the LVK signal outward at speed c, with far-field amplitude decreasing as R^{-1}. The two black disks indicate the compact binary components, and the color scale represents an arbitrary normalized signed DDF-shear amplitude.

Dispersion constraints (LVK "no dispersion" results).

Ordinary shear waves in soft media disperse because the carrier has dissipation and significant microstructure. In the DDF, the relevant LVK carrier is the locally stiffened/jammed φ network, whose leading-order long-wavelength dispersion is linear,

$$\omega = c\,k \qquad (\text{stiff/jammed limit}), \tag{390}$$

so that $v_g = d\omega/dk = c$ (dispersionless at leading order). Any residual dispersion arises only from higher-gradient corrections suppressed by a microscopic correlation scale ℓ_φ of the jammed network,

$$\omega^2 = c^2k^2\Big[1 + \mathcal{O}\Big((k\ell_\varphi)^2\Big)\Big], \qquad \frac{\Delta v_g}{c} = \mathcal{O}\Big((k\ell_\varphi)^2\Big), \tag{391}$$

© 2026 by the author(s). Distributed under a Creative Commons CC BY license.

Preprints.org (www.preprints.org) | NOT PEER-REVIEWED | Posted: 7 September 2026 doi:10.20944/preprints202608.2283.v2

thus LVK "no-dispersion" results translate in this framework into an upper bound on the microscopic scale ℓ_φ (or, more generally, on the magnitude of higher-gradient corrections), rather than ruling out a transverse-medium carrier in the stiff/jammed limit; equivalently, the LVK band probes the regime $k\ell_\varphi \ll 1$.

Polarization content and the detector-response map.

The LVK observable is the differential arm-length response of an interferometer, which in GR is described by a transverse-traceless rank-two strain. A Helmholtz-transverse displacement vector $\mathbf{u}$ also has two independent polarizations, but the interferometer response depends on how this carrier variable couples to the rank-two material strain measured by the detector. For a plane vector shear wave propagating along $\hat{\mathbf{z}}$,

$$e_{ij} = \frac{1}{2}\left(\partial_i u_j + \partial_j u_i\right) \tag{392}$$

generically produces the shear components e_{xz} and e_{yz}, rather than the transverse-traceless components $e_{xx} = -e_{yy}$ and $e_{xy} = e_{yx}$. The DDF detector sector therefore introduces a microscopic coupling or rank-two collective variable that maps the φ disturbance to the observed tensor antenna pattern. Polarization data directly test this map: the two transverse carrier modes establish the available propagation degrees of freedom, while the material coupling determines whether their measured response is equivalent to the LVK tensor pattern.

Energy flux and detector coupling.

In the saturation-fixed stiff φ branch, the shear-wave energy density and intensity are

$$\mathcal{E} = \frac{1}{2}\varrho_\varphi^{\max}\dot{\mathbf{u}}^2 + \frac{1}{2j_\varphi^{\min}}\left(\boldsymbol{\nabla}\times\mathbf{u}\right)^2, \qquad I = \mathcal{E}c. \tag{393}$$

For a monochromatic transverse plane wave, $\mathbf{u} = \mathbf{U}\cos(\omega t - \mathbf{k}\cdot\mathbf{r})$ with $\omega = ck$, the cycle-averaged intensity scales as

$$\langle I\rangle \propto \varrho_\varphi^{\max}\omega^2 U^2 c. \tag{394}$$

If the source radiates luminosity $L_{\rm src}$, the sphere-averaged radiation-zone flux is

$$\langle I(R)\rangle = \frac{L_{\rm src}}{4\pi R^2}, \tag{395}$$

up to the quadrupolar angular pattern.

The field equations determine propagation, polarization, and flux, but they do not by themselves determine the response of an LVK test mass. That response requires a constitutive coupling between the macroscopic φ-shear and the quantized-vortex structure of ordinary matter. Writing the detector tensor as D^{ij}, the observable strain may be parameterized at leading order by

$$h_{\rm DDF}(t) = \mathcal{C}_{\rm det}\, D^{ij} e_{ij}(t), \tag{396}$$

where $\mathcal{C}_{\rm det}$ is determined by the same microscopic matter–φ coupling used elsewhere in the theory. This coupling is constrained by the observed differential-arm response, its composition independence, and the calibrated amplitude–distance relation. No independent radiation-pressure formula for mirror motion is assumed here.

Interpretation.

LVK-class signals are directly generated macroscopic simple-shear waves of the φ medium, not coherent electromagnetic radiation and not a superposition of on-shell photon quanta. Their mechanical source is the large-scale time-dependent stress of the compact binary, whereas photon emission originates microscopically when vortex-supported charged constituents transfer transition

© 2026 by the author(s). Distributed under a Creative Commons CC BY license.

Preprints.org (www.preprints.org) | NOT PEER-REVIEWED | Posted: 7 September 2026 doi:10.20944/preprints202608.2283.v2

energy to the surrounding φ population and trigger the coupled transverse phonon. The two processes therefore differ in source scale, field organization, and quantum status even though they share the same saturated material stiffness and limiting propagation speed. The quadrupolar source pattern and frequency 2Ω are retained, while the rank-two detector response is carried by the constitutive coupling (396). Possible ϕ-sector relaxation modes are distinct and are not used in these observable claims.

14.2.1. Shear-wave-driven Orbital Decay in Binaries

Compact-binary decay is attributed to radiative energy loss into the macroscopic transverse φ-shear channel, not to along-track drag. The local speed-dependent jamming response remains part of the conservative DDF inertial sector. Above the shear threshold, the outgoing carrier approaches

$$c_T = (\varrho_\varphi j_\varphi)^{-1/2} \longrightarrow c = (\varrho_\varphi^{\max} j_\varphi^{\min})^{-1/2},$$

and its luminosity is the flux through a large sphere,

$$L_{\rm rad} = \int I \, dA = 4\pi R^2 I(R). \tag{397}$$

Effective quadrupole luminosity.

In the stiff regime the φ sector obeys the linear transverse wave equation (388), so the far field contains outgoing macroscopic shear waves at speed c. At the effective isolated-source level, the total active mechanical load is conserved and its first spatial moment follows the center of mass. In the center-of-mass frame one may write

$$\begin{aligned} M_{\rm act} &= \int \rho_{\rm act} \, d^3x = \text{const.}, \\ \mathbf{D}_{\rm act} &= \int \rho_{\rm act} \mathbf{x} \, d^3x = M_{\rm act} \mathbf{X}_{\rm CM}, \qquad \ddot{\mathbf{D}}_{\rm act} = 0. \end{aligned} \tag{398}$$

so the time-dependent monopole and dipole source terms do not radiate for an isolated binary at this order. The leading varying source moment is therefore quadrupolar. This establishes the effective multipole hierarchy but not the absolute source-to-shear conversion coefficient, which remains the calibrated quantity identified below [232,233].

At orbital scale a, binding and orbital kinematics are controlled by the Bernoulli potential. Define the positive effective coupling

$$G_{\rm B}(a) \equiv -\frac{\Delta P_\phi(a)}{\varrho_{\phi,0}} \frac{a}{M} = -\Phi_\phi(a) \frac{a}{M} > 0. \tag{399}$$

In the Newtonian–isothermal exterior, $G_{\rm B} = G_\phi$, and the Kepler scaling is

$$\Omega^2 \simeq G_{\rm B}(a) \frac{M}{a^3}. \tag{400}$$

For a circular binary the relevant quadrupole scale is $Q \sim \mu a^2$, hence $\dddot{Q} \sim \mu a^2 \Omega^3$. Since the far-field energy flux is quadratic in the wave amplitude and scales as $I \propto (\text{amplitude})^2 \, c$, dimensional consistency together with quadrupolar transverse radiation implies

$$L_{\rm rad} \propto \frac{G_{\rm B}(a)}{c^5} (\dddot{Q})^2,$$

up to the usual angular factor associated with two transverse polarizations. Expressing a in terms of Ω then yields the standard $(\mathcal{M}\Omega)^{10/3}$ scaling.

© 2026 by the author(s). Distributed under a Creative Commons CC BY license.

Preprints.org (www.preprints.org) | NOT PEER-REVIEWED | Posted: 7 September 2026 doi:10.20944/preprints202608.2283.v2

Accordingly, the effective DDF quadrupole luminosity is written as $L_{\rm rad} \equiv L_{\rm src}$,

$$L_{\rm src} = \mathcal{C}_Q \left(\varrho_\varphi^{\max} j_\varphi^{\min}\right)^{5/2} G_{\rm B}^{7/3}(a)(\mathcal{M}\Omega)^{10/3}, \tag{401}$$

where Ω is the orbital frequency and $\mathcal{M} = \mu^{3/5} M^{2/5}$ is the chirp mass ($M = m_1 + m_2$, $\mu = m_1 m_2/M$).

The transverse wave equation fixes the propagation law and quadrupolar scaling, whereas its long-wavelength form does not by itself determine the effective binary-to-carrier source coefficient $\mathcal{C}_Q$. At the present level of theory, $\mathcal{C}_Q = 32/5$ is fixed by the observed leading quadrupole normalization. This fixes the radiative amplitude, not the transverse-carrier mechanism or the independently obtained frequency and mass scaling.

In the NI exterior, setting $G_{\rm B} = G$, $\mathcal{C}_Q = 32/5$, and $c^2 = 1/(\varrho_\varphi^{\max} j_\varphi^{\min})$, Eq. (401) reduces algebraically to

$$L_{\rm rad} = \frac{32}{5}\frac{c^5}{G}\left(\frac{G\,\mathcal{M}\,\Omega}{c^3}\right)^{10/3}. \tag{402}$$

This reduction should be read as an important consistency check of the DDF effective radiative channel in the NI exterior, not as a complete microscopic derivation of compact-binary radiation from first principles.

Orbital energy balance and decay law.

For a Keplerian binary in the NI exterior, assuming that $G_{\rm B}(a)$ is effectively constant over the orbital-decay interval,

$$\begin{aligned} E_{\rm orb} &= -\frac{G_{\rm B}(a) m_1 m_2}{2a} \\ &= -\frac{1}{2}\mu [G_{\rm B}(a) M\Omega]^{2/3}. \end{aligned} \tag{403}$$

Radiative loss into transverse φ-shear waves then gives

$$\dot{E}_{\rm orb} = -L_{\rm rad}. \tag{404}$$

Combining Eqs. (401) and (403) yields, for circular orbits,

$$\dot{a} = -2\mathcal{C}_Q \left(\varrho_\varphi^{\max} j_\varphi^{\min}\right)^{5/2} G_{\rm B}^3(a)\frac{\mu M^2}{a^3}, \tag{405}$$

and therefore

$$\boxed{\dot{P}_b = -6\pi \mathcal{C}_Q \left(\varrho_\varphi^{\max} j_\varphi^{\min}\right)^{5/2} [G_{\rm B}(a)\mathcal{M}]^{5/3} \left(\frac{2\pi}{P_b}\right)^{5/3}} \tag{406}$$

For eccentric binaries, the same quadrupolar channel gives

$$\dot{a} = -2\mathcal{C}_Q \left(\varrho_\varphi^{\max} j_\varphi^{\min}\right)^{5/2} G_{\rm B}^3(a)\frac{\mu M^2}{a^3} F(e), \tag{407}$$

with

$$F(e) = \frac{1 + \frac{73}{24}e^2 + \frac{37}{96}e^4}{(1-e^2)^{7/2}}. \tag{408}$$

In the NI exterior, where Eq. (402) applies, these expressions reduce to the standard orbital-decay scalings used in binary-pulsar and inspiral phenomenology. The difference lies in the interpretation of the radiative carrier, not in the leading effective decay law.

© 2026 by the author(s). Distributed under a Creative Commons CC BY license.

Preprints.org (www.preprints.org) | NOT PEER-REVIEWED | Posted: 7 September 2026 doi:10.20944/preprints202608.2283.v2

Numerical check: Hulse–Taylor pulsar.

For PSR B1913+16 one has $m_1 \simeq 1.441\,M_\odot$, $m_2 \simeq 1.387\,M_\odot$, $P_b = 7.751938773864\,\mathrm{hr}$, and $e = 0.6171334$. Using the NI Bernoulli normalization $G_\mathrm{B} = G$ and the observationally fixed effective coefficient $\mathcal{C}_Q = 32/5$, Eq. (406) with the eccentric correction factor $F(e)$ gives

$$\begin{aligned} \dot{P}_b &\approx -2.4 \times 10^{-12}\,\mathrm{s\,s^{-1}}, \\ \Delta P_b &\approx -7.6 \times 10^{-5}\,\mathrm{s\,yr^{-1}} \;=\; -76\,\mu\mathrm{s/yr}, \end{aligned} \tag{409}$$

in numerical agreement with the observed orbital decay of the system [234,235]. Because the effective source coefficient has been fixed by the observed quadrupole normalization, this is a consistency check of the DDF carrier mechanism rather than an independent prediction of the absolute amplitude.

The recovered leading decay law is therefore a consistency result for the transverse-carrier interpretation: its absolute quadrupole normalization is fixed through $\mathcal{C}_Q = 32/5$, while the carrier, propagation law, and energy balance are specified by the DDF constitutive model.

15. Quantum Completion Route for DDF Material Spacetime: Lorentz Kinematics and Bernoulli Gravity

The material-spacetime premise makes a quantum completion a natural continuation of the preceding construction, but the term is used here in a specifically DDF sense. The objective is not to quantize an independently fundamental Einstein metric or to introduce a quantum gravitational force. Rather, it is to determine how the Lorentz-form kinematics and classical Bernoulli gravity developed above arise from the quantum many-body dynamics of the material $\phi + \varphi$ substrate, and to retain explicitly the finite-core and many-body correlation terms beyond the leading coarse-grained limit.

The logical order mirrors the construction of the theory itself. The DDF substrate and its vortex-supported particle states are already quantum at the microscopic level. The first task is therefore to complete the quantum description of the Lorentz-form dressed-vortex branch. The second is to derive the active-source, pressure, and flow observables whose coarse-grained limit produces Bernoulli gravity and its PG/GR comparison map. Propagating φ-shear modes constitute a separate quantum sector and are not identified with quanta of the gravitational force.

15.1. Scope and Departure from Metric-Quantization Programs

The principal approaches conventionally grouped under quantum gravity begin from microscopic assumptions different from those of the DDF. Canonical geometrodynamics and related metric/connection approaches promote gravitational geometric variables to quantum observables [236,237]. Covariant perturbative approaches expand the metric and quantize its spin–2 fluctuations; their ultraviolet structure is represented by the one- and two-loop results and by higher-derivative or low-energy effective-field-theory treatments [31,238–241]. Loop quantum gravity assigns quantum states directly to geometry [32,119–121], while Sakharov-type programs seek to induce an effective gravitational action from underlying quantum degrees of freedom [33,242]. Asymptotic safety instead seeks a nonperturbative ultraviolet completion of metric quantum field theory [34,237,243,244]. Semiclassical and stochastic gravity retain a geometric gravitational field sourced by expectation values and fluctuations of quantum stress–energy [35].

The DDF construction does not assume compliance with any of these routes. Its defining distinctions are:

(i) The metric, Einstein tensor, and PG shift are not independent microscopic DDF fields and are not promoted to fundamental quantum operators.

(ii) Gravity has no elementary quantum in the model. The gravitational interaction is the classical Bernoulli force generated by the specific-enthalpy gradient of the coherent ϕ sector. Its quantum origin lies instead in the quantized circulation and winding, the microscopic density and phase structure, and the many-body state of the material source.

© 2026 by the author(s). Distributed under a Creative Commons CC BY license.

Preprints.org (www.preprints.org) | NOT PEER-REVIEWED | Posted: 7 September 2026 doi:10.20944/preprints202608.2283.v2

(iii) The ϕ and φ bosons are massive, ubiquitous material constituents of an occupied background, but their inertial masses do not by themselves constitute active gravitational charge. Active gravitational sourcing instead arises from the quantized ϕ-vortices that constitute massive particles and from the bound dynamics of their composite configurations, whose circulation generates the ϕ-sector Bernoulli pressure and specific-enthalpy gradients identified with gravity. An isolated vortex produces its microscopic near field, while composite sources generate the corresponding collective or coarse-grained gravitational field.

(iv) Photons and LVK-class signals both involve transverse response of the φ sector but are not the same excitation. A photon is the microscopic coupled transverse phonon of the electromagnetic sector. An LVK-class disturbance is a directly driven macroscopic simple-shear wave produced when strong binary or merger dynamics stress the dispersed medium collectively; it is not constructed as an ordered sum, coherent state, or coarse-graining of microscopic transverse φ-phonons. It is neither a perturbation of a fundamental gravitational metric nor a quantum of the Bernoulli force.

(v) PG metrics and the associated Einstein equations remain comparison encodings of material DDF observables. Their quantum completion consists in deriving the underlying pressure, flow, vortex, and bound-state quantities from the microscopic DDF state, not in assigning an independent quantum ontology to the comparison geometry.

Accordingly, the phrase *DDF quantum completion of the GR sector* will denote the derivation of the material variables whose classical, coarse-grained limit reproduces specified GR benchmark relations, together with the finite-scale and correlation terms associated with that coarse-graining. It does not denote canonical or perturbative quantization of Einstein's field equations, nor does it imply the existence of a graviton.

15.2. Quantum DDF Substrate and Vortex Sector

The vortex-supported source sector is not awaiting a first quantization. Section 3 already assigns integer circulation, internal winding, and topological data to the quantized ϕ-vortex configurations, while Sec. 5 embeds the coupled ϕ and φ sectors in the number-conserving operator $\hat{H}_{\rm DDF}$ and the microscopic action (103). The remaining microscopic work is to obtain from that quantum many-body theory the all-speed translational dynamics of the DDF-dressed vortex configuration and the explicit state-dependent profiles and correlators of the source, pressure, and flow observables entering the macroscopic gravitational sector.

In the DDF ontology, the field operators are second-quantized descriptions of the material particles of a permanently occupied substrate, rather than an ontological construction of the substrate from an empty vacuum. The use of operator fields over macroscopically occupied states follows standard quantum-fluid practice [44,45,245], whereas the physical interpretation assigned to those states is specific to the DDF. Denote the macroscopic reference state by

$$|\Omega_{\mathcal{D}}\rangle \in \mathcal{H}_\phi \otimes \mathcal{H}_\varphi, \qquad \langle \hat{N}_\phi \rangle_{\Omega_{\mathcal{D}}} \gg 1, \quad \langle \hat{N}_\varphi \rangle_{\Omega_{\mathcal{D}}} \gg 1. \tag{410}$$

Localized massive-particle states are topological and dressed departures from this occupied material state. They may be denoted schematically by $|\Psi_{\mathrm{v},\alpha}\rangle$, where α collects the circulation, winding, framing, bound-state, and internal φ-loading data introduced in Sec. 3.

This common quantum substrate is therefore the starting point for both branches considered below. No additional gravitational Hilbert space or independent metric degrees of freedom are introduced.

15.3. Quantum Completion of the Lorentz-form Material Sector

The Lorentz sector is already fixed at the classical material level by the limiting-branch profile, the conservative momentum–energy closure, and the proper-time action derived in Secs. 6–7. Its quantum completion concerns the collective translational dynamics of an already quantized, DDF-dressed vortex configuration; it is not a quantization of special relativity as an independent theory.

© 2026 by the author(s). Distributed under a Creative Commons CC BY license.

Preprints.org (www.preprints.org) | NOT PEER-REVIEWED | Posted: 7 September 2026 doi:10.20944/preprints202608.2283.v2

For a vortex configuration with fixed internal quantum numbers, let $\hat{\mathbf{R}}$ denote its collective center coordinate and $\hat{\mathbf{P}}$ its total translational momentum. They satisfy

$$[\hat{R}_i, \hat{P}_j] = i\hbar\delta_{ij}. \tag{411}$$

The constrained moving-vortex problem defined by Eq. (95) has so far been reduced microscopically only in the low-speed regime. A full microscopic completion requires the coupled DDF Hamiltonian to generate the all-speed translational branch of the dressed configuration,

$$\boxed{E_v^2(P) = m^2c^4 + c^2P^2,} \tag{412}$$

where the limiting speed c is fixed by the saturated transverse φ branch. Equation (412) therefore concerns the collective motion of the coupled material configuration, not an intrinsic dispersion assigned to the underlying ϕ-vortex structure alone.

Once Eq. (412) has been obtained from $\hat{H}_{\mathrm{DDF}}$, the positive-energy translational sector of a dressed vortex state with fixed internal quantum numbers is represented by the effective Hamiltonian

$$\boxed{\hat{H}_{\mathrm{v}}^{\mathrm{eff}} = \sqrt{m^2c^4 + c^2\hat{\mathbf{P}}^2}.} \tag{413}$$

Its wave packet then obeys

$$i\hbar\partial_t|\psi_{\mathrm{v}}\rangle = \hat{H}_{\mathrm{v}}^{\mathrm{eff}}|\psi_{\mathrm{v}}\rangle. \tag{414}$$

Equation (413) is therefore the effective quantization of the Lorentz-form material dispersion after that dispersion has been recovered from the microscopic coupled DDF dynamics. It does not substitute for the microscopic derivation of Eq. (412).

The chronometric sector has an equally direct quantum interpretation. For a bound internal clock carried by the same DDF-coupled material system, phase accumulation is governed by the DDF proper time derived in Sec. 7,

$$\boxed{\hat{U}_{\mathrm{int}} = \mathcal{T}\exp\left[-\frac{i}{\hbar}\int \hat{H}_{\mathrm{int}}\, d\tau_{\mathcal{D}}\right], \qquad d\tau_{\mathcal{D}} = \frac{dt}{\gamma_\varphi(v)}.} \tag{415}$$

Different clock Hamiltonians may possess different internal frequencies and level structures, but their comparison between inertial material frames is controlled by the same DDF proper-time element $d\tau_{\mathcal{D}}$. This universality follows from the common φ-sector jamming response governing all massive material configurations, independently of their microscopic vortex composition.

15.4. Active-source Operator, Bernoulli Observables, and the Classical Gravitational Limit

The gravitational sector requires a different construction. Since the inertial mass density of the homogeneous DDF is not identified with active gravitational charge, the source operator cannot be the total ϕ or φ number-density operator. It must instead encode the quantized ϕ-vortex content of massive matter together with the bound-state contributions that modify the associated Bernoulli pressure field.

Represent this source-selection rule by the state-dependent functional

$$\boxed{\begin{aligned}\hat{\rho}_{\mathrm{act}}(\mathbf{x}) &\equiv \mathcal{F}_{\mathrm{act}}\big[\hat{n}_\phi, \hat{S}_\phi, \hat{\mathbf{A}}_v, \hat{\Xi}_{\mathrm{bound}}\big](\mathbf{x}) \\ &= \hat{\rho}_{\mathrm{vort}}(\mathbf{x}) + \hat{\rho}_{\mathrm{bound/conf}}(\mathbf{x}).\end{aligned}} \tag{416}$$

Here $\hat{\rho}_{\mathrm{bound/conf}}$ is a signed configurational contribution: internal field energy can increase the active source strength, whereas negative binding energy reduces it. The variables $\hat{\Xi}_{\mathrm{bound}}$ collectively encode the bound-field and configurational degrees of freedom through which these contributions modify the

© 2026 by the author(s). Distributed under a Creative Commons CC BY license.

Preprints.org (www.preprints.org) | NOT PEER-REVIEWED | Posted: 7 September 2026 doi:10.20944/preprints202608.2283.v2

Bernoulli source strength of a vortex-supported material configuration. The defining source-selection conditions are

$$\begin{aligned} \langle \hat{\rho}_{\rm act} \rangle|_{\text{homogeneous free Œ,'}} &= 0, \\ \langle \hat{\rho}_{\rm act} \rangle|_{\text{free transverse modes}} &= 0. \end{aligned} \tag{417}$$

Equation (416) is the operator counterpart of the source ontology already used in Secs. 9.1 and 10.3. At the present level, $\mathcal{F}_{\rm act}$ implements this microscopic source-selection rule; its explicit realization from $\hat{H}_{\rm DDF}$ requires the corresponding vortex and bound-state matrix elements and their coupling to the ϕ-pressure field. The same operator description must also reproduce the transition rule of Eqs. (204)–(205): when energy is transferred from a vortex-supported bound configuration into an on-shell transverse photon, the corresponding bound contribution to $\hat{\rho}_{\rm act}$ decreases while the free transverse mode remains in the source-null sector, with the reverse change occurring upon absorption.

In the long-wavelength density–phase representation of the coherent ϕ branch, the local fluctuations obey the standard quantum-hydrodynamic canonical relation [44,245],

$$\big[\delta\hat{n}_\phi(\mathbf{x}), \delta\hat{S}_\phi(\mathbf{y})\big] = i\,\delta^3(\mathbf{x}-\mathbf{y}). \tag{418}$$

The full circulation velocity and the smooth microscopic condensate velocity become composite material operators consistent with Eqs. (20)–(24),

$$\hat{\mathbf{v}}_{\rm B} = \frac{\hbar}{m_\phi}\boldsymbol{\nabla}\hat{S}_\phi, \qquad \hat{\mathbf{v}}_{\phi,\rm mic} = \hat{\mathbf{v}}_{\rm B} - \hat{\mathbf{A}}_v. \tag{419}$$

Let $\Delta\hat{P}_\phi$ denote the scalar part of the stress-equivalent pressure perturbation of the coherent medium, including any isotropic finite-core contribution. Residual anisotropic, finite-core, and connected quantum stresses are retained separately in $\boldsymbol{\Pi}^{\rm Q}_\phi$ below. For the nearly incompressible microscopic-to-classical bridge considered here, define the composite observables

$$\boxed{\hat{\Phi}_\phi \equiv \frac{\Delta\hat{P}_\phi}{\varrho_{\phi,0}}, \qquad \hat{\mathbf{g}}_\phi \equiv -\boldsymbol{\nabla}\hat{\Phi}_\phi.} \tag{420}$$

These operators describe the microscopic material quantities whose macroscopic expectation values enter the gravitational phenomenology. In compressible regimes, the corresponding scalar observable is the specific enthalpy introduced in the classical DDF treatment. Their definition does not introduce an elementary gravitational-field operator or a graviton.

For an operator with no explicit time dependence, microscopic evolution is generated by

$$i\hbar\,\partial_t\hat{\mathcal{O}} = \big[\hat{\mathcal{O}}, \hat{H}_{\rm DDF}\big]. \tag{421}$$

Applied to the ϕ density, this yields the exact operator continuity law

$$\partial_t\hat{n}_\phi + \boldsymbol{\nabla}\cdot\hat{\mathbf{j}}_\phi = 0, \qquad \hat{\mathbf{j}}_\phi \equiv \frac{1}{2}\big\{\hat{n}_\phi, \hat{\mathbf{v}}_{\rm B}\big\}. \tag{422}$$

After coarse-graining on a scale ℓ larger than the vortex core and the microscopic φ-contact scale, define

$$\bar{n}_\phi \equiv \langle\hat{n}_\phi\rangle_\ell, \qquad \mathbf{v}_\phi \equiv \langle\hat{\mathbf{v}}_{\rm B}\rangle_\ell, \qquad \Phi_\phi \equiv \langle\hat{\Phi}_\phi\rangle_\ell. \tag{423}$$

Writing $\delta\hat{n}_\phi = \hat{n}_\phi - \bar{n}_\phi$ and $\delta\hat{\mathbf{v}}_{\rm B} = \hat{\mathbf{v}}_{\rm B} - \mathbf{v}_\phi$, the averaged current is

$$\boxed{\bar{\mathbf{j}}_\phi = \bar{n}_\phi\mathbf{v}_\phi + \mathbf{J}^{\rm corr}_\phi,} \tag{424}$$

with

$$\mathbf{J}^{\rm corr}_\phi \equiv \frac{1}{2}\big\langle\big\{\delta\hat{n}_\phi, \delta\hat{\mathbf{v}}_{\rm B}\big\}\big\rangle_\ell. \tag{425}$$

© 2026 by the author(s). Distributed under a Creative Commons CC BY license.

Preprints.org (www.preprints.org) | NOT PEER-REVIEWED | Posted: 7 September 2026 doi:10.20944/preprints202608.2283.v2

Consequently,

$$\boxed{\partial_t \bar{n}_\phi + \boldsymbol{\nabla}\cdot\left(\bar{n}_\phi \mathbf{v}_\phi + \mathbf{J}_\phi^{\mathrm{corr}}\right) = 0,} \tag{426}$$

which is the operator derivation of the current bridge used in Eqs. (210)–(214). The macroscopic PG/DDF river velocity is therefore a genuine material mean flow, while exact number conservation is carried by the full correlated current.

The corresponding momentum equation contains the Euler–Bernoulli terms together with operator-ordering, finite-core, and connected-correlation stresses. The mean equation can then be organized in the form

$$\boxed{\partial_t \mathbf{v}_\phi + (\mathbf{v}_\phi\cdot\boldsymbol{\nabla})\mathbf{v}_\phi = -\boldsymbol{\nabla}\Phi_\phi - \frac{1}{\varrho_{\phi,0}}\boldsymbol{\nabla}\cdot\boldsymbol{\Pi}_\phi^{\mathrm{Q}}.} \tag{427}$$

Here $\boldsymbol{\Pi}_\phi^{\mathrm{Q}}$ collects the connected phase, density, vortex-position, bound-state, and ϕ–φ correlation stresses left after coarse-graining. It is the operator-level realization of the coarse-grained stress $\boldsymbol{\Pi}_\phi^{\mathrm{corr}}$ introduced in Eqs. (218) and (263). Organizing a macroscopic equation into mean fields and connected correlators is methodologically analogous to procedures used in semiclassical and stochastic gravity [35], but the ontology is different: the fluctuating quantities here are material DDF observables, and no independent metric field is made stochastic.

A representative velocity-correlation contribution is

$$\Pi_{\phi,ij}^{\mathrm{Q}} \supset \frac{\varrho_{\phi,0}}{2}\left\langle\left\{\delta\hat{v}_{\mathrm{B},i}, \delta\hat{v}_{\mathrm{B},j}\right\}\right\rangle_\ell^{\mathrm{conn}}. \tag{428}$$

When the connected and finite-core corrections are negligible, Eq. (427) reduces to the classical DDF closure

$$\frac{D\mathbf{v}_\phi}{Dt} = -\boldsymbol{\nabla}\Phi_\phi. \tag{429}$$

Gravity is therefore classical at the observable coarse-grained level while retaining a microscopic quantum origin in the vortex-supported state that generates the pressure and flow fields.

In the weak-field, stationary limit, the coarse-grained Poisson representation of the previously derived classical source closure is

$$\boxed{\boldsymbol{\nabla}^2\Phi_\phi = 4\pi G_\phi\,\bar{\rho}_{\mathrm{act}} + \mathcal{Q}_{\mathrm{corr}},} \qquad \bar{\rho}_{\mathrm{act}} \equiv \langle\hat{\rho}_{\mathrm{act}}\rangle_\ell, \tag{430}$$

where $\mathcal{Q}_{\mathrm{corr}}$ denotes the finite-core and connected many-body corrections to the classical source closure. The quantum-stress sector contributes schematically through terms of the form

$$\mathcal{Q}_{\mathrm{corr}} \supset -\frac{1}{\varrho_{\phi,0}}\partial_i\partial_j\Pi_{\phi,ij}^{\mathrm{Q}}. \tag{431}$$

The explicit form of $\mathcal{Q}_{\mathrm{corr}}$ is determined by the coarse-graining of the microscopic momentum and source equations; the term above represents one contribution and is not assumed to exhaust the full correlation structure.

When the finite-core and connected-correlation corrections become negligible, the classical DDF gravitational closure is recovered. The fundamental relation remains the Bernoulli law $\mathbf{g}_\phi = -\boldsymbol{\nabla}\Phi_\phi$, while G_ϕ denotes the macroscopic coefficient by which the coarse-grained source–field relation is expressed in conventional Newtonian form. The inverse-square exterior field therefore represents the classical large-scale limit of the underlying vortex-generated ϕ-pressure field, rather than the action of an independent microscopic gravitational charge.

15.5. PG and Einstein Equations as Expectation-Value Encodings

The PG representation can inherit fluctuations from the underlying quantum superflow without becoming a fundamental quantum geometry. Quantum-fluid analog-gravity studies provide a

© 2026 by the author(s). Distributed under a Creative Commons CC BY license.

Preprints.org (www.preprints.org) | NOT PEER-REVIEWED | Posted: 7 September 2026 doi:10.20944/preprints202608.2283.v2

methodological precedent for encoding effective propagation geometries in material flow variables [53,246], but the role of the PG form in the DDF is more specific: it is the geometric encoding of a proposed literal cosmic medium, not an independently quantized acoustic or gravitational metric.

To keep the operator and macroscopic levels distinct, let

$$\hat{\mathbf{v}}_\phi^{(\ell)} \equiv \mathcal{C}_\ell[\hat{\mathbf{v}}_{\rm B}], \qquad \left\langle \hat{\mathbf{v}}_\phi^{(\ell)} \right\rangle = \mathbf{v}_\phi, \tag{432}$$

where $\mathcal{C}_\ell$ denotes coarse-graining on the same scale ℓ used above. In the flat-slice PG representation one may then introduce the composite shorthand

$$\hat{g}_{tt}^{\rm map} \equiv -\left(c^2 - |\hat{\mathbf{v}}_\phi^{(\ell)}|^2\right), \quad \hat{g}_{ti}^{\rm map} \equiv -\hat{v}_{\phi,i}^{(\ell)}, \quad \hat{g}_{ij}^{\rm map} \equiv \delta_{ij}. \tag{433}$$

The physical operator is the coarse-grained material flow on the right-hand side. The symbols $\hat{g}_{\mu\nu}^{\rm map}$ merely package that flow in the PG algebraic form for comparison with GR; they do not constitute fundamental metric operators.

The corresponding classical coefficients are constructed from the macroscopic DDF superflow,

$$g_{\mu\nu}^{\rm map} = g_{\mu\nu}^{\rm PG}[\mathbf{v}_\phi]. \tag{434}$$

The specific-enthalpy field, determined by the underlying pressure and density configuration, determines $\mathbf{v}_\phi$ dynamically through the DDF Bernoulli equations; it is therefore not an independent algebraic argument of the flat-slice PG representation. Connected flow correlators quantify fluctuations of the material observable entering this encoding. Because the PG map is nonlinear,

$$\left\langle \hat{g}_{\mu\nu}^{\rm map} \right\rangle \neq g_{\mu\nu}^{\rm PG}\left[\left\langle \hat{\mathbf{v}}_\phi^{(\ell)} \right\rangle\right] \tag{435}$$

in general, and their difference is itself a correlation effect. Neither side is interpreted as a quantum metric.

Where a classical DDF solution reproduces a GR benchmark, its quantum-corrected comparison may be organized as

$$\boxed{G_{\mu\nu}\left[g_{\alpha\beta}^{\rm map}\right] = \frac{8\pi G_\phi}{c^4}\overline{T}_{\mu\nu}^{\rm act} + \mathcal{C}_{\mu\nu}^{\rm DDF}.} \tag{436}$$

Here $\overline{T}_{\mu\nu}^{\rm act}$ is the macroscopic tensor encoding of the quantized-vortex and bound configurational contributions that generate the active Bernoulli source. Define the residual mapped contribution by

$$\mathcal{C}_{\mu\nu}^{\rm DDF} \equiv G_{\mu\nu}\left[g_{\alpha\beta}^{\rm map}\right] - \frac{8\pi G_\phi}{c^4}\overline{T}_{\mu\nu}^{\rm act}. \tag{437}$$

Thus $\mathcal{C}_{\mu\nu}^{\rm DDF}$ is not an independently postulated source term: it is the residual contribution required to represent the same material DDF solution on the GR side of the map. Its microscopic content can include finite-core structure, anisotropy, nonlocal material response, connected correlations, and terms associated with exchange between active and source-null sectors.

Equation (436) is not an operator Einstein equation and is not postulated as an additional DDF field equation. It is the GR-side encoding of a quantum-corrected material solution. In the regime in which finite-structure and connected-correlation contributions become negligible, $\mathcal{C}_{\mu\nu}^{\rm DDF} \to 0$, and the corresponding classical GR benchmark is recovered. A nonzero $\mathcal{C}_{\mu\nu}^{\rm DDF}$ therefore represents material finite-structure, many-body, or exchange contributions to the mapped DDF solution, not a virtual-graviton effect.

By the Bianchi identity, this mapped decomposition obeys

$$\nabla_{\rm map}^\mu\left(\frac{8\pi G_\phi}{c^4}\overline{T}_{\mu\nu}^{\rm act} + \mathcal{C}_{\mu\nu}^{\rm DDF}\right) = 0. \tag{438}$$

© 2026 by the author(s). Distributed under a Creative Commons CC BY license.

Preprints.org (www.preprints.org) | NOT PEER-REVIEWED | Posted: 7 September 2026 doi:10.20944/preprints202608.2283.v2

This condition applies to the complete mapped right-hand side and does not require $\overline{T}^{\rm act}_{\mu\nu}$ to be conserved separately. The active-source tensor represents only the gravitationally active part of the material DDF system, whereas the underlying Hamiltonian dynamics conserves the total material energy and momentum while allowing exchange among vortex, bound, background, and propagating sectors.

Define the corresponding mapped exchange current by

$$\mathcal{J}^{\rm ex}_{\nu} \equiv \nabla^{\mu}_{\rm map}\overline{T}^{\rm act}_{\mu\nu}. \tag{439}$$

Equation (438) then gives

$$\boxed{\nabla^{\mu}_{\rm map}\mathcal{C}^{\rm DDF}_{\mu\nu} = -\frac{8\pi G_{\phi}}{c^4}\mathcal{J}^{\rm ex}_{\nu}.} \tag{440}$$

The nonvanishing divergence of the active-source contribution therefore records the mapped balance associated with energy–momentum exchange between the active and source-null material sectors; it does not assign active gravitational charge to the source-null sector. The emission and absorption rules of Eqs. (204)–(205) provide a direct example: transfer of energy from a vortex-supported bound configuration into a free transverse mode decreases the active-source contribution while the emitted mode remains in the source-null sector, with the reverse transfer occurring upon absorption. Total DDF energy–momentum remains conserved throughout the process.

The Bianchi identity thus provides the geometric balance relation associated with the mapped representation, while the underlying DDF Hamiltonian supplies the corresponding conservation of total material energy–momentum. What remains to be calculated microscopically is the explicit distribution and exchange of that conserved energy–momentum among the active and source-null DDF sectors for specific material configurations, together with their contribution to $\mathcal{C}^{\rm DDF}_{\mu\nu}$.

15.6. Quantized Photon Branch and Macroscopic LVK Shear without a Graviton Sector

The microscopic transverse φ branch is quantized in the ordinary many-body sense, but this quantization is distinct from the quantum origin of gravity. The fundamental φ bosons are massive material constituents of the dispersed background; the normal-mode operators of the saturated quadratic Hamiltonian create collective transverse excitations above that occupied state.

Let $\hat{b}_{\mathbf{k}\lambda}$ denote the normal-mode operators of the saturated long-wavelength transverse branch. Relative to the reference energy of the occupied material state,

$$\hat{H}^{\rm sat}_{T} - E_{\Omega,T} = \sum_{\lambda=1}^{2}\int d^3k\,\hbar\omega_k\hat{b}^{\dagger}_{\mathbf{k}\lambda}\hat{b}_{\mathbf{k}\lambda}, \qquad \omega_k = ck. \tag{441}$$

Here $E_{\Omega,T}$ denotes the reference energy assigned to that effective transverse sector, including its zero-point term. Subtracting it defines excitation energies relative to the occupied DDF state and does not assign the homogeneous background an active gravitational charge.

A photon is a quantum of the electromagnetically coupled transverse φ-phonon mode. Quantization of Eq. (441) refers to that microscopic radiative branch. An LVK-class signal has a different status in the present DDF construction: it is a directly driven macroscopic simple-shear disturbance of the dispersed medium, generated when binary or merger stress acts on the φ phase collectively. It is not constructed as an ordered sum, coherent state, or coarse-graining of microscopic transverse φ-phonons. The common value c reflects the same limiting ratio of saturated shear stiffness to inertial density, $G^{\rm max}_{\varphi}/\varrho^{\rm max}_{\varphi}$, not an identity of the two excitations.

© 2026 by the author(s). Distributed under a Creative Commons CC BY license.

Preprints.org (www.preprints.org) | NOT PEER-REVIEWED | Posted: 7 September 2026 doi:10.20944/preprints202608.2283.v2

The physical production chain is

$$\begin{array}{c} \text{strong binary or merger dynamics} \\ \Downarrow \\ \text{mechanical stress transferred through the DDF} \\ \Downarrow \\ \text{macroscopic transverse } \varphi\text{-shear emission.} \end{array} \tag{442}$$

The microscopic transverse quanta of Eq. (441) are the photon-sector phononic excitations of the dispersed material phase. The macroscopic LVK field introduced in Eq. (442) is not assigned a corresponding graviton or photon-number interpretation. No massless spin–2 quantum is required by the DDF gravitational ontology because the Bernoulli force itself is not a fundamental quantum field.

The rank-two detector response discussed in Sec. 14.2 consequently remains a material coupling map between the propagating transverse disturbance and the measured differential strain. Demonstrating that this coupling reproduces the observed tensor antenna response is a separate microscopic requirement; it does not change the identity of the carrier into a quantum of gravity.

15.7. Microscopic Completion Program and Scope

The preceding sections establish the operator structure of the quantum DDF description and its connection to the classical material limit. The remaining microscopic work concerns the explicit all-speed reduction and state-dependent evaluation of quantities whose physical roles and macroscopic limits have already been specified. The principal calculations are:

(i) solve the constrained moving-vortex problem beyond the low-speed reduction and derive from $\hat{H}_{\rm DDF}$ the all-speed translational branch of the DDF-dressed vortex configuration,

$$E_v^2(P) = m^2c^4 + c^2P^2,$$

with the limiting speed c given by the saturated transverse φ branch;

(ii) construct the explicit microscopic realization of the active-source functional $\mathcal{F}_{\rm act}$ from $\hat{H}_{\rm DDF}$, including the bound-to-on-shell source-transfer rule of Eqs. (204)–(205) and the DDF source-null rule for the homogeneous free DDF background and freely propagating transverse modes;

(iii) calculate the quantum density, phase, quantum-stress, and pressure profiles of individual quantized ϕ-vortices and representative bound multivortex configurations, thereby providing the microscopic input to their Bernoulli pressure fields and collective coarse-grained dynamics;

(iv) evaluate $\mathbf{\Pi}^{\rm Q}_{\phi}$, $\mathcal{Q}_{\rm corr}$, $\mathcal{C}^{\rm DDF}_{\mu\nu}$, and the corresponding exchange current $\mathcal{J}^{\rm ex}_{\nu}$ for representative material configurations, thereby quantifying finite-core, many-body, correlation, and intersector energy–momentum contributions and their reduction to the classical Bernoulli and mapped-GR limits;

(v) derive the conversion efficiency from strong binary or merger shear into the macroscopic transverse φ-wave channel and the material coupling by which this excitation produces the observed rank-two detector strain response, without reinterpreting the carrier as a graviton.

The scope of the quantum DDF construction is therefore precise. Quantized ϕ-vortices provide the microscopic structure of massive matter and individually generate their Bernoulli near fields, while bound and composite vortex configurations determine the corresponding modified and collective active-source fields. The common φ-sector jamming response governs the Lorentz-form inertial and chronometric behavior of massive material systems, with the saturated transverse branch fixing the universal limiting speed c. At larger scales, expectation values and coarse-grained correlations of the ϕ pressure and superflow fields produce the classical Bernoulli gravitational dynamics developed in the preceding sections.

The PG metric and Einstein equations are not additional microscopic DDF dynamics. They enter as geometric encodings of the corresponding macroscopic pressure and flow observables wherever

© 2026 by the author(s). Distributed under a Creative Commons CC BY license.

Preprints.org (www.preprints.org) | NOT PEER-REVIEWED | Posted: 7 September 2026 doi:10.20944/preprints202608.2283.v2

the DDF solution reproduces the relevant GR benchmark. Likewise, the conservation condition of Sec. 15.5 is the mapped expression of the local energy–momentum conservation already enforced by the underlying DDF Hamiltonian; the remaining microscopic task is to calculate explicitly how that conserved energy and momentum are distributed and exchanged among the active and source-null material sectors in particular configurations.

Quantum corrections in this construction arise from finite material structure, operator correlations, and the many-body dynamics of the coupled DDF substrate. They are therefore corrections to the material pressure, superflow, source, and propagation observables, rather than fluctuations of an independently fundamental spacetime geometry, and their description does not require gravitational quanta.

16. Large-Scale Structure as a Vortex–Filament Web of a "Doped" Dark Superfluid

The large-scale-structure construction begins from an empirical morphological clue. In laboratory He II, intense local forcing, heat deposition, counterflow, vortex reconnections, and the trapping of foreign particles can produce an irregular, visibly decorated vortex–filament network (VFN) [41,104, 229]. The filament–void morphology traced by galaxies, gas, and gravitational lensing is strikingly similar at a qualitative level [247,248], as shown in Figure 8.

This resemblance motivates the hypothesis that the large-scale structure of the Universe is a matter-traced manifestation of a VFN in the coupled DDF. The analogy is constitutive rather than a direct scale identification: the continuous ϕ phase carries quantized vorticity, while the dispersed φ phase already pervades the medium and can be locally organized, entrained, and stressed by the filamentary flow.

The large-scale network is statistically unpolarized,

$$n_{\rm abs} = n_+ + n_- > 0, \qquad n_{\rm net} = n_+ - n_- \simeq 0,$$

so individual filament bundles may possess local axial circulation while their signed circulation averages to approximately zero over sufficiently large volumes.

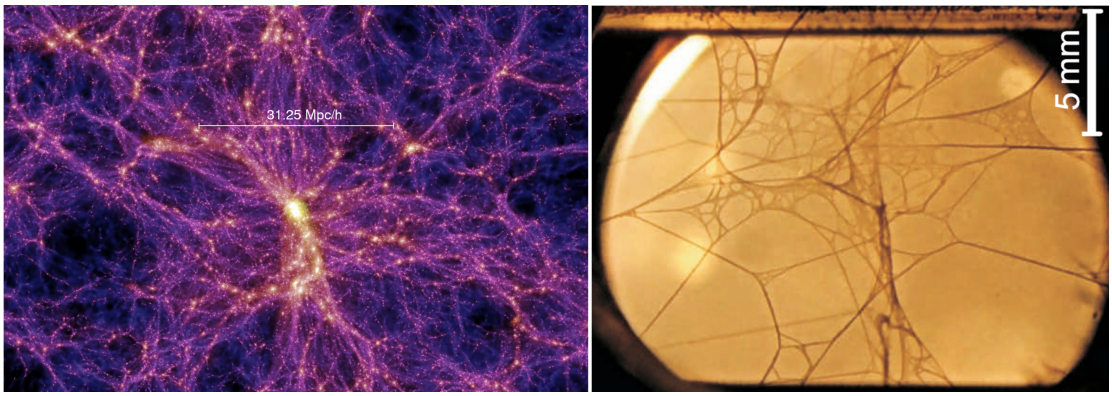


Figure 8. Large-scale structure of the Universe compared with filamentary structures in a stationary, doped superfluid. Left: the cosmic filament–void network traced by baryonic and dark matter (Credit: Max Planck Institute for Astrophysics; Virgo Consortium; Springel et al. [42]). Right: laser-ablated copper nanofragments trapped and aggregated along structures attributed to quantized vortices in He II (Credit: Moroshkin et al. [41]). In the DDF interpretation, the comparison motivates a statistically unpolarized vortex network whose nearby dispersed φ-quanta can be locally organized and entrained by the ϕ-filament flow. The analogy is morphological and constitutive: a dispersed component already present in a superfluid can reveal and mechanically load vortical structures without acting as an additional active gravitational source.

© 2026 by the author(s). Distributed under a Creative Commons CC BY license.

Preprints.org (www.preprints.org) | NOT PEER-REVIEWED | Posted: 7 September 2026 doi:10.20944/preprints202608.2283.v2

Field description and working mass benchmarks.

The coupled GP description of ϕ and coarse-grained constitutive dynamics of φ are used with the working benchmarks established in Sec. 2:

$$\begin{aligned} m_\phi &\approx 2\times 10^{-19}\ \mathrm{eV}/c^2, \\ \kappa_\phi &\equiv \frac{h}{m_\phi} \approx 1.86\times 10^{21}\ \mathrm{m^2\,s^{-1}}, \end{aligned} \tag{443}$$

$$m_\varphi \approx 2\times 10^{-16}\ \mathrm{eV}/c^2, \qquad m_\varphi/m_\phi \approx 10^3. \tag{444}$$

These are macroscopic-matching values rather than unique microscopic predictions. The hierarchy keeps ϕ coherent and superfluid-dominated while allowing the heavier but still ultralight φ population to act as a dilute, mechanically active jamming fraction. All estimates below use these benchmarks.

Internal vortex-line spacing and mean bundle spacing.

The VFN contains two distinct levels of spatial organization. The internal spacing $\ell_{v,b}$ characterizes the quantized vortex lines contained within an individual filament bundle, whereas the mean bundle spacing D_{MBS} characterizes the statistical separation of the bundles forming the large-scale network.

The relevant hierarchy is

$$\xi \ll \ell_{v,b} \ll R_b \ll D_{\mathrm{MBS}}, \tag{445}$$

where ξ is the healing length and R_b is the effective bundle radius. This is a hierarchy of levels of organization; it does not imply that $\ell_{v,b}$ is microscopic in absolute astrophysical units.

Within a bundle, let $n_{+,b}$ and $n_{-,b}$ denote the positive- and negative-circulation vortex-line areal densities. Define

$$\begin{aligned} n_{\mathrm{abs},b} &\equiv n_{+,b} + n_{-,b}, \\ n_{\mathrm{net},b} &\equiv n_{+,b} - n_{-,b}. \end{aligned} \tag{446}$$

The internal vortex-line spacing and the local circulation-polarization fraction are

$$\ell_{v,b} \equiv n_{\mathrm{abs},b}^{-1/2}, \qquad p_b \equiv \frac{n_{\mathrm{net},b}}{n_{\mathrm{abs},b}}, \qquad -1 \le p_b \le 1. \tag{447}$$

For a many-vortex bundle whose coarse-grained interior approximates solid-body rotation, the local Feynman relation is

$$\boxed{n_{\mathrm{net},b} = \frac{2\Omega_b}{\kappa_\phi}, \qquad \Omega_b = \frac{\kappa_\phi p_b}{2\ell_{v,b}^2}, \qquad \kappa_\phi \equiv \frac{h}{m_\phi}}. \tag{448}$$

Equation (448) constrains the signed excess of quantized vortex lines inside a locally rotating bundle. It does not determine the mean separation of the bundles forming the cosmic network.

Let s denote the separation between neighboring reconstructed vortex-filament bundle axes and let $P_{\mathrm{bun}}(s)$ be its normalized network distribution,

$$\int_0^\infty P_{\mathrm{bun}}(s)\, ds = 1. \tag{449}$$

The mean bundle spacing is then

$$D_{\mathrm{MBS}} \equiv \langle s \rangle_{\mathrm{VFN}} = \int_0^\infty s\, P_{\mathrm{bun}}(s)\, ds. \tag{450}$$

Approximate density-based estimators are

$$D_{\mathrm{MBS}}^{(3)} \sim \mathcal{C}_3 \left(n_{\mathrm{bun}}^{(3)}\right)^{-1/3}, \qquad D_{\mathrm{MBS}}^{(\perp)} \sim \mathcal{C}_\perp \Sigma_{\mathrm{bun}}^{-1/2}, \tag{451}$$

© 2026 by the author(s). Distributed under a Creative Commons CC BY license.

Preprints.org (www.preprints.org) | NOT PEER-REVIEWED | Posted: 7 September 2026 doi:10.20944/preprints202608.2283.v2

where $n_{\rm bun}^{(3)}$ is an effective three-dimensional bundle density, $\Sigma_{\rm bun}$ is the projected bundle density, and the geometrical factors $\mathcal{C}_3$ and $\mathcal{C}_\perp$ account for the fact that the VFN is a reconnecting and bundled line network rather than a Poisson distribution of point objects.

Individual quantized vortex lines are not assumed to terminate freely or to form stable fundamental Y-junctions in the bulk of a single ϕ order parameter. They occur as closed loops, reach physical or phase boundaries, or reconnect with other vortex lines. Apparent branches and nodes in a coarse-grained cosmic-filament map therefore represent bundle overlap, reconnection regions, projected crossings, or matter-traced network nodes rather than literal endpoints of elementary vortex lines.

For projected bundles with characteristic radius R_b, define the effective bundle-area fraction

$$f_A \simeq \mathcal{C}_A \frac{\pi R_b^2}{\left[D_{\rm MBS}^{(\perp)}\right]^2}, \tag{452}$$

where $\mathcal{C}_A = \mathcal{O}(1)$ accounts for network topology, curvature, overlap, branching, and projection.

The working interval

$$D_{\rm MBS} \sim 10\text{–}100\,{\rm Mpc} \tag{453}$$

is a phenomenological input used to bracket Mpc-scale network separations. It must ultimately be replaced by the measured distribution $P_{\rm bun}(s)$ of a specified filament catalogue and must not be interpreted as the spacing between the individual quantized vortex lines contained within a bundle.

Local incompressibility convention. Across individual filament cross–sections the ϕ fluid is approximately incompressible in mass-density form, $\varrho_\phi(\mathbf{r}) \simeq \varrho_{\phi,0}$, so Bernoulli relations use $\varrho_{\phi,0}$. Slow, large–scale variations of ϱ_ϕ are allowed.

Local organization, loading, and entrainment.

The dispersed φ population is already present throughout the DDF and is not supplied by long-range gravitational capture. Near a ϕ-vortex or bundle, the local superflow, contact stresses, and collisional relaxation can reorganize the nearby dispersed quanta, producing decoration, transient loading, and entrainment along the filament. This is a local transport and constitutive response of the coupled medium.

True pinning should be reserved for cases in which a separate long-lived inhomogeneity or effectively stationary defect is specified. The large-scale construction relies primarily on local advection, contact rearrangement, and entrainment rather than on a capture radius or a particle-attraction law. The resulting φ loading may affect filament visibility, inertia, and shear-jamming response, but it does not supply an independent Bernoulli source density.

Bundles versus cores: local circulation occupancy.

The healing length ξ is a vortex-core scale, whereas an observable cosmic filament is modeled as a macroscopic bundle. For the illustrative large-scale estimates below, adopt the working effective-radius interval

$$R_b \sim 0.3\text{–}3\,{\rm Mpc}.$$

This phenomenological interval is not derived from the microscopic vortex-core scale; it is an input to be replaced by the width distribution of the filament sample under analysis. Its vortex-line occupancy is determined by the internal spacing $\ell_{v,b}$, not by the mean bundle spacing $D_{\rm MBS}$.

© 2026 by the author(s). Distributed under a Creative Commons CC BY license.

Preprints.org (www.preprints.org) | NOT PEER-REVIEWED | Posted: 7 September 2026 doi:10.20944/preprints202608.2283.v2

Let $N_{+,b}$ and $N_{-,b}$ denote the positive- and negative-circulation vortex counts crossing a representative bundle cross-section. Define

$$N_{\mathrm{abs},b} \equiv N_{+,b} + N_{-,b} \simeq \pi R_b^2 n_{\mathrm{abs},b} = \frac{\pi R_b^2}{\ell_{v,b}^2}, \qquad N_{\mathrm{net},b} \equiv N_{+,b} - N_{-,b} = p_b N_{\mathrm{abs},b}. \tag{454}$$

The net circulation carried by the bundle is

$$\Gamma_b = N_{\mathrm{net},b}\kappa_\phi, \tag{455}$$

and its coarse-grained angular velocity is

$$\Omega_b = \frac{\Gamma_b}{2\pi R_b^2} = \frac{N_{\mathrm{net},b}\kappa_\phi}{2\pi R_b^2}. \tag{456}$$

The mean bundle spacing D_{MBS} controls the statistical separation and projected abundance of observable vortex-filament bundles. It does not determine $N_{\mathrm{abs},b}$, $N_{\mathrm{net},b}$, or $\ell_{v,b}$ without an additional nonlinear bundle-formation model.

Outside a coherently circulating bundle, local dispersed-sector transport is controlled by the coarse-grained circulation $\Gamma_b = N_{\mathrm{net},b}\kappa_\phi$, the bundle radius R_b, and the relevant contact and relaxation times. Inside the bundle, local organization depends on the absolute vortex population $N_{\mathrm{abs},b}$. These quantities characterize entrainment and mechanical loading, not gravitational capture of a remote φ-particle reservoir.

Dopant loading and shear–jamming threshold.

Let $x \equiv n_\varphi/n_\phi$ be the dopant number ratio, $D \geq 1$ the stress-induced packing magnification, and α_{pack} the effective geometric/contact amplification. Then

$$\Phi_{\mathrm{eff}} = \frac{x\alpha_{\mathrm{pack}} D}{1 + x\alpha_{\mathrm{pack}} D}. \tag{457}$$

The threshold $\Phi_{\mathrm{eff}} \geq \Phi_\star$, with the representative, nonuniversal shear-jamming value $\Phi_\star \simeq 0.5 \pm 0.05$ [2,49,65], requires

$$\boxed{x \geq x_{\min} \equiv \frac{\Phi_\star}{1-\Phi_\star}\frac{1}{\alpha_{\mathrm{pack}} D} \simeq \frac{1}{\alpha_{\mathrm{pack}} D}} \quad (\Phi_\star \simeq 0.5), \tag{458}$$

whereas the quiescent packing

$$\Phi_0 = \frac{x\alpha_{\mathrm{pack}}}{1 + x\alpha_{\mathrm{pack}}} \tag{459}$$

must remain below jamming. The effective factor is intended to represent finite-volume occupancy, direct-contact connectivity, shape, hydrocluster, and collective-network effects; it is not a literal hard-sphere radius ratio.

A fiducial few-percent dispersed mass loading is adopted,

$$2\% \lesssim f_M \lesssim 5\%, \qquad f_M \equiv \frac{\varrho_\varphi}{\varrho_\phi + \varrho_\varphi} = \frac{\mu_m x}{1 + \mu_m x}, \tag{460}$$

with $\mu_m \equiv m_\varphi/m_\phi \simeq 10^3$. This is a morphology-supporting range, not a derived cosmological abundance: it leaves the bulk medium ϕ-dominated while permitting φ to decorate, load, and mechanically stress filament bundles [2,41,49,64,65,71,73,104]. The corresponding number ratio is

$$x = \frac{f_M}{\mu_m(1-f_M)} \simeq \frac{f_M}{\mu_m} \sim (2\text{–}5) \times 10^{-5}. \tag{461}$$

© 2026 by the author(s). Distributed under a Creative Commons CC BY license.

Preprints.org (www.preprints.org) | NOT PEER-REVIEWED | Posted: 7 September 2026 doi:10.20944/preprints202608.2283.v2

Combining this range with Eq. (458) exposes the demanding constitutive condition

$$\alpha_{\mathrm{pack}} D \gtrsim (2\text{–}5) \times 10^4, \tag{462}$$

which must emerge from the microscopic contact geometry and collective correlations; failure to obtain it would exclude this low-number-fraction realization.

Continuum support of ambient transverse modes of wavelength λ_{mode} additionally requires

$$n_\varphi^{\mathrm{amb}} \gtrsim \frac{N_{\mathrm{min}}}{\lambda_{\mathrm{mode}}^3}. \tag{463}$$

Here N_{min} is a heuristic minimum occupancy per wavelength-scale cell, not a derived universal constant. Taking $N_{\mathrm{min}} \sim 10$–100 and, for illustration, $\lambda_{\mathrm{mode}} \sim 1\,\mathrm{mm}$, gives $n_\varphi^{\mathrm{amb}} \gtrsim 10^{10}$–$10^{11}\,\mathrm{m}^{-3}$ and, through Eq. (461), $n_\phi^{\mathrm{amb}} \sim 2 \times 10^{14}$–$5 \times 10^{15}\,\mathrm{m}^{-3}$. Thus φ can remain dilute by number while acting as a continuum carrier and mechanically active dopant.

Observable content of the large-scale hypothesis.

The VFN provides a phenomenological large-scale construction and the material substrate for the cosmological outlook developed below. Its direct observational content is the proposed morphology, local circulation, finite-core profile, and matter–filament entrainment; background expansion and early-universe transfer physics are treated at the effective cosmological level in Sec. 17. A widespread detection of coherent filament circulation would not uniquely select the DDF, because conventional tidal-torque and anisotropic-accretion mechanisms can also generate large-scale angular momentum [249]. It would, nevertheless, strengthen the case for a vortical or superfluid origin of the cosmic web if the circulation were generic across dynamically cold filaments and exhibited the finite-core profile, longitudinal coherence, node continuity, and circulation scaling expected for vortex bundles. The corresponding signed filament-spin test is formulated in Appendix B.2.

17. Cosmological Outlook: The Standard Hot Big Bang on a Material DDF Background

The present work does not construct a replacement precision cosmology. It treats the standard hot Big Bang chronology within a material DDF background. Nucleosynthesis, recombination, relic CMB radiation, the acoustic BAO ruler, and the phenomenological expansion history may be represented in their standard operational form [250–254]. The scale factor, normalized by $a_{\mathcal{D}}(t_0) = 1$, is then read as a coarse-grained material deformation of the pervasive DDF rather than as a primitive geometrical degree of freedom:

$$d\ell_{\mathrm{phys}} = a_{\mathcal{D}}(t)\, d\ell, \qquad H_{\mathcal{D}} = \frac{\dot{a}_{\mathcal{D}}}{a_{\mathcal{D}}}. \tag{464}$$

At the level of an observational background fit, the usual hot Big Bang parameterization can therefore be retained,

$$H_{\mathcal{D}}^2(a_{\mathcal{D}}) = H_0^2 \left[\Omega_r a_{\mathcal{D}}^{-4} + \Omega_m a_{\mathcal{D}}^{-3} + \Omega_k a_{\mathcal{D}}^{-2} + \Omega_\Lambda \right], \tag{465}$$

while its microscopic DDF realization, including the late-time term, is the dynamical target of the material-background model.

Equation (465) is a phenomenological background representation rather than a DDF Friedmann equation. It also exposes a precise consistency condition: the radiation-era expansion, BBN, and CMB acoustic dynamics require an effective conserved cosmological source compatible with the restricted long-range photon-source rule adopted in the local gravitational sector. The cosmological extension must either realize that source through the collective medium or identify the domain in which the restricted rule changes.

The DDF is taken to pre-exist the modeled hot epoch in a quiescent or metastable state. Within the vortex–antivortex interpretation of matter and antimatter developed in Sec. 3, a possible primordial

© 2026 by the author(s). Distributed under a Creative Commons CC BY license.

Preprints.org (www.preprints.org) | NOT PEER-REVIEWED | Posted: 7 September 2026 doi:10.20944/preprints202608.2283.v2

antecedent of the hot epoch is provided by the interaction of large DDF domains with opposite net circulation biases. A transient local angular momentum can favor the nucleation of defects with one circulation sign, as occurs in rotating laboratory superfluids, where same-sign vortices organize into coherent arrays [45]. Different primordial DDF domains or bubbles could therefore have contained predominantly vortices or predominantly antivortices.

If oppositely circulation-biased domains came into contact, matched vortex–antivortex pairs would annihilate through the hydrodynamic channel described above, converting their defect energy and bound φ-loading into excitations of the DDF. Because photons are the quanta of the transverse φ branch, the resulting luminous release can be represented as a high-occupancy excitation

$$\Delta E_{\rm ph} = \sum_{\mathbf{k},\lambda=\pm} \hbar\omega_{\mathbf{k}}\, \Delta N_{\mathbf{k},\lambda}, \qquad \omega_{\mathbf{k}} = c|\mathbf{k}|, \tag{466}$$

together with possible compressional, vortical, and ordinary-matter channels. If the two domains contained unequal populations of oppositely charged defects, pairwise annihilation would leave a residual net topological population

$$\Delta N_{\rm top} = |N_{\rm v} - N_{\bar{\rm v}}|, \tag{467}$$

where $N_{\rm v}$ and $N_{\bar{\rm v}}$ denote the vortex and antivortex populations involved in the interaction. Under the proposed correspondence between topological charge and the matter–antimatter distinction, this surviving defect population offers a possible topological origin of the observed baryon asymmetry.

A sufficiently large and rapid annihilation event could generate an ultrahot, radiation-rich state and initiate a rapid material expansion of the DDF, followed by slower expansion and cooling. In this interpretation, the hot primordial event marks neither the creation of the DDF nor the beginning of physical space, but a dramatic transition within a pre-existing dark medium. The scenario is proposed as a qualitative extension of the DDF annihilation mechanism; a quantitative treatment must determine the relation between topological charge and baryon number, the resulting matter-to-photon ratio, and whether the released energy and DDF stress response can sustain an inflation-like accelerated-expansion phase.

Cosmological redshift follows from the material scale factor exactly as in the standard expanding description. For the photon branch,

$$k_{\rm phys} = \frac{k_{\rm com}}{a_{\mathcal{D}}}, \qquad \omega_\gamma = c k_{\rm phys}, \qquad 1 + z = \frac{a_{\mathcal{D}}(t_0)}{a_{\mathcal{D}}(t_{\rm em})}. \tag{468}$$

The frequency change is parametric: the material background stretches the physical wavelength and changes the instantaneous eigenfrequency as $\omega_\gamma \propto a_{\mathcal{D}}^{-1}$. Reversibility therefore does not require fixed $\hbar\omega_\gamma$ in a time-dependent background; it excludes irreversible conversion into heat, longitudinal motion, or configurational disorder. The photon mode and its reversible loading cycle were established in Sec. 4. Locally,

$$\oint \sigma_{ij}\, d\epsilon_{ij} = 0, \qquad \partial_t \mathcal{E}_{\rm tot} + \boldsymbol{\nabla}\cdot\mathbf{S}_{\rm ac} = 0, \tag{469}$$

while possible cosmological leakage must be specified separately.

Possible irreversible leakage is separately encoded by the retarded transverse-mode propagator,

$$\omega^2 - c^2k^2 - \Sigma_R(\omega, k) = 0, \qquad \Gamma_\gamma = -\frac{\mathrm{Im}\,\Sigma_R}{2\omega}. \tag{470}$$

The real part of Σ_R renormalizes the elastic inertia and stiffness, whereas its imaginary part measures conversion into internal relaxational channels. On the maximally stiff on-shell branch, transversality, fixed contact topology, and energy–momentum and polarization selection isolate the two photon

© 2026 by the author(s). Distributed under a Creative Commons CC BY license.

Preprints.org (www.preprints.org) | NOT PEER-REVIEWED | Posted: 7 September 2026 doi:10.20944/preprints202608.2283.v2

helicities from the submaximal longitudinal and configurational modes. The ideal constitutive limit therefore has

$$\mathrm{Im}\,\Sigma_R(\omega_\gamma, k) = 0, \qquad \Gamma_\gamma = 0, \tag{471}$$

while a nonideal realization remains observationally transparent provided

$$2\int_{t_{\rm em}}^{t_0} \Gamma_\gamma(t)\, dt \ll 1. \tag{472}$$

The separation between reversible redshift and dissipative attenuation is made explicit by the adiabatic wave action. For $\epsilon_{\rm ad} \equiv H_{\mathcal{D}}/\omega_\gamma \ll 1$, define for each comoving helicity mode

$$\mathcal{I}_{\mathbf{k},\lambda} \equiv \frac{E_{\mathbf{k},\lambda}}{\omega_\gamma} = \hbar N_{\mathbf{k},\lambda}. \tag{473}$$

Its leading transport equations are

$$\frac{d\ln\omega_\gamma}{dt} = -H_{\mathcal{D}}, \qquad \frac{d\ln\mathcal{I}_{\mathbf{k},\lambda}}{dt} = -2\Gamma_\gamma + \mathcal{O}(\epsilon_{\rm ad}^2). \tag{474}$$

Hence, in the ideal saturation-fixed branch, the occupation of a comoving mode is conserved even though the energy per photon redshifts:

$$\begin{aligned} N_{\mathbf{k},\lambda} &= \text{const.}, \quad E_\gamma = \hbar\omega_\gamma \propto a_{\mathcal{D}}^{-1}, \\ n_\gamma &\propto a_{\mathcal{D}}^{-3}, \qquad \rho_\gamma \propto a_{\mathcal{D}}^{-4}. \end{aligned} \tag{475}$$

The first factor is the redshift of each quantum and the second is the ordinary material-volume dilution of photon number. No cumulative "tired-light" scattering, image blurring, or entropy-producing spectral degradation is invoked. Any residual nonzero Γ_γ is an additional attenuation channel, constrained independently of the scale-factor redshift.

The equations above define the material interpretation of expansion, scale-factor redshift, photon-number dilution, and conservative transverse-mode transport. A dedicated cosmological development must use the common DDF parameters to calculate the background coefficients, primordial perturbations, CMB and BAO observables, light-element abundances, and nonlinear vortex-network evolution. The present construction therefore establishes the kinematic background correspondence; recovery of the full hot Big Bang observational structure remains a quantitative test of the model.

18. Conclusions

Although material-substrate theories are not new, the distinctive result of the DDF construction is that, within a dilatant-fluid framework, the exact Lorentz factor is derived from the constitutive mechanics of a fundamental two-component medium, drawing on the established classical physics of shear thickening and stress-induced jamming applied to the dark sector:

$$\gamma_\varphi(v) = \frac{1}{\sqrt{1 - v^2/c^2}},$$

with the limiting speed c fixed by the saturated transverse response of the dispersed φ phase. In the DDF ontology, this material medium assumes the foundational role assigned to spacetime geometry in standard relativity. The geometric description is not discarded, but physically reinterpreted: Lorentz geometry encodes the common material kinematics generated by the φ-sector jamming response, while the curved geometries of GR provide the quantitative macroscopic encoding of the Bernoulli pressure, specific-enthalpy, and superflow structure realized in the coherent ϕ medium. Electromagnetic radiation and LVK-class transverse disturbances belong instead to the φ sector, sharing its saturation-fixed luminal propagation scale while remaining physically distinct excitations.

© 2026 by the author(s). Distributed under a Creative Commons CC BY license.

Preprints.org (www.preprints.org) | NOT PEER-REVIEWED | Posted: 7 September 2026 doi:10.20944/preprints202608.2283.v2

The Lorentz factor is therefore neither introduced as a kinematic postulate nor assigned phenomenologically to a material ether. The corresponding transformations of material lengths, clock rates, momentum, energy, and electromagnetic propagation follow from the same speed-dependent material response. A uniformly moving substrate consequently cannot be revealed by ordinary local inertial measurements, because the DDF itself governs the rods, clocks, particles, and signals by which those measurements are performed. In this sense, the DDF provides a concrete example in which a material substrate and Lorentz invariance are not competing assumptions: *the invariance is a consequence of the material dynamics*.

This reduction of Lorentz kinematics to material constitutive dynamics is accompanied by an analogous reduction in gravitation. Gravity is not introduced as an additional fundamental interaction and does not require an independently quantized metric or graviton. It is identified with the Bernoulli force of the coherent ϕ superfluid, $\mathbf{g}_\phi = -\boldsymbol{\nabla} h_\phi$, with $\mathbf{g}_\phi = -(\boldsymbol{\nabla} P_\phi)\varrho_{\phi,0}^{-1}$ in the nearly incompressible limit. Quantized ϕ-vortices generate Bernoulli pressure fields individually, while bound and composite vortex configurations generate the corresponding collective source fields. The classical character of observable gravity is therefore compatible with a microscopic quantum origin: the same vortex architecture whose quantized circulation and winding encode the intrinsic structure of massive particles, including their spin, also generates the hydrodynamic pressure field from which gravity emerges. Gravity is thus identified with the Bernoulli force generated by the hydrodynamic spin of vortex matter: the toroidal–poloidal winding ratio $s_{\mathrm{v}} = n_\theta / n_\chi$ determines the associated circulation and superflow, whose pressure gradient produces the gravitational acceleration.

The division of roles between the two DDF components is essential. The dispersed φ sector supplies the universal inertial and chronometric response responsible for Lorentz-form kinematics, whereas the superfluid ϕ sector supplies the Bernoulli pressure and superflow structure responsible for gravitation. The resulting material fields can be represented geometrically by Painlevé–Gullstrand variables and, where the corresponding benchmark is recovered, by the Einstein equations. Those geometric quantities are therefore macroscopic encodings of the DDF solution rather than independent microscopic degrees of freedom. The agreement with relativistic geometry is therefore both mathematical and operational: the DDF reproduces the corresponding Lorentz-form relations and GR benchmark equations, and thus the same numerical predictions within their domain of validity, without requiring the geometric and material descriptions to share the same ontology. The transverse φ-phonon sector follows the same economy. Photons are quanta of the electromagnetically coupled, saturation-fixed transverse φ-phonon branch, whose propagation speed is determined by

$$c^2 = \frac{G_\varphi^{\max}}{\varrho_\varphi^{\max}} = \frac{1}{\varrho_\varphi^{\max} j_\varphi^{\min}}.$$

LVK-class signals are physically distinct macroscopic transverse shear disturbances of the same dispersed phase, generated when binary or merger dynamics stress the φ medium collectively. Their common luminal speed reflects the same saturated stiffness-to-inertia ratio, not an identity between photons and LVK excitations and not the propagation of a fundamental gravitational quantum. Electromagnetic radiation, relativistic inertia, and the luminal LVK carrier can therefore be related to one material sector, while gravity, identified with the Bernoulli force, remains a separate ϕ-sector phenomenon.

The same two-component medium also supplies a common route to the larger-scale phenomenology considered in this work. In galaxies, the pressure and superflow fields of the pre-existing ϕ medium govern stellar dynamics and the deflection of photon trajectories, without requiring a separately accumulated galaxy-centered φ-mass halo. In the weakly forced outskirts, the approximately isothermal ϕ closure yields the flat outer rotation profile, while coherent circulation of the superfluid motivates the vortex-bundle interpretation of cosmic filaments. Filament rotation by itself is not distinctive, since conventional structure formation can also generate large-scale angular momentum; the proposed signature is instead the combined finite-core, longitudinally coherent, node-connected,

© 2026 by the author(s). Distributed under a Creative Commons CC BY license.

Preprints.org (www.preprints.org) | NOT PEER-REVIEWED | Posted: 7 September 2026 doi:10.20944/preprints202608.2283.v2

statistically unpolarized circulation pattern developed in Appendix B.2. Cosmological deformation is likewise treated as a macroscopic state of the same material substrate rather than as an independent sector appended to the theory.

The quantum-completion route of Sec. 15 preserves this economy. The material substrate and vortex-supported matter are already quantum many-body systems governed by the common Hamiltonian $\hat{H}_{\mathrm{DDF}}$, so no separate quantum geometry is required. Further microscopic reduction concerns the explicit Hamiltonian realization of results already fixed at the material level—including the all-speed dressed-vortex dispersion and the state-dependent source and correlation structure—together with the detailed source–carrier–detector coupling of the LVK channel. These are refinements of the microscopic implementation, not missing physical principles of the DDF construction. Likewise, G_ϕ appears only as the macroscopic coefficient used to express the coarse-grained Bernoulli source–field relation in conventional Newtonian form, not as a new fundamental gravitational coupling requiring independent quantization.

The clearest direct distinction from GR lies in the active gravitational sourcing of freely propagating radiation. In the DDF source ontology, a free on-shell photon carries energy and momentum but does not independently establish the ϕ-sector Bernoulli sink associated with vortex-supported matter and bound configurations. GR instead includes freely propagating radiation in the active stress–energy source [255–257]. A reciprocal gravitational interaction between freely propagating photons with the GR scaling would therefore falsify this DDF source rule. Conversely, a sufficiently sensitive null result capable of excluding the corresponding GR signal would provide a distinctive positive test of the DDF gravitational ontology. The filament-circulation test of Appendix B.2, together with the proposed laboratory tests of the dilatant response developed in the Appendices, would provide complementary probes of the DDF material interpretation.

The present construction is intended as a foundational step toward a broader DDF research program, encompassing microscopic completion, Standard Model embedding, a quantum-hydrodynamic reframing of the Higgs sector, further quantitative phenomenology beyond the exactly recovered relativistic benchmarks, cosmological development, and dedicated experimental tests. Its central objective is to determine whether these sectors can remain quantitatively consistent as consequences of a single two-component quantum-hydrodynamic substrate.

Appendix A. Compatibility with Established Precision Tests in the DDF Framework

The DDF material-spacetime kinematic closure is locally Lorentz-form. For a body measured at speed u in a laboratory material frame,

$$d\tau_{\mathcal{D}} = \frac{dt}{\gamma_\varphi(u)}, \tag{A1}$$

and the saturation-fixed dispersions are

$$\boxed{E_\gamma = p_\gamma c, \qquad \omega_\gamma = ck, \qquad E_m^2 = p_m^2 c^2 + m^2 c^4.} \tag{A2}$$

These relations use observer-relative three-speeds and the invariant DDF four-speed in each stated local material comparison.

Michelson–Morley, Kennedy–Thorndike, and symmetric resonators.

Local photon propagation at c, together with the material Lorentz transformation of rods and clocks, gives identical round-trip proper times in all orientations. The observed nulls therefore follow from the same Lorentz-form spatial, chronometric, and electromagnetic relations as in SR and do not distinguish the material DDF ontology from the geometric SR description [14,16].

© 2026 by the author(s). Distributed under a Creative Commons CC BY license.

Preprints.org (www.preprints.org) | NOT PEER-REVIEWED | Posted: 7 September 2026 doi:10.20944/preprints202608.2283.v2

Modern high-precision Lorentz-invariance tests.

Modern rotating resonator experiments extend these tests to progressively higher precision, including cryogenic sapphire oscillators and optical resonators in the experiments of Stanwix, Herrmann, Nagel, and collaborators [18–20,153]. In the DDF framework, however, their compatibility is not a matter of experimental precision or of an approximate recovery of Lorentz invariance. The DDF closure developed here gives the same Lorentz-form transformations of material lengths, clock rates, resonance frequencies, and electromagnetic propagation as SR, while the transverse φ-phonon branch propagates locally at the universal speed c. The orientation- and boost-dependent observables tested by these experiments therefore have the same functional form and yield the same null predictions as in SR, including at the precision reached by modern resonator experiments.

Decay clocks and fast-ion spectroscopy.

For atmospheric or accelerator muons, $P = \exp[-L/(u\gamma_\varphi(u)\tau_{\mathcal{D},0})]$. Ives–Stilwell-type experiments retain

$$\frac{\nu_{\rm app} + \nu_{\rm rec}}{2} = \nu_0\gamma_\varphi(u), \tag{A3}$$

as observed [258–262]. These experiments test the local DDF proper-time law and its Lorentz-form speed dependence.

Bound-electron orientation and accelerator-threshold tests.

The translational factor depends on the measured center-of-vortex speed, not on spin orientation or the orientation of a bound momentum distribution. Hughes–Drever and trapped-ion orientation nulls are therefore compatible with an isotropic DDF material spacetime. The common limiting speed of the massive and photon branches also prevents local vacuum Cherenkov emission or spontaneous photon decay [263–269].

Collisions, Compton edges, and synchrotron motion.

The conservative vortex–sheath–field functionals preserve the accelerator-supplied material dressing energy and yield the standard asymptotic dispersion and Mandelstam relations. Compton-edge and synchrotron observables therefore use the measured beam speed u and $\gamma_\varphi(u)$. Their precision constrains the proposed microscopic interaction and radiation closures [270,271].

Dielectric propagation, aberration, and electromagnetic stress.

Fresnel–Fizeau drag, Airy-type aberration, asymmetric-ring nulls, and the Trouton–Noble balance remain tests of the coupled electromagnetic–material response. At leading order their established Lorentz-form results are reproduced; dispersion, interfaces, and the complete stress tensor provide the relevant higher-order constitutive constraints [17,272–278].

Empirical classification.

The tests above establish severe consistency requirements on the local DDF material-spacetime law, but they do not distinguish its material ontology from SR. Source-dependent gravitational observations still test the Bernoulli and propagation sectors. The direct ontology-level difference is the active gravitational sourcing of freely propagating on-shell photons, examined in Appendix B.1.

Appendix B. Prospective Empirical Tests and Laboratory Constitutive Tests

Under the material-spacetime closure, local symmetric kinematic tests retain Lorentz form. The principal direct discriminant examined below is the active gravitational sourcing of freely propagating photons, which tests the DDF source rule against GR. The proposed filament-circulation observation probes the superfluid interpretation of the cosmic web, while the two laboratory protocols test constitutive plausibility rather than the cosmic substrate directly. Their differing empirical status is stated separately.

© 2026 by the author(s). Distributed under a Creative Commons CC BY license.

Preprints.org (www.preprints.org) | NOT PEER-REVIEWED | Posted: 7 September 2026 doi:10.20944/preprints202608.2283.v2

Appendix B.1. Gravity as Bernoulli Force: Testing the Active Gravitational Sourcing of On-Shell Photons

Competing source rules.

GR assigns active gravitational sourcing to the complete stress–energy tensor, including freely propagating radiation [255–257]. In the DDF framework, by contrast, gravity is the persistent ϕ-sector Bernoulli field

$$\mathbf{g}_\phi = -\frac{\boldsymbol{\nabla} P_\phi}{\varrho_{\phi,0}} \equiv -\boldsymbol{\nabla}\Phi_\phi, \tag{A4}$$

generated by quantized-vortex defects and bound configurations that sustain a pressure deficit in the superfluid background. On-shell photons are transverse φ modes: they are passively advected by an existing $(\Phi_\phi, \mathbf{v}_\phi)$ carrier background,

$$(\omega - \mathbf{k}\cdot\mathbf{v}_\phi)^2 = c^2k^2, \tag{A5}$$

but are not assumed to generate an independent $\boldsymbol{\nabla} P_\phi$.

Introduce

$$T^{\text{source}}_{\mu\nu} = T^{\text{def/bound}}_{\mu\nu} + \eta^{\text{act}}_\gamma T^{\gamma,\text{on}}_{\mu\nu}, \tag{A6}$$

with

$$H_{\text{GR}}:\ \eta^{\text{act}}_\gamma = 1, \qquad H_{\text{DDF}}:\ \eta^{\text{act}}_\gamma = 0. \tag{A7}$$

The discriminant is therefore the additional gravitational influence of one free radiation distribution on another, not the passive fall, deflection, or redshift of light in a pre-existing gravitational field.

The distinction concerns the physical origin of gravitational sourcing. A confirmed mutual photon–photon gravitational interaction would support the GR rule that freely propagating energy contributes directly to the active source. A verified null at the sensitivity required to resolve the GR signal would instead disfavor that universal source rule and support the DDF alternative, in which gravity arises from vortex-supported Bernoulli deficits rather than from every form of energy. Within this interpretation, the result would also be consistent with, and would lend indirect support to, the material superfluid ϕ background required by the DDF to host the quantized-vortex defects. It would not uniquely establish that substrate, because alternative source ontologies could in principle produce the same null.

Non-co-propagating dual-beam test.

Two laterally separated or skew beams, or synchronized pulse trains, are arranged with minimum separation $b > 0$ and crossing angle

$$0 < \Theta \le \pi. \tag{A8}$$

The exactly co-propagating limit is unsuitable because the leading GR interaction cancels. For the inward transverse changes of the two outgoing wavevectors define

$$\begin{aligned} \delta\theta_1 &\equiv \frac{\Delta\mathbf{k}_{\perp,1}\cdot\widehat{\mathbf{b}}_{12}}{|\mathbf{k}_1|}, \\ \delta\theta_2 &\equiv -\frac{\Delta\mathbf{k}_{\perp,2}\cdot\widehat{\mathbf{b}}_{12}}{|\mathbf{k}_2|}. \end{aligned} \tag{A9}$$

For finite beams the GR response scales as

$$\alpha^{\text{GR}}_{1\leftarrow 2} = \mathcal{K}_{1\leftarrow 2}\frac{GE_2}{c^4 b}, \tag{A10}$$

$$\alpha^{\text{GR}}_{2\leftarrow 1} = \mathcal{K}_{2\leftarrow 1}\frac{GE_1}{c^4 b}, \tag{A11}$$

© 2026 by the author(s). Distributed under a Creative Commons CC BY license.

Preprints.org (www.preprints.org) | NOT PEER-REVIEWED | Posted: 7 September 2026 doi:10.20944/preprints202608.2283.v2

where the dimensionless kernels depend on Θ, beam widths, pulse durations, timing, diffraction, and the complete transverse and longitudinal profiles. They satisfy

$$\mathcal{K}_{i\leftarrow j} \to 0 \qquad (\Theta \to 0), \tag{A12}$$

and for quasi-continuous beams the energy simultaneously present in the interaction region is

$$E_i^{\mathrm{int}} \simeq \frac{P_i L_{\mathrm{int}}}{c}. \tag{A13}$$

The direct DDF prediction for the mutual gravitational interaction of the on-shell photon distributions is

$$\boxed{\alpha_{1\leftarrow 2}^{\mathrm{DDF}} = \alpha_{2\leftarrow 1}^{\mathrm{DDF}} = 0.} \tag{A14}$$

The absolute beam trajectories may still respond to static gravitational fields generated by the Earth, the apparatus, and other persistent sources; the experiment isolates only the coincidence-synchronous mutual term produced by the freely propagating beams.

Alternate an interaction configuration, in which both beams occupy the near-passage region, with a reference configuration having matched emitters, absorbers, power flow, and mechanical loading but no simultaneous near passage. Define

$$\Delta\theta_i \equiv \theta_i^I - \theta_i^R \tag{A15}$$

and the reciprocal inward estimator

$$\mathcal{A}_{12} \equiv \frac{1}{2}\left(\Delta\theta_1^{\mathrm{in}} + \Delta\theta_2^{\mathrm{in}}\right). \tag{A16}$$

GR predicts $\mathcal{A}_{12} > 0$, with the calculated dependence on beam energy and geometry, whereas DDF predicts $\mathcal{A}_{12} = 0$.

A valid GR template must include the complete conserved source,

$$\begin{aligned} T_{\mu\nu}^{\mathrm{total}} = {} & T_{\mu\nu}^{\mathrm{beam}} + T_{\mu\nu}^{\mathrm{emitter}} + T_{\mu\nu}^{\mathrm{absorber}} \\ & + T_{\mu\nu}^{\mathrm{power\,supply}} + T_{\mu\nu}^{\mathrm{return\,path}} + T_{\mu\nu}^{\mathrm{support}}, \end{aligned} \tag{A17}$$

so the experimental subtraction must preserve all nonpropagating loads as closely as possible.

Controls, feasibility, and inference.

The candidate signal must vanish under temporal non-overlap and approach the co-propagating null; it must reverse with the signed impact parameter, scale with the energy of the opposite beam, and survive beam-label interchange. Residual gas, plasma, thermal lensing, nonlinear refraction, scattered light, radiation-pressure recoil, mirror motion, support strain, electromagnetic pickup, and absorber loading require independent monitoring and modulation controls. Polarization and wavelength scans can help distinguish a gravitational signal from optical cross-talk.

The fundamental scale is extraordinarily small: for $E \sim 30\,\mathrm{J}$ and $b \sim 1\,\mu\mathrm{m}$, $4GE/(c^4 b) \sim 10^{-36}$ before the geometry kernel. High pulse energy, long interaction length, repeated crossings, pulse stacking, balanced interferometry, and heterodyne or spatial-mode homodyne readout may improve sensitivity, but they do not remove the G/c^4 suppression. The protocol is therefore a theoretically decisive future discriminant rather than a near-term experiment.

Define

$$\widehat{\eta}_\gamma^{\mathrm{act}} \equiv \frac{\mathcal{A}_{12}^{\mathrm{meas}} - \mathcal{A}_{12}^{\mathrm{nongrav}} - \mathcal{A}_{12}^{\mathrm{apparatus}}}{\mathcal{A}_{12}^{\mathrm{GR}}}. \tag{A18}$$

© 2026 by the author(s). Distributed under a Creative Commons CC BY license.

Preprints.org (www.preprints.org) | NOT PEER-REVIEWED | Posted: 7 September 2026 doi:10.20944/preprints202608.2283.v2

Then

$$\widehat{\eta}_{\gamma}^{\mathrm{act}} \simeq \begin{cases} 1, & \text{universal GR-like sourcing,} \\ 0, & \text{DDF direct on-shell-photon null.} \end{cases} \tag{A19}$$

A reciprocal deflection with the predicted GR geometry, energy, and timing scaling would falsify the DDF source rule. Conversely, a statistically significant null would falsify the corresponding standard-GR prediction that freely propagating on-shell radiation contributes directly to the active gravitational source, provided that

$$\sigma(\widehat{\eta}_{\gamma}^{\mathrm{act}}) \ll 1 \tag{A20}$$

and the calculated GR signal lies above the independently verified systematic floor.

Under those conditions, a DDF-predicted null would have a broader significance than the exclusion of a single photon-sourcing term. It would favor a source ontology in which gravitational fields are generated by vortex-supported material structures and by the bound and configurational energy that modifies their Bernoulli source strength, rather than universally by every form of energy. In the DDF framework, those structures are quantized-vortex defects whose sustained Bernoulli pressure deficits require a coherent superfluid ϕ background. The result would therefore support not only the exclusion of freely propagating on-shell photons from the active gravitational source, but also the vortex-based Bernoulli mechanism and, indirectly, the material superfluid substrate on which that mechanism depends.

The evidential significance of such a result would be strengthened by the internal economy and explanatory scope of the framework. The DDF is not introduced solely as an alternative gravitational source rule, but as a single bicomponent material ontology from which several physical sectors are developed. Within the stated constitutive closure, the Lorentz-form jamming factor follows from the limiting-branch response of the dispersed φ phase rather than being inserted as an independent phenomenological factor. Likewise, once the coherent superfluid ϕ background and its quantized-vortex defects are admitted, circulation-induced Bernoulli pressure gradients provide a natural material origin for gravitational attraction. A null favoring the DDF photon-source rule would thus support a gravitational mechanism structurally linked to the same substrate used to account for transverse radiation and Lorentz-form material kinematics, rather than an isolated modification devised for this particular test. The experiment would directly discriminate between the source rules in Eq. (A7).

Appendix B.2. Local Spin of Cosmic Filaments as a Potential Superfluid-Origin Signature

The DDF cosmic-web hypothesis permits coherent circulation in individual filament bundles while the ensemble remains statistically unpolarized. Conventional tidal torques, mergers, and anisotropic accretion can also generate large-scale angular momentum, so the detection of filament rotation alone would not uniquely select the DDF. The discriminating test must instead combine several properties of the same velocity field: a resolved finite-core transverse circulation profile, signed persistence along the filament, kinematic continuity with its endpoint nodes, a high occurrence rate among dynamically cold filaments, and circulation amplitudes consistent with the common DDF parameters entering the large-scale construction of Sec. 16.

For an oriented filament tangent $\hat{\boldsymbol{\ell}}_f$ and line of sight $\hat{\mathbf{n}}$, define

$$\mathbf{e}_{1,f} = \frac{\hat{\mathbf{n}} \times \hat{\boldsymbol{\ell}}_f}{|\hat{\mathbf{n}} \times \hat{\boldsymbol{\ell}}_f|}, \qquad \sin i_f = |\hat{\mathbf{n}} \times \hat{\boldsymbol{\ell}}_f|. \tag{A21}$$

The orientation convention for $\hat{\boldsymbol{\ell}}_f$ must be fixed from the reconstructed filament geometry before examining the velocity data, and segments with poorly conditioned $\sin i_f$ are excluded. For transverse coordinate y,

$$v_{\mathrm{los}} - v_{\mathrm{sys}} = b_{\mathrm{ent}} v_{\phi}(r) \sin i_f \frac{y}{r} + v_{\mathrm{nuis}}, \tag{A22}$$

© 2026 by the author(s). Distributed under a Creative Commons CC BY license.

Preprints.org (www.preprints.org) | NOT PEER-REVIEWED | Posted: 7 September 2026 doi:10.20944/preprints202608.2283.v2

where $b_{\rm ent}$ transfers the underlying DDF flow velocity to the chosen tracer and $v_{\rm nuis}$ contains infall, tidal flow, redshift-space distortions, tracer dispersion, and measurement noise. The initial side-to-side statistic is

$$\widehat{\Delta v}_{AB}(r) = \frac{c[\bar{z}_A(r) - \bar{z}_B(r)]}{1+z_f}, \tag{A23}$$

but a circulation claim requires a signed transverse profile fit in the predefined geometrical basis.

A minimal finite-core bundle profile is

$$\begin{aligned} v_\phi(r) &= \begin{cases} \Omega_b r, & r \le R_b, \\ \Omega_b R_b^2/r, & r > R_b, \end{cases} \\ \Gamma_b &= 2\pi R_b^2 \Omega_b = N_{{\rm net},b}\frac{h}{m_\phi}. \end{aligned} \tag{A24}$$

The first branch describes a regular finite core and the second the exterior circulation profile. The last equality expresses the DDF vortex-bundle scaling. Its evidential content requires m_ϕ to be common to the filament population and the bundle and entrainment quantities not to be treated as arbitrary continuous amplitudes independently adjustable for each filament.

A local detection statistic may be defined by

$$S_{\rm spin} = 2\Big[\ln \mathcal{L}(\widehat{\Omega}_b, \widehat{R}_b, \widehat{b}_{\rm ent}) - \ln \mathcal{L}(\Omega_b = 0)\Big], \tag{A25}$$

with its null distribution calibrated from matched nonrotating and conventional structure-formation mocks. The fitted sign of Ω_b is retained rather than discarded.

Define the orientation-independent circulation vector

$$\widehat{\boldsymbol{\Gamma}}_f = \widehat{\Gamma}_f \hat{\boldsymbol{\ell}}_f, \tag{A26}$$

where reversal of the geometrical filament orientation reverses the fitted signed scalar $\widehat{\Gamma}_f$ as well, leaving the physical circulation vector unchanged. Longitudinal coherence is then measured by

$$C_\Gamma(\Delta s) = \frac{\left\langle \widehat{\boldsymbol{\Gamma}}(s)\cdot\widehat{\boldsymbol{\Gamma}}(s+\Delta s)\right\rangle}{\sqrt{\left\langle |\widehat{\boldsymbol{\Gamma}}(s)|^2\right\rangle\left\langle |\widehat{\boldsymbol{\Gamma}}(s+\Delta s)|^2\right\rangle}}, \tag{A27}$$

so that a vortex-bundle interpretation requires a resolved positive coherence range along the filament rather than an isolated transverse velocity gradient.

For a filament terminating at a node with reconstructed kinematic-vorticity vector $\widehat{\boldsymbol{\omega}}_N$, define the node-continuity excess

$$\Delta C_{fN} = \left\langle \frac{\widehat{\boldsymbol{\Gamma}}_f \cdot \widehat{\boldsymbol{\omega}}_N}{|\widehat{\boldsymbol{\Gamma}}_f||\widehat{\boldsymbol{\omega}}_N|} \right\rangle - C_{fN}^{\rm shuf}, \tag{A28}$$

where the shuffled baseline preserves the filament and node samples while destroying their physical pairings. A positive excess tests whether the signed circulation remains kinematically connected to the endpoint dynamics rather than appearing as an unrelated local velocity asymmetry.

The hypothesis also makes an ensemble-level statement. Let $f_{\rm spin}$ denote the fraction of filaments satisfying a predefined circulation-detection threshold. It should be measured as a function of a dynamical-coldness indicator, such as the residual velocity dispersion about the fitted coherent flow,

$$f_{\rm spin}(\sigma_{\rm res}) = \frac{N(S_{\rm spin} > S_\star\,;\,\sigma_{\rm res})}{N_{\rm fil}(\sigma_{\rm res})}. \tag{A29}$$

© 2026 by the author(s). Distributed under a Creative Commons CC BY license.

Preprints.org (www.preprints.org) | NOT PEER-REVIEWED | Posted: 7 September 2026 doi:10.20944/preprints202608.2283.v2

The DDF vortex-bundle interpretation is strengthened if coherent finite-core circulation is common in the dynamically cold subset rather than being confined to disturbed, strongly accreting, or merging filaments. At the same time, statistical isotropy requires no preferred circulation handedness. For any geometrically fixed orientation convention,

$$A_{\rm sign} = \frac{N_+ - N_-}{N_+ + N_-} \simeq 0 \tag{A30}$$

for a sufficiently large unbiased sample, even though individual filaments may retain a definite signed circulation over large longitudinal distances.

A credible DDF-oriented signal therefore requires the joint occurrence of (i) a resolved finite-core circulation profile, (ii) a positive longitudinal-coherence range, (iii) node-continuity excess, (iv) widespread occurrence among dynamically cold filaments, (v) statistical absence of a preferred global circulation sign, and (vi) circulation amplitudes consistent, in a population-level analysis, with the common DDF parameters and vortex-bundle scaling of Eq. (A24).

The complete pipeline must be applied without modification to conventional structure-formation mocks with matched environment, accretion history, spine reconstruction, tracer selection, peculiar velocities, redshift-space distortions, and survey boundaries. Antisymmetric kSZ stacking may provide an independent gas-velocity channel. Because conventional tidal-torque and anisotropic-accretion mechanisms can themselves generate coherent filament rotation, support for a DDF superfluid origin would arise only if the combined finite-core, longitudinal, node-connected, population, and circulation-scaling pattern is observed and is not reproduced with comparable frequency and structure by the conventional mocks.

Conversely, a robust absence of the predicted finite-core and coherent circulation pattern in the dynamically cold filament population, at sensitivity sufficient to test the DDF parameter range specified by the large-scale construction, would falsify the corresponding vortex-bundle realization rather than the general existence of cosmic-filament angular momentum.

Appendix B.3. Laboratory Test of a Transverse-Wave-Speed Limit in Dynamically Shear-Jammed Matter

Dense shear-thickening suspensions provide, in some respects, an accessible laboratory analog of the constitutive stiffening and jamming mechanism assigned to φ. The proposed experiment tests a specific correspondence that has not yet been established for ordinary dilatant materials: whether the transverse elastic-wave speed c_T of a dynamically jammed medium acts as an unattainable upper speed boundary for a material intruder as long as the dynamically generated, load-bearing jammed region is not fractured or destroyed. The hypothesis is therefore that the intruder remains restricted to $v < c_T$, with increasing mechanical resistance as c_T is approached from below, while $v = c_T$ itself cannot be attained as long as the load-bearing jammed region remains unbroken.

Indeed, an ordinary laboratory suspension has finite material strength, and dynamically jammed structures can fracture or be destroyed under sufficiently strong loading [279–283]. The saturated φ state of the DDF, by contrast, is not assigned a corresponding finite-energy failure channel. This distinction is not introduced as an independent protective postulate, but follows from the DDF saturated-state closure, in which the cosmic φ medium reaches an extraordinarily high-density, high-rigidity saturated state. As $v \to c^-$, the speed-dependent constitutive jamming factor grows without bound, corresponding physically to the asymptotic impenetrability of the medium to massive matter, while transverse φ-phonon waves propagate through the same saturated state at c. The same constitutive limit therefore makes c unattainable for massive bodies while defining the propagation speed of the transverse mechanical φ-phonon branch, whose quanta are identified with photons in the DDF framework.

© 2026 by the author(s). Distributed under a Creative Commons CC BY license.

Preprints.org (www.preprints.org) | NOT PEER-REVIEWED | Posted: 7 September 2026 doi:10.20944/preprints202608.2283.v2

Let $\mathcal{J}_{\mathrm{jam}} = 1$ denote a dynamically jammed region that remains load-bearing and unbroken during the motion. The proposed limiting condition is then

$$\boxed{\mathcal{J}_{\mathrm{jam}} = 1 \quad \Longrightarrow \quad v < c_T,} \tag{A31}$$

where $\mathcal{J}_{\mathrm{jam}} = 0$ denotes fracture or destruction of that load-bearing jammed region. Defining $v_{\max}^{\mathrm{jam}}$ as the greatest intruder speed attained before such fracture or destruction,

$$\boxed{v_{\max}^{\mathrm{jam}} < c_T,} \tag{A32}$$

with the limiting value experimentally approached from below.

This condition does not forbid the intruder from subsequently reaching or exceeding c_T. In an ordinary suspension, sufficiently large supplied mechanical energy can fracture or destroy the dynamically jammed region, after which continued motion with $v \geq c_T$ can occur. The proposed restriction therefore concerns motion while the load-bearing jammed state remains unbroken, rather than an absolute speed limit of the laboratory material.

A servo-driven spherical or cylindrical intruder should translate through a well-characterized dense suspension, initially cornstarch and subsequently a density-matched silica or comparable system. A load cell and independent position sensor determine $F(t)$, $x(t)$, $v(t)$, and acceleration, while high-speed imaging, particle-image velocimetry, or ultrasound resolves the formation, evolution, continuity, fracture, and destruction of the dynamically jammed region. A lateral or torsional pulse introduced within the same stressed region directly measures its transverse elastic-wave speed c_T. In a predominantly elastic jammed state this speed should satisfy approximately

$$c_T(\sigma, \omega) \simeq \left[\frac{G'(\sigma, \omega)}{\varrho_{\mathrm{eff}}} \right]^{1/2}, \tag{A33}$$

where G' is the storage modulus of the jammed state and ϱ_{eff} its effective density. This quantity is the relevant transverse sound speed of the dynamically jammed, solid-like region and must be distinguished both from the acoustic response of the unjammed suspension and from the jamming-front propagation speed u_{f}.

Protocol and observables.

Reproducible acceleration ramps should drive the intruder progressively from the unjammed regime through shear thickening and into the dynamically jammed regime, continuing until fracture or destruction of the load-bearing jammed region occurs. Constant-velocity stages below this threshold may be used to characterize the quasi-steady resistance and the local value of c_T. The supplied mechanical work is

$$W(v) = \int_{x_1}^{x_2} F(x; v)\, dx, \tag{A34}$$

and the resistance observable $\mathcal{R}(v)$ may be expressed through force, work, or an effective inertial-loading quantity after independently calibrated viscous, inertial, and added-mass baselines have been removed.

Fracture or destruction must be identified independently of the force measurement, through direct observation of the loss of the load-bearing jammed structure, supported where useful by loss of coherent transverse-wave transmission or a discontinuous force drop. Let v_{fail} denote the intruder speed at the first detected fracture or destruction of the dynamically jammed region.

The central dimensionless control parameter is

$$\mathcal{M}_T \equiv \frac{v}{c_T}, \tag{A35}$$

© 2026 by the author(s). Distributed under a Creative Commons CC BY license.

Preprints.org (www.preprints.org) | NOT PEER-REVIEWED | Posted: 7 September 2026 doi:10.20944/preprints202608.2283.v2

with c_T measured locally in the stressed jammed region. The primary test is whether motion accompanied by an unbroken load-bearing jammed region remains restricted to

$$\mathcal{M}_T < 1, \tag{A36}$$

and whether attempted attainment of $\mathcal{M}_T = 1$ is accompanied by fracture or destruction before that speed can be reached while the jammed region remains unbroken. Operationally, the predicted relation is

$$\boxed{\begin{aligned} &v_{\mathrm{fail}} \lesssim c_T, \\ &\mathcal{J}_{\mathrm{jam}} = 0 \quad \text{for any sustained state with} \quad v \geq c_T. \end{aligned}} \tag{A37}$$

A positive result would require v_{fail} to approach or systematically track the independently measured c_T from below within experimental uncertainty. Sustained motion above c_T would therefore occur only after fracture or destruction of the load-bearing jammed region. A failure threshold controlled instead by fixed accumulated strain, elapsed time, imposed force, travel distance, or wall contact, with no corresponding dependence on c_T, would not support the proposed transverse-wave-speed interpretation.

A secondary analysis tests whether the mechanical cost of approaching the fracture threshold exhibits a strong nonlinear growth. A general limiting form may be fitted as

$$\begin{aligned} \mathcal{R}(v) &= \mathcal{R}_{\mathrm{base}}(v) \\ &\quad + A\left[\left(1 - \frac{v^2}{c_*^2}\right)^{-p} - 1\right], \qquad v < v_{\mathrm{fail}}, \end{aligned} \tag{A38}$$

and compared with nondivergent power-law, exponential, viscoelastic, and fracture-controlled models. The parameters c_* and p should first be determined freely from the sub-failure data and only subsequently compared with the DDF-motivated values

$$c_* \simeq c_T, \qquad p \simeq \frac{1}{2}. \tag{A39}$$

An ordinary laboratory suspension need not realize the mathematical divergence because its finite material strength allows fracture or destruction to intervene first. The relevant DDF-motivated ordering is therefore

$$v_{\mathrm{max}}^{\mathrm{jam}} \simeq v_{\mathrm{fail}} \lesssim c_T \simeq c_*, \tag{A40}$$

where the strict theoretical condition while the jammed region remains unbroken is always $v_{\mathrm{max}}^{\mathrm{jam}} < c_T$, and the approximate relations above refer to finite experimental resolution.

Controls and interpretation.

The essential controls should determine whether the observed threshold is specifically associated with the dynamically jammed state and with its transverse elastic-wave speed c_T, rather than with ordinary drag, inertial loading, or an apparatus-imposed boundary. Particle fraction, intruder geometry, and container dimensions should therefore be varied over a suitable range, with corresponding measurements of the local c_T and of the fracture threshold v_{fail}. In particular, container dimensions should be sufficient to identify and exclude a threshold determined primarily by boundary-spanning jamming. The decisive signature would be that v_{fail} systematically tracks the independently measured c_T across these variations, while no corresponding transverse-wave-speed threshold appears when a load-bearing jammed region is not formed.

A positive result would require v_{fail} to track the independently measured c_T from below, with no unbroken load-bearing jammed state observed at $v \geq c_T$. A correlated nonlinear increase in resistance as $v \to c_T^-$ would further strengthen the constitutive analogy with the DDF. The laboratory medium

© 2026 by the author(s). Distributed under a Creative Commons CC BY license.

Preprints.org (www.preprints.org) | NOT PEER-REVIEWED | Posted: 7 September 2026 doi:10.20944/preprints202608.2283.v2

could nevertheless exceed c_T after finite-strength fracture, whereas the saturated cosmic φ closure retains the asymptotic massive-body barrier at c.

Conversely, reproducible $v \geq c_T$ with an unbroken load-bearing jammed region, or failure thresholds uncorrelated with the locally measured c_T, would disfavor the proposed transverse-wave-speed bound.

Appendix B.3.1. Possible Failure Threshold of the Saturated φ State

The laboratory comparison also defines the present scope of the analogy. Ordinary shear-jammed materials demonstrably possess finite material strength, whereas no corresponding finite-energy fracture channel is contained in the present DDF description of the saturated φ state. Its absence is therefore not an additional rule imposed to preserve the limiting speed, but belongs to the saturated constitutive closure associated with the extreme density and rigidity of the cosmic medium. Nevertheless, a more complete microscopic theory could in principle reveal that, above some presently unknown and extremely high stress or energy threshold, the saturated φ structure itself undergoes structural failure. Such a possibility is not predicted by the current DDF construction, but its consequences can be represented explicitly.

Let

$$\beta \equiv \frac{v}{c}, \qquad \beta_{\mathrm{f},0} \equiv \frac{v_{\mathrm{f},0}}{c} = 1 - \epsilon, \qquad 0 < \epsilon \ll 1, \tag{A41}$$

where $v_{\mathrm{f},0}$ is the hypothetical speed at which failure of the saturated φ structure might occur. Thus $\beta_{\mathrm{f},0}$ lies very close to, but below, the constitutive limit $\beta = 1$. For $\beta < \beta_{\mathrm{f},0}$, the speed-dependent jamming factor follows the Lorentz-form constitutive law. At $\beta = \beta_{\mathrm{f},0}$, structural failure would terminate the mechanism responsible for any further increase in jamming. The corresponding effective relation may then be represented as

$$\gamma_{\varphi}^{\mathrm{eff}}(\beta) = \begin{cases} \dfrac{1}{\sqrt{1-\beta^2}}, & \text{if } \beta < \beta_{\mathrm{f},0}, \\ \dfrac{1}{\sqrt{1-\beta_{\mathrm{f},0}^2}}, & \text{if } \beta \geq \beta_{\mathrm{f},0}, \end{cases} \tag{A42}$$

where the second branch is a constant horizontal plateau whose ordinate is fixed by the value of the jamming factor at the switching point $\beta = \beta_{\mathrm{f},0}$. It does not represent a continuation of the Lorentz-form law beyond failure. Rather, once the saturated structure has failed, increasing the speed to any

$$\beta_{\mathrm{f}} \equiv \frac{v_{\mathrm{f}}}{c} \geq \beta_{\mathrm{f},0}$$

would produce no additional increase in $\gamma_{\varphi}^{\mathrm{eff}}$: the speed-dependent jamming contribution would remain fixed at

$$\gamma_{\mathrm{f},0} \equiv \frac{1}{\sqrt{1-\beta_{\mathrm{f},0}^2}}. \tag{A43}$$

The corresponding kinetic-energy relation may then be represented schematically as

$$K(\beta) = \begin{cases} mc^2\left[\dfrac{1}{\sqrt{1-\beta^2}} - 1\right], & \beta < \beta_{\mathrm{f},0}, \\ K_{\mathrm{f},0} + \dfrac{1}{2}mc^2\left(\beta^2 - \beta_{\mathrm{f},0}^2\right), & \beta \geq \beta_{\mathrm{f},0}, \end{cases} \tag{A44}$$

where

$$K_{\mathrm{f},0} = mc^2(\gamma_{\mathrm{f},0} - 1) \tag{A45}$$

is the kinetic energy accumulated upon reaching the hypothetical structural failure threshold. Beyond $\beta_{\mathrm{f},0}$, no additional work would be required to increase the jamming factor, since its effective value would remain fixed at the horizontal plateau. Further supplied work would therefore contribute only

© 2026 by the author(s). Distributed under a Creative Commons CC BY license.

Preprints.org (www.preprints.org) | NOT PEER-REVIEWED | Posted: 7 September 2026 doi:10.20944/preprints202608.2283.v2

to the ordinary classical kinetic-energy increment represented by the second branch of Eq. (A44). In such a hypothetical post-failure regime, acceleration through $\beta = 1$ and subsequently to $\beta > 1$ would no longer encounter the Lorentz-form divergence, because the jammed structure responsible for that divergence would already have failed.

A finite structural-failure threshold would thus truncate the rising Lorentz-form jamming curve at $\beta_{\mathrm{f},0} \lesssim 1$, replacing the otherwise divergent branch by a constant plateau and leaving only classical acceleration beyond the failure point. Conversely, if no finite structural-failure threshold exists,

$$\epsilon \to 0^{+}, \qquad \beta_{\mathrm{f},0} \to 1^{-}, \qquad \gamma_{\mathrm{f},0} \to \infty, \tag{A46}$$

so that the hypothetical switching point is displaced to the constitutive limit and no finite plateau is reached. The original DDF result is then recovered: the jamming factor grows without bound as $v \to c^{-}$, and c remains unattainable for massive matter. Whether the cosmic φ medium possesses any finite structural-failure threshold is presently unknown; the current Lorentz-sector closure corresponds to the latter, non-failing case.

Appendix B.3.2. Possible High-Energy Destabilization of Vortex Matter

A logically distinct extreme-energy possibility concerns the mechanical stability of the vortex structure representing massive matter itself. In the DDF construction, a massive particle, distinct from the dark quanta of ϕ and φ, is a quantized vortex of the coherent ϕ medium dynamically dressed by the φ sector. The present theory assumes the stability of this vortex structure throughout the experimentally accessible regime, but it has not yet been established microscopically whether an arbitrarily large energy loading can be sustained without destabilizing or destroying the vortex itself.

One may therefore introduce, purely hypothetically, a critical vortex energy $E_{\mathrm{v}}^{\mathrm{crit}}$, such that

$$\begin{aligned} E_{\mathrm{v}} < E_{\mathrm{v}}^{\mathrm{crit}} \quad &\Longrightarrow \quad \text{stable vortex,} \\ E_{\mathrm{v}} \geq E_{\mathrm{v}}^{\mathrm{crit}} \quad &\Longrightarrow \quad \text{vortex destruction.} \end{aligned} \tag{A47}$$

Here E_{v} denotes the total energy carried by the dynamically dressed vortex configuration. Neither $E_{\mathrm{v}}^{\mathrm{crit}}$ nor its microscopic failure mechanism is presently derived.

If such a threshold existed, a vortex accelerated to sufficiently high energy, while its speed is already extremely close to c, could eventually cease to sustain the organized circulation that defines the massive particle. Destruction of the vortex would then convert its organized energy and its associated φ-sector dressing into phononic excitations of the two DDF components, schematically,

$$E_{\mathrm{v}} \longrightarrow E_{\phi}^{\mathrm{ph}} + E_{\varphi}^{\mathrm{ph}}, \tag{A48}$$

where the ϕ-sector phonons would remain dark, whereas the transverse φ-phonon component would be detectable as electromagnetic photons.

In the present DDF construction, electric charge belongs to the organized dynamics of the particle vortex itself. Destruction of the vortex would therefore also terminate the dynamical configuration responsible for its electric charge: the charge would be switched off together with the particle, rather than transferred to a separate carrier.

The experimental signature would be qualitatively different from ordinary synchrotron radiation. In ordinary emission, the accelerated particle survives while losing part of its supplied energy through radiation. Under the hypothetical vortex-failure mechanism, by contrast, the particle itself would disappear from the circulating beam once $E_{\mathrm{v}}^{\mathrm{crit}}$ were reached, with its organized vortex energy released into ϕ- and φ-phonon excitations and its electric charge disappearing together with the vortex configuration that sustains it. In the detectable sector, this could appear as an impulsive conversion of the particle energy into transverse φ-phonons, identified in the DDF framework with photons.

© 2026 by the author(s). Distributed under a Creative Commons CC BY license.

Preprints.org (www.preprints.org) | NOT PEER-REVIEWED | Posted: 7 September 2026 doi:10.20944/preprints202608.2283.v2

Observation in a future accelerator, at energies beyond those presently accessible, of reproducible disappearance of individual accelerated charged particles above a sharply defined energy threshold, accompanied by an impulsive photon release and after exclusion of conventional beam loss, scattering, decay, or instrumental effects, would therefore constitute a possible signature of vortex destruction induced by the extreme jamming response of the surrounding dark background. The relevant correlation would be with the energy supplied to the vortex particle rather than with β alone, since particles in present high-energy accelerators already reach $\beta \simeq 1$ to extremely high precision while their energy can continue to increase by orders of magnitude.

No such vortex-failure threshold is predicted by the present DDF closure, and the survival of accelerated particles in existing experiments implies only that, if such a threshold exists, it lies above the energies so far explored.

The possibility nevertheless distinguishes two logically separate ultra-high-energy limits of the theory: failure of the saturated φ background would terminate the further increase of the speed-dependent jamming factor responsible for the Lorentz-like speed barrier and could permit subsequent classical acceleration, whereas failure of the particle vortex would instead destroy the massive excitation itself at a finite energy before the asymptotic c limit is attained.

Appendix B.4. Laboratory Compatibility of Dilatancy with a Superfluid Continuous Phase and Possible Enhancement of the Dilatant Response

The minimal DDF requirement is coexistence: a coherent superfluid continuous phase must permit, rather than suppress, stress-induced shear thickening and jamming of a dispersed component capable of forming a load-bearing contact network. This does not require the equilibrium φ sector itself to possess the high dispersed-phase concentration characteristic of ordinary laboratory dilatant suspensions. In the DDF constitutive law, the excess jamming

$$\gamma_\varphi(v) - 1 = \frac{1}{\sqrt{1 - v^2/c^2}} - 1 \tag{A49}$$

remains negligible for $v \ll c$ and becomes strongly nonlinear only when the speed constitutes a substantial fraction of the transverse φ-phonon speed c. The relevant DDF behavior is therefore a stress- and velocity-induced jamming of the dispersed sector that distinctly emerges only at sufficiently large fractions of the transverse φ-phonon speed, rather than a requirement that the unperturbed background be intrinsically densely packed.

In this respect, the two-component configuration is qualitatively analogous to particle-doped superfluids, in which a coherent superfluid continuous phase coexists with a relatively sparse dispersed particulate component (see Figure 8) [41,71–73,102]. Although such systems do not establish dilatancy, they demonstrate the compatibility of superfluid coherence with a non-densely packed dispersed phase and provide a laboratory basis for testing whether strong forcing at large fractions of the relevant transverse-wave speed can drive that phase into shear thickening and jamming.

Enhancement of this response by low-dissipation interstitial transport in the superfluid continuous phase is a possible secondary effect, not a premise. The laboratory test should therefore determine first whether dilatancy remains possible when the carrier fluid becomes superfluid and, secondarily, whether the superfluid state modifies or enhances the resulting nonlinear response. For experimental accessibility, the same deliberately concentrated particulate suspension can be studied in liquid ^{4}He immediately above and below the lambda transition. The comparatively high particle concentration in this laboratory realization is an experimental means of bringing shear thickening and jamming into an accessible regime; it is not intended as a direct estimate of the equilibrium φ fraction of the cosmic DDF.

Cryogenically stable frictional particles such as micrometric silica or alumina are suitable initial candidates; more elaborate particles with a smaller density mismatch may follow. Existing particle-doped He II experiments already establish that dispersed particles can coexist with a superfluid

© 2026 by the author(s). Distributed under a Creative Commons CC BY license.

Preprints.org (www.preprints.org) | NOT PEER-REVIEWED | Posted: 7 September 2026 doi:10.20944/preprints202608.2283.v2

continuous phase and with quantized vortices [41,71–73,102], although they do not test the stress-induced shear-thickening and jamming response proposed here.

Apparatus and protocol.

A sealed annular-Couette or parallel-plate cryogenic cell with roughened surfaces should measure torque, shear rate, axial normal force, temperature, and, where possible, the particle-network structure by imaging or ultrasound. A movable boundary or compliant bellows permits a constant-normal-load measurement of the gap change Δh; under fixed-gap confinement define the contact-generated normal-force increment

$$\Delta N(\tau, \gamma, T) \equiv |N(\tau, \gamma, T)| - |N_0(T)|, \qquad \Delta N > 0$$

for dilatant loading. Differential pressure sensors can separate particle-network dilation from ordinary helium pressure transients.

At several near-jamming particle fractions, apply matched stress- and shear-rate ramps, startup, oscillatory, reversal, and drainage protocols first in He I, then through the lambda transition as the superfluid fraction grows, and finally during a warming cycle. Stress, accumulated strain, confinement, geometry, particle fraction, and preparation history should be matched across the transition. The apparent viscosity is

$$\eta_{\mathrm{app}} = \frac{\tau}{\dot{\gamma}}.$$

The principal observables are the onset stress and slope of the thickening branch, maximum η_{app}, normal force, gap dilation, dilation time, hysteresis, and the stress or strain at which a connected contact network forms.

Primary and secondary outcomes.

Compatibility requires a finite He-II interval satisfying

$$\left.\frac{\partial \eta_{\mathrm{app}}}{\partial \dot{\gamma}}\right|_{\mathrm{He\,II}} > 0$$

together with

$$\Delta h_{\mathrm{He\,II}} > 0 \qquad \text{or} \qquad \Delta N_{\mathrm{He\,II}} > 0.$$

The He-II response need not equal the He-I response; it must retain particle rearrangement, contact-network formation, and macroscopic dilation or normal stress.

Possible enhancement may be summarized by

$$\mathcal{E}_h(T) = \frac{\Delta h_{\mathrm{He\,II}}(T)}{\Delta h_{\mathrm{He\,I}}(T)}, \qquad \mathcal{E}_N(T) = \frac{\Delta N_{\mathrm{He\,II}}(T)}{\Delta N_{\mathrm{He\,I}}(T)}.$$

Reproducible $\mathcal{E}_h > 1$ or $\mathcal{E}_N > 1$, especially with a lower onset stress, shorter dilation time, or systematic dependence on the superfluid fraction, would indicate enhancement. A possible mechanism is facilitated redistribution of the continuous phase through narrowing pores, but this must be inferred from drainage and pressure measurements rather than assumed.

Controls and interpretation.

Particle size, concentration, roughness, cell gap, drainage, heat flux, shear history, and dilute nonthickening controls must distinguish dilatancy from ordinary viscosity, inertia, sedimentation, wall slip, aggregation, and boundary-spanning solidification. Quantized-vortex production is a specific confounder: second-sound attenuation or another vortex-density diagnostic should test whether rheological changes correlate with a shear- or heat-driven vortex tangle. Thermal contraction and the resulting particle-fraction change must also be calibrated.

© 2026 by the author(s). Distributed under a Creative Commons CC BY license.

Preprints.org (www.preprints.org) | NOT PEER-REVIEWED | Posted: 7 September 2026 doi:10.20944/preprints202608.2283.v2

Persistence of dilatancy below the lambda transition would demonstrate the constitutive compatibility required by the DDF analogy; enhancement would strengthen but is not required by the framework. A reproducible disappearance after packing, boundary, sedimentation, thermal, and vortex effects are excluded would rule out this laboratory realization, not every possible microscopic two-component DDF medium.

References

1. Brown, E.; Jaeger, H.M. Dynamic Jamming Point for Shear Thickening Suspensions. *Physical Review Letters* **2009**, *103*, 086001. https://doi.org/10.1103/physrevlett.103.086001.
2. Brown, E.; Jaeger, H. Shear thickening in concentrated suspensions: phenomenology, mechanisms and relations to jamming. *Reports on Progress in Physics* **2014**, *77*, 046602. https://doi.org/10.1088/0034-4885/77/4/046602.
3. Fedi, M. Physical Vacuum as a Dilatant Fluid Yields Exact Solutions to Pioneer Anomaly and Mercury's Perihelion Precession. *Canadian Journal of Physics* **2019**, *97*, 417–420. https://doi.org/10.1139/cjp-2018-0744.
4. Huang, K. *A Superfluid Universe*; World Scientific: Singapore, 2016.
5. Volovik, G., The superfluid universe. In *Novel Superfluids*; Oxford University Press: Oxford; Oxford Academic, 2013; Vol. 1, pp. 570–618. https://doi.org/10.1093/acprof:oso/9780199585915.003.0011.
6. Sinha, K.; Sivaram, C.; Sudarshan, E. Aether as a superfluid state of particle-antiparticle pairs. *Foundations of Physics* **1976**, *6*, 65–70. https://doi.org/10.1007/bf00708664.
7. Sinha, K.; Sivaram, C.; Sudarshan, E. The superfluid vacuum state, time-varying cosmological constant, and nonsingular cosmological models. *Foundations of Physics* **1976**, *6*, 717–726. https://doi.org/10.1007/bf00708950.
8. Sinha, K.; Sudarshan, E. The superfluid as a source of all interactions. *Foundations of Physics* **1978**, *8*, 823–831. https://doi.org/10.1007/bf00715056.
9. Volovik, G.E. Field theory in superfluid 3 He: What are the lessons for particle physics, gravity, and high-temperature superconductivity? *Proceedings of the National Academy of Sciences* **1999**, *96*, 6042–6047. https://doi.org/10.1073/pnas.96.11.6042.
10. Volovik, G. Superfluid analogies of cosmological phenomena. *Physics Reports* **2001**, *351*, 195–348, [arXiv:gr-qc/0005091]. https://doi.org/10.1016/s0370-1573(00)00139-3.
11. Volovik, G. The Universe in a Helium Droplet. *International Series of Monographs on Physics* **2003**, *117*, 1–507. https://doi.org/10.1093/acprof:oso/9780199564842.001.0001.
12. Berezhiani, L.; Khoury, J. Theory of dark matter superfluidity. *Physical Review D* **2015**, *92*. https://doi.org/10.1103/physrevd.92.103510.
13. Sbitnev, V.I. Physical Vacuum is a Special Superfluid Medium. In *Selected Topics in Applications of Quantum Mechanics*; Pahlavani, M.R., Ed.; InTech: Rijeka, 2015.
14. Michelson, A.A.; Morley, E.W. On the Relative Motion of the Earth and the Luminiferous Ether. *American Journal of Science* **1887**, *34*, 333–345.
15. Michelson, A.A.; Pease, F.G.; Pearson, F. Repetition of the Michelson-Morley Experiment. *Journal of the Optical Society of America* **1929**, *18*, 181.
16. Kennedy, R.; Thorndike, E. Experimental Establishment of the Relativity of Time. *Physical Review* **1932**, *42*, 400–418. https://doi.org/10.1103/physrev.42.400.
17. Trouton, F.T.; Noble, H.R. The Mechanical Forces Acting on a Charged Electric Condenser Moving Through Space. *Philosophical Transactions of the Royal Society A* **1904**, *202*, 346–358. https://doi.org/10.1088/1478-7814/20/1/337.
18. Herrmann, S.; Senger, A.; Möhle, K.; Nagel, M.; Kovalchuk, E.V.; et al. Rotating Optical Cavity Experiment Testing Lorentz Invariance at the 10^{-17} Level. *Physical Review D* **2009**, *80*, 105011.
19. Stanwix, P.L.; Tobar, M.E.; Wolf, P.; Susli, M.; Locke, C.R.; Ivanov, E.N.; Winterflood, J.; van Kann, F. Test of Lorentz Invariance in Electrodynamics Using Rotating Cryogenic Sapphire Microwave Oscillators. *Physical Review Letters* **2005**, *95*, 040404. https://doi.org/10.1103/physrevlett.95.040404.
20. Stanwix, P.; Tobar, M.; Wolf, P.; Locke, C.; Ivanov, E. Improved test of Lorentz invariance in electrodynamics using rotating cryogenic sapphire oscillators. *Physical Review D* **2006**, *74*. https://doi.org/10.1103/physrevd.74.081101.

© 2026 by the author(s). Distributed under a Creative Commons CC BY license.

Preprints.org (www.preprints.org) | NOT PEER-REVIEWED | Posted: 7 September 2026 doi:10.20944/preprints202608.2283.v2

21. Ismail, N.; Kores, C.; Geskus, D.; Pollnau, M. Fabry-Pérot resonator: spectral line shapes, generic and related Airy distributions, linewidths, finesses, and performance at low or frequency-dependent reflectivity. *Optics Express* **2016**, *24*, 16366. https://doi.org/10.1364/oe.24.016366.
22. Martel, K.; Poisson, E. Regular coordinate systems for Schwarzschild and other spherical spacetimes. *American Journal of Physics* **2001**, *69*, 476–480. https://doi.org/10.1119/1.1336836.
23. Hamilton, A.J.S.; Lisle, J.P. The river model of black holes. *American Journal of Physics* **2008**, *76*, 519–532. https://doi.org/10.1119/1.2830526.
24. Doran, C. New form of the Kerr solution. *Physical Review D* **2000**, *61*, 067503. https://doi.org/10.1103/physrevd.61.067503.
25. LIGO Scientific Collaboration; Virgo Collaboration. GW170817: Observation of Gravitational Waves from a Binary Neutron Star Inspiral. *Physical Review Letters* **2017**, *119*, 161101. https://doi.org/10.1103/physrevlett.119.161101.
26. Abbott, B.P.; Abbott, R.; Abbott, T.D.; Acernese, F.; Ackley, K.; et al. Gravitational Waves and Gamma-Rays from a Binary Neutron Star Merger: GW170817 and GRB 170817A. *The Astrophysical Journal Letters* **2017**, *848*, L13. https://doi.org/10.3847/2041-8213/aa920c.
27. Goldstein, A.; Veres, P.; Burns, E.; Briggs, M.S.; Hamburg, R.; et al. An Ordinary Short Gamma-Ray Burst with Extraordinary Implications: Fermi-GBM Detection of GRB 170817A. *The Astrophysical Journal Letters* **2017**, *848*, L14. https://doi.org/10.3847/2041-8213/aa8f41.
28. Savchenko, V.; Ferrigno, C.; Kuulkers, E.; Bazzano, A.; Bozzo, E.; et al. INTEGRAL Detection of the First Prompt Gamma-Ray Signal Coincident with the Gravitational-wave Event GW170817. *The Astrophysical Journal Letters* **2017**, *848*, L15. https://doi.org/10.3847/2041-8213/aa8f94.
29. LIGO/Virgo. Tests of general relativity with the binary black hole signals from the LIGO-Virgo catalog GWTC-1. *Physical Review D* **2019**, *100*, 104036. https://doi.org/10.1103/physrevd.100.104036.
30. Abbott, R.; Abe, H.; Acernese, F.; Ackley, K.; Adhikari, N.; et al. Tests of general relativity with GWTC-3. *Physical Review D* **2025**, *112*, 084080. https://doi.org/10.1103/physrevd.112.084080.
31. Donoghue, J.F. Quantum General Relativity and Effective Field Theory. In *Handbook of Quantum Gravity*; Bambi, C.; Modesto, L.; Shapiro, I., Eds.; Springer Singapore, 2023; pp. 1–24, [arXiv:gr-qc/2211.09902]. https://doi.org/10.1007/978-981-19-3079-9_1-1.
32. Ashtekar, A.; Bianchi, E. A Short Review of Loop Quantum Gravity. *Reports on Progress in Physics* **2021**, *84*, 042001, [arXiv:gr-qc/2104.04394]. https://doi.org/10.1088/1361-6633/abed91.
33. Visser, M. Sakharov's Induced Gravity: A Modern Perspective. *Modern Physics Letters A* **2002**, *17*, 977–991, [gr-qc/0204062]. https://doi.org/10.1142/S0217732302006886.
34. Reuter, M.; Saueressig, F. *Quantum Gravity and the Functional Renormalization Group*; Cambridge University Press, 2019. https://doi.org/10.1017/9781316227596.
35. Hu, B.L.B.; Verdaguer, E. *Semiclassical and Stochastic Gravity: Quantum Field Effects on Curved Spacetime*; Cambridge University Press, 2020. https://doi.org/10.1017/9780511667497.
36. Milgrom, M. A modification of the Newtonian dynamics as a possible alternative to the hidden mass hypothesis. *The Astrophysical Journal* **1983**, *270*, 365. https://doi.org/10.1086/161130.
37. Milgrom, M. A modification of the Newtonian dynamics - Implications for galaxies. *The Astrophysical Journal* **1983**, *270*, 371. https://doi.org/10.1086/161131.
38. Milgrom, M. A Modification of the Newtonian Dynamics - Implications for Galaxy Systems. *The Astrophysical Journal* **1983**, *270*, 384. https://doi.org/10.1086/161132.
39. McGaugh, S.S.; Lelli, F.; Schombert, J.M. Radial Acceleration Relation in Rotationally Supported Galaxies. *Physical Review Letters* **2016**, *117*, 201101. https://doi.org/10.1103/PhysRevLett.117.201101.
40. Lelli, F.; McGaugh, S.S.; Schombert, J.M. SPARC: MASS MODELS FOR 175 DISK GALAXIES WITH SPITZER PHOTOMETRY AND ACCURATE ROTATION CURVES. *The Astronomical Journal* **2016**, *152*, 157. https://doi.org/10.3847/0004-6256/152/6/157.
41. Moroshkin, P.; Lebedev, V.; Grobety, B.; Neururer, C.; Gordon, E.; Weis, A. Nanowire formation by gold nano-fragment coalescence on quantized vortices in He II. *EPL (Europhysics Letters)* **2010**, *90*, 34002. https://doi.org/10.1209/0295-5075/90/34002.
42. Springel, V.; White, S.D.M.; Jenkins, A.; Frenk, C.S.; Yoshida, N.; et al. Simulations of the formation, evolution and clustering of galaxies and quasars. *Nature* **2005**, *435*, 629–636. https://doi.org/10.1038/nature03597.
43. Landau, L. Theory of the Superfluidity of Helium II. *Physical Review* **1941**, *60*, 356–358. https://doi.org/10.1103/physrev.60.356.

© 2026 by the author(s). Distributed under a Creative Commons CC BY license.

Preprints.org (www.preprints.org) | NOT PEER-REVIEWED | Posted: 7 September 2026 doi:10.20944/preprints202608.2283.v2

44. Dalfovo, F.; Giorgini, S.; Pitaevskii, L.P.; Stringari, A. Theory of Bose-Einstein Condensation in Trapped Gases. *Reviews of Modern Physics* **1999**, *71*, 463. https://doi.org/10.1103/RevModPhys.71.463.
45. Fetter, A. Rotating trapped Bose-Einstein condensates. *Reviews of Modern Physics* **2009**, *81*, 647–691. https://doi.org/10.1103/revmodphys.81.647.
46. Brax, P.; Valageas, P. 3D vortices and rotating solitons in ultralight dark matter. *Physical Review D* **2025**, *111*. https://doi.org/10.1103/s91m-pldz.
47. Torquato, S.; Stillinger, F. Jammed hard-particle packings: From Kepler to Bernal and beyond. *Reviews of Modern Physics* **2010**, *82*, 2633–2672. https://doi.org/10.1103/revmodphys.82.2633.
48. van Hecke, M. Jamming of soft particles: geometry, mechanics, scaling and isostaticity. *Journal of Physics: Condensed Matter* **2009**, *22*, 033101. https://doi.org/10.1088/0953-8984/22/3/033101.
49. Wyart, M.; Cates, M. Discontinuous Shear Thickening without Inertia in Dense Non-Brownian Suspensions. *Physical Review Letters* **2014**, *112*, 98302. https://doi.org/10.1103/physrevlett.112.098302.
50. Born, M.; Infeld, L. Foundations of the new field theory. *Proceedings of the Royal Society of London. Series A, Containing Papers of a Mathematical and Physical Character* **1934**, *144*, 425–451. https://doi.org/10.1098/rspa.1934.0059.
51. Paul, A.; Dirac. Is there an Æther? *Nature* **1951**, *168*, 906–907.
52. Jacobson, T.; Mattingly, D. Gravity with a dynamical preferred frame. *Physical Review D* **2001**, *64*, 24028. https://doi.org/10.1103/physrevd.64.024028.
53. Barceló, C.; Liberati, S.; Visser, M. Analogue Gravity. *Living Reviews in Relativity* **2011**, *14*. https://doi.org/10.12942/lrr-2011-3.
54. Hossenfelder, S.; Mistele, T. Strong lensing with superfluid dark matter. *Journal of Cosmology and Astroparticle Physics* **2019**, *2019*, 001–001. https://doi.org/10.1088/1475-7516/2019/02/001.
55. Copeland, E.J.; Sami, M.; Tsujikawa, S. Dynamics of Dark Energy. *International Journal of Modern Physics D* **2006**, *15*, 1753–1935. https://doi.org/10.1142/s021827180600942x.
56. Clifton, T.; Ferreira, P.G.; Padilla, A.; Skordis, C. Modified gravity and cosmology. *Physics Reports* **2012**, *513*, 1–189. https://doi.org/10.1016/j.physrep.2012.01.001.
57. Koyama, K. Cosmological tests of modified gravity. *Reports on Progress in Physics* **2016**, *79*, 046902. https://doi.org/10.1088/0034-4885/79/4/046902.
58. Deser, S.; Woodard, R.P. Nonlocal Cosmology. *Physical Review Letters* **2007**, *99*, 111301. https://doi.org/10.1103/physrevlett.99.111301.
59. Woodard, R.P. Nonlocal Models of Cosmic Acceleration. *Foundations of Physics* **2014**, *44*, 213–233. https://doi.org/10.1007/s10701-014-9780-6.
60. Aghanim, N.; Akrami, Y.; Arroja, F.; Ashdown, M.; Aumont, J.; et al. Planck 2018 results: I. Overview and the cosmological legacy of Planck. *Astronomy & Astrophysics* **2020**, *641*, A1. https://doi.org/10.1051/0004-6361/201833880.
61. Frenk, C.; White, S. Dark matter and cosmic structure. *Annalen der Physik* **2012**, *524*, 507–534. https://doi.org/10.1002/andp.201200212.
62. Wilson, K. The renormalization group and the ϵ expansion. *Physics Reports* **1974**, *12*, 75–199. https://doi.org/10.1016/0370-1573(74)90023-4.
63. Hohenberg, P.C.; Halperin, B.I. Theory of dynamic critical phenomena. *Reviews of Modern Physics* **1977**, *49*, 435–479. https://doi.org/10.1103/revmodphys.49.435.
64. Barnes, H. Shear-Thickening ("Dilatancy") in Suspensions of Nonaggregating Solid Particles Dispersed in Newtonian Liquids. *Journal of Rheology* **1989**, *33*, 329–366. https://doi.org/10.1122/1.550017.
65. Seto, R.; Mari, R.; Morris, J.; Denn, M. Discontinuous Shear Thickening of Frictional Hard-Sphere Suspensions. *Physical Review Letters* **2013**, *111*, 218301. https://doi.org/10.1103/physrevlett.111.218301.
66. Hui, L.; Ostriker, J.; Tremaine, S.; Witten, E. Ultralight scalars as cosmological dark matter. *Physical Review D* **2017**, *95*, 43541. https://doi.org/10.1103/physrevd.95.043541.
67. Sikivie, P.; Yang, Q. Bose-Einstein Condensation of Dark Matter Axions. *Physical Review Letters* **2009**, *103*, 111301. https://doi.org/10.1103/physrevlett.103.111301.
68. Marsh, D.J. Axion cosmology. *Physics Reports* **2016**, *643*, 1–79. https://doi.org/10.1016/j.physrep.2016.06.005.
69. Jaeckel, J.; Ringwald, A. The Low-Energy Frontier of Particle Physics. *Annual Review of Nuclear and Particle Science* **2010**, *60*, 405–437. https://doi.org/10.1146/annurev.nucl.012809.104433.
70. Irastorza, I.G.; Redondo, J. New experimental approaches in the search for axion-like particles. *Progress in Particle and Nuclear Physics* **2018**, *102*, 89–159. https://doi.org/10.1016/j.ppnp.2018.05.003.

© 2026 by the author(s). Distributed under a Creative Commons CC BY license.

Preprints.org (www.preprints.org) | NOT PEER-REVIEWED | Posted: 7 September 2026 doi:10.20944/preprints202608.2283.v2

71. Lebedev, V.; Moroshkin, P.; Grobety, B.; Gordon, E.; Weis, A. Formation of Metallic Nanowires by Laser Ablation in Liquid Helium. *Journal of Low Temperature Physics* **2011**, *165*, 166–176. https://doi.org/10.1007/s10909-011-0384-7.
72. Gordon, E.; Karabulin, A.; Matyushenko, V.; Sizov, V.; Khodos, I. The role of vortices in the process of impurity nanoparticles coalescence in liquid helium. *Chemical Physics Letters* **2012**, *519-520*, 64–68. https://doi.org/10.1016/j.cplett.2011.11.020.
73. Pshenichnyuk, I. Static and dynamic properties of heavily doped quantum vortices. *New Journal of Physics* **2017**, *19*, 105007. https://doi.org/10.1088/1367-2630/aa8745.
74. Hu, W.; Barkana, R.; Gruzinov, A. Fuzzy Cold Dark Matter: The Wave Properties of Ultralight Particles. *Physical Review Letters* **2000**, *85*, 1158–1161. https://doi.org/10.1103/physrevlett.85.1158.
75. Schive, H.Y.; Chiueh, T.; Broadhurst, T. Cosmic structure as the quantum interference of a coherent dark wave. *Nature Physics* **2014**, *10*, 496–499. https://doi.org/10.1038/nphys2996.
76. Graham, P.W.; Rajendran, S. New observables for direct detection of axion dark matter. *Physical Review D* **2013**, *88*, 035023. https://doi.org/10.1103/physrevd.88.035023.
77. Weinberg, S. Phenomenological Lagrangians. *Physica A: Statistical Mechanics and its Applications* **1979**, *96*, 327–340. https://doi.org/10.1016/0378-4371(79)90223-1.
78. Onsager, L. Statistical hydrodynamics. *Il Nuovo Cimento* **1949**, *6*, 279–287. https://doi.org/10.1007/bf02780991.
79. Feynman, R.P., Chapter II Application of Quantum Mechanics to Liquid Helium. In *Progress in Low Temperature Physics*; Number 1, Elsevier, 1955; pp. 17–53. https://doi.org/10.1016/s0079-6417(08)60077-3.
80. Tsubota, M.; Kobayashi, M.; Takeuchi, H. Quantum hydrodynamics. *Physics Reports* **2013**, *522*, 191–238. https://doi.org/10.1016/j.physrep.2012.09.007.
81. Landau, L.D.; Lifshits, E.M. *Fluid Mechanics*, 2 ed.; Vol. 6, Pergamon Press, 1987.
82. Maxwell, J. On Physical Lines of Force. *Philosophical Magazine, London* **1861**, *21*.
83. Maxwell, J.C. *A Treatise on Electricity and Magnetism*; Oxford University Press, 1998. Reprint of the 1873 first edition.
84. Milton, K. The Casimir effect: recent controversies and progress. *Journal of Physics A: Mathematical and General* **2004**, *37*, R209–R277. https://doi.org/10.1088/0305-4470/37/38/r01.
85. Crispino, L.; Higuchi, A.; Matsas, G. The Unruh effect and its applications. *Reviews of Modern Physics* **2008**, *80*, 787–838. https://doi.org/10.1103/revmodphys.80.787.
86. Heisenberg, W.; Euler, H. Folgerungen aus der Diracschen Theorie des Positrons. *Zeitschrift für Physik* **1936**, *98*, 714–732. https://doi.org/10.1007/bf01343663.
87. Della Valle, F.; Ejlli, A.; Gastaldi, U.; Messineo, G.; Milotti, E.; Pengo, R.; Ruoso, G.; Zavattini, G. The PVLAS experiment: measuring vacuum magnetic birefringence and dichroism with a birefringent Fabry–Perot cavity. *The European Physical Journal C* **2016**, *76*, 24. https://doi.org/10.1140/epjc/s10052-015-3869-8.
88. Mignani, R.; Testa, V.; González Caniulef, D.; Taverna, R.; Turolla, R.; et al. Evidence for vacuum birefringence from the first optical-polarimetry measurement of the isolated neutron star RX J1856.5-3754. *Monthly Notices of the Royal Astronomical Society* **2017**, *465*, 492–500. https://doi.org/10.1093/mnras/stw2798.
89. Prokhovnik, S. Neo-Lorentzian relativity. *Journal of the Australian Mathematical Society* **1965**, *5*, 273–284. https://doi.org/10.1017/s1446788700026835.
90. Linford, D. Neo-Lorentzian relativity and the beginning of the universe. *European Journal for Philosophy of Science* **2021**, *11*, 1–38. https://doi.org/10.1007/s13194-021-00417-x.
91. Irgens, F. *Rheology and Non-Newtonian Fluids*; Springer International Publishing: Cham, 2014. https://doi.org/10.1007/978-3-319-01053-3.
92. Reynolds, O. LVII. On the dilatancy of media composed of rigid particles in contact. With experimental illustrations. *The London, Edinburgh, and Dublin Philosophical Magazine and Journal of Science* **1885**, *20*, 469–481. https://doi.org/10.1080/14786448508627791.
93. Bagnold, R. Experiments on a gravity-free dispersion of large solid spheres in a Newtonian fluid under shear. *Proceedings of the Royal Society of London. Series A. Mathematical and Physical Sciences* **1954**, *225*, 49–63. https://doi.org/10.1098/rspa.1954.0186.
94. Gillespie, T. Application of the hydrodynamic-structural theory of non-Newtonian flow to suspensions which exhibit moderate shear thickening with particular reference to "dilatant" vinyl plastisols. *Journal of Colloid and Interface Science* **1966**, *22*, 554–562. https://doi.org/10.1016/0021-9797(66)90049-x.
95. De Waele, A. Viscometry and plastometry. *J. Oil & Colour Chemists' Assoc* **1923**, *6*, 33–88.

© 2026 by the author(s). Distributed under a Creative Commons CC BY license.

Preprints.org (www.preprints.org) | NOT PEER-REVIEWED | Posted: 7 September 2026 doi:10.20944/preprints202608.2283.v2

96. Ostwald, W. Ueber die Geschwindigkeitsfunktion der Viskosität disperser Systeme. I. *Kolloid-Zeitschrift* **1925**, *36*, 99–117. https://doi.org/10.1007/bf01431449.
97. Hoffman, R. Discontinuous and Dilatant Viscosity Behavior in Concentrated Suspensions. I. Observation of a Flow Instability. *Transactions of the Society of Rheology* **1972**, *16*, 155–173. https://doi.org/10.1122/1.549250.
98. Hoffman, R. Discontinuous and dilatant viscosity behavior in concentrated suspensions. II. Theory and experimental tests. *Journal of Colloid and Interface Science* **1974**, *46*, 491–506. https://doi.org/10.1016/0021-9797(74)90059-9.
99. Brady, J.; Bossis, G. Stokesian Dynamics. *Annual Review of Fluid Mechanics* **1988**, *20*, 111–157. https://doi.org/10.1146/annurev.fl.20.010188.000551.
100. Every, A.G. General closed-form expressions for acoustic waves in elastically anisotropic solids. *Physical Review B* **1980**, *22*, 1746–1760. https://doi.org/10.1103/physrevb.22.1746.
101. Thomsen, L. Weak elastic anisotropy. *Geophysics* **1986**, *51*, 1954–1966. https://doi.org/10.1190/1.1442051.
102. Donnelly, R. *Quantized vortices in helium II*; Cambridge University Press, 1991.
103. Barenghi, C.F.; Donnelly, R.J. Vortex rings in classical and quantum systems. *Fluid Dynamics Research* **2009**, *41*, 051401. https://doi.org/10.1088/0169-5983/41/5/051401.
104. Barenghi, C.; Skrbek, L.; Sreenivasan, K. *Quantum Turbulence*; Cambridge University Press, 2023.
105. Seddon, J.R.; Thurlow, M.S.; Lees, M.J.; Lucas, P.G. Quantised vortex line visualisation in superfluid helium using low-temperature optics. *Physica B: Condensed Matter* **2003**, *329-333*, 220–221. https://doi.org/10.1016/s0921-4526(02)01966-x.
106. Minowa, Y.; Aoyagi, S.; Inui, S.; Nakagawa, T.; Asaka, G.; Tsubota, M.; Ashida, M. Visualization of quantized vortex reconnection enabled by laser ablation. *Science Advances* **2022**, *8*, 1143. https://doi.org/10.1126/sciadv.abn1143.
107. Stasiak, P.Z.; Xing, Y.; Alihosseini, Y.; Barenghi, C.F.; Baggaley, A.; Guo, W.; Galantucci, L.; Krstulovic, G. Experimental and theoretical evidence of universality in superfluid vortex reconnections. *Proceedings of the National Academy of Sciences* **2025**, *122*. https://doi.org/10.1073/pnas.2426064122.
108. Rayfield, G.; Reif, F. Quantized Vortex Rings in Superfluid Helium. *Physical Review* **1964**, *136*, A1194–A1208. https://doi.org/10.1103/physrev.136.a1194.
109. Tang, Y.; Guo, W.; Kobayashi, H.; Yui, S.; Tsubota, M.; Kanai, T. Imaging quantized vortex rings in superfluid helium to evaluate quantum dissipation. *Nature Communications* **2023**, *14*, 3274. https://doi.org/10.1038/s41467-023-38787-w.
110. Maxworthy, T. The structure and stability of vortex rings. *Journal of Fluid Mechanics* **1972**, *51*, 15–32. https://doi.org/10.1017/s0022112072001041.
111. Recami, E.; Salesi, G. Kinematics and hydrodynamics of spinning particles. *Physical Review A* **1998**, *57*, 98–105. https://doi.org/10.1103/physreva.57.98.
112. Salesi, G.; Recami, E. Hydrodynamical Reformulation and Quantum Limit of the Barut-Zanghi Theory. *Foundations of Physics Letters* **1997**, *10*.
113. Jehle, H. Topological Characterization of Leptons, Quarks and Hadrons. *Physics Letters B* **1981**, *104*, 207–211.
114. Simula, T.; Davis, M.; Helmerson, K. Emergence of Order from Turbulence in an Isolated Planar Superfluid. *Physical Review Letters* **2014**, *113*, 165302. https://doi.org/10.1103/physrevlett.113.165302.
115. Billam, T.; Reeves, M.; Anderson, B.; Bradley, A. Onsager-Kraichnan Condensation in Decaying Two-Dimensional Quantum Turbulence. *Physical Review Letters* **2014**, *112*, 145301. https://doi.org/10.1103/physrevlett.112.145301.
116. Gauthier, G.; Reeves, M.; Yu, X.; Bradley, A.; Baker, M.; Bell, T.; Rubinsztein-Dunlop, H.; Davis, M.; Neely, T. Giant vortex clusters in a two-dimensional quantum fluid. *Science* **2019**, *364*, 1264–1267. https://doi.org/10.1126/science.aat5718.
117. Ashtekar, A.; Lewandowski, J. Quantum theory of geometry: I. Area operators. *Classical and Quantum Gravity* **1997**, *14*, A55–A81. https://doi.org/10.1088/0264-9381/14/1a/006.
118. Rovelli, C. Loop Quantum Gravity. *Living Reviews in Relativity* **1998**, *1*, 1. https://doi.org/10.12942/lrr-1998-1.
119. Ashtekar, A.; Lewandowski, J. Background independent quantum gravity: a status report. *Classical and Quantum Gravity* **2004**, *21*, R53–R152. https://doi.org/10.1088/0264-9381/21/15/r01.
120. Rovelli, C.; Vidotto, F. *Covariant Loop Quantum Gravity: An Elementary Introduction to Quantum Gravity and Spinfoam Theory*; Cambridge University Press, 2014.
121. Ashtekar, A.; Pullin, J. *Loop Quantum Gravity*; World Scientific, 2017.

© 2026 by the author(s). Distributed under a Creative Commons CC BY license.

Preprints.org (www.preprints.org) | NOT PEER-REVIEWED | Posted: 7 September 2026 doi:10.20944/preprints202608.2283.v2

122. Einstein, A. Letter to Besso (Einstein Archives at the Hebrew University of Jerusalem, cataloged as AEA 7-401). Letter, 1951.
123. Dirac, P. The quantum theory of the emission and absorption of radiation. *Proceedings of the Royal Society of London. Series A, Containing Papers of a Mathematical and Physical Character* **1927**, *114*, 243–265. https://doi.org/10.1098/rspa.1927.0039.
124. Loudon, R. *The Quantum Theory of Light*, 3rd ed.; Oxford University Press, 2000.
125. Scully, M.; Zubairy, M. *Quantum Optics*; Cambridge University Press, 1997.
126. Süsstrunk, R.; Huber, S. Observation of phononic helical edge states in a mechanical topological insulator. *Science* **2015**, *349*, 47–50. https://doi.org/10.1126/science.aab0239.
127. Maxwell, J. A dynamical theory of the electromagnetic field. *Philosophical Transactions of the Royal Society of London* **1865**, *155*, 459–512. https://doi.org/10.5479/sil.423156.39088007130693.
128. Gremaud, G. Maxwell's Equations as a Special Case of Deformation of a Solid Lattice in Euler's Coordinates. https://arxiv.org/abs/1610.00753.
129. Gremaud, G. The Crystalline Ether. *European Journal of Applied Sciences* **2023**, *11*.
130. Parker, N.; Proukakis, N.; Barenghi, C.; Adams, C. Controlled Vortex-Sound Interactions in Atomic Bose-Einstein Condensates. *Physical Review Letters* **2004**, *92*, 160403. https://doi.org/10.1103/physrevlett.92.160403.
131. Einstein, A. Ist die Trägheit eines Körpers von seinem Energieinhalt abhängig? *Annalen der Physik* **1905**, *323*, 639–641. https://doi.org/10.1002/andp.19053231314.
132. Neely, T.; Samson, E.; Bradley, A.; Davis, M.; Anderson, B. Observation of Vortex Dipoles in an Oblate Bose-Einstein Condensate. *Physical Review Letters* **2010**, *104*, 160401. https://doi.org/10.1103/physrevlett.104.160401.
133. Han, J.; Tsubota, M. Annihilation and recurrence of vortex-antivortex pairs in two-component Bose-Einstein condensates. *Physical Review A* **2021**, *103*, 53313. https://doi.org/10.1103/physreva.103.053313.
134. Seo, S.; Ko, B.; Kim, J.; Shin, Y. Observation of vortex-antivortex pairing in decaying 2D turbulence of a superfluid gas. *Scientific Reports* **2017**, *7*, 4587. https://doi.org/10.1038/s41598-017-04122-9.
135. Barenghi, C.; Parker, N.; Proukakis, N.; Adams, C. Decay of quantised vorticity by sound emission. *Journal of Low Temperature Physics* **2005**, *138*, 629–634. https://doi.org/10.1007/s10909-005-2272-5.
136. Leadbeater, M.; Winiecki, T.; Samuels, D.; Barenghi, C.; Adams, C. Sound Emission due to Superfluid Vortex Reconnections. *Physical Review Letters* **2001**, *86*, 1410–1413. https://doi.org/10.1103/physrevlett.86.1410.
137. Kwon, W.; Del Pace, G.; Xhani, K.; Galantucci, L.; Muzi Falconi, A.; Inguscio, M.; Scazza, F.; Roati, G. Sound emission and annihilations in a programmable quantum vortex collider. *Nature* **2021**, *600*, 64–69. https://doi.org/10.1038/s41586-021-04047-4.
138. Fonda, E.; Meichle, D.; Ouellette, N.; Hormoz, S.; Lathrop, D. Direct observation of Kelvin waves excited by quantized vortex reconnection. *Proceedings of the National Academy of Sciences* **2014**, *111*, 4707–4710. https://doi.org/10.1073/pnas.1312536110.
139. Hänninen, R. Kelvin waves from vortex reconnection in superfluid helium at low temperatures. *Physical Review B* **2015**, *92*, 184508. https://doi.org/10.1103/physrevb.92.184508.
140. Baggaley, A.; Laurie, J. Kelvin-wave cascade in the vortex filament model. *Physical Review B* **2014**, *89*, 14504. https://doi.org/10.1103/physrevb.89.014504.
141. Bewley, G.; Paoletti, M.; Sreenivasan, K.; Lathrop, D. Characterization of reconnecting vortices in superfluid helium. *Proceedings of the National Academy of Sciences* **2008**, *105*, 13707–13710. https://doi.org/10.1073/pnas.0806002105.
142. Vinen, W.F. Decay of superfluid turbulence at a very low temperature: The radiation of sound from a Kelvin wave on a quantized vortex. *Physical Review B* **2001**, *64*, 134520. https://doi.org/10.1103/physrevb.64.134520.
143. Vinen, W.F.; Tsubota, M.; Mitani, A. Kelvin-Wave Cascade on a Vortex in SuperfluidHe4at a Very Low Temperature. *Physical Review Letters* **2003**, *91*, 135301. https://doi.org/10.1103/physrevlett.91.135301.
144. Lattimer, J.; Prakash, M. The Physics of Neutron Stars. *Science* **2004**, *304*, 536–542. https://doi.org/10.1126/science.1090720.
145. Lattimer, J.M.; Prakash, M. The Ultimate Energy Density of Observable Cold Matter. *Physical Review Letters* **2005**, *94*, 111101. https://doi.org/10.1103/PhysRevLett.94.111101.
146. Einstein, A. Zur Elektrodynamik bewegter Körper. *Annalen der Physik* **1905**, *17*, 891–921. https://doi.org/10.1007/978-3-663-19510-8_3.

© 2026 by the author(s). Distributed under a Creative Commons CC BY license.

Preprints.org (www.preprints.org) | NOT PEER-REVIEWED | Posted: 7 September 2026 doi:10.20944/preprints202608.2283.v2

147. Einstein, A. Manuscript on the Special Theory of Relativity. George Braziller in association with the Israel Museum, Jerusalem, 1912.
148. Mandelstam, S. Determination of the Pion-Nucleon Scattering Amplitude from Dispersion Relations and Unitarity. General Theory. *Physical Review* **1958**, *112*, 1344–1360. https://doi.org/10.1103/physrev.112.1344.
149. Eckart, C. The Thermodynamics of Irreversible Processes. III. Relativistic Theory of the Simple Fluid. *Physical Review* **1940**, *58*, 919–924. https://doi.org/10.1103/physrev.58.919.
150. Hiscock, W.A.; Lindblom, L. Generic instabilities in first-order dissipative relativistic fluid theories. *Physical Review D* **1985**, *31*, 725–733. https://doi.org/10.1103/physrevd.31.725.
151. Israel, W.; Stewart, J. Transient relativistic thermodynamics and kinetic theory. *Annals of Physics* **1979**, *118*, 341–372. https://doi.org/10.1016/0003-4916(79)90130-1.
152. Eisele, C.; Nevsky, A.Y.; Schiller, S. Laboratory Test of the Isotropy of Light Propagation at the 10^{-17} Level. *Physical Review Letters* **2009**, *103*, 090401.
153. Nagel, M.; Parker, S.; Kovalchuk, E.; Stanwix, P.; Hartnett, J.; Ivanov, E.; Peters, A.; Tobar, M. Direct terrestrial test of Lorentz symmetry in electrodynamics to 10^{-18}. *Nature Communications* **2015**, *6*. Article number 8174, https://doi.org/10.1038/ncomms9174.
154. Barceló, C.; Liberati, S.; Visser, M. Analogue gravity from Bose-Einstein condensates. *Classical and Quantum Gravity* **2001**, *18*, 1137–1156. https://doi.org/10.1088/0264-9381/18/6/312.
155. Barceló, C.; Visser, M.; Liberati, S. EINSTEIN GRAVITY AS AN EMERGENT PHENOMENON? *International Journal of Modern Physics D* **2001**, *10*, 799–806. https://doi.org/10.1142/s0218271801001591.
156. Oriti, D. Emergent non-commutative matter fields from group field theory models of quantum spacetime. *Journal of Physics: Conference Series* **2009**, *174*, 012047. https://doi.org/10.1088/1742-6596/174/1/012047.
157. Liberati, S.; Maccione, L. Quantum Gravity phenomenology: achievements and challenges. *Journal of Physics: Conference Series* **2011**, *314*, 012007. https://doi.org/10.1088/1742-6596/314/1/012007.
158. Liberati, S. Analogue gravity models of emergent gravity: lessons and pitfalls. *Journal of Physics: Conference Series* **2017**, *880*, 012009. https://doi.org/10.1088/1742-6596/880/1/012009.
159. Cahill, R. Gravity as Quantum Foam In-Flow. *Apeiron* **2003**, *11*, 1–52, [arXiv:physics/0307003]. https://doi.org/10.48550/arXiv.physics/0307003.
160. Verlinde, E. On the origin of gravity and the laws of Newton. *Journal of High Energy Physics* **2011**, *2011*. https://doi.org/10.1007/jhep04(2011)029.
161. Verlinde, E. Emergent Gravity and the Dark Universe. *SciPost Physics* **2017**, *2*, 16. https://doi.org/10.21468/scipostphys.2.3.016.
162. Simula, T. Gravitational vortex mass in a superfluid. *Physical Review A* **2020**, *101*. https://doi.org/10.1103/physreva.101.063616.
163. Silvera, I.F. Ultimate fate of a gas of atomic hydrogen in a liquid-helium chamber: Recombination and burial. *Physical Review B* **1984**, *29*, 3899–3904. https://doi.org/10.1103/physrevb.29.3899.
164. Fujisaki, A.; Sano, K.; Kinoshita, T.; Takahashi, Y.; Yabuzaki, T. Implantation of neutral atoms into liquid helium by laser sputtering. *Physical Review Letters* **1993**, *71*, 1039–1042. https://doi.org/10.1103/physrevlett.71.1039.
165. Gordon, E.B.; Nishida, R.; Nomura, R.; Okuda, Y. Filament formation by impurities embedding into superfluid helium. *JETP Letters* **2007**, *85*, 581–584. https://doi.org/10.1134/s0021364007110112.
166. V. Eötvös, R.; Pekár, D.; Fekete, E. Beiträge zum Gesetze der Proportionalität von Trägheit und Gravität. *Annalen der Physik* **1922**, *373*, 11–66. https://doi.org/10.1002/andp.19223730903.
167. Schlamminger, S.; Choi, K.Y.; Wagner, T.; Gundlach, J.; Adelberger, E. Test of the Equivalence Principle Using a Rotating Torsion Balance. *Physical Review Letters* **2008**, *100*, 41101. https://doi.org/10.1103/physrevlett.100.041101.
168. Wagner, T.; Schlamminger, S.; Gundlach, J.; Adelberger, E. Torsion-balance tests of the weak equivalence principle. *Classical and Quantum Gravity* **2012**, *29*, 184002. https://doi.org/10.1088/0264-9381/29/18/184002.
169. Touboul, P.; Métris, G.; Rodrigues, M.; André, Y.; Baghi, Q.; et al. MICROSCOPE Mission: First Results of a Space Test of the Equivalence Principle. *Physical Review Letters* **2017**, *119*, 231101. https://doi.org/10.1103/physrevlett.119.231101.
170. Peters, A.; Chung, K.; Chu, S. High-precision gravity measurements using atom interferometry. *Metrologia* **2001**, *38*, 25–61. https://doi.org/10.1088/0026-1394/38/1/4.
171. Rosi, G.; D'amico, G.; Cacciapuoti, L.; Sorrentino, F.; Prevedelli, M.; et al. Quantum test of the equivalence principle for atoms in coherent superposition of internal energy states. *Nature Communications* **2017**, *8*, 15529. https://doi.org/10.1038/ncomms15529.

© 2026 by the author(s). Distributed under a Creative Commons CC BY license.

Preprints.org (www.preprints.org) | NOT PEER-REVIEWED | Posted: 7 September 2026 doi:10.20944/preprints202608.2283.v2

172. Asenbaum, P.; Overstreet, C.; Kim, M.; Curti, J.; Kasevich, M. Atom-Interferometric Test of the Equivalence Principle at the 10^{-12} Level. *Physical Review Letters* **2020**, *125*, 191101. https://doi.org/10.1103/physrevlett.125.191101.
173. Kreuzer, L. Experimental Measurement of the Equivalence of Active and Passive Gravitational Mass. *Physical Review* **1968**, *169*, 1007–1012. https://doi.org/10.1103/physrev.169.1007.
174. Bartlett, D.; Van Buren, D. Equivalence of active and passive gravitational mass using the moon. *Physical Review Letters* **1986**, *57*, 21–24. https://doi.org/10.1103/physrevlett.57.21.
175. Williams, J.; Turyshev, S.; Boggs, D. Lunar laser ranging tests of the equivalence principle. *Classical and Quantum Gravity* **2012**, *29*, 184004. https://doi.org/10.1088/0264-9381/29/18/184004.
176. Singh, V.; Müller, J.; Biskupek, L.; Hackmann, E.; Lämmerzahl, C. Equivalence of Active and Passive Gravitational Mass Tested with Lunar Laser Ranging. *Physical Review Letters* **2023**, *131*, 21401. https://doi.org/10.1103/physrevlett.131.021401.
177. Audi, G.; Wapstra, A.; Thibault, C. The Ame2003 atomic mass evaluation. *Nuclear Physics A* **2003**, *729*, 337–676. https://doi.org/10.1016/j.nuclphysa.2003.11.003.
178. Ji, X. Breakup of hadron masses and the energy-momentum tensor of QCD. *Physical Review D* **1995**, *52*, 271–281. https://doi.org/10.1103/physrevd.52.271.
179. Brambilla, N.; Pineda, A.; Soto, J.; Vairo, A. Effective-field theories for heavy quarkonium. *Reviews of Modern Physics* **2005**, *77*, 1423–1496. https://doi.org/10.1103/revmodphys.77.1423.
180. Cardoso, M.; Cardoso, N.; Bicudo, P. Lattice QCD computation of the color fields for the static hybrid quark-gluon-antiquark system, and microscopic study of the Casimir scaling. *Physical Review D* **2010**, *81*, 34504. https://doi.org/10.1103/physrevd.81.034504.
181. Alcubierre, M. *Introduction to 3+1 Numerical Relativity*; Oxford University Press, 2008. https://doi.org/10.1093/acprof:oso/9780199205677.001.0001.
182. Gourgoulhon, E.; Jaramillo, J.L. A 3+1 perspective on null hypersurfaces and isolated horizons. *Physics Reports* **2006**, *423*, 159–294. https://doi.org/10.1016/j.physrep.2005.10.005.
183. Unruh, W.G. Experimental Black-Hole Evaporation? *Physical Review Letters* **1981**, *46*, 1351–1353. https://doi.org/10.1103/physrevlett.46.1351.
184. Visser, M. Acoustic black holes: horizons, ergospheres and Hawking radiation. *Classical and Quantum Gravity* **1998**, *15*, 1767–1791. https://doi.org/10.1088/0264-9381/15/6/024.
185. Kerr, R. Gravitational Field of a Spinning Mass as an Example of Algebraically Special Metrics. *Physical Review Letters* **1963**, *11*, 237–238. https://doi.org/10.1103/physrevlett.11.237.
186. Schäfer, G. Gravitomagnetism in Physics and Astrophysics. *Space Science Reviews* **2009**, *148*, 37–52. https://doi.org/10.1007/s11214-009-9537-2.
187. Ciufolini, I.; Pavlis, E.C. A confirmation of the general relativistic prediction of the Lense–Thirring effect. *Nature* **2004**, *431*, 958–960. https://doi.org/10.1038/nature03007.
188. Everitt, C.W.F.; DeBra, D.B.; Parkinson, B.W.; Turneaure, J.P.; Conklin, J.W.; et al. Gravity Probe B: Final Results of a Space Experiment to Test General Relativity. *Physical Review Letters* **2011**, *106*, 221101. https://doi.org/10.1103/physrevlett.106.221101.
189. Reissner, H. Über die Eigengravitation des elektrischen Feldes nach der Einsteinschen Theorie. *Annalen der Physik* **1916**, *355*, 106–120. https://doi.org/10.1002/andp.19163550905.
190. Weyl, H.; Gravitationstheorie, Z. Zur Gravitationstheorie. *Annalen der Physik* **1917**, *359*, 117–145. https://doi.org/10.1002/andp.19173591804.
191. Nordström, G. On the Energy of the Gravitational Field in Einstein's Theory. *Proc. K. Ned. Akad. Wet.* **1918**, *20*, 1238–1245.
192. Jeffery, G. The field of an electron on Einstein's theory of gravitation. *Proceedings of the Royal Society of London. Series A, Containing Papers of a Mathematical and Physical Character* **1921**, *99*, 123–134. https://doi.org/10.1098/rspa.1921.0028.
193. Chandrasekhar, S., The Mathematical Theory of Black Holes. In *General Relativity and Gravitation*; Bertotti, B.; de Felice, F.; Pascolini, A., Eds.; Springer Netherlands: Dordrecht, 1984; Vol. 9, pp. 5–26. https://doi.org/10.1007/978-94-009-6469-3_2.
194. Lin, C.Y.; Soo, C. Generalized Painlevé–Gullstrand metrics. *Physics Letters B* **2009**, *671*, 493–495. https://doi.org/10.1016/j.physletb.2008.12.051.
195. Newman, E.; Couch, E.; Chinnapared, K.; Exton, A.; Prakash, A.; Torrence, R. Metric of a Rotating, Charged Mass. *Journal of Mathematical Physics* **1965**, *6*, 918–919. https://doi.org/10.1063/1.1704351.

© 2026 by the author(s). Distributed under a Creative Commons CC BY license.

Preprints.org (www.preprints.org) | NOT PEER-REVIEWED | Posted: 7 September 2026 doi:10.20944/preprints202608.2283.v2

196. Tolman, R.C. Static Solutions of Einstein's Field Equations for Spheres of Fluid. *Physical Review* **1939**, *55*, 364–373. https://doi.org/10.1103/physrev.55.364.
197. Oppenheimer, J.R.; Volkoff, G.M. On Massive Neutron Cores. *Physical Review* **1939**, *55*, 374–381. https://doi.org/10.1103/physrev.55.374.
198. Bowers, R.L.; Liang, E.P.T. Anisotropic Spheres in General Relativity. *The Astrophysical Journal* **1974**, *188*, 657. https://doi.org/10.1086/152760.
199. Blanchet, L. Post-Newtonian theory for gravitational waves. *Living Reviews in Relativity* **2024**, *27*. https://doi.org/10.1007/s41114-024-00050-z.
200. Blanchet, L.; Faye, G.; Nissanke, S. Structure of the post-Newtonian expansion in general relativity. *Physical Review D* **2005**, *72*, 44024. https://doi.org/10.1103/physrevd.72.044024.
201. Blanchet, L. Gravitational Radiation from Post-Newtonian Sources and Inspiralling Compact Binaries. *Living Reviews in Relativity* **2006**, *9*, 4. https://doi.org/10.12942/lrr-2006-4.
202. Will, C. On the unreasonable effectiveness of the post-Newtonian approximation in gravitational physics. *Proceedings of the National Academy of Sciences* **2011**, *108*, 5938–5945. https://doi.org/10.1073/pnas.1103127108.
203. de Sitter, W. On Einstein's Theory of Gravitation and its Astronomical Consequences. First Paper. *Monthly Notices of the Royal Astronomical Society* **1916**, *76*, 699–728. https://doi.org/10.1093/mnras/76.9.699.
204. Einstein, A. Erklärung der Perihelbewegung des Merkur ausder allgemeinen Relativitätstheorie. *Sitzungsberichte der Preussischen Akademie der Wissenschaften* **1915**, pp. 831–839.
205. Stokes, G.G. On the theories of internal friction of fluids in motion, and of the equilibrium and motion of elastic solids. *Transactions of the Cambridge Philosophical Society* **1845**, *8*, 287–305.
206. Blandford, R.; Narayan, R. Cosmological Applications of Gravitational Lensing. *Annual Review of Astronomy and Astrophysics* **1992**, *30*, 311–358. https://doi.org/10.1146/annurev.aa.30.090192.001523.
207. Schneider, P.; Ehlers, J.; Falco, E. *Gravitational Lenses*; Springer New York, 1992. https://doi.org/10.1007/978-1-4612-2756-4.
208. Bartelmann, M. Gravitational lensing. *Classical and Quantum Gravity* **2010**, *27*, 233001. https://doi.org/10.1088/0264-9381/27/23/233001.
209. Blandford, R.; Narayan, R. Fermat's principle, caustics, and the classification of gravitational lens images. *The Astrophysical Journal* **1986**, *310*, 568. https://doi.org/10.1086/164709.
210. Petters, A. Arnold's singularity theory and gravitational lensing. *Journal of Mathematical Physics* **1993**, *34*, 3555–3581. https://doi.org/10.1063/1.530045.
211. Petters, A.; Levine, H.; Wambsganss, J., Critical Points and Stability. In *Singularity Theory and Gravitational Lensing*; Progress in Mathematical Physics, Birkhäuser Boston, 2001; pp. 209–286. https://doi.org/10.1007/978-1-4612-0145-8_7.
212. Kakigi, Y.; Okamura, T.; Fukuyama, T. GRAVITATIONAL LENSING AND CATASTROPHE THEORY. *International Journal of Modern Physics D* **1995**, *04*, 685–710. https://doi.org/10.1142/s0218271895000466.
213. Petters, A.; Werner, M. Mathematics of gravitational lensing: multiple imaging and magnification. *General Relativity and Gravitation* **2011**, *42*, 2011–2046. https://doi.org/10.1007/s10714-010-0968-6.
214. Pound, R.; Rebka, G. Apparent Weight of Photons. *Physical Review Letters* **1960**, *4*, 337–341. https://doi.org/10.1103/physrevlett.4.337.
215. Ashby, N. Relativity and the Global Positioning System. *Physics Today* **2002**, *55*, 41–47. https://doi.org/10.1063/1.1485583.
216. Petit, G.; Wolf, P. Relativistic theory for time comparisons: a review. *Metrologia* **2005**, *42*, S138–S144. https://doi.org/10.1088/0026-1394/42/3/s14.
217. Shapiro, I. Fourth Test of General Relativity. *Physical Review Letters* **1964**, *13*, 789–791.
218. Shapiro, I.; Pettengill, G.; Ash, M.; Stone, M.; Smith, W.; Ingalls, R.; Brockelman, R. Fourth Test of General Relativity: Preliminary Results. *Physical Review Letters* **1968**, *20*, 1265–1269. https://doi.org/10.1103/physrevlett.20.1265.
219. Navarro, J.; Frenk, C.; White, S. A Universal Density Profile from Hierarchical Clustering. *The Astrophysical Journal* **1997**, *490*, 493–508. https://doi.org/10.1086/304888.
220. Sharma, A.; Khoury, J.; Lubensky, T. The equation of state of dark matter superfluids. *Journal of Cosmology and Astroparticle Physics* **2019**, *2019*, 054–054. https://doi.org/10.1088/1475-7516/2019/05/054.
221. Berezhiani, L.; Cintia, G.; Khoury, J. Thermalization, fragmentation, and tidal disruption: The complex galactic dynamics of dark matter superfluidity. *Physical Review D* **2023**, *107*, 123010. https://doi.org/10.1103/physrevd.107.123010.

© 2026 by the author(s). Distributed under a Creative Commons CC BY license.

Preprints.org (www.preprints.org) | NOT PEER-REVIEWED | Posted: 7 September 2026 doi:10.20944/preprints202608.2283.v2

222. Barceló, C.; Liberati, S.; Sonego, S.; Visser, M. Fate of gravitational collapse in semiclassical gravity. *Physical Review D* **2008**, *77*, 44032. https://doi.org/10.1103/physrevd.77.044032.
223. Barceló, C.; Liberati, S.; Sonego, S.; Visser, M. Black Stars, Not Holes. *Scientific American* **2009**, *301*, 38–45. https://doi.org/10.1038/scientificamerican1009-38.
224. Steinhauer, J. Observation of quantum Hawking radiation and its entanglement in an analogue black hole. *Nature Physics* **2016**, *12*, 959–965. https://doi.org/10.1038/nphys3863.
225. Weinfurtner, S.; Tedford, E.; Penrice, M.; Unruh, W.; Lawrence, G. Measurement of Stimulated Hawking Emission in an Analogue System. *Physical Review Letters* **2011**, *106*, 21302. https://doi.org/10.1103/physrevlett.106.021302.
226. Hawking, S. Black hole explosions? *Nature* **1974**, *248*, 30–31. https://doi.org/10.1038/248030a0.
227. Hawking, S. Particle creation by black holes. *Communications In Mathematical Physics* **1975**, *43*, 199–220. https://doi.org/10.1007/bf02345020.
228. Stefan, J. Über die Beziehung zwischen der Wärmestrahlung und der Temperatur. *Sitzungsberichte der Kaiserlichen Akademie der Wissenschaften in Wien* **1879**, *79*, 391–428.
229. Vinen, W.; Niemela, J. Quantum Turbulence. *Journal of Low Temperature Physics* **2002**, *128*, 167–231. https://doi.org/10.1023/a:1019695418590.
230. Almheiri, A.; Engelhardt, N.; Marolf, D.; Maxfield, H. The entropy of bulk quantum fields and the entanglement wedge of an evaporating black hole. *Journal of High Energy Physics* **2019**, *2019*, 63. https://doi.org/10.1007/jhep12(2019)063.
231. Penington, G. Entanglement wedge reconstruction and the information paradox. *Journal of High Energy Physics* **2020**, *2020*. https://doi.org/10.1007/JHEP04(2020)002.
232. Peters, P.; Mathews, J. Gravitational Radiation from Point Masses in a Keplerian Orbit. *Physical Review* **1963**, *131*, 435–440. https://doi.org/10.1103/physrev.131.435.
233. Peters, P. Gravitational Radiation and the Motion of Two Point Masses. *Physical Review* **1964**, *136*, B1224–B1232. https://doi.org/10.1103/physrev.136.b1224.
234. Taylor, J.; Weisberg, J. A new test of general relativity - Gravitational radiation and the binary pulsar PSR 1913+16. *The Astrophysical Journal* **1982**, *253*, 908. https://doi.org/10.1086/159690.
235. Weisberg, J.; Huang, Y. RELATIVISTIC MEASUREMENTS FROM TIMING THE BINARY PULSAR PSR B1913+16. *The Astrophysical Journal* **2016**, *829*, 55. https://doi.org/10.3847/0004-637x/829/1/55.
236. DeWitt, B.S. Quantum Theory of Gravity. I. The Canonical Theory. *Physical Review* **1967**, *160*, 1113–1148. https://doi.org/10.1103/PhysRev.160.1113.
237. Ferrero, R. Asymptotic Safety and Canonical Quantum Gravity. *International Journal of Modern Physics A* **2026**, *41*, 2530023, [arXiv:gr-qc/2507.14296]. https://doi.org/10.1142/S0217751X25300236.
238. 't Hooft, G.; Veltman, M.J.G. One-loop divergencies in the theory of gravitation. *Annales de l'Institut Henri Poincaré A* **1974**, *20*, 69–94.
239. Goroff, M.H.; Sagnotti, A. The ultraviolet behavior of Einstein gravity. *Nuclear Physics B* **1986**, *266*, 709–736. https://doi.org/10.1016/0550-3213(86)90193-8.
240. Stelle, K.S. Renormalization of Higher-Derivative Quantum Gravity. *Physical Review D* **1977**, *16*, 953–969. https://doi.org/10.1103/PhysRevD.16.953.
241. Burgess, C.P. Quantum Gravity in Everyday Life: General Relativity as an Effective Field Theory. *Living Reviews in Relativity* **2004**, *7*. https://doi.org/10.12942/lrr-2004-5.
242. Sakharov, A. Violation of CP Invariance, C asymmetry, and baryon asymmetry of the universe. *JETP Lett.* **1967**, *5*, 24–27. https://doi.org/10.1142/9789812815941_0013.
243. Reuter, M. Nonperturbative Evolution Equation for Quantum Gravity. *Physical Review D* **1998**, *57*, 971–985. https://doi.org/10.1103/PhysRevD.57.971.
244. Eichhorn, A. Asymptotically Safe Quantum Gravity and Its Phenomenology—A Review, 2026, [arXiv:gr-qc/2606.21522]. https://doi.org/10.48550/arXiv.2606.21522.
245. Pitaevskii, L.; Stringari, S. *Bose–Einstein Condensation and Superfluidity*; Vol. 164, *International Series of Monographs on Physics*, Oxford University Press, 2016. https://doi.org/10.1093/acprof:oso/9780198758884.001.0001.
246. Braunstein, S.L.; Faizal, M.; Krauss, L.M.; Marino, F.; Shah, N.A. Analogue Simulations of Quantum Gravity with Fluids. *Nature Reviews Physics* **2023**, *5*, 612–622, [arXiv:gr-qc/2402.16136]. https://doi.org/10.1038/s42254-023-00630-y.

© 2026 by the author(s). Distributed under a Creative Commons CC BY license.

Preprints.org (www.preprints.org) | NOT PEER-REVIEWED | Posted: 7 September 2026 doi:10.20944/preprints202608.2283.v2

247. Eckert, D.; Jauzac, M.; Shan, H.; Kneib, J.P.; Erben, T.; Israel, H.; Jullo, E.; Klein, M.; Massey, R.; Richard, J.; et al. Warm–hot baryons comprise 5–10 per cent of filaments in the cosmic web. *Nature* **2015**, *528*, 105–107. https://doi.org/10.1038/nature16058.
248. De Graaff, A.; Cai, Y.C.; Heymans, C.; Peacock, J. Missing baryons in the cosmic web revealed by the Sunyaev-Zel'dovich effect. *Science* **2018**, *361*, 282–284. https://doi.org/10.1126/science.aau0824.
249. Codis, S.; Pichon, C.; Pogosyan, D. Spin alignments within the cosmic web: a theory of constrained tidal torques near filaments. *Monthly Notices of the Royal Astronomical Society* **2015**, *452*, 3369–3393. https://doi.org/10.1093/mnras/stv1570.
250. Steigman, G. Primordial Nucleosynthesis in the Precision Cosmology Era. *Annual Review of Nuclear and Particle Science* **2007**, *57*, 463–491. https://doi.org/10.1146/annurev.nucl.56.080805.140437.
251. Cooke, R.; Pettini, M.; Steidel, C. One Percent Determination of the Primordial Deuterium Abundance. *The Astrophysical Journal* **2018**, *855*, 102. https://doi.org/10.3847/1538-4357/aab530.
252. Penzias, A.; Wilson, R. A Measurement of Excess Antenna Temperature at 4080 Mc/s. *The Astrophysical Journal* **1965**, *142*, 419. https://doi.org/10.1086/148307.
253. Planck Collaboration. Planck 2018 results. *Astronomy and Astrophysics* **2020**, *641*, A6. https://doi.org/10.1051/0004-6361/201833910.
254. Alam, S.; Aubert, M.; Avila, S.; Balland, C.; Bautista, J.E.; et al. Completed SDSS-IV extended Baryon Oscillation Spectroscopic Survey: Cosmological implications from two decades of spectroscopic surveys at the Apache Point Observatory. *Physical Review D* **2021**, *103*, 083533. https://doi.org/10.1103/physrevd.103.083533.
255. Tolman, R.; Ehrenfest, P.; Podolsky, B. On the Gravitational Field Produced by Light. *Physical Review* **1931**, *37*, 602–615. https://doi.org/10.1103/physrev.37.602.
256. Faraoni, V.; Dumse, R.M. The Gravitational Interaction of Light: From Weak to Strong Fields. *General Relativity and Gravitation* **1999**, *31*, 91–105. https://doi.org/10.1023/a:1018867405133.
257. Rätzel, D.; Wilkens, M.; Menzel, R. Gravitational properties of light—the gravitational field of a laser pulse. *New Journal of Physics* **2016**, *18*, 023009. https://doi.org/10.1088/1367-2630/18/2/023009.
258. Rossi, B.; Hall, D. Variation of the Rate of Decay of Mesotrons with Momentum. *Physical Review* **1941**, *59*, 223–228. https://doi.org/10.1103/physrev.59.223.
259. Frisch, D.H.; Smith, J.H. Measurement of the Relativistic Time Dilation Using μ-Mesons. *American Journal of Physics* **1963**, *31*, 342–355. https://doi.org/10.1119/1.1969508.
260. Ives, H.; Stilwell, G. An Experimental Study of the Rate of a Moving Atomic Clock. *Journal of the Optical Society of America* **1938**, *28*, 215. https://doi.org/10.1364/josa.28.000215.
261. Saathoff, G.; Karpuk, S.; Eisenbarth, U.; Huber, G.; Krohn, S.; et al. Improved Test of Time Dilation in Special Relativity. *Physical Review Letters* **2003**, *91*, 190403. https://doi.org/10.1103/physrevlett.91.190403.
262. Botermann, B.; Bing, D.; Geppert, C.; Gwinner, G.; Hänsch, T.W.; et al. Test of Time Dilation Using Stored Li+Ions as Clocks at Relativistic Speed. *Physical Review Letters* **2014**, *113*, 120405. https://doi.org/10.1103/physrevlett.113.120405.
263. Pruttivarasin, T.; Ramm, M.; Porsev, S.G.; Tupitsyn, I.I.; Safronova, M.S.; et al. Michelson-Morley analogue for electrons using trapped ions to test Lorentz symmetry. *Nature* **2015**, *517*, 592–595. https://doi.org/10.1038/nature14091.
264. Smiciklas, M.; Brown, J.M.; Cheuk, L.W.; Smullin, S.J.; Romalis, M.V. New Test of Local Lorentz Invariance Using aNe21–Rb–KComagnetometer. *Physical Review Letters* **2011**, *107*, 171604. https://doi.org/10.1103/physrevlett.107.171604.
265. Hohensee, M.A.; Leefer, N.; Budker, D.; Harabati, C.; Dzuba, V.A.; Flambaum, V.V. Limits on Violations of Lorentz Symmetry and the Einstein Equivalence Principle using Radio-Frequency Spectroscopy of Atomic Dysprosium. *Physical Review Letters* **2013**, *111*, 050401. https://doi.org/10.1103/physrevlett.111.050401.
266. Kostelecký, V.A.; Vargas, A.J. Lorentz and CPT tests with clock-comparison experiments. *Physical Review D* **2018**, *98*, 036003. https://doi.org/10.1103/physrevd.98.036003.
267. Hohensee, M.A.; Lehnert, R.; Phillips, D.F.; Walsworth, R.L. Particle-Accelerator Constraints on Isotropic Modifications of the Speed of Light. *Physical Review Letters* **2009**, *102*, 170402. https://doi.org/10.1103/physrevlett.102.170402.
268. Altschul, B. Bounding isotropic Lorentz violation using synchrotron losses at LEP. *Physical Review D* **2009**, *80*, 091901. https://doi.org/10.1103/physrevd.80.091901.
269. Altschul, B. Laboratory bounds on electron Lorentz violation. *Physical Review D* **2010**, *82*, 016002. https://doi.org/10.1103/physrevd.82.016002.

© 2026 by the author(s). Distributed under a Creative Commons CC BY license.

Preprints.org (www.preprints.org) | NOT PEER-REVIEWED | Posted: 7 September 2026 doi:10.20944/preprints202608.2283.v2

270. Bocquet, J.P.; Moricciani, D.; Bellini, V.; Beretta, M.; Casano, L.; et al. Limits on Light-Speed Anisotropies from Compton Scattering of High-Energy Electrons. *Physical Review Letters* **2010**, *104*, 241601. https://doi.org/10.1103/physrevlett.104.241601.
271. Zhou, L.; Ma, B.Q. A theoretical diagnosis on light speed anisotropy from GRAAL experiment. *Astroparticle Physics* **2012**, *36*, 37–41. https://doi.org/10.1016/j.astropartphys.2012.04.015.
272. Jones, R.V. Aberration of light in a moving medium. *Journal of Physics A: General Physics* **1971**, *4*, L1–L3. https://doi.org/10.1088/0305-4470/4/1/018.
273. Drezet, A. The physical origin of the Fresnel drag of light by a moving dielectric medium. *The European Physical Journal B* **2005**, *45*, 103–110. https://doi.org/10.1140/epjb/e2005-00169-4.
274. Artoni, M.; Carusotto, I.; La Rocca, G.C.; Bassani, F. Fresnel Light Drag in a Coherently Driven Moving Medium. *Physical Review Letters* **2001**, *86*, 2549–2552. https://doi.org/10.1103/physrevlett.86.2549.
275. Baynes, F.N.; Luiten, A.N.; Tobar, M.E. Testing Lorentz invariance using an odd-parity asymmetric optical resonator. *Physical Review D* **2011**, *84*, 081101. https://doi.org/10.1103/physrevd.84.081101.
276. Michimura, Y.; Matsumoto, N.; Ohmae, N.; Kokuyama, W.; Aso, Y.; et al. New Limit on Lorentz Violation Using a Double-Pass Optical Ring Cavity. *Physical Review Letters* **2013**, *110*, 200401. https://doi.org/10.1103/physrevlett.110.200401.
277. Teukolsky, S.A. The explanation of the Trouton-Noble experiment revisited. *American Journal of Physics* **1996**, *64*, 1104–1109. https://doi.org/10.1119/1.18329.
278. Franklin, J. The lack of rotation in the Trouton-Noble experiment. *European Journal of Physics* **2006**, *27*, 1251–1256. https://doi.org/10.1088/0143-0807/27/5/024.
279. Waitukaitis, S.R.; Jaeger, H.M. Impact-activated solidification of dense suspensions via dynamic jamming fronts. *Nature* **2012**, *487*, 205–209. https://doi.org/10.1038/nature11187.
280. Han, E.; Peters, I.R.; Jaeger, H.M. High-speed ultrasound imaging in dense suspensions reveals impact-activated solidification due to dynamic shear jamming. *Nature Communications* **2016**, *7*. https://doi.org/10.1038/ncomms12243.
281. Han, E.; Wyart, M.; Peters, I.R.; Jaeger, H.M. Shear fronts in shear-thickening suspensions. *Physical Review Fluids* **2018**, *3*, 073301. https://doi.org/10.1103/physrevfluids.3.073301.
282. Rømcke, O.; Peters, I.R.; Hearst, R.J. Getting jammed in all directions: Dynamic shear jamming around a cylinder towed through a dense suspension. *Physical Review Fluids* **2021**, *6*, 063301. https://doi.org/10.1103/physrevfluids.6.063301.
283. Slutzky, M.; Pelosse, A.; van der Naald, M.; Jaeger, H.M. Fracture and failure of shear-jammed dense suspensions under impact. *Physical Review E* **2026**, *113*. https://doi.org/10.1103/dtp1-hrzp.

Disclaimer/Publisher's Note: The statements, opinions and data contained in all publications are solely those of the individual author(s) and contributor(s) and not of MDPI and/or the editor(s). MDPI and/or the editor(s) disclaim responsibility for any injury to people or property resulting from any ideas, methods, instructions or products referred to in the content.

© 2026 by the author(s). Distributed under a Creative Commons CC BY license.